Effects of Torsional Dynamics on Nonlinear Generator Control

by

Eric H. Allen

Submitted to the Department of Electrical Engineering and Computer Science
in partial fulfillment of the requirements for the degree of

Master of Science in Electrical Engineering

at the

MASSACHUSETTS INSTITUTE OF TECHNOLOGY

February 1995

Author .....
Department of Electrical Engineering and Computer Science
January 20, 1995

Certified by .....
Marija D. Ilić
Senior Research Scientist
Thesis Supervisor

Accepted by .....
Frederic Morgenthaler
Chairman, Departmental Committee on Graduate Students

Effects of Torsional Dynamics on Nonlinear Generator Control

by

Eric H. Allen

Submitted to the Department of Electrical Engineering and Computer Science
on January 20, 1995, in partial fulfillment of the
requirements for the degree of
Master of Science in Electrical Engineering

Abstract

Feedback linearizing generator excitation control designs have demonstrated improved performance over conventional controls, such as power system stabilizers, in simulations. This type of control aims to cancel the nonlinearities in the dynamics of the generator, resulting in a closed-loop system that is linear. However, feedback linearizing control, or FBLC, depends on a measurement of the rotor acceleration, which is subject to considerable noise from shaft vibrations. This thesis examines the impact that these vibrations have on the operation of FBLC. Several possibilities for reducing the effects of torsional shaft dynamics on control performance are also explored.

The torsional dynamics are represented by a linear model. The addition of these dynamics does not affect the linearity of the closed-loop FBLC system, although the closed-loop eigenvalue placement is distorted. Furthermore, the damping of the shaft modes is much larger in the presence of FBLC. In fact, FBLC is capable of damping out shaft oscillations that are otherwise unstable due to subsynchronous resonance. However, the torsional dynamics greatly increase the tendency of the field voltage to saturate at its upper and lower limits, degrading the performance of FBLC.

Several options for improving FBLC performance are considered. The acceleration measurement may be low-pass filtered; however, the phase shift from the filter in the torsional range is capable of exciting the shaft modes, leading to instability. Redesigning FBLC to include torsional dynamics produces even larger oscillations in the field voltage and poor performance in practical situations. An alternative control strategy is sliding mode control, which allows for a range of modeling errors. Because torsional oscillations produce large, high frequency uncertainties, sliding mode control does not provide any improvement over FBLC. Without modifications, FBLC is observed to remain stable over large variations in shaft parameters.

Thesis Supervisor: Marija D. Ilić
Title: Senior Research Scientist

Acknowledgments

The author wishes to acknowledge the following people who made this thesis possible:

Dr. Marija Ilić, who has provided continual support and advice for this project;

Jeff Chapman, for his knowledge of power systems, feedback linearizing control, and the quirks of Simulink;

Vivian Mizuno, who has offered her time and work as well as lots of cheer every day;

The students and faculty of LEES, who have provided friendship as well as help and answers to even the simplest questions;

My parents Owen and Candace, my sister Debbie, my brother Scott, and all members of my family, who have given unending love and concern;

God, for all of the gifts He has given me

Contents

List of Figures

List of Tables

Chapter 1

Introduction

Recently, several nonlinear schemes for generator excitation control have been proposed [1, 2]. These nonlinear schemes have demonstrated superior performance in simulations to conventional controls. However, nonlinear generator excitation control requires a measurement of the acceleration of the rotor, and this measurement is very susceptable to noise arising from torsional vibrations in the generator shaft. The goal of this thesis is to determine the effects of these vibrations on the performance of nonlinear control and find ways to minimize the impact of the shaft dynamics on the closed-loop operation of the system.

The principle nonlinear control method that is examined is Feedback Linearizing Control, or FBLC. The rationale of FBLC is to use the control input to cancel the nonlinearities of the generator dynamics and produce a closed-loop generator model that is linear [2, 3]. Sliding mode control is another nonlinear control method which allows for uncertainties in the system parameters. A sliding control design will be developed and compared with FBLC to see which design is less sensitive to the presence of shaft oscillations.

There are two basic approaches for examining dynamical systems of interest in this thesis. The first approach is to develop a state-space model for the system and use analytical methods of study. In particular, if the state-space model is linear, there is a large body of theory which can be applied in order to characterize the system's behavior [4, 5]. The second method is to use numerical simulation routines to calculate the response of the system to known inputs [6]. This method does not provide the insight that the linear analysis does, but the simulation routines can provide accurate results despite the presence of highly nonlinear dynamics. Simulation is also much more generally applicable; it is not as restricted as the analytical methods. Both methods complement each other very well; the simulation routines can verify the predictions of the analysis and show the effects of dynamics not included in the linear model.

The first step in studying the problem is to obtain a good dynamic model of the shaft. Shaft models have been developed and used in the study of subsynchronous resonance because of the importance of shaft dynamics in the phenomenon [7, 8, 9, 10]. Shaft models have also been used in other studies, such as the effect of torsional dynamics on shaft fatigue [11]. The shaft models used for these purposes are linear

models, and we will use a similar model to simulate shaft vibrations.

After a shaft model is developed, it is coupled with the generator model to form a composite state-space model of the generator/shaft system. The feedback linearizing controller without torsional modeling is used to control the generator/shaft with torsional dynamics. It can be shown that this combination is still a stable linear system, although the addition of torsional dynamics do alter the performance of the system. The most significant consequence of the torsional dynamics is that they cause the field voltage to experience high amplitude, high frequency oscillations. The field voltage thus reaches its upper and lower limits much more frequently with the presence of torsional oscillations. Field voltage saturation transforms the system into a nonlinear, open-loop system, reducing the effectiveness of the control.

Since the field voltage oscillations cause problems, it is reasonable to try to remove the oscillations by averaging the field voltage over one cycle of a 60 Hz wave. This technique, however, is observed to be ineffective and even damaging. The averaged field voltage does not damp the torsional oscillations and in some cases, even excites these modes. The use of a Butterworth filter on the acceleration measurement allows more control of the phase, and in certain cases, is able to suppress the field voltage saturation and effectively decouple the torsional dynamics from the low frequency generator response, allowing FBLC to perform almost as well as it did without torsional dynamics. However, this approach is potentially dangerous, as unmodeled dynamics at certain frequencies are likely to be excited by the presence of the filter.

Another possible scheme for handling the torsional oscillations is to redesign the controller to include torsional state information. However, this technique is observed to produce enormous oscillations in the field voltage, and it provides little control of the system.

The FBLC controller significantly reduces the damping of the torsional modes. In fact, the damping of these modes is sufficient to prevent these modes from being excited due to the presence of a series capacitor on the transmission line. FBLC is capable of stabilizing a system which is otherwise unstable from subsynchronous resonance. Since an FBLC controller with filtering is much less effective at damping out the torsional oscillations, it is not surprising that the filtering makes FBLC less effective in stabilizing systems prone to subsynchronous resonance, although the filtered controller is able to prevent the oscillations from growing without bound.

Since it may well be best to not modify FBLC to include torsional dynamics, it is important to know whether FBLC without torsional modeling remains stable in the presence of torsional dynamics. It is observed that the system does indeed remain stable for a variety of parameter values, although proving this assertion is difficult.

Finally, a sliding mode controller will be implemented and tested on a generator with torsional dynamics. It is expected that sliding control will improve on the performance of FBLC, since sliding control takes into account uncertainties in the model. However, it is observed that the uncertainties from torsional dynamics are high frequency oscillations of large amplitude, and the resulting performance of sliding control is essentially no different from FBLC.

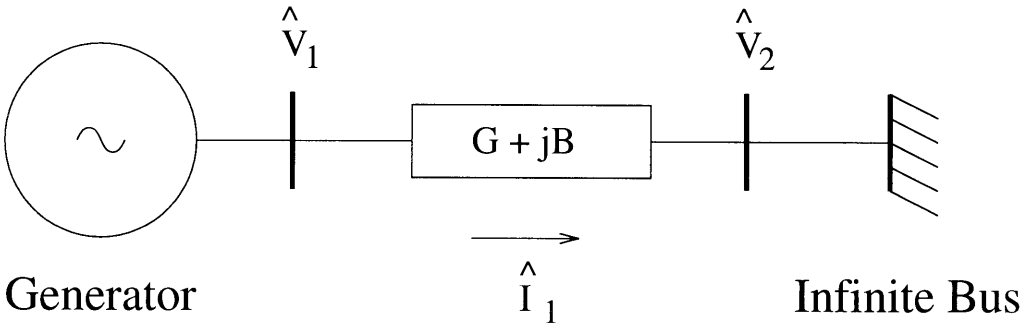

Figure 1-1: Diagram of the single machine, infinite bus model.

1.1 Single Machine Infinite Bus (SMIB) Model

Throughout this thesis, the system being studied is a single generator connected through a transmission line to an infinite bus, as shown in Figure 1-1. This model generally provides a good representation of a single generator connected to a large network and will allow us to analyze the effects of torsional oscillations in the shaft without being burdened by extraneous complications.

1.1.1 Generator Model

For the purposes of controller design, a third order dynamic model is used to represent the generator. This model has a state vector $[\delta\, \omega\, E'_q]^T$ and evolves according to:

$$\dot{\delta} = \omega - \omega_o \tag{1.1}$$

$$\dot{\omega} = -\frac{\omega_o}{2H}\left[D\frac{\omega}{\omega_o} + E'_d i_d + E'_q i_q - P_m\right] \tag{1.2}$$

$$\dot{E}'_q = \frac{1}{T'_{d0}}\left[-E'_q - (x_d - x'_d)i_d + E_{fd}\right] \tag{1.3}$$

$$E'_d = (x_q - x'_q)i_q \tag{1.4}$$

The third order generator model is used in all of the theoretical developments throughout this text.

However, in numerical simulations a higher order model of the generator is used in order to include the effects of generator dynamics that are not modeled in the controller design. The generator model for simulations is a sixth order model with state vector $[\delta\, \omega\, E'_d\, E'_q\, E''_d\, E''_q]^T$) [2, 12, 13]. This model is used *only* for simulations and is not used for theoretical explanations of the results.

1.1.2 Model of the Network

The transmission line model is simply a constant admittance of $G + jB$ between the generator and the infinite bus (Figure 1-1). $\hat{V}_1 = V_{d1} + jV_{q1}$ is the generator voltage, and $\hat{V}_2 = W_d + jW_q$ is the infinite bus voltage. Note that the transmission line admittance includes the armature resistance and transient reactance, so that $\hat{V}_1$ may be calculated by taking the inverse Park transform of E'_d and E'_q [2]:

$$\hat{V}_1 = (E'_d + jE'_q)e^{-j(\pi/2-\delta)} \tag{1.5}$$

The exponential in this equation may be written as:

$$e^{-j(\pi/2-\delta)} = \sin\delta - j\cos\delta \tag{1.6}$$

The real and imaginary components of $\hat{V}_1$ are easily found by multiplication:

$$V_{d1} = E'_d \sin\delta + E'_q \cos\delta \tag{1.7}$$

$$V_{q1} = E'_q \sin\delta - E'_d \cos\delta \tag{1.8}$$

In the SMIB model, it is possible to express the armature currents i_d and i_q as functions of the state variable E'_q. These equations are used in order to analytically evaluate the partial derivatives which are required by nonlinear control methods. Equation (1.5) demonstrates that the generator terminal voltage is a function of E'_q. Since $\hat{V}_1$ and $\hat{V}_2$ are both known, we can find the transmission line current $\hat{I}_1 = I_{d1} + jI_{q1}$:

$$\hat{I}_1 = (G + jB)(\hat{V}_1 - \hat{V}_2) \tag{1.9}$$

Upon substituting for $\hat{V}_1$ and $\hat{V}_2$ and separating the real and imaginary parts, we find:

$$I_{d1} = G(V_{d1} - W_d) - B(V_{q1} - W_q) \tag{1.10}$$

$$I_{q1} = B(V_{d1} - W_d) + G(V_{q1} - W_q) \tag{1.11}$$

Finally, we apply a Park transform to $\hat{I}_1$ to find the armature currents in the machine frame of reference:

$$i_d + ji_q = \hat{I}_1 e^{j(\pi/2-\delta)} \tag{1.12}$$

Note from complex algebra that:

$$e^{j(\pi/2-\delta)} = \sin\delta + j\cos\delta \tag{1.13}$$

Combining equations (1.10) and (1.11) with equation (1.13):

$$i_d = [G(V_{d1} - W_d) - B(V_{q1} - W_q)]\sin\delta - [B(V_{d1} - W_d) + G(V_{q1} - W_q)]\cos\delta \tag{1.14}$$

$$i_q = [G(V_{d1} - W_d) - B(V_{q1} - W_q)]\cos\delta + [B(V_{d1} - W_d) + G(V_{q1} - W_q)]\sin\delta \tag{1.15}$$

We will rearrange the terms into a more convenient form:

$$\begin{aligned} i_d &= (-GW_d + BW_q)\sin\delta + (BW_d + GW_q)\cos\delta + V_{d1}(G\sin\delta - B\cos\delta) \\ &\quad + V_{q1}(-B\sin\delta - G\cos\delta) \end{aligned} \tag{1.16}$$

$$\begin{aligned} i_q &= (-GW_d + BW_q)\cos\delta - (BW_d + GW_q)\sin\delta + V_{d1}(G\cos\delta + B\sin\delta) \\ &\quad + V_{q1}(-B\cos\delta + G\sin\delta) \end{aligned} \tag{1.17}$$

The next step in the derivation is to substitute equations (1.7) and (1.8) into equations (1.16) and (1.17):

$$\begin{aligned} i_d &= (-GW_d + BW_q)\sin\delta + (BW_d + GW_q)\cos\delta + E'_d G\sin^2\delta \\ &\quad + (E'_q G - E'_d B)\sin\delta\cos\delta - E'_q B\cos^2\delta - E'_q B\sin^2\delta \\ &\quad + (E'_d B - E'_q G)\sin\delta\cos\delta + E'_d G\cos^2\delta \end{aligned} \tag{1.18}$$

$$\begin{aligned} i_q &= (-GW_d + BW_q)\cos\delta - (BW_d + GW_q)\sin\delta + E'_d B\sin^2\delta \\ &\quad + (E'_q B + E'_d G)\sin\delta\cos\delta + E'_q G\cos^2\delta + E'_q G\sin^2\delta \\ &\quad + (-E'_d G - E'_q B)\sin\delta\cos\delta + E'_d B\cos^2\delta \end{aligned} \tag{1.19}$$

These equations reduce to:

$$i_d = GE'_d - BE'_q + (BW_q - GW_d)\sin\delta + (BW_d + GW_q)\cos\delta \tag{1.20}$$

$$i_q = GE'_q + BE'_d + (-BW_d - GW_q)\sin\delta + (BW_q - GW_d)\cos\delta \tag{1.21}$$

The final step is to remove E'_d from these equations. Recall that in the third order machine model, E'_d is expressed as an algebriac constraint:

$$E'_d = (x_q - x'_q)i_q \tag{1.22}$$

Since E'_d is a function of i_q, we first substitute the relation for E'_d into equation (1.21) to find i_q explicitly as a function of E'_q and network parameters:

$$i_q = \frac{GE'_q + (-BW_d - GW_q)\sin\delta + (BW_q - GW_d)\cos\delta}{1 - B(x_q - x'_q)} \tag{1.23}$$

Similarly, i_d may be expressed

$$i_d = G(x_q - x'_q)i_q - BE'_q + (BW_q - GW_d)\sin\delta + (BW_d + GW_q)\cos\delta \tag{1.24}$$

Instead of substituting for i_q in this last equation, we will simply express i_d as a function of i_q.

Feedback linearizing excitation control requires knowledge of the partial derivatives $\frac{\partial i_d}{\partial E'_q}$ and $\frac{\partial i_q}{\partial E'_q}$ [2]. Since we now have mathematical expressions for i_d and i_q, we

can evaluate these partial derivatives analytically:

$$\frac{\partial i_q}{\partial E'_q} = \frac{G}{1 - B(x_q - x'_q)} \tag{1.25}$$

$$\frac{\partial i_d}{\partial E'_q} = \frac{G^2(x_q - x'_q)}{1 - B(x_q - x'_q)} - B \tag{1.26}$$

FBLC also requires the time derivative of i_d and i_q, denoted as $\dot{i}_d$ and $\dot{i}_q$. We can express these derivatives analytically as well:

$$\begin{aligned} \dot{i}_q &= \frac{1}{1 - B(x_q - x'_q)} \left[\frac{G}{T'_{d0}}[-E'_q - (x_d - x'_d)i_d] + \frac{G}{T'_{d0}} E_{fd} \right. \\ &\quad \left. + (\omega - \omega_o)[(-BW_d - GW_q)\cos\delta + (GW_d - BW_q)\sin\delta] \right] \end{aligned} \tag{1.27}$$

$$\begin{aligned} \dot{i}_d &= \frac{B}{T'_{d0}} \left(E'_q + (x_d - x'_d)i_d \right) - \frac{B}{T'_{d0}} E_{fd} + G(x_q - x'_q)\dot{i}_q \\ &\quad + (\omega - \omega_o)[(-GW_q - BW_d)\sin\delta + (BW_q - GW_d)\cos\delta] \end{aligned} \tag{1.28}$$

In these equations, we have used the state equation from the generator model (equation (1.3)) to substitute for E'_q.

1.1.3 Sample Model for Simulations

In order to obtain meaningful simulation results, the equations must include numbers that are representative values of the generator and network parameters. The generator parameters for all simulations in this thesis may be found under the Oswego unit (bus 4305) on page 102 in [12]. The network parameters are: $G = 0.072758$, $B = -1.1126$, $W_d = 0.9164$, and $W_q = 0.20473$. With these parameters, the equilibrium value of δ, denoted as δ_o, is 1.3036 radians.

Chapter 2

Modeling of Torsional Dynamics

2.1 Model of Shaft Dynamics

Figure 2-1 shows a typical shaft in a power generator. The generator, turbine, and shaft are commonly modeled as a series of rotating masses connected by torsional springs. Each mass also experiences damping torques. The two turbines will be denoted as masses 1 and 2, while the generator will be referred to as mass e.

We can develop a mathematical model for the system by starting with Newton's law for rotating masses:

$$J\frac{d^2\theta}{dt^2} = \sum_{i=1}^{n} \tau_i \tag{2.1}$$

where J is the moment of inertia and τ_i is one of n torques acting on the mass. The equations for our shaft system are [7, 11]:

$$J\frac{d^2\theta_1}{dt^2} = \tau_{m1} - D_1\omega_1 - K_{12}(\theta_1 - \theta_2) \tag{2.2}$$

$$J\frac{d^2\theta_2}{dt^2} = \tau_{m2} - D_2\omega_2 - K_{12}(\theta_2 - \theta_1) - K_{2e}(\theta_2 - \theta_e) \tag{2.3}$$

$$J\frac{d^2\theta_e}{dt^2} = -\tau_e - D_e\omega_e - K_{2e}(\theta_e - \theta_2) \tag{2.4}$$

θ_i and ω_i are the angle and speed of each of the masses. τ_{m1} and τ_{m2} are the mechanical torques generated by the turbines, while τ_e is the electrical torque used by the generator. The springs are assumed to obey Hooke's Law; the restoring torque is proportional to the angle of displacement. K_{12} and K_{2e} are the spring constants for the two spring sections in the shaft. The damping torques are proportional to the angular speed of the masses; D_i represents the damping coefficient of each mass. Some models [7] also include shaft damping torques which are proportional to the speed difference across the shaft section. Such models include torque terms of the form $-D_{12}(\omega_1 - \omega_2)$. Generally, the shaft damping torques are very small and often neglected; this approach is used in [11] and is also used throughout this thesis.

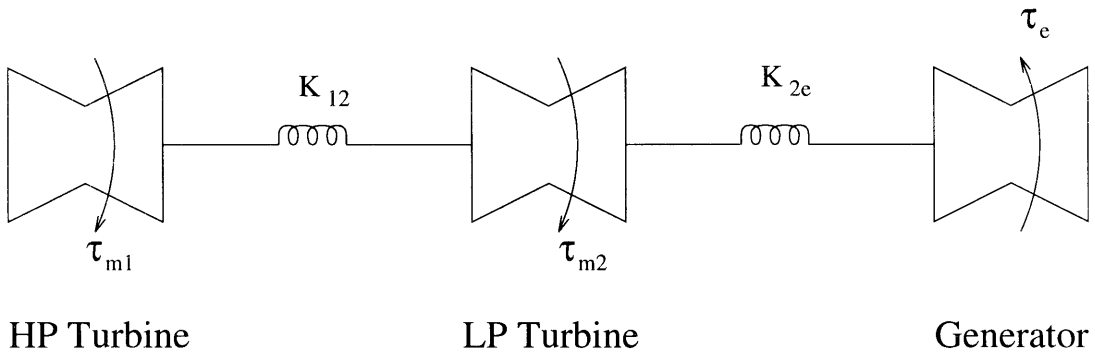

Figure 2-1: The torsional spring-mass model.

2.2 Per Unit Equations

In common practice, per unit equations are used, where the quantities are dimensionless and given with respect to a fixed base. To convert the torsional model to a per unit system, we first multiply equations (2.2) through (2.4) by ω_o, which is the base frequency of the system. Since $P_i = \tau_i \omega_o$, where P is power, we have:

$$J\omega_o \frac{d^2\theta_1}{dt^2} = P_{m1} - D_1\omega_o\omega_1 - K_{12}\omega_o(\theta_1 - \theta_2) \tag{2.5}$$

$$J\omega_o \frac{d^2\theta_2}{dt^2} = P_{m2} - D_2\omega_o\omega_2 - K_{12}\omega_o(\theta_2 - \theta_1) - K_{2e}\omega_o(\theta_2 - \theta_e) \tag{2.6}$$

$$J\omega_o \frac{d^2\theta_e}{dt^2} = -P_e - D_e\omega_o\omega_e - K_{2e}\omega_o(\theta_e - \theta_2) \tag{2.7}$$

Next, we define a base quantity and denote it by S_{B3}. S_{B3} has dimensions of power. After dividing the preceding equations by S_{B3}, each term will be dimensionless. We further define:

$$H_i = \frac{J\omega_o^2}{2S_{B3}} \tag{2.8}$$

$$D_{iu} = \frac{D_i\omega_o^2}{S_{B3}} \tag{2.9}$$

$$K_{iu} = \frac{K_i\omega_o^2}{S_{B3}} \tag{2.10}$$

$$P_{iu} = \frac{P_i}{S_{B3}} \tag{2.11}$$

H_i has units of time, K_{iu} has units of time^{-1}, and D_{iu} and P_{iu} are dimensionless. After dividing equations (2.5) through (2.7) by S_{B3} and substituting the quantities

defined above, we obtain [7]:

$$\frac{2H_1}{\omega_o}\frac{d^2\theta_1}{dt^2} = P_{1u} - D_{1u}\frac{\omega_1}{\omega_o} - K_{12u}\frac{\theta_1 - \theta_2}{\omega_o} \tag{2.12}$$

$$\frac{2H_2}{\omega_o}\frac{d^2\theta_2}{dt^2} = P_{2u} - D_{2u}\frac{\omega_2}{\omega_o} - K_{12u}\frac{\theta_2 - \theta_1}{\omega_o} - K_{2eu}\frac{\theta_2 - \theta_e}{\omega_o} \tag{2.13}$$

$$\frac{2H_e}{\omega_o}\frac{d^2\theta_e}{dt^2} = -P_{eu} - D_{eu}\frac{\omega_e}{\omega_o} - K_{2eu}\frac{\theta_e - \theta_2}{\omega_o} \tag{2.14}$$

Up to this point, we have been giving angles with respect to an absolute, fixed reference. However, electric machines normally operate at a given speed (ω_o), which is non-zero. We wish to change the angles in the equations so that the component which is proportional to (ω_o) is eliminated. In other words, we will substitute:

$$\theta_i = \delta_i + \omega_o t \tag{2.15}$$

Actually, since $\ddot{\theta}_i = \ddot{\delta}_i$, and the $\omega_o t$ terms cancel in equations (2.12) through (2.14), we can simply replace θ_i with δ_i in these equations, giving:

$$\frac{2H_1}{\omega_o}\frac{d^2\delta_1}{dt^2} = P_{1u} - D_{1u}\frac{\omega_1}{\omega_o} - K_{12u}\frac{\delta_1 - \delta_2}{\omega_o} \tag{2.16}$$

$$\frac{2H_2}{\omega_o}\frac{d^2\delta_2}{dt^2} = P_{2u} - D_{2u}\frac{\omega_2}{\omega_o} - K_{12u}\frac{\delta_2 - \delta_1}{\omega_o} - K_{2eu}\frac{\delta_2 - \delta_e}{\omega_o} \tag{2.17}$$

$$\frac{2H_e}{\omega_o}\frac{d^2\delta_e}{dt^2} = -P_{eu} - D_{eu}\frac{\omega_e}{\omega_o} - K_{2eu}\frac{\delta_e - \delta_2}{\omega_o} \tag{2.18}$$

Equations (2.16) through (2.18) are the per unit equations for the torsional shaft system.

2.3 State-Space Model of Shaft

The equations in the previous section can be readily converted into a state-space model. A state-space model has equations of the form [4, 5]:

$$\dot{\mathbf{x}} = \mathbf{A}\mathbf{x} + \mathbf{B}\mathbf{u} \tag{2.19}$$

$$\mathbf{y} = \mathbf{C}\mathbf{x} + \mathbf{D}\mathbf{u} \tag{2.20}$$

$\mathbf{x}$ is the vector of states, $\mathbf{u}$ is the inputs, and $\mathbf{y}$ is the outputs. For the shaft model, the choice of outputs is rather arbitrary and not related to the dynamics of the states; hence, we are only concerned with equation (2.19) here.

The torsional model has six states; namely, the angle and rotational speed of each mass. There are three inputs to the system: the two mechanical powers and the electric power. Because:

$$\dot{\delta}_i = \omega_i - \omega_o \tag{2.21}$$

we must include some constants in the state vectors. The conversion of equations (2.16) through (2.18) into matrix form produces the state-space representation of the torsional shaft model:

$$\mathbf{x} = \begin{bmatrix} \delta_1 \\ \omega_1 - \omega_o \\ \delta_2 \\ \omega_2 - \omega_o \\ \delta_e \\ \omega_e - \omega_o \end{bmatrix} \tag{2.22}$$

$$\mathbf{u} = \begin{bmatrix} P_{1u} - D_{1u} \\ P_{2u} - D_{2u} \\ P_{eu} + D_{eu} \end{bmatrix} \tag{2.23}$$

$$\mathbf{A} = \begin{bmatrix} 0 & 1 & 0 & 0 & 0 & 0 \\ -\frac{K_{12u}}{2H_1} & -\frac{D_{1u}}{2H_1} & \frac{K_{12u}}{2H_1} & 0 & 0 & 0 \\ 0 & 0 & 0 & 1 & 0 & 0 \\ \frac{K_{12u}}{2H_2} & 0 & -\frac{K_{12u}+K_{2eu}}{2H_2} & -\frac{D_{2u}}{2H_2} & \frac{K_{2eu}}{2H_2} & 0 \\ 0 & 0 & 0 & 0 & 0 & 1 \\ 0 & 0 & \frac{K_{2eu}}{2H_e} & 0 & -\frac{K_{2eu}}{2H_e} & -\frac{D_{eu}}{2H_e} \end{bmatrix} \tag{2.24}$$

$$\mathbf{B} = \begin{bmatrix} 0 & 0 & 0 \\ \frac{\omega_o}{2H_1} & 0 & 0 \\ 0 & 0 & 0 \\ 0 & \frac{\omega_o}{2H_2} & 0 \\ 0 & 0 & 0 \\ 0 & 0 & -\frac{\omega_o}{2H_e} \end{bmatrix} \tag{2.25}$$

2.4 Sample Torsional Shaft Model

In order to represent the effects of shaft oscillations on nonlinear control, a shaft model with typical parameters is needed. The model developed here was created by using values for J_i, K_i, and D_i from examples in [7]. After converting these quantities to per unit values, the parameters were normalized so that the shaft/generator system would have a predetermined total inertia ($H_{tot} = 3.5$s) while preserving the frequencies of

Number(s)	Eigenvalue	Frequency (Hz)
1,2	$-0.07 \pm j196.54$	31.28
3,4	$-0.07 \pm j151.24$	24.07
5	0.00	–
6	-0.14	–

Table 2.1: Eigenvalues and frequencies of the torsional state-space shaft model.

the original system. The resulting shaft parameters are:

$$\begin{array}{lll} H_1 = 0.3474\text{s} & K_{12u} = 20158\text{s}^{-1} & D_{1u} = 0.08869 \\ H_2 = 1.9927\text{s} & K_{2eu} = 40219\text{s}^{-1} & D_{2u} = 0.5521 \\ H_e = 1.160\text{s} & & D_{eu} = 0.3131 \end{array} \tag{2.26}$$

Now that we have some representative numbers, we can build the matrices that describe the state-space model for the shaft. With the parameters shown above, the eigenvalues of the matrix in equation (2.24) are shown in Table 2.1. In this example, the shaft has oscillatory modes at 24.07 Hz and 31.28 Hz. Typical shaft frequencies are in the range of 10 to 50 Hz, so our example frequencies are well within that range [7].

Chapter 3

Effects of Torsional Dynamics on Feedback Linearizing Control

3.1 The Combined Shaft and Generator Model

We will now develop a model for the entire shaft/generator system by combining the shaft model of the last section with the third order model for the generator from the introduction. Recall that the generator model includes the state variables δ, ω, and E'_q, while E'_d is treated as an algebraic variable. Notice that $\delta = \delta_e$ and $\omega = \omega_e$, meaning that two generator states are also state variables in the shaft dynamics. These two states form a bridge between the shaft and the generator. The equations for the shaft/generator model are:

$$\dot{\delta}_e = \omega_e - \omega_o \tag{3.1}$$

$$\dot{\omega}_e = \frac{\omega_o}{2H_e}\left[K_{2eu}\frac{\delta_2}{\omega_o} - K_{2eu}\frac{\delta_e}{\omega_o} - D_{eu}\frac{\omega_e}{\omega_o} - E'_d i_d - E'_q i_q\right] \tag{3.2}$$

$$\dot{E}'_q = \frac{1}{T'_{d0}}\left[-E'_q - (x_d - x'_d)i_d + E_{fd}\right] \tag{3.3}$$

$$E'_d = (x_q - x'_q)i_q \tag{3.4}$$

$$\dot{\delta}_1 = \omega_1 - \omega_o \tag{3.5}$$

$$\dot{\omega}_1 = \frac{\omega_o}{2H_1}\left[-K_{12u}\frac{\delta_1}{\omega_o} - D_{1u}\frac{\omega_1}{\omega_o} + K_{12u}\frac{\delta_2}{\omega_o} + P_{1u}\right] \tag{3.6}$$

$$\dot{\delta}_2 = \omega_2 - \omega_o \tag{3.7}$$

$$\dot{\omega}_2 = \frac{\omega_o}{2H_2}\left[K_{12u}\frac{\delta_1}{\omega_o} - (K_{12u} + K_{2eu})\frac{\delta_2}{\omega_o} - D_{2u}\frac{\omega_2}{\omega_o} + K_{2eu}\frac{\delta_e}{\omega_o} + P_{2u}\right] \tag{3.8}$$

Notice that $P_{eu} = E'_d i_d + E'_q i_q$.

3.2 Equilibrium Conditions

The model shown in the last section has three inputs. Since the two mechanical power terms change very slowly with time and are virtually unchanged during a fault, we would like to treat these terms as constants and remove them from the equations, so that the only system input is the field voltage. To do this, we will need to find an equilibrium point and subtract the conditions for equilibrium out of the equations, so that only deviations from equilibrium are shown in the equations. We are only concerned here with the steady state value of the six mechanical states (δ_i, ω_i).

To find an equilibrium point, we simply note that at equilibrium, all time derivatives must be zero. We quickly discover that at equilibrium,

$$\omega_1 = \omega_2 = \omega_e = \omega_o \tag{3.9}$$

Next, we must perform some algebra to find the steady state values of the angles. Recall from Chapter 1 that the steady state value of δ_e is δ_o. Then, from equation (3.2), we find that the equilibrium value δ_{2o} of δ_2 is:

$$\delta_{2o} = \delta_o + \frac{\omega_o}{K_{2eu}}(P_{eu} + D_{eu}) \tag{3.10}$$

where we have replaced $E'_d i_d + E'_q i_q$ with P_{eu}. From equation (3.6):

$$\delta_{1o} = \delta_{2o} + \frac{\omega_o}{K_{12u}}(P_{1u} - D_{1u}) \tag{3.11}$$

or:

$$\delta_{1o} = \delta_o + \frac{\omega_o}{K_{12u}}(P_{1u} - D_{1u}) + \frac{\omega_o}{K_{2eu}}(P_{eu} + D_{eu}) \tag{3.12}$$

However, these equations are invalid and meaningless unless equation (3.8) is also zero with these equilibrium values. Substitution of $\delta_1 = \delta_{1o}$, $\delta_2 = \delta_{2o}$, and $\delta_e = \delta_o$ into equation (3.8) gives the relation:

$$P_{1u} - D_{1u} - P_{eu} - D_{eu} - D_{2u} + P_{2u} = 0 \tag{3.13}$$

or:

$$P_{1u} + P_{2u} = P_{eu} + D_{1u} + D_{2u} + D_{eu} \tag{3.14}$$

This equation simply states the obvious observation that the power in must equal the power out in order for equilibrium to exist. Power enters the shaft/generator from the mechanical turbines and is taken out by the generator and also the frictional damping on each mass.

Note that P_{eu} is not constant and changes significantly in a short time during a fault. Therefore, equations (3.10) and (3.12) are only true if the equilibrium value of P_{eu} is used in these equations. Before continuing, we wish to remove P_{eu} from the

equations for δ_{1o} and δ_{2o}:

$$\delta_{1o} = \delta_o + \frac{\omega_o}{K_{12u}}(P_{1u} - D_{1u}) + \frac{\omega_o}{K_{2eu}}(P_{1u} + P_{2u} - D_{1u} - D_{2u}) \tag{3.15}$$

$$\delta_{2o} = \delta_o + \frac{\omega_o}{K_{2eu}}(P_{1u} + P_{2u} - D_{1u} - D_{2u}) \tag{3.16}$$

Now that we know the equilibrium conditions and state values, we may rewrite the generator/shaft model equations as:

$$\dot{\delta}_e = \omega_e - \omega_o \tag{3.17}$$

$$\dot{\omega}_e = \frac{\omega_o}{2H_e}\left[K_{2eu}\frac{\delta_2}{\omega_o} - K_{2eu}\frac{\delta_e}{\omega_o} - D_{eu}\frac{\omega_e}{\omega_o} - E'_d i_d - E'_q i_q\right] \tag{3.18}$$

$$\dot{E}'_q = \frac{1}{T'_{d0}}\left[-E'_q - (x_d - x'_d)i_d + E_{fd}\right] \tag{3.19}$$

$$E'_d = (x_q - x'_q)i_q \tag{3.20}$$

$$\dot{\delta}_1 = \omega_1 - \omega_o \tag{3.21}$$

$$\dot{\omega}_1 = \frac{\omega_o}{2H_1}\left[-K_{12u}\frac{\delta_1 - \delta_{1o}}{\omega_o} - D_{1u}\frac{\omega_1 - \omega_o}{\omega_o} + K_{12u}\frac{\delta_2 - \delta_{2o}}{\omega_o}\right] \tag{3.22}$$

$$\dot{\delta}_2 = \omega_2 - \omega_o \tag{3.23}$$

$$\dot{\omega}_2 = \frac{\omega_o}{2H_2}\left[K_{12u}\frac{\delta_1 - \delta_{1o}}{\omega_o} - (K_{12u} + K_{2eu})\frac{\delta_2 - \delta_{2o}}{\omega_o} - D_{2u}\frac{\omega_2 - \omega_o}{\omega_o} + K_{2eu}\frac{\delta_e - \delta_o}{\omega_o}\right] \tag{3.24}$$

3.3 Conversion to Brunovsky Form

Since we wish to apply feedback linearizing control to the generator, we need to convert the three generator states into Brunovsky form. (We will ignore the four shaft states for now.) A third order system in Brunovsky form with one input has states such that [2]:

$$\dot{z}_1 = z_2 \tag{3.25}$$

$$\dot{z}_2 = z_3 \tag{3.26}$$

$$\dot{z}_3 = \rho(\mathbf{z}) + \beta(\mathbf{z})u \tag{3.27}$$

where $\rho(\mathbf{z})$ and $\beta(\mathbf{z})$ are nonlinear functions of the state variables $\mathbf{z} = [z_1\ z_2\ z_3]^T$. In our case, since the only input to the generator is the field voltage, $u = E_{fd}$.

The procedure for converting the third order model to Brunovsky form is discussed in detail in [2, 3]; we only give here the result, which is:

$$z_1 = \delta_e - \delta_o \tag{3.28}$$

$$z_2 = \omega_e - \omega_o \tag{3.29}$$

$$z_3 = \dot{\omega}_e = \alpha_e \tag{3.30}$$

$$\dot{z}_3 = \dot{\alpha}_e = \rho(\mathbf{x}_g) + \beta(\mathbf{x}_g) E_{fd} \tag{3.31}$$

$$\begin{aligned}
\rho(\mathbf{x}_g) \;=\; & -\frac{\omega_o}{2H_e}\left[-K_{2eu}\frac{\omega_2}{\omega_o} + K_{2eu}\frac{\omega_e}{\omega_o} + D_{eu}\frac{\dot{\omega}_e}{\omega_o}\right. \\
& \left. + E'_d\dot{i}_d + \dot{E}'_d i_d + E'_q\dot{i}_q - E'_q\frac{\partial i_q}{\partial E'_q}\dot{E}'_q - E'_d\frac{\partial i_d}{\partial E'_q}\dot{E}'_q\right] \\
& + \frac{\omega_o}{2H_e T'_{d0}}\left[E'_q + (x_d - x'_d)i_d\right]\left[E'_q\frac{\partial i_q}{\partial E'_q} + E'_d\frac{\partial i_d}{\partial E'_q} + i_q\right]
\end{aligned} \tag{3.32}$$

$$\beta(\mathbf{x}_g) = -\frac{\omega_o}{2H_e T'_{d0}}\left[E'_q\frac{\partial i_q}{\partial E'_q} + E'_d\frac{\partial i_d}{\partial E'_q} + i_q\right] \tag{3.33}$$

The equation for $\dot{z}_3 = \ddot{\omega}_e$ was derived by differentiation of equation (3.18); the partial derivative terms are needed in order to account for the fact that i_d and i_q are functions of E_{fd} [2].

Note that these equations are expressed in terms of the old state variables $\mathbf{x}_g = [\delta_e\, \omega_e\, E'_q]^T$. Although it is theoretically possible to transform $\mathbf{x}_g$ into $\mathbf{z}$, the transform is extremely complex and difficult to express analytically. Since the components of $\mathbf{x}_g$ are readily available through measurement, ρ and β are expressed as functions of $\mathbf{x}_g$.

3.4 Feedback Linearization of the Generator

The theory of feedback linearization is discussed in great detail in [2, 3]; for now, it simply suffices to say that by applying the following input:

$$u = \frac{\mathbf{a}^T\mathbf{z} - \rho_d(\mathbf{x}_g)}{\beta_d(\mathbf{x}_g)} \tag{3.34}$$

the resulting system will be linear, with poles placed according to the components of $\mathbf{a} = [a_0\; a_1\; a_2]^T$. The d subscript refers to the equations for $\rho(\mathbf{x}_g)$ and $\beta(\mathbf{x}_g)$ used to design the controller. A feedback linearizing controller (FBLC) was designed in [2], and this design will be analyzed here. However, the design of the controller did not account for torsional modes in the shaft; instead, $\rho_d(\mathbf{x}_g)$ and $\beta_d(\mathbf{x}_g)$ were calculated as:

$$\begin{aligned}
\rho_d(\mathbf{x}_g) \;=\; & -\frac{\omega_o}{2H}\left[D\frac{\dot{\omega}_e}{\omega_o} + E'_d\dot{i}_d + \dot{E}'_d i_d + E'_q\dot{i}_q - E'_q\frac{\partial i_q}{\partial E'_q}\dot{E}'_q - E'_d\frac{\partial i_d}{\partial E'_q}\dot{E}'_q\right] \\
& + \frac{\omega_o}{2HT'_{d0}}\left[E'_q + (x_d - x'_d)i_d\right]\left[E'_q\frac{\partial i_q}{\partial E'_q} + E'_d\frac{\partial i_d}{\partial E'_q} + i_q\right]
\end{aligned} \tag{3.35}$$

$$\beta_d(\mathbf{x}_g) = -\frac{\omega_o}{2HT'_{d0}}\left[E'_q\frac{\partial i_q}{\partial E'_q} + E'_d\frac{\partial i_d}{\partial E'_q} + i_q\right] \tag{3.36}$$

where $H = H_1 + H_2 + H_e$. Note that the shaft damping is assumed to be D instead of D_{eu} in the controller design.

Because $\beta(\mathbf{x}_g) = \frac{H}{H_e}\beta_d(\mathbf{x}_g)$, when the generator/shaft model is linearized with $\rho_d(\mathbf{x}_g)$, the resulting system is still linear, although some extra terms appear in the relation for $\dot{\alpha}_e$:

$$\dot{z}_3 = \dot{\alpha}_e = \frac{H}{H_e}\mathbf{a}^T\mathbf{z} - \frac{\omega_o}{2H_e}\left[-K_{2eu}\frac{\omega_2}{\omega_o} + K_{2eu}\frac{\omega_e}{\omega_o} + D_{eu}\frac{\dot{\omega}_e}{\omega_o} - D\frac{\dot{\omega}_e}{\omega_o}\right] \tag{3.37}$$

The consequence of the additional terms of equation (3.37) is that the poles of the system may be moved from their intended locations.

3.5 Feedback Linearized State-Space Model

The state-space model is formed simply by writing equations (3.17) through (3.24) and equation (3.37) in matrix form:

$$\dot{\mathbf{x}} = \mathbf{A}\mathbf{x} \tag{3.38}$$

$$\mathbf{x} = \begin{bmatrix} \delta_e - \delta_o \\ \omega_e - \omega_o \\ \alpha_e \\ \delta_1 - \delta_{1o} \\ \omega_1 - \omega_o \\ \delta_2 - \delta_{2o} \\ \omega_2 - \omega_o \end{bmatrix} \tag{3.39}$$

$$\mathbf{A} = \begin{bmatrix} 0 & 1 & 0 & 0 & 0 & 0 & 0 \\ 0 & 0 & 1 & 0 & 0 & 0 & 0 \\ \frac{a_0 H}{H_e} & \frac{2a_1 H - K_{2eu}}{2H_e} & \frac{2a_2 H + D - D_{eu}}{2H_e} & 0 & 0 & 0 & \frac{K_{2eu}}{2H_e} \\ 0 & 0 & 0 & 0 & 1 & 0 & 0 \\ 0 & 0 & 0 & -\frac{K_{12u}}{2H_1} & -\frac{D_{1u}}{2H_1} & \frac{K_{12u}}{2H_1} & 0 \\ 0 & 0 & 0 & 0 & 0 & 0 & 1 \\ \frac{K_{2eu}}{2H_2} & 0 & 0 & \frac{K_{12u}}{2H_2} & 0 & -\frac{K_{12u}+K_{2eu}}{2H_2} & -\frac{D_{2u}}{2H_2} \end{bmatrix} \tag{3.40}$$

Note that, with the feedback linearizing controller, the system is closed loop (no inputs). Furthermore, the components of the state vector $\mathbf{x}$ are all deviations from

Number(s)	Eigenvalue	Frequency (Hz)
1	-6.99	–
2,3	$-4.12 \pm j1.04$	0.1662
4,5	$-2.69 \pm j195.55$	31.12
6,7	$-12.52 \pm j150.52$	23.96

Table 3.1: Eigenvalues and frequencies of the shaft/generator model with feedback linearizing control.

equilibrium. It is both interesting and important to point out that even though the shaft dynamics were not modeled in the controller design, the closed-loop generator system with feedback linearizing control (FBLC) remains linear in the presence of the shaft dynamics.

3.6 Sample Model of FBLC with Torsional Dynamics

Since we have a model for an FBLC-controlled generator with shaft dynamics, we can use the shaft model parameters from Section 2.4 to find the eigenvalues of the entire shaft/generator system with feedback linearizing control, as represented by equation (3.40). We will assume that the controller was designed to place three poles at -5, so that $a_0 = -125$, $a_1 = -75$, and $a_2 = -15$. With this controller design, the resulting eigenvalues of the system are shown in Table 3.1. Notice that the torsional modes are still present at 24 Hz and 31 Hz, but the damping of these modes has increased greatly with the addition of FBLC. Furthermore, the poles which were originally located at -5 have now moved. Two of these poles form a conjugate pair, giving rise to a slow oscillatory mode at 0.17 Hz.

3.7 Verification of the Feedback Linearized Generator Model with Shaft Dynamics

It would be nice to find a way to show that the model in equation (3.40) is a valid representation of the system. In fact, it is possible to do so by forming a model of the generator, shaft, and FBLC controller and numerically simulating the model. The simulation results should be the same as the results predicted by equation (3.40).

We will compare the two models by disturbing the states slightly from equilibrium and then observing the transient response. Using the same state vector as equation (3.39), the initial values of the states for the test will be:

$$\mathbf{x}(0) = \begin{bmatrix} 1.45 \times 10^{-6} \\ 1.18 \times 10^{-2} \\ -3.80 \times 10^{-2} \\ 0 \\ 0 \\ 0 \\ 0 \end{bmatrix} \tag{3.41}$$

From linear systems theory, the time response of a state-space system to a given initial condition is [4, 5]:

$$\mathbf{x}(t) = e^{\mathbf{A}t}\mathbf{x}(0) \tag{3.42}$$

The predicted time response is calculated by applying equation (3.42) with $\mathbf{A}$ as defined in equation (3.40).

The predicted and simulated responses to the given disturbance are shown in Figures 3-1 through 3-7. Note that since the purpose is to verify the matrix model, the generator model used in these simulations is the third order model. The predicted and simulated results are virtually identical, thus indicating that the state matrix of equation (3.40) is an accurate model of a feedback linearized generator with torsional shaft dynamics.

Another way to verify the matrix model is to perform a numerical linearization of the model used for the simulations. The linearization can be performed by the same math package used to perform the simulations. Table 3.2 shows the eigenvalues of the simulated model linearized at the equilibrium point. These eigenvalues are almost identical to the eigenvalues of $\mathbf{A}$ in equation (3.40), again establishing the validity of the linear matrix model.

3.8 Reduction of the Feedback Linearized Generator Model with Shaft Dynamics

As we have seen, the model for the generator/shaft system has seven states. We would like to be able to reduce the order of the model to facilitate our analysis. Some possible methods for doing so are examined below.

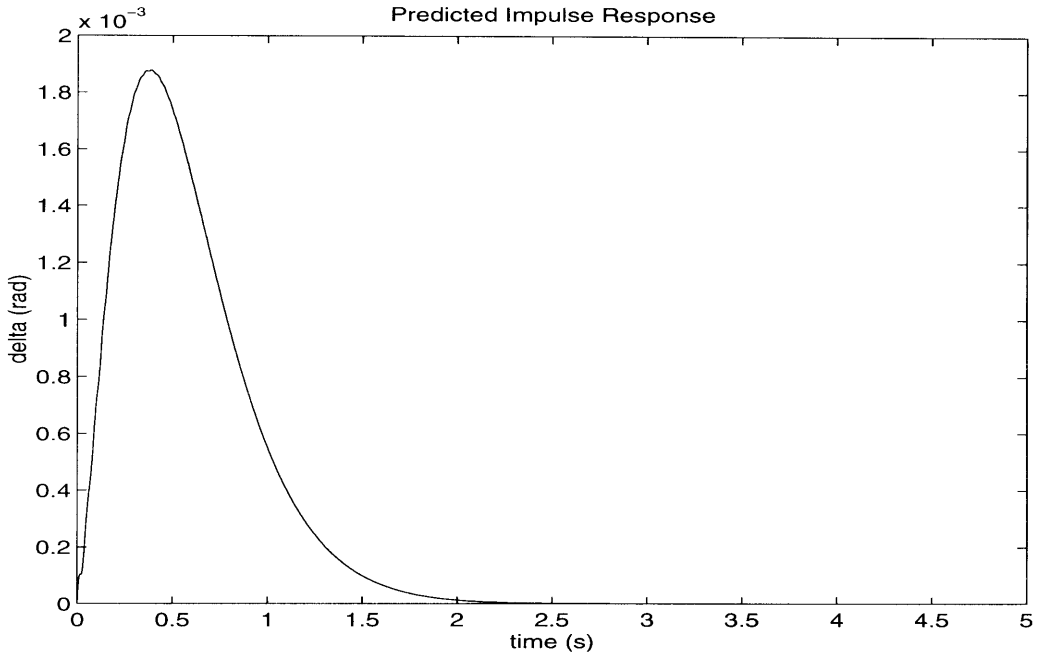

Figure 3-1: Predicted response of $\delta - \delta_o$ to a small disturbance.

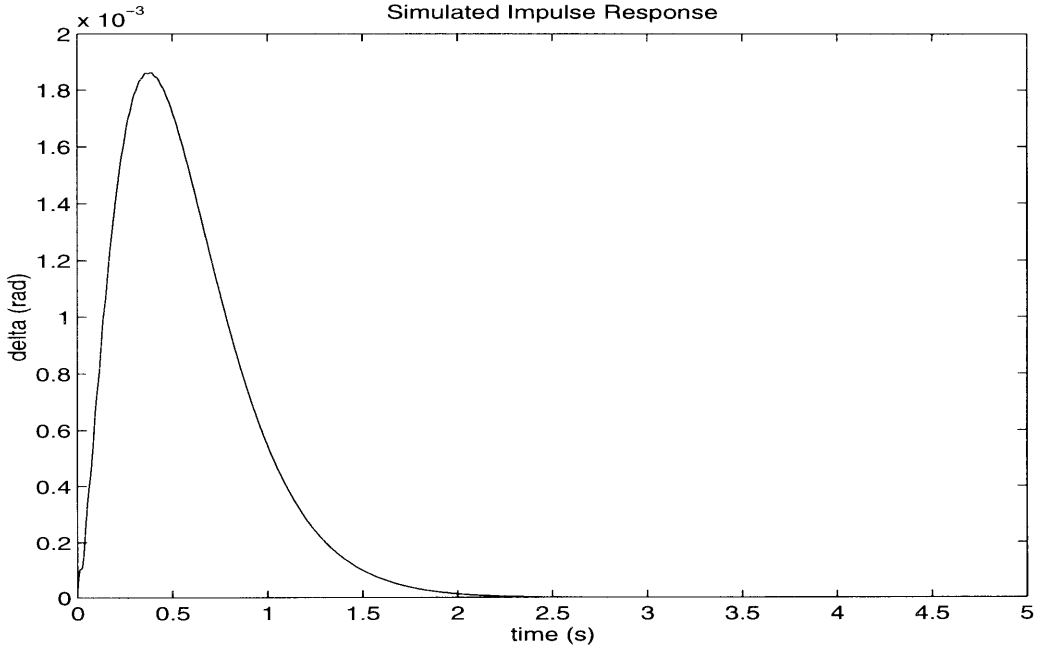

Figure 3-2: Simulated response of $\delta - \delta_o$ to a small disturbance. This response is essentially identical to the predicted response.

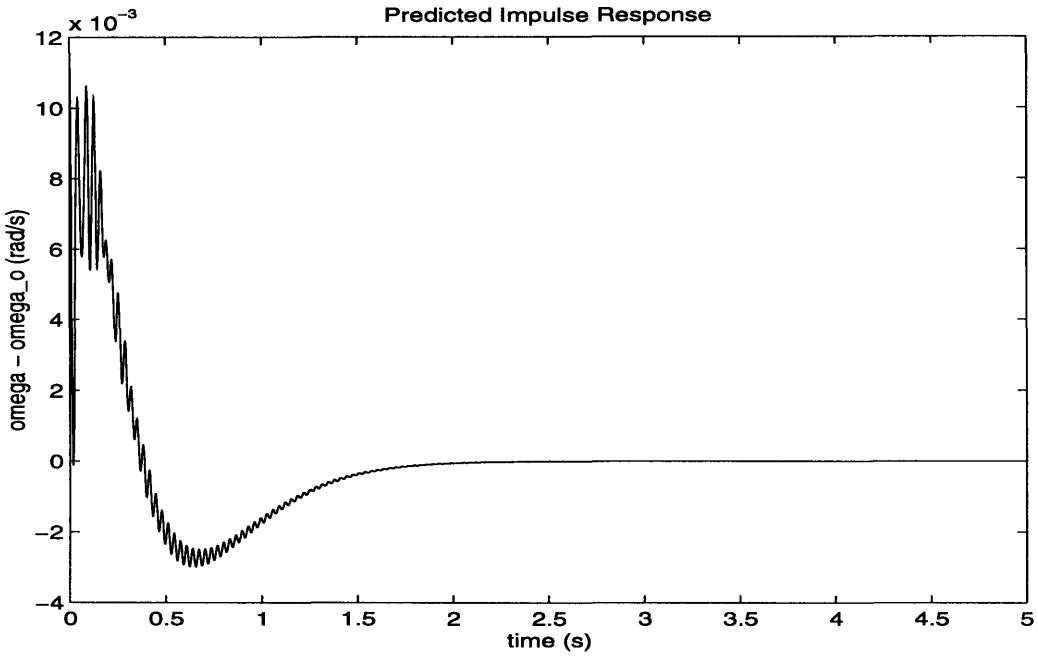

Figure 3-3: Predicted response of $\omega - \omega_o$ to a small disturbance.

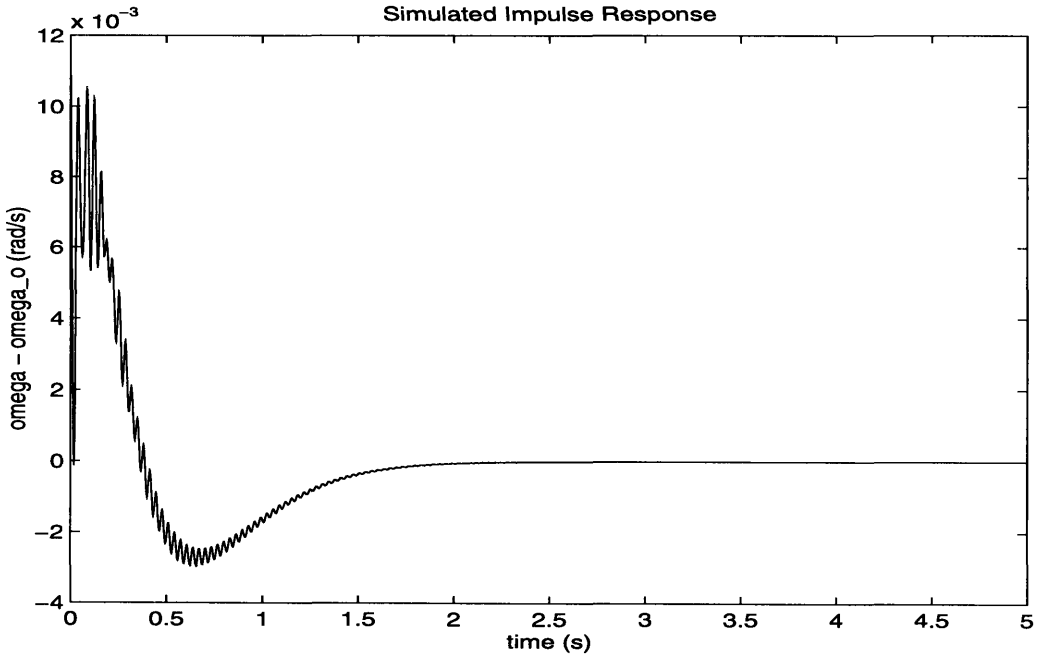

Figure 3-4: Simulated response of $\omega - \omega_o$ to a small disturbance. Again, this response matches the predicted response.

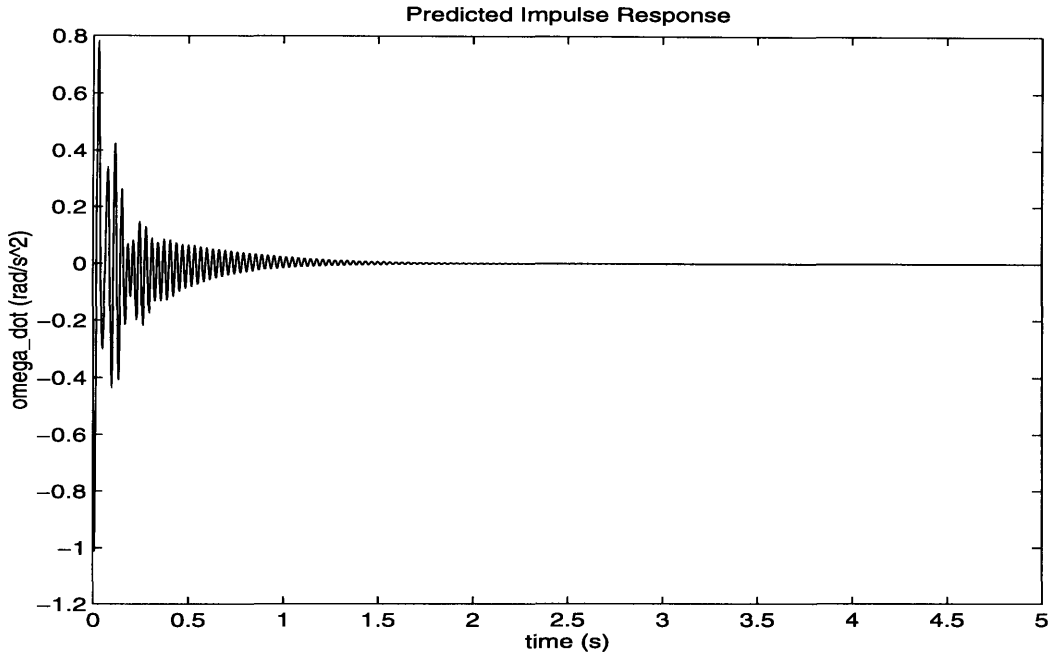

Figure 3-5: Predicted response of $\dot{\omega}$ to a small disturbance.

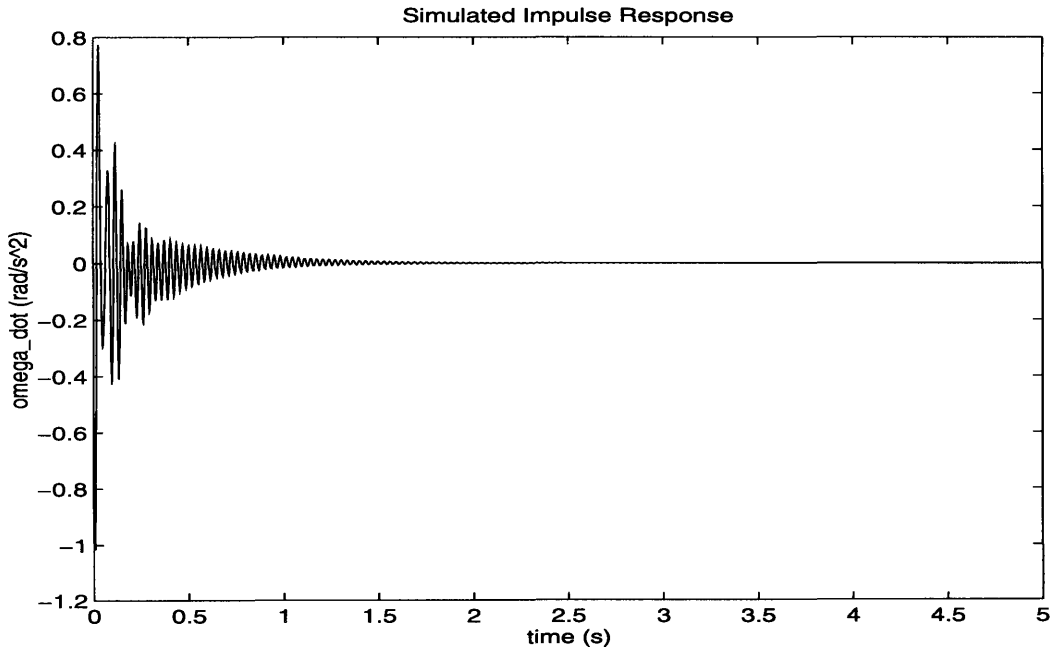

Figure 3-6: Simulated response of $\dot{\omega}$ to a small disturbance. The simulation produces the expected result.

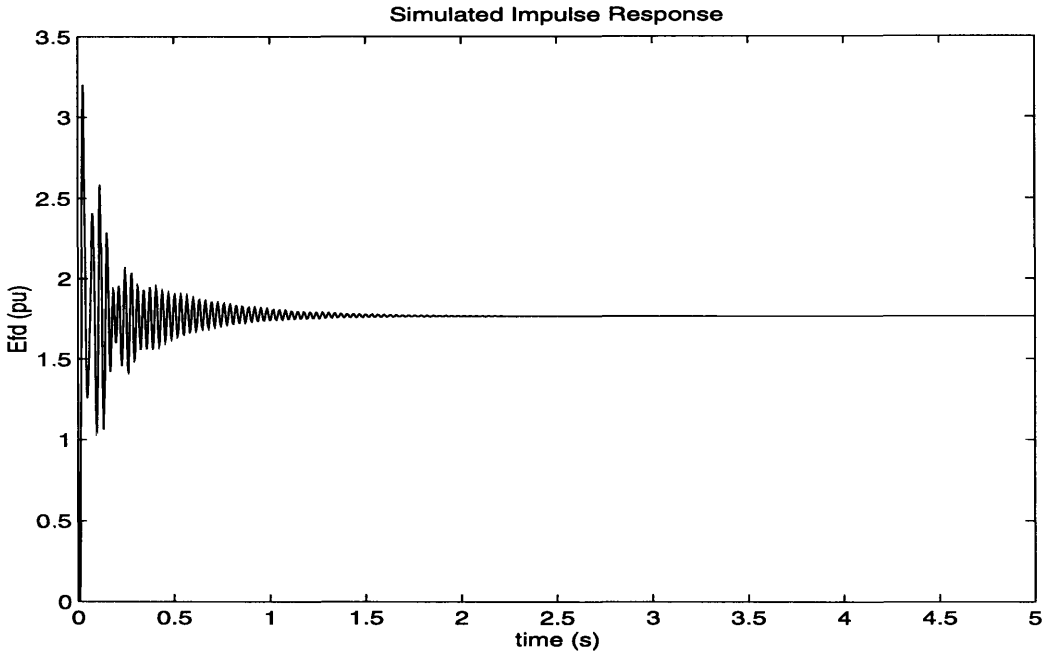

Figure 3-7: Simulated response of E_{fd} to a small disturbance. The field voltage does not saturate at its upper or lower limits, so the system remains linear for all time.

Number(s)	Eigenvalue	Frequency (Hz)
1	-7.00	–
2,3	$-4.12 \pm j1.05$	0.1665
4,5	$-2.69 \pm j195.55$	31.12
6,7	$-12.52 \pm j150.52$	23.96

Table 3.2: Eigenvalues and frequencies of the numerically linearized shaft/generator model with feedback linearizing control. These values match closely to the values in Table 3.1.

3.8.1 Singular Perturbations

One method for model reduction is based on the argument that some states settle down to equilibrium much more quickly than others. If the state vector $\mathbf{x}$ is broken down into a slow component $\mathbf{x}_1$ and a fast component $\mathbf{x}_2$, then the state-space model:

$$\dot{\mathbf{x}} = \mathbf{A}\mathbf{x} \tag{3.43}$$

may be written as:

$$\dot{\mathbf{x}}_1 = \mathbf{A}_{11}\mathbf{x}_1 + \mathbf{A}_{12}\mathbf{x}_2 \tag{3.44}$$

$$\dot{\mathbf{x}}_2 = \mathbf{A}_{21}\mathbf{x}_1 + \mathbf{A}_{22}\mathbf{x}_2 \tag{3.45}$$

We can convert $\mathbf{x}_2$ from a dynamic state to an algebraic variable by imposing the condition:

$$\dot{\mathbf{x}}_2 = \mathbf{0} \tag{3.46}$$

meaning that after any appreciable time, the states in $\mathbf{x}_2$ will have reached steady state. With this condition, $\mathbf{x}_2$ is related to $\mathbf{x}_1$ by:

$$\mathbf{x}_2 = -\mathbf{A}_{22}^{-1}\mathbf{A}_{21}\mathbf{x}_1 \tag{3.47}$$

and the model reduces to [14]:

$$\dot{\mathbf{x}}_1 = [\mathbf{A}_{11} - \mathbf{A}_{12}\mathbf{A}_{22}^{-1}\mathbf{A}_{21}]\mathbf{x}_1 \tag{3.48}$$

We would like to assume that the torsional dynamics (δ_1, δ_2, ω_1, ω_2) are fast relative to the generator dynamics. Unfortunately, this method does not work when applied to the feedback linearized generator/shaft model. Note in Table 3.1 that the real parts of the eigenvalues are all of the same order of magnitude, meaning that disturbances will decay at approximately the same rate in all of the states. These eigenvalues indicate that none of the states decays at a fast rate relative to the other states; therefore, there is no basis for time scale separation. If we try to apply this method, we find that $\mathbf{A}_{12}\mathbf{A}_{22}^{-1}\mathbf{A}_{21} = \mathbf{0}$ and the reduced order model is:

$$\dot{\mathbf{x}}_1 = \mathbf{A}_{11}\mathbf{x}_1 \tag{3.49}$$

The eigenvalues of $\mathbf{A}_{11}$ are -0.02 and $-22.69 \pm j130.57$. None of these eigenvalues are close to the eigenvalues in Table 3.1. If the singular perturbations assumption were valid, we would find that the eigenvalues of the reduced system are a subset of the eigenvalues of the full order system. The main cause for this situation is the fact that in this case, $O(\|\mathbf{A}_{11}\|) \approx O(\|\mathbf{A}_{12}\|)$. The starting assumption in singular perturbation theory is that the model has $O(\|\mathbf{A}_{11}\|) \approx O(\|\mathbf{A}_{22}\|) = 1$ and $O(\|\mathbf{A}_{12}\|) \approx O(\|\mathbf{A}_{21}\|) = \epsilon \ll 1$. Consequently, we must find another approach for examining the dynamics of the system.

3.8.2 Selective Modal Analysis

Another method for obtaining a reduced order model is known as selective modal analysis, or SMA. In this method, a participation matrix is used to determine which states contribute to the various modes of the system. Recall that the unforced system:

$$\dot{\mathbf{x}} = \mathbf{A}\mathbf{x} \tag{3.50}$$

has the solution:

$$\mathbf{x}(t) = e^{\mathbf{A}t}\mathbf{x}(0) \tag{3.51}$$

If we assume that $\mathbf{A}$ is diagonalizable, then by definition [15]:

$$\mathbf{M}^{-1}\mathbf{A}\mathbf{M} = \mathbf{D} \tag{3.52}$$

where:

$$\mathbf{D} = \begin{bmatrix} \lambda_1 & & \\ & \ddots & \\ & & \lambda_n \end{bmatrix} \tag{3.53}$$

$$\mathbf{M} = \begin{bmatrix} \mathbf{v}_1 & \cdots & \mathbf{v}_n \end{bmatrix} \tag{3.54}$$

$$\mathbf{M}^{-1} = \begin{bmatrix} \mathbf{w}_1^T \\ \vdots \\ \mathbf{w}_n^T \end{bmatrix} \tag{3.55}$$

The λ_i are the eigenvalues of $\mathbf{A}$, while $\mathbf{v}_i$ are the right eigenvectors and $\mathbf{w}_i^T$ are the left eigenvectors. Notice that $\mathbf{w}_i^T\mathbf{v}_j$ equals 1 if $i = j$ and 0 if $i \neq j$. If we rewrite equation (3.51) in terms of the eigenvalues and eigenvectors, we find that [16]:

$$\mathbf{x}(t) = \sum_{i=1}^{n} \mathbf{w}_i^T\mathbf{x}(0)e^{\lambda_i t}\mathbf{v}_i \tag{3.56}$$

This equation shows how the eigenvalues and eigenvectors of $\mathbf{A}$ dictate the system response. Each right eigenvector $\mathbf{v}_i$ indicates a mode of the system, which decays (or grows) at a rate determined by λ_i. The left eigenvector $\mathbf{w}_i^T$ indicates how much contribution the initial state $\mathbf{x}(0)$ gives to mode i.

The participation matrix $\mathbf{P}$ is calculated by performing element-by-element multiplication (*not* standard matrix multiplication) of the matrices $(\mathbf{M}^{-1})^T$ and $\mathbf{M}$. In other words, each column of $\mathbf{P}$ consists of the element-by-element product of $\mathbf{w}_i$ and $\mathbf{v}_i$. If p_{ki} denotes the element in the k-th row and i-th column of $\mathbf{P}$, then p_{ki} indicates the contribution of the k-th state to the i-th mode, or equivalently, of the i-th mode to the k-th state. To illustrate what this means, let's set the initial value of state k to 1 while all other states start at zero. The response of the k-th state for all time will then become [16]:

$$\mathbf{x}_k(t) = \sum_{i=1}^{n} p_{ki}e^{\lambda_i t} \tag{3.57}$$

Equation (3.57) clearly demonstrates that the elements in each column of the k-th row show how much of each mode appears in the time response of the k-th state.

Next, we'll choose $\mathbf{x}(0) = \mathbf{v}_j$ so that only the j-th mode is excited. Since all terms of the summation in equation (3.56) will be zero except for $i = j$, we have [16]:

$$\mathbf{x}(t) = \mathbf{w}_j^T \mathbf{v}_j e^{\lambda_j t} \mathbf{v}_j \tag{3.58}$$

The dot product may be expressed as elements of $\mathbf{P}$:

$$\mathbf{x}(t) = \left(\sum_{k=1}^{n} p_{ki} \right) e^{\lambda_j t} \mathbf{v}_j \tag{3.59}$$

We already know that the summation in equation (3.59) is one; in fact, the sum of the elements along any row or column of $\mathbf{P}$ will always be one. This form of the equation, however, illustrates how the element in the k-th row of the j-th column is a description of how much state k contributes to mode j.

Now that we have an understanding of the participation matrix, we can calculate $\mathbf{P}$ for our torsional generator/shaft system and interpret the results. Using a standard math package, we find that the participation matrix, with our representative choices for parameter values, is given in Table 3.3. The state and eigenmode order is the same as in equation (3.39) and Table 3.1. We notice from the first row that δ_e depends primarily on the first three modes of the system. However, δ_2, a torsional state, is also extremely important in these modes. We also note that $\dot{\omega}_e$ has a small dependence on modes 6 and 7, in which δ_1 and ω_1 participate significantly. We therefore can conclude from $\mathbf{P}$ that it is not possible to decouple the shaft states from the generator states when examining our dynamic model.

P	Column 1	Column 2	Column 3
Row 1	629.5	$-314.4 - j864.8$	$-314.4 + j864.8$
Row 2	-9.78	$5.04 + j7.80$	$5.04 - j7.80$
Row 3	1.78	$-0.72 - j0.63$	$-0.72 + j0.63$
Row 4	0.52	$-0.21 - j0.18$	$-0.21 + j0.18$
Row 5	0.53	$-0.21 - j0.19$	$-0.21 + j0.19$
Row 6	-624.6	$312.7 + j859.1$	$312.7 - j859.1$
Row 7	3.03	$-1.23 - j1.09$	$-1.23 + j1.09$

P	Column 4	Column 5	Column 6	Column 7
Row 1	$0.03 + j0.01$	$0.03 - j0.01$	$0.07 - j0.04$	$0.07 + j0.04$
Row 2	$0.05 + j0.03$	$0.05 - j0.03$	$0.29 - j0.03$	$0.29 + j0.03$
Row 3	$0.04 + j0.04$	$0.04 - j0.04$	$0.28 + j0.05$	$0.28 - j0.05$
Row 4	$0.28 - j0.05$	$0.28 + j0.05$	$0.17 + j0.04$	$0.17 - j0.04$
Row 5	$0.28 - j0.05$	$0.28 + j0.05$	$0.17 + j0.04$	$0.17 - j0.04$
Row 6	$0.14 - j0.00$	$0.14 + j0.00$	$-0.03 - j0.01$	$-0.03 + j0.01$
Row 7	$0.17 + j0.01$	$0.17 - j0.01$	$0.04 - j0.05$	$0.04 + j0.05$

Table 3.3: Participation matrix of the feedback linearized generator with torsional dynamics.

Chapter 4

Field Voltage Saturation

Mathematically, a generator with FBLC will always behave as a linear system. However, in the real world there are many unmodeled dynamics and physical limitations that distort the linearity of the system. One of the most important limitations is field voltage saturation. The field voltage E_{fd} has both a minimum and maximum limit and can not exceed these boundaries. For all simulations in this thesis, $0 \leq E_{fd} \leq 6.16$.

Once the field voltage saturates at the maximum or minimum limit, the closed-loop, linear generator/controller system becomes an open-loop, nonlinear system. Typically, in simulations, the field voltage saturates immediately following a disturbance of significant magnitude and then comes out of saturation as the generator states return toward equilibrium.

The torsional dynamics are observed to greatly increase the tendency of the field voltage to saturate. If the shaft dynamics are not modeled, the field voltage generally saturates for only a short period following a disturbance (see Figures 4-1 through 4-13). However, the presence of shaft dynamics causes E_{fd} to swing rapidly between the upper and lower limits for a much longer time after the disturbance (Figures 4-2 through 4-14).

The large swings in E_{fd} primarily result from the high frequency oscillations produced in the shaft acceleration. The shaft dynamics also produce oscillations in $\rho_d(\mathbf{x}_g)$ which add to the oscillations observed in the acceleration measurement. Notice in Figure 4-6 that the amplitude of the high frequency oscillations in $\dot{\omega}$ is about 6 rad/s^2 at $t = 0.5$s. Since E_{fd} includes the acceleration measurement multiplied by $a_2/\beta_d(\mathbf{x}_g)$, these oscillations have an amplitude of about 12 in E_{fd}, which is clearly more than sufficient to saturate E_{fd} at both limits. Additionally, there are high frequency oscillations of amplitude 12 in $\rho_d(\mathbf{x}_g)$, which appear in E_{fd} with an amplitude of about 1.5. Figure 4-15 is a plot of:

$$f(t) = \frac{\mathbf{a}^T\mathbf{z} - \rho_d(\mathbf{x}_g)}{\beta_d(\mathbf{x}_g)} \tag{4.1}$$

which is the field voltage without the saturation limits. (Note that the field voltage with saturation limits is the quantity that affects the dynamics in the simulation.) The high frequency oscillations have amplitude of approximately 13 at $t = 0.5$s, thus

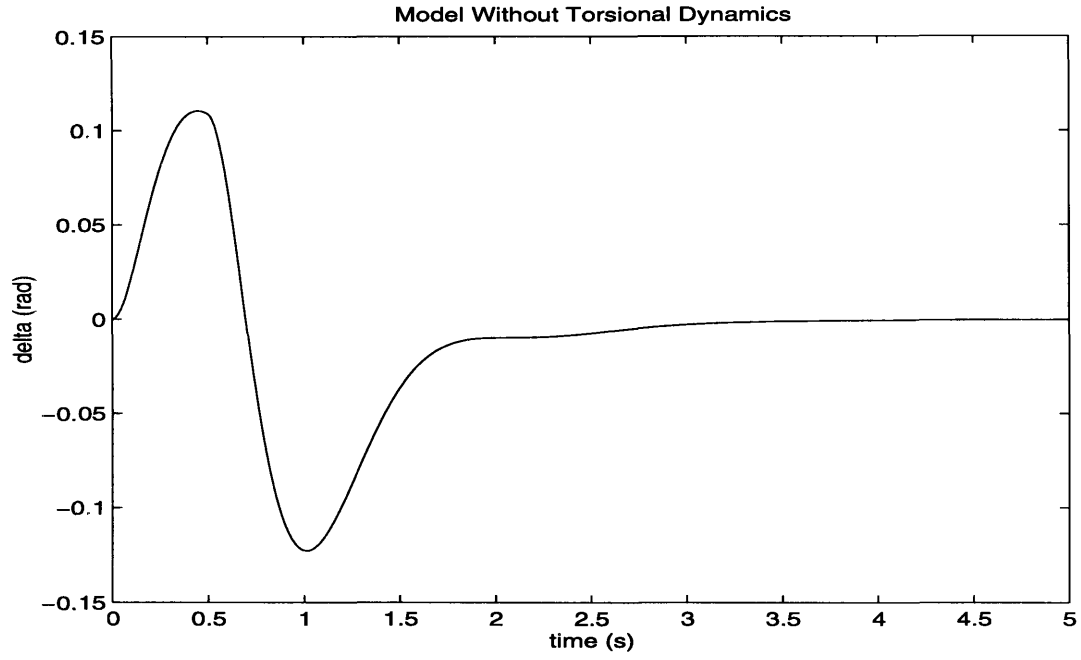

Figure 4-1: Response of $\delta - \delta_o$ to a 0.5 second fault, without torsional modeling.

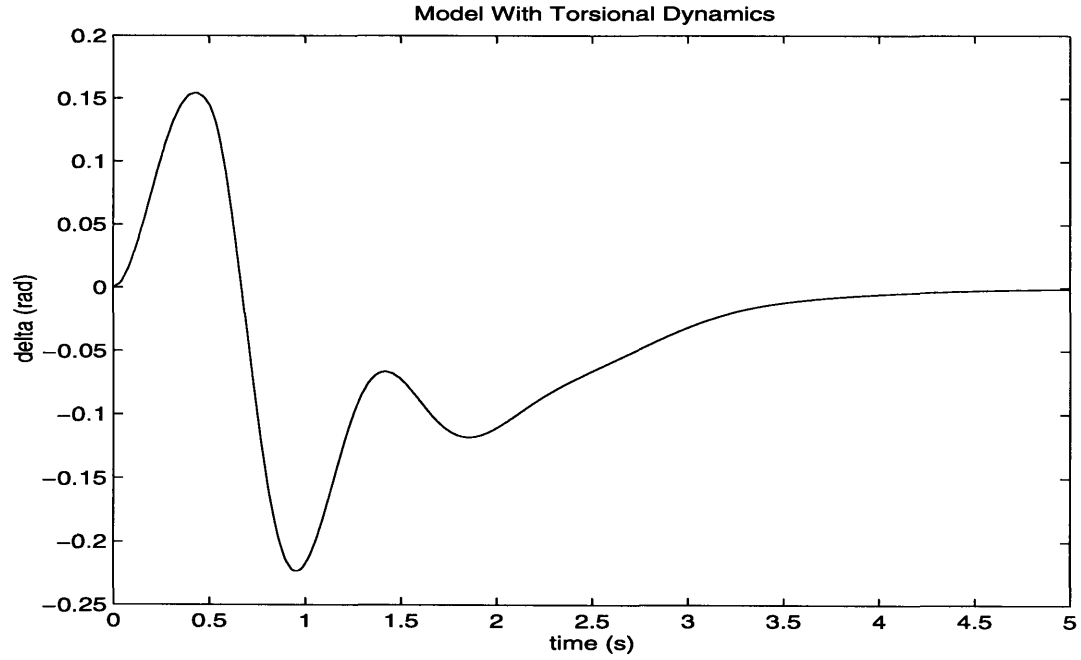

Figure 4-2: Response of $\delta - \delta_o$ to a 0.5 second fault, with torsional modeling. The torsional dynamics affect the response of δ, although δ still returns to equilibrium within a reasonable time.

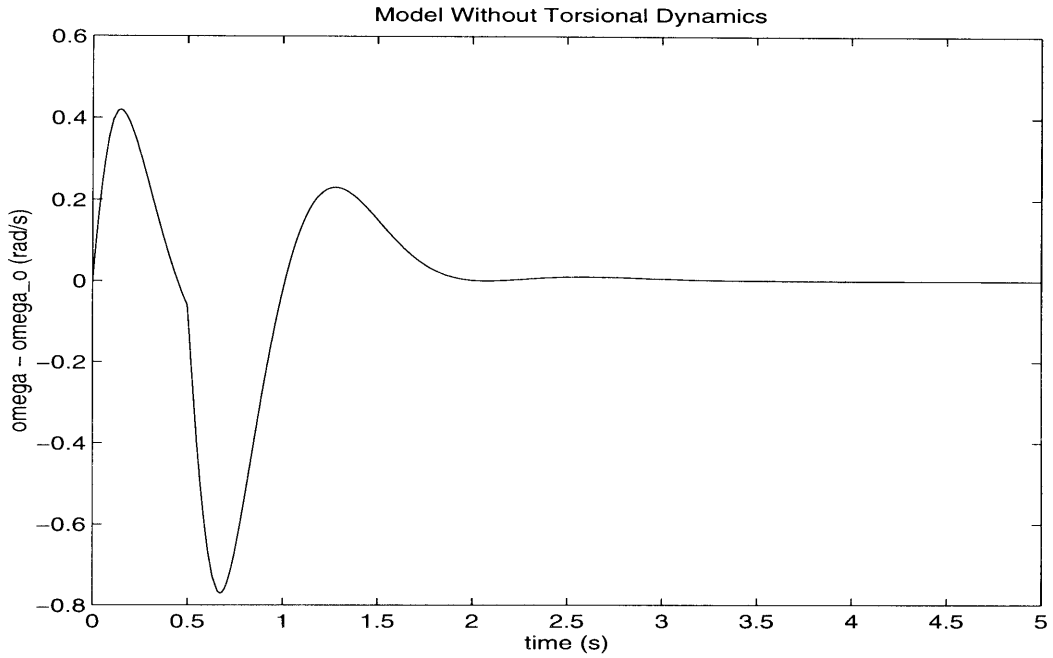

Figure 4-3: Response of $\omega - \omega_o$ to a 0.5 second fault, without torsional modeling.

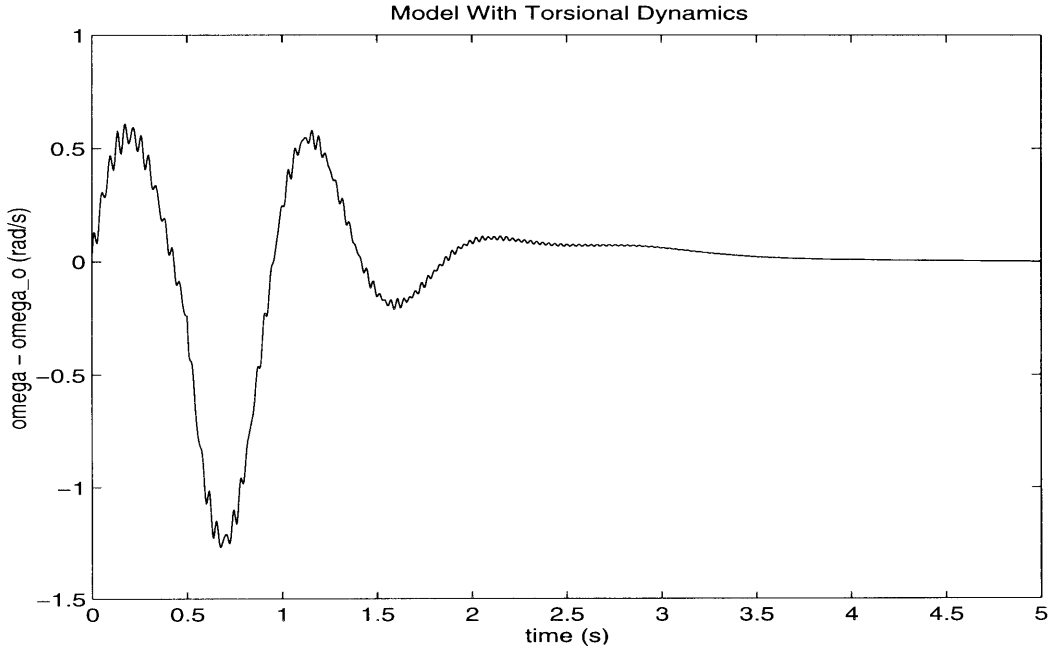

Figure 4-4: Response of $\omega - \omega_o$ to a 0.5 second fault, with torsional modeling. The torsional oscillations appear in ω, although their amplitude is small.

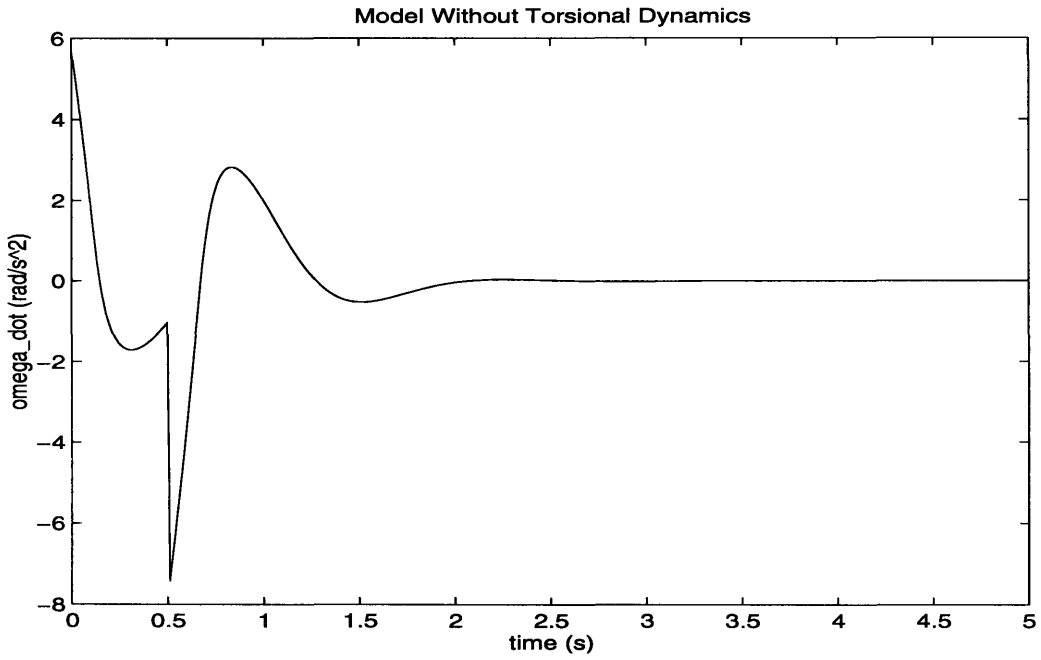

Figure 4-5: Response of $\dot{\omega}$ to a 0.5 second fault, without torsional modeling.

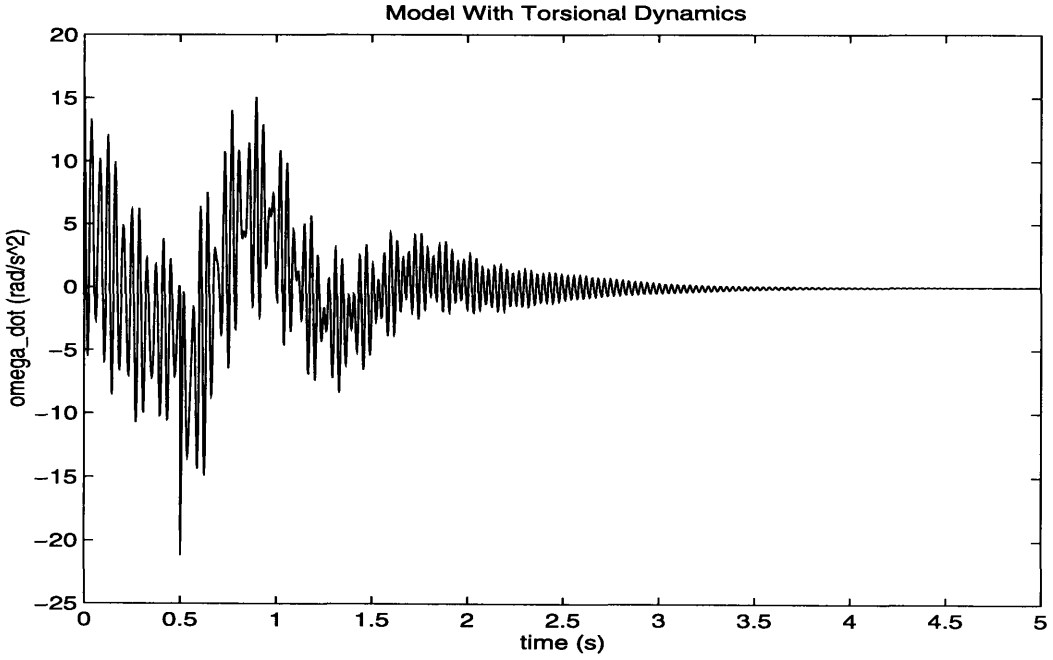

Figure 4-6: Response of $\dot{\omega}$ to a 0.5 second fault, with torsional modeling. The shaft oscillations form a large portion of the acceleration measurement.

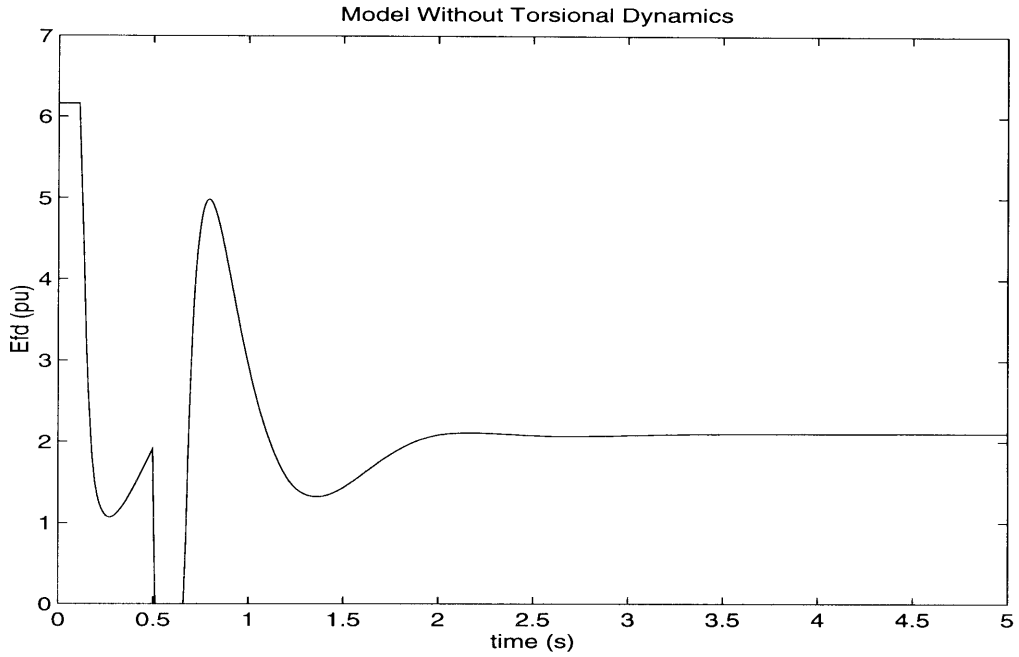

Figure 4-7: Response of E_{fd} to a 0.5 second fault, without torsional modeling. E_{fd} only saturates briefly following a disturbance.

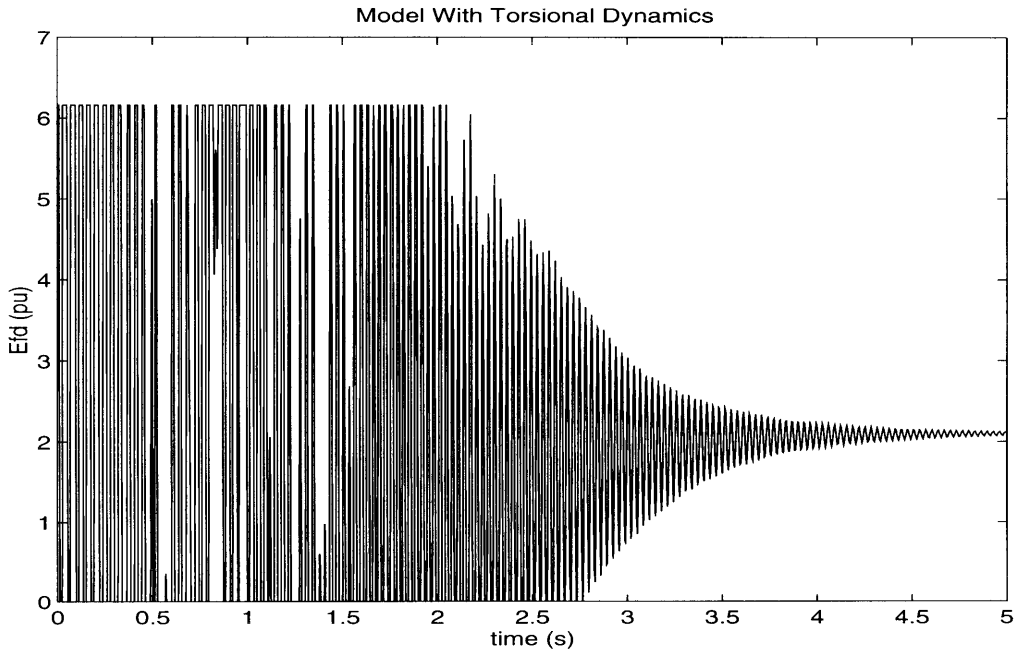

Figure 4-8: Response of E_{fd} to a 0.5 second fault, with torsional modeling. Clearly, the torsional dynamics cause E_{fd} to saturate for an extended period following the disturbance.

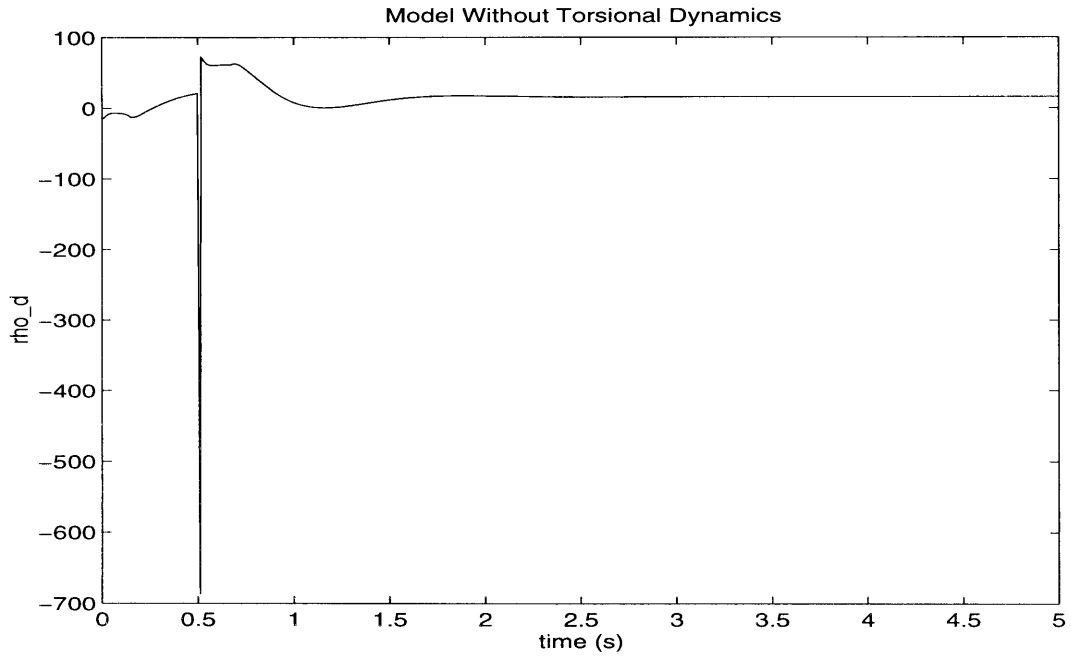

Figure 4-9: Response of $\rho_d(\mathbf{x}_g)$ to a 0.5 second fault, without torsional modeling.

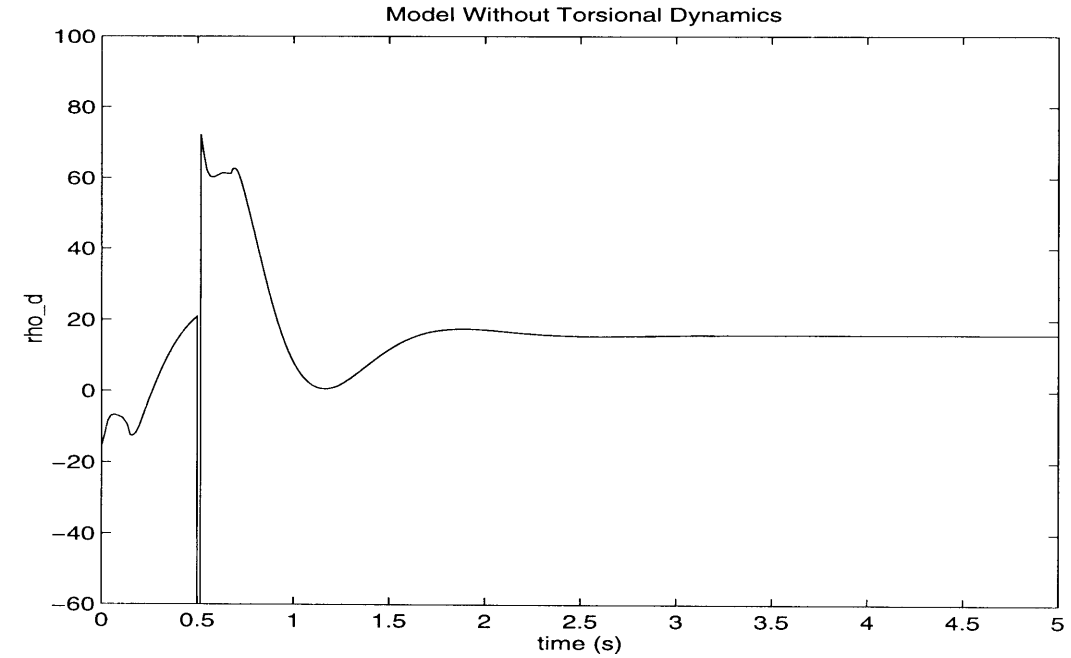

Figure 4-10: Response of $\rho_d(\mathbf{x}_g)$ to a 0.5 second fault, without torsional modeling.

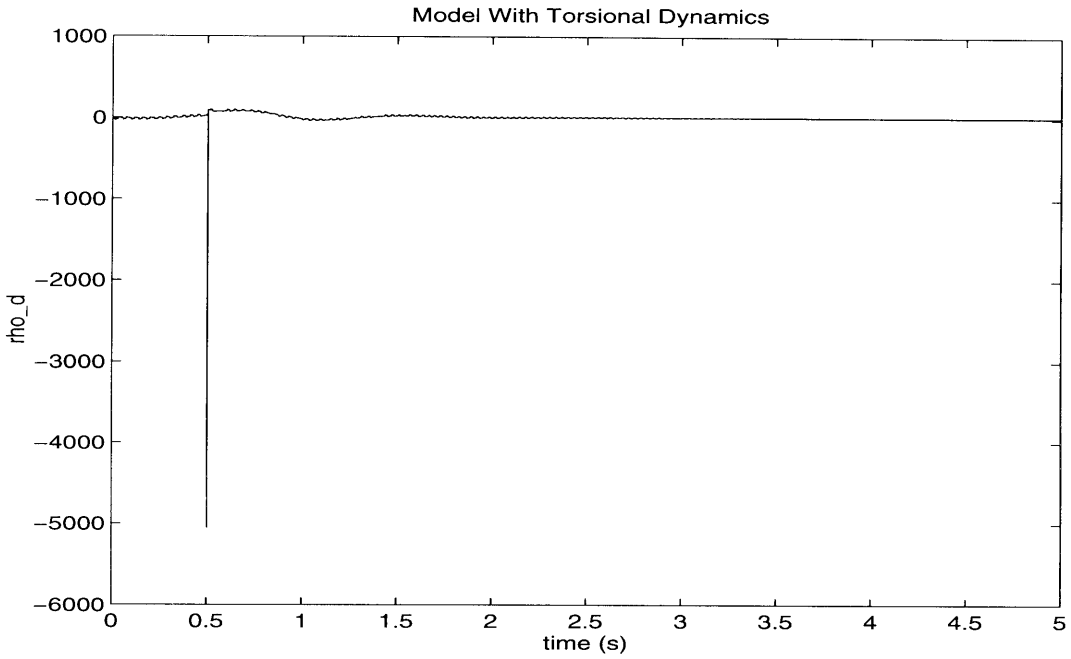

Figure 4-11: Response of $\rho_d(\mathbf{x}_g)$ to a 0.5 second fault, with torsional modeling.

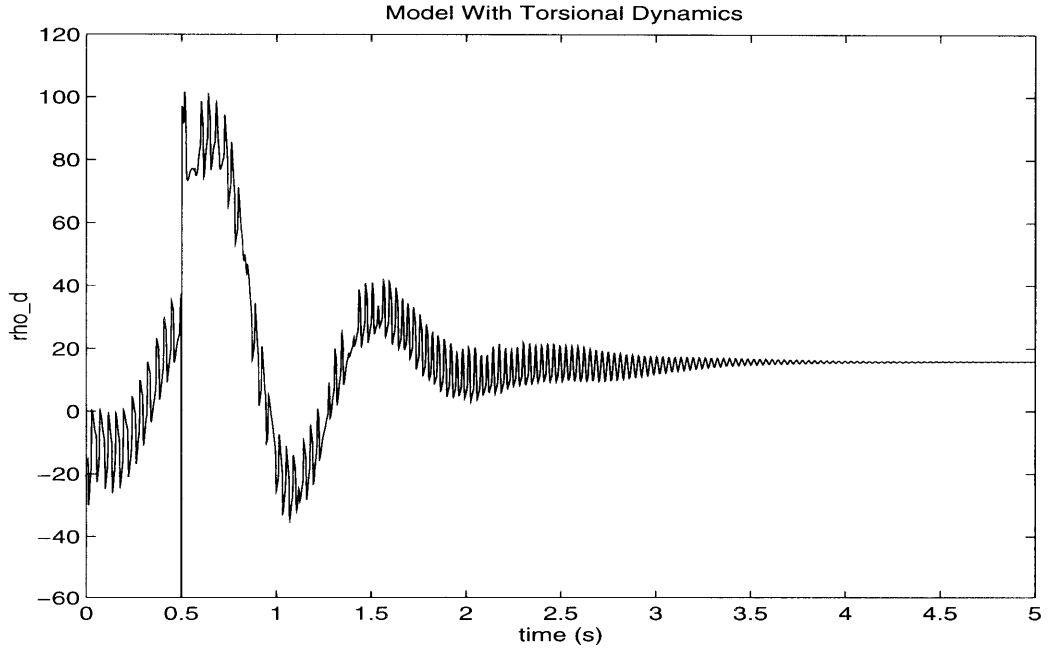

Figure 4-12: Response of $\rho_d(\mathbf{x}_g)$ to a 0.5 second fault, with torsional modeling. The shaft oscillations are noticeable, but they do not dominate the measurement.

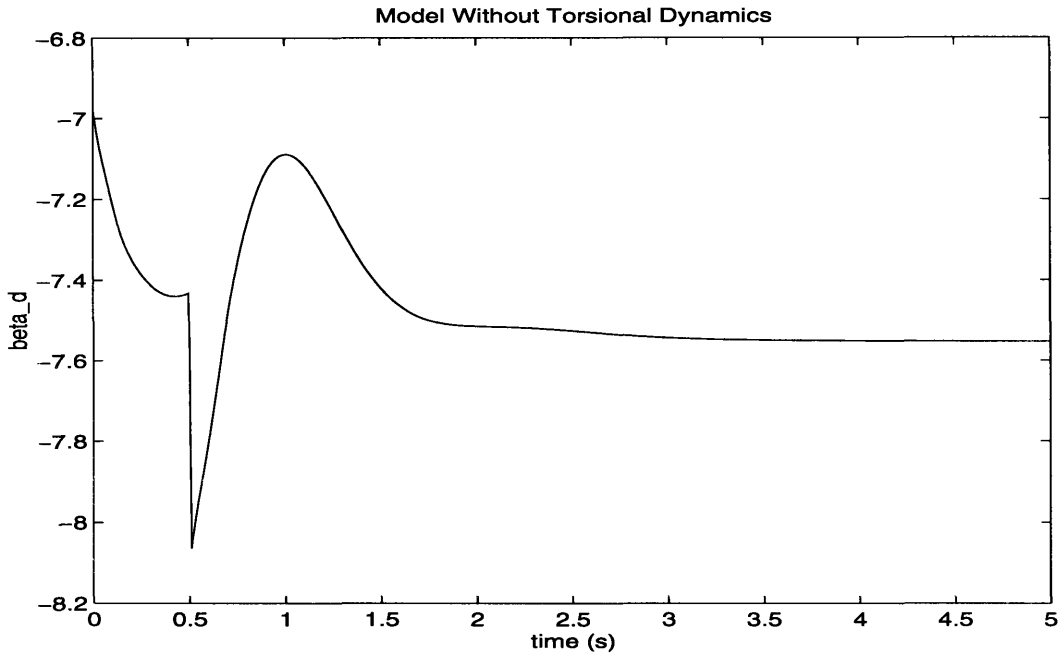

Figure 4-13: Response of $\beta_d(\mathbf{x}_g)$ to a 0.5 second fault, without torsional modeling.

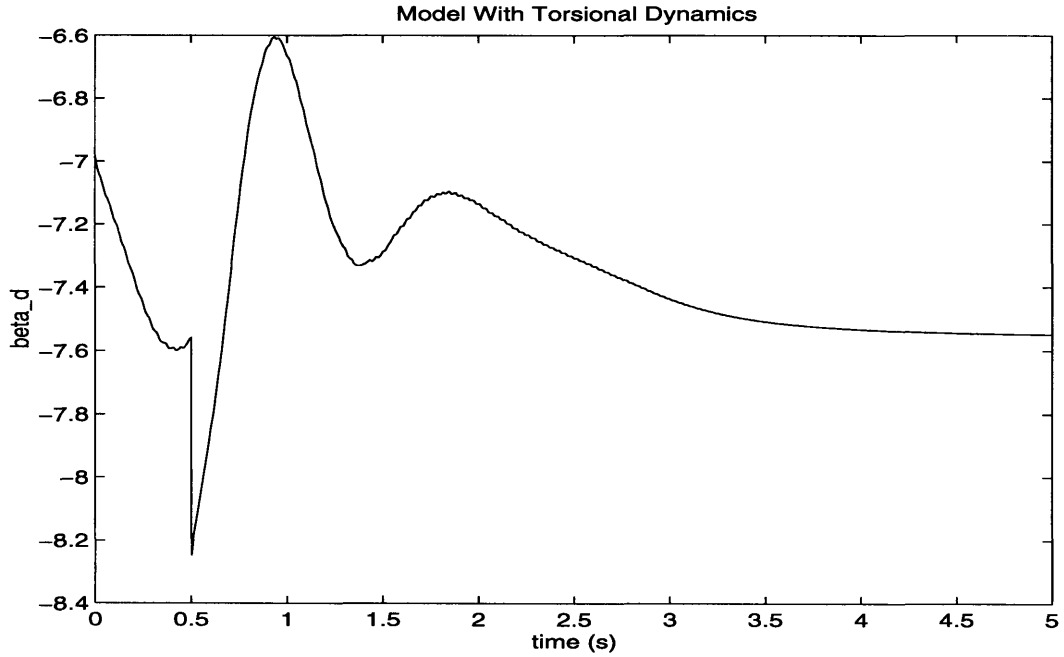

Figure 4-14: Response of $\beta_d(\mathbf{x}_g)$ to a 0.5 second fault, with torsional modeling.

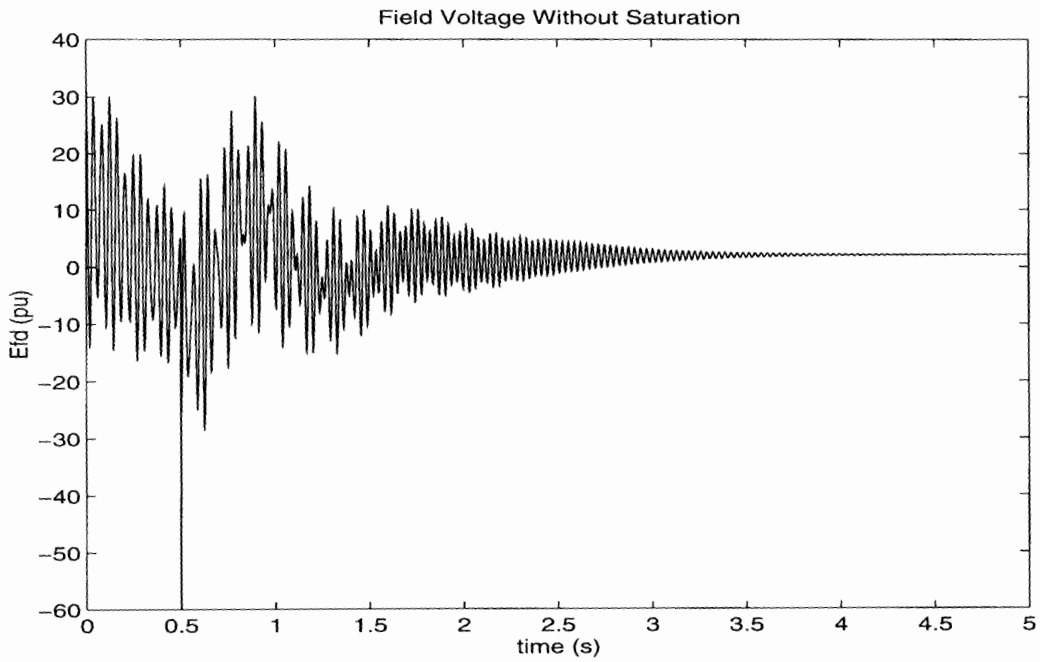

Figure 4-15: E_{fd} calculated without the saturation limits for a 0.5 second fault.

validating the preceding argument.

Chapter 5

FBLC with Field Voltage Averaging

We have seen that the presence of shaft dynamics causes high amplitude, high frequency swings to appear in the field voltage. These swings cause the field voltage to saturate frequently and limit the performance of the system. In this chapter, we will use a field voltage averaging method to reduce the high frequency swings and examine its impact on the system.

5.1 Field Voltage Averaging Simulations

The averaging scheme is quite simple; the previous equation for E_{fd} will be averaged over one cycle of a 60 Hz wave to obtain the field voltage. Mathematically:

$$E_{fd} = \frac{1}{T_0} \int_{t-T_0}^{t} \frac{\mathbf{a}^T \mathbf{z} - \rho_d(\mathbf{x}_g)}{\beta_d(\mathbf{x}_g)} d\tau \tag{5.1}$$

where $T_0 = 1/60$s. This method of averaging is used for the simulations shown in Figures 5-1 to 5-7, using the same 0.5 second fault as in Figures 4-1 to 4-14. Although the averaged field input initially responds adequately to the disturbance, it does not return the rotor angle to its equilibrium value. Furthermore, the averaged field voltage does not attenuate the shaft vibrations; consequently, the field voltage exhibits high frequency rail-to-rail swings, even though the control was designed to remove these swings in the first place.

5.2 Heuristic Model of the System with FBLC Averaging

Unfortunately, the insertion of the integral into the field voltage input creates a system that is nonlinear, so it is not possible to produce a matrix like equation (3.40) that represents the generator/shaft system with averaged feedback linearized control.

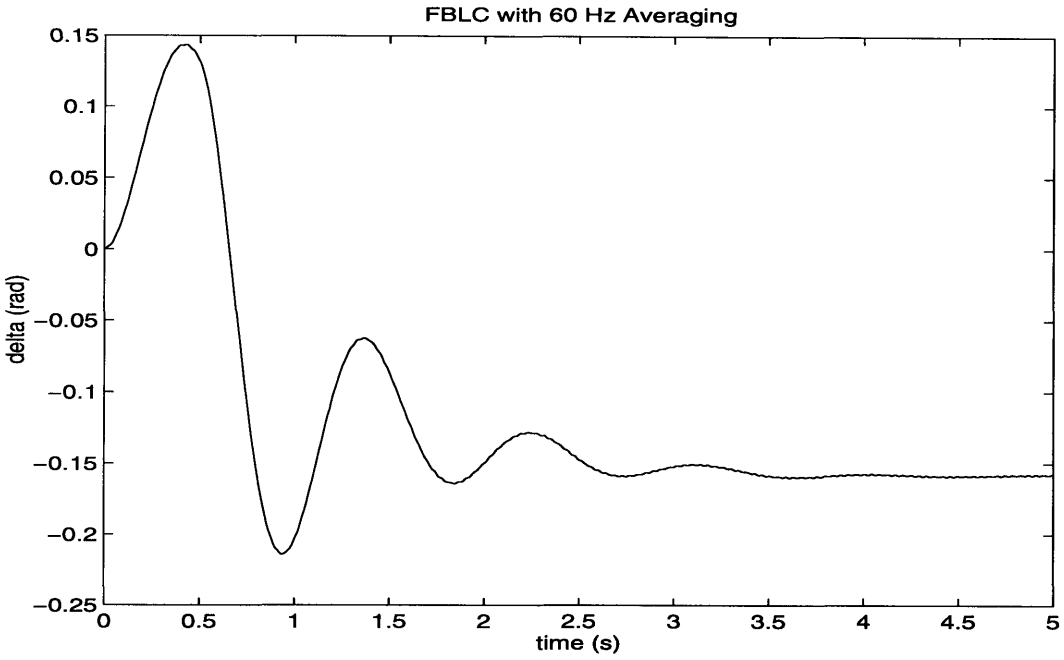

Figure 5-1: Response of $\delta - \delta_o$ to a 0.5 second fault with FBLC averaging. Clearly, δ does not return to equilibrium within a reasonable time.

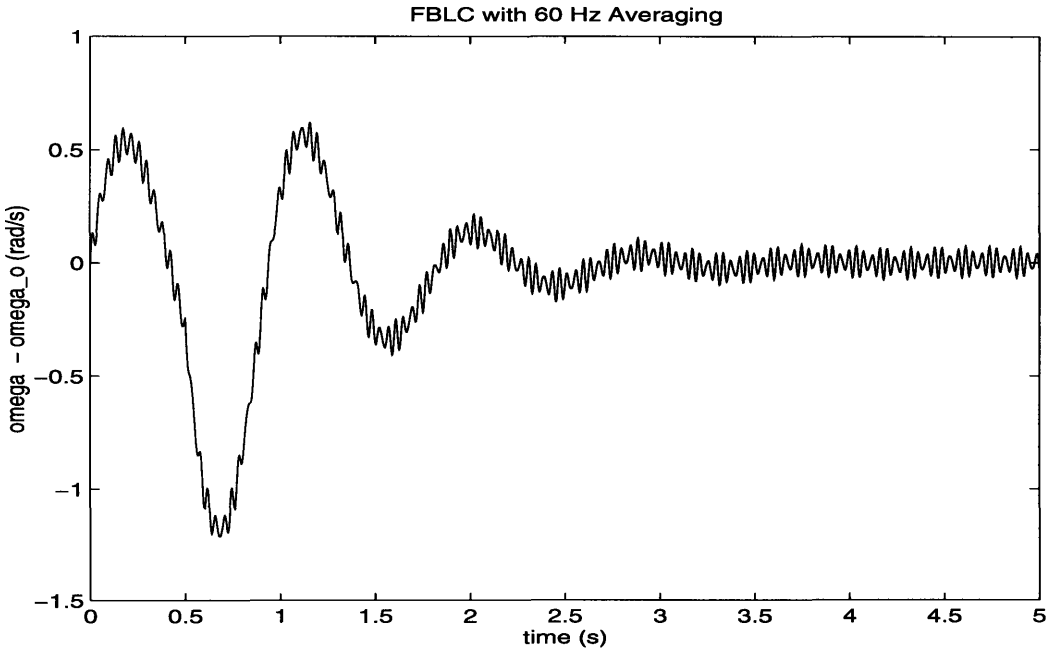

Figure 5-2: Response of $\omega - \omega_o$ to a 0.5 second fault with FBLC averaging.

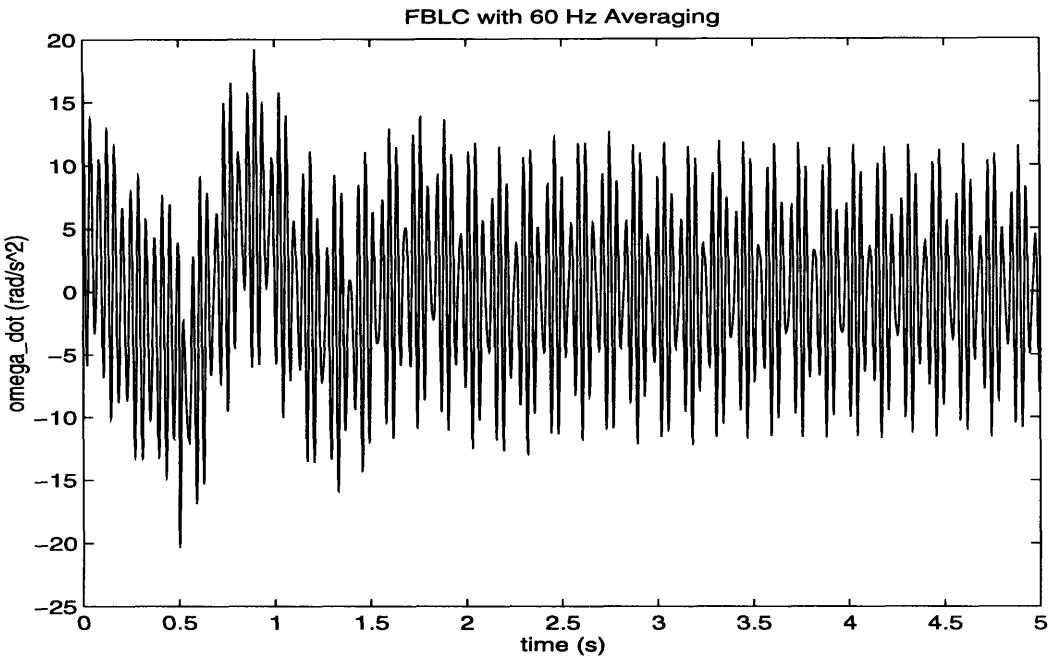

Figure 5-3: Response of $\dot{\omega}$ to a 0.5 second fault with FBLC averaging. The torsional oscillations are much more poorly damped when field voltage averaging is used.

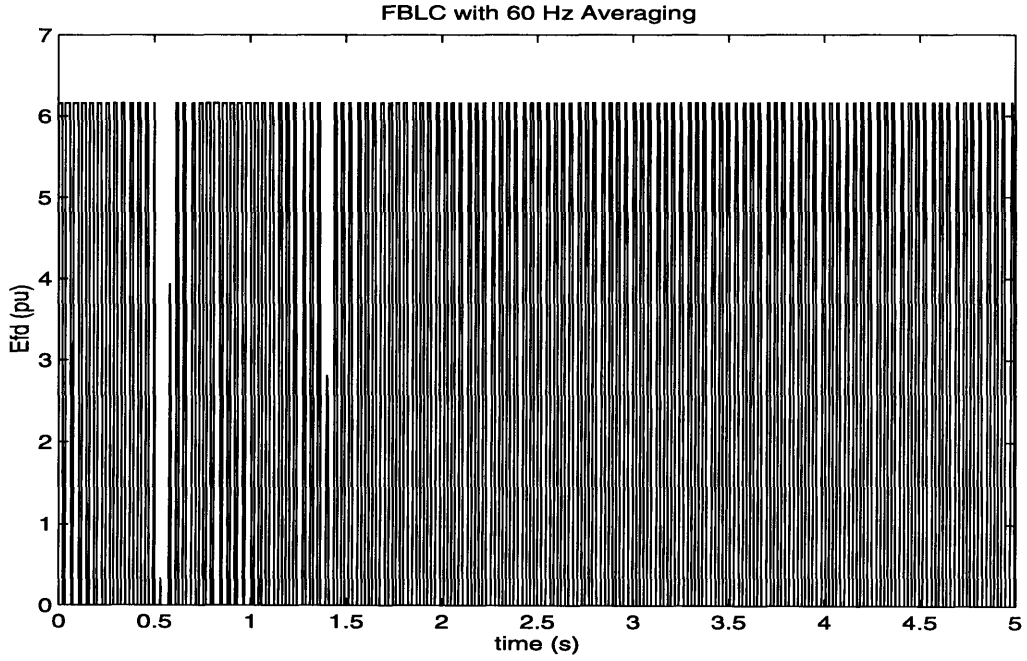

Figure 5-4: Response of E_{fd} to a 0.5 second fault with FBLC averaging. Amazingly, more saturation occurs with averaging in place, even though the averaging was intended to prevent the saturation!

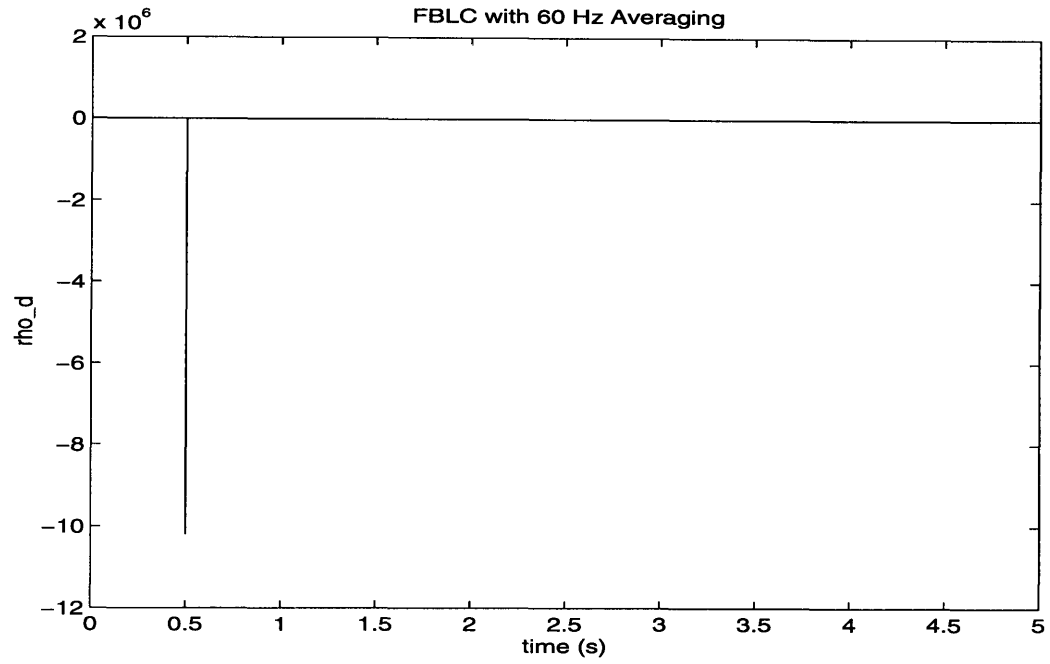

Figure 5-5: Response of $\rho_d(\mathbf{x}_g)$ to a 0.5 second fault with FBLC averaging, showing a large, brief spike when the fault is corrected.

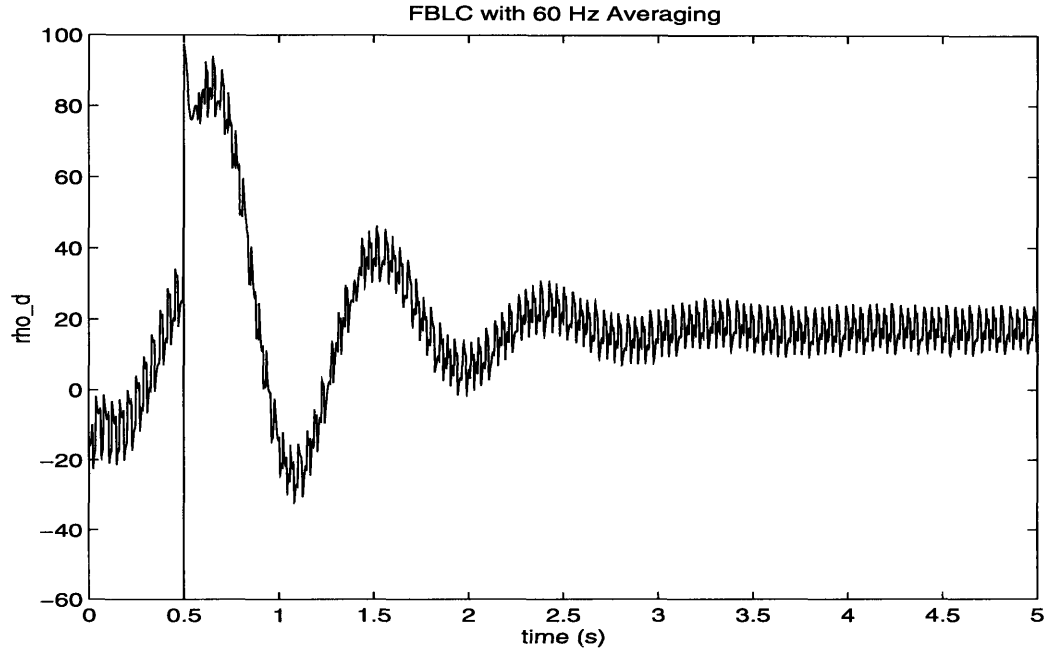

Figure 5-6: Response of $\rho_d(\mathbf{x}_g)$ to a 0.5 second fault with FBLC averaging.

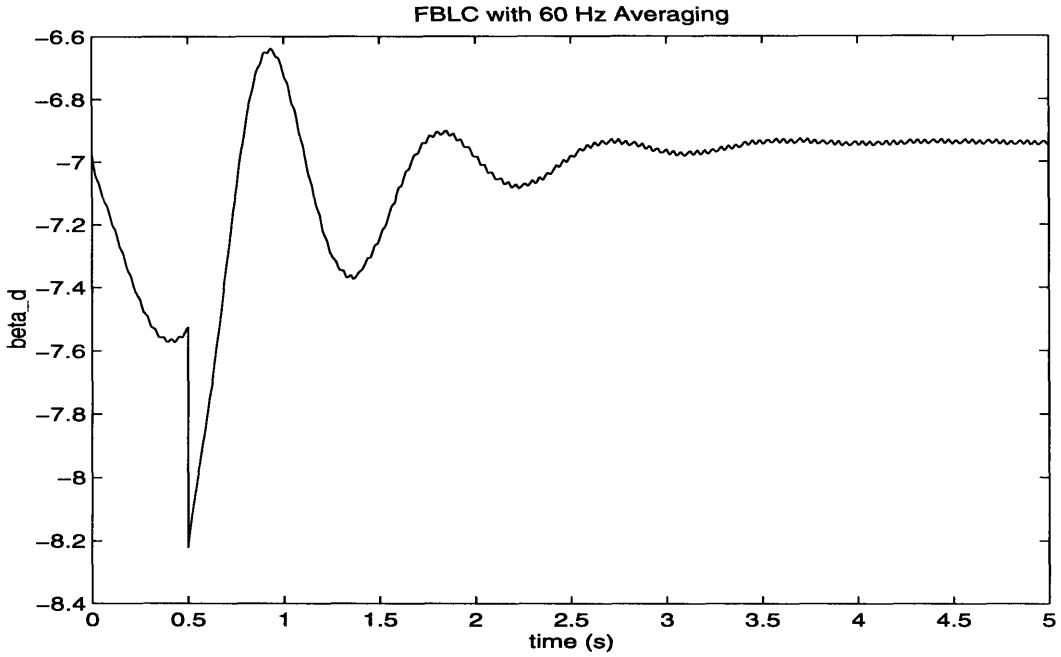

Figure 5-7: Response of $\beta_d(\mathbf{x}_g)$ to a 0.5 second fault with FBLC averaging.

However, we will use a rather heuristic argument to produce a pseudo-linear model that will provide insight into the observed results of averaged FBLC.

First, recall that the system without averaging is linear and has seven modes. Three of the modes have zero or low frequency, and the other four modes have frequencies in the torsional range. In the discussion of singular modal analysis, we noted that each mode in a linear system evolves independently of the other modes. If a mode is not initially excited by the initial conditions (i.e. $\mathbf{w}_i^T\mathbf{x}(0) = 0$ for that mode), then the mode will remain unexcited for all time, regardless of what happens in the other modes. We will model the averaged FBLC system as a composition of seven modes that continue to act independently, an assumption that we justify later.

Second, note that the averaging process acts as a low-pass filter. Signals that change slowly appear as constants to the integration, and consequently are virtually unchanged by the averaging. However, the amplitude of high frequency signals is greatly reduced by the averaging process. We will assume that all quantities except $\dot{\omega}$ change slowly during 1/60 s and can be treated as constants in the integration.

Third, we note that $\dot{\omega}$ includes components from all seven modes. As noted earlier, each mode operates at a different frequency. We will assume that the integration of $\dot{\omega}$ is equivalent to multiplying each modal component of $\dot{\omega}$ by a constant which depends on the frequency of that mode. This constant is 1 for low frequency modes, and approaches 0 for high frequency modes. This approximation is reasonable since,

using equation (3.56):

$$\dot{\omega}(t) = \sum_{i=1}^{n} \mathbf{w}_i^T \mathbf{x}(0) e^{\lambda_i t} [0\,0\,1\,0\,0\,0\,0] \mathbf{v}_i \tag{5.2}$$

Using the notation:

$$\lambda_i = \sigma_i + j\omega_i \tag{5.3}$$

we can now write:

$$\dot{\omega}(t) = \sum_{i=1}^{n} \mathbf{w}_i^T \mathbf{x}(0) e^{\sigma_i t} [0\,0\,1\,0\,0\,0\,0] \mathbf{v}_i e^{j\omega_i t} \tag{5.4}$$

Notice in Table 3.1 that for all of the modes in the system, the real parts of the eigenvalues are much larger than -60, so that during 1/60 of a second, we can treat $e^{\sigma_i t}$ as a constant. As a result:

$$\frac{1}{T_0} \int_{t-T_0}^{t} \dot{\omega}(\tau) d\tau = \sum_{i=1}^{n} C(\omega_i) \mathbf{w}_i^T \mathbf{x}(0) e^{\sigma_i t} [0\,0\,1\,0\,0\,0\,0] \mathbf{v}_i e^{j\omega_i t} \tag{5.5}$$

$C(\omega_i)$ is a constant which reflects the amount of attenuation imposed by the integration on $e^{j\omega t}$. In fact, $C(\omega_i)$ can be adjusted to reflect the effects of all sorts of filters, so that equation (5.5) is valid for any sort of filter applied to $\dot{\omega}_e$, as long as T_0 is short enough to meet the previous assumptions regarding σ_i. Note that $C(\omega_i)$ is a complex number and carries both magnitude and phase information.

The effect of the filtering of $\dot{\omega}_i$ is that the constant a_2 is replaced by $a_2 C(\omega_i)$. Since $C(\omega_i)$ has a different value for different modes, we must use a different matrix $\mathbf{A}$ to represent each mode of the system. We will henceforth use the notation $\mathbf{A}_{C(\omega_i)}$ to denote the matrix $\mathbf{A}$ from equation (3.40) with the element in the third row and third column replaced by:

$$a_{33} = \frac{2a_2 C(\omega_i) H + D - D_{eu}}{2H_e} \tag{5.6}$$

Based on all of the assumptions in this section, if a given eigenvalue and eigenvector pair of frequency ω_i represents a mode of $\mathbf{A}_{C(\omega_i)}$, then that mode must also be a mode of the averaged FBLC system. We know this must be true from the following reasoning: If the initial condition ($\mathbf{x}(0)$) of the averaged FBLC system is a multiple of the eigenvector $\mathbf{v}_k$, meaning that only mode k is excited, then $\dot{\mathbf{x}} = \mathbf{A}_{C(\omega_i)}\mathbf{x}$ for all time and mode k will evolve in the same fashion as if the system were linear with matrix $\mathbf{A}_{C(\omega_i)}$ The modes are implicitly defined to act independently of each other. By finding the eigenvectors and eigenvalues of $\mathbf{A}_{C(\omega_i)}$ for each modal frequency ω_i and picking out the modes that represent modes of the averaged FBLC system, we can construct a matrix to represent a linear model of the averaged feedback linearized system.

5.2.1 Calculation of $C(\omega_i)$ for 60 Hz Averaging

We are now ready to find a formula for $C(\omega_i)$ for the averaging scheme used in the simulations. If the input signal to the averager is $e^{j\omega t}$, then:

$$\frac{1}{T_0}\int_{t-T_0}^{t} e^{j\omega\tau}d\tau = \frac{1}{j\omega T_0}(e^{j\omega t} - e^{j\omega(t-T_0)}) \tag{5.7}$$

After factoring out an $e^{j\omega t}$ and expanding the complex exponentials into real and imaginary parts, this equation becomes:

$$\frac{1}{T_0}\int_{t-T_0}^{t} e^{j\omega\tau}d\tau = \frac{1}{j\omega T_0}e^{j\omega t}[1 - \cos(\omega T_0) + j\sin(\omega T_0)] \tag{5.8}$$

We can bring the j inside the brackets, giving:

$$\frac{1}{T_0}\int_{t-T_0}^{t} e^{j\omega\tau}d\tau = \frac{1}{\omega T_0}e^{j\omega t}[\sin(\omega T_0) + j(\cos(\omega T_0) - 1)] \tag{5.9}$$

We will now concentrate on the quantity inside the brackets. We wish to replace that quantity with an equivalent polar representation. In other words, we want to find A and ϕ such that:

$$Ae^{j\phi} = \sin(\omega T_0) + j(\cos(\omega T_0) - 1) \tag{5.10}$$

This equation is the same as:

$$A\cos\phi + jA\sin\phi = \sin(\omega T_0) + j(\cos(\omega T_0) - 1) \tag{5.11}$$

Equation 5.11 comprises two real equations with two unknowns. A is easy to find by taking the square root of the sum of the squares of the real and imaginary parts:

$$A = \sqrt{\sin^2(\omega T_0) + \cos^2(\omega T_0) - 2\cos(\omega T_0) + 1} \tag{5.12}$$

which reduces to:

$$A = \sqrt{2 - 2\cos(\omega T_0)} \tag{5.13}$$

The angle ϕ is obtained by dividing the imaginary part by the real part:

$$\tan\phi = \frac{\cos(\omega T_0) - 1}{\sin(\omega T_0)} \tag{5.14}$$

Therefore, the average of $e^{j\omega t}$ over T_0 is:

$$\frac{1}{T_0}\int_{t-T_0}^{t} e^{j\omega\tau}d\tau = \frac{e^{j\phi}\sqrt{2 - 2\cos(\omega T_0)}}{\omega T_0}e^{j\omega t} \tag{5.15}$$

and by definition:

$$C(\omega) = \frac{\sqrt{2 - 2\cos(\omega T_0)}}{\omega T_0}e^{j\phi} \tag{5.16}$$

$$\tan\phi = \frac{\cos(\omega T_0) - 1}{\sin(\omega T_0)}$$

Equation (5.16) describes how sinusoids are attenuated by the integration. Clearly, as ωT_0 becomes large, $C(\omega T_0)$ approaches zero. However, what happens when $\omega \to 0$? To answer this question, we note that the cosine function may be expressed as a infinite series [17]:

$$\cos x = 1 - \frac{x^2}{2!} + \frac{x^4}{4!} - \cdots \tag{5.17}$$

Therefore, when x is small, $1 - \cos x \approx \frac{1}{2}x^2$, and:

$$|C(\omega)| \approx \frac{\omega T_0}{\omega T_0} = 1 \tag{5.18}$$

We expect this result, since we know that low frequency signals pass through the averaging process unaltered.

Equation (5.16) tells us how complex exponentials are attenuated, but in the real world, there are only sines and cosines. Actually, since:

$$\cos(\omega t + \theta) = \frac{1}{2}e^{j\theta}e^{j\omega t} + \frac{1}{2}e^{-j\theta}e^{-j\omega t} \tag{5.19}$$

$$\sin(\omega t + \theta) = \frac{1}{2j}e^{j\theta}e^{j\omega t} - \frac{1}{2j}e^{-j\theta}e^{-j\omega t} \tag{5.20}$$

the sine and cosine terms in the system response are the result of the sum of two modes with conjugate eigenvalues and eigenvectors, as shown by equations (5.19), (5.20), and (3.56). Since the averaged FBLC system produces real outputs, we expect that $C(\omega)$ and $C(-\omega)$ will also form a conjugate pair. Denoting:

$$\tan\phi_- = \frac{\cos(-\omega T_0) - 1}{\sin(-\omega T_0)} \tag{5.21}$$

we see that $\sin\phi_- = \sin\phi$, but $\cos\phi_- = -\cos\phi$. These relations require that:

$$\phi_- = \pi - \phi \tag{5.22}$$

Finally, since:

$$C(-\omega) = -\frac{\sqrt{2 - 2\cos(-\omega T_0)}}{\omega T_0}e^{j\phi_-} = \frac{\sqrt{2 - 2\cos(\omega T_0)}}{\omega T_0}e^{j(\pi+\phi_-)} \tag{5.23}$$

and therefore:

$$C(-\omega) = \frac{\sqrt{2 - 2\cos(\omega T_0)}}{\omega T_0}e^{-j\phi} \tag{5.24}$$

indicating that $C(\omega)$ and $C(-\omega)$ are indeed complex conjugates.

Number(s)	Eigenvalue	Frequency (Hz)
1	-6.99	–
2,3	$-4.12 \pm j1.04$	0.1662
4,5	$0.19 \pm j198.92$	31.66
6,7	$-2.24 \pm j160.64$	25.57

Table 5.1: Eigenvalues and frequencies of the linear model of averaged feedback linearizing control.

5.2.2 Computation of Linear Model

We are finally in a position to build the linear model of the averaged feedback linearized generator/shaft system. We start with the eigenvalues from Table 3.1. The first three eigenvalues and corresponding eigenvectors are of low frequency and can be directly used in the averaged FBLC model.

Next, we employ an iterative scheme to find the remaining modes. We select an initial guess for ω_i from the eigenvalues of $\mathbf{A}$. Then we calculate $C(\omega_i)$ and subsequently $\mathbf{A}_{C(\omega_i)}$. We obtain a new guess for ω_i from the eigenvalues of $\mathbf{A}_{C(\omega_i)}$ and continue iterating until convergence. There is no proof that this algorithm actually does converge, but the frequencies are observed to experience only small shifts as $C(\omega_i)$ changes, and for this example, three to six iterations are sufficient to provide an accurate estimate for ω_i. Finally, we select the eigenvalue of $\mathbf{A}_{C(\omega_i)}$ that has imaginary part ω_i and its corresponding eigenvector to add to the linear averaged FBLC model, along with their conjugates. (The conjugate eigenvalue and eigenvector are modes of $\mathbf{A}_{C(-\omega_i)}$.) This process is repeated for each high frequency mode; in our case, there are two such modes.

Finally, the matrix $\mathbf{A}_{avg}$ of the averaged FBLC system is calculated via equation (3.52):

$$\mathbf{A}_{avg} = \mathbf{M}\mathbf{D}\mathbf{M}^{-1} \tag{5.25}$$

A linear model was calculated for the sample torsional FBLC model that has been used throughout this thesis. The eigenvalues of this linear model of an averaged FBLC system are given in Table 5.1. The model predicts that one of the torsional modes is unstable.

5.3 Response of Linear Model

We can now compare the linear model of averaged FBLC with the simulated model. The initial conditions for the two simulations are:

$$\mathbf{x}(0) = \begin{bmatrix} 2.33 \times 10^{-5} \\ 2.12 \times 10^{-3} \\ 1.68 \times 10^{-1} \\ 0 \\ 0 \\ 0 \\ 0 \end{bmatrix} \tag{5.26}$$

As before, this represents a minor disturbance from equilibrium, one that is small enough to keep E_{fd} from saturating. The simulations of the averaged FBLC model and the responses predicted by the linear model are shown in Figures 5-8 to 5-16. Clearly, averaged FBLC is unstable, as predicted by the linear model. In fact, the oscillations grow faster than predicted. The main source of error in the linear model would appear to be the assumption that $\rho_d(\mathbf{x}_g)$ varies slowly over time. Although the linear response does not perfectly match the averaged FBLC simulations, it seems that the linear model does provide an explanation for the observed instability.

5.4 Conclusions

Based on these simulations, it is clear that removing the high frequency oscillations in the field voltage also removes the damping of the torsional modes. The eigenvalues of $\mathbf{A}_{C(\omega_i)}$ demonstrate that when a_2 is small, the only damping of the torsional modes is the natural damping on each mass. Furthermore, the phase shift in the filtering of E_{fd} causes the torsional modes to become unstable, a claim again demonstrated by eigenvalue computation of $\mathbf{A}_{C(\omega_i)}$. Interestingly, it is observed in all simulations that the field voltage continues to saturate even with the low pass filtering of E_{fd}, leading to the conclusion that filtering the field voltage is both ineffective and counterproductive. The high frequency oscillations in E_{fd} are vital for damping the high frequency modes.

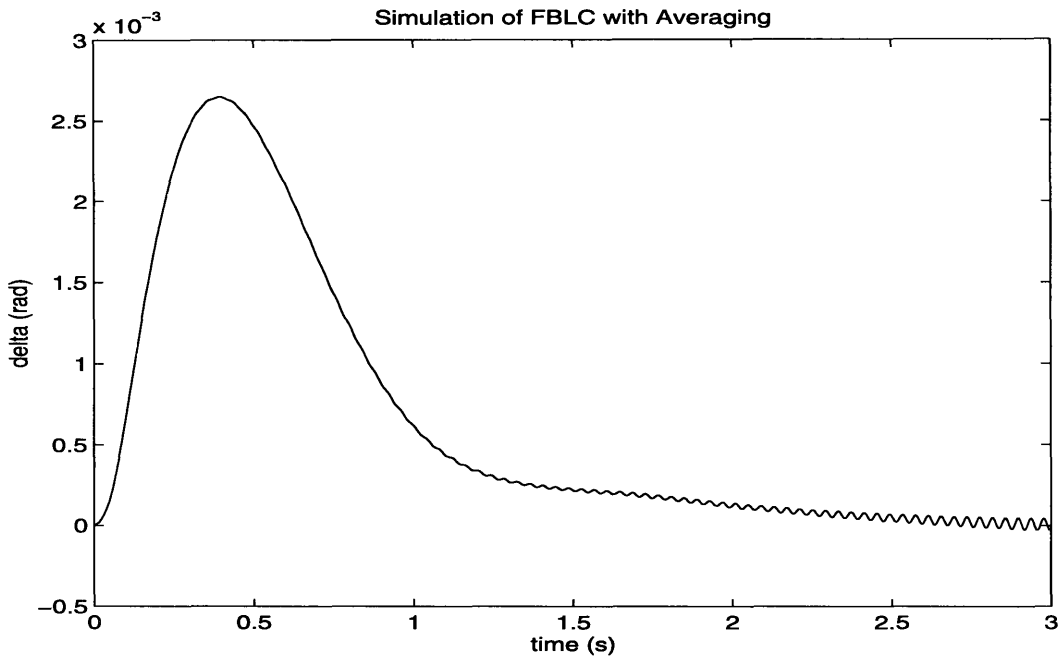

Figure 5-8: Simulated response of $\delta - \delta_o$ to a small disturbance with averaged FBLC.

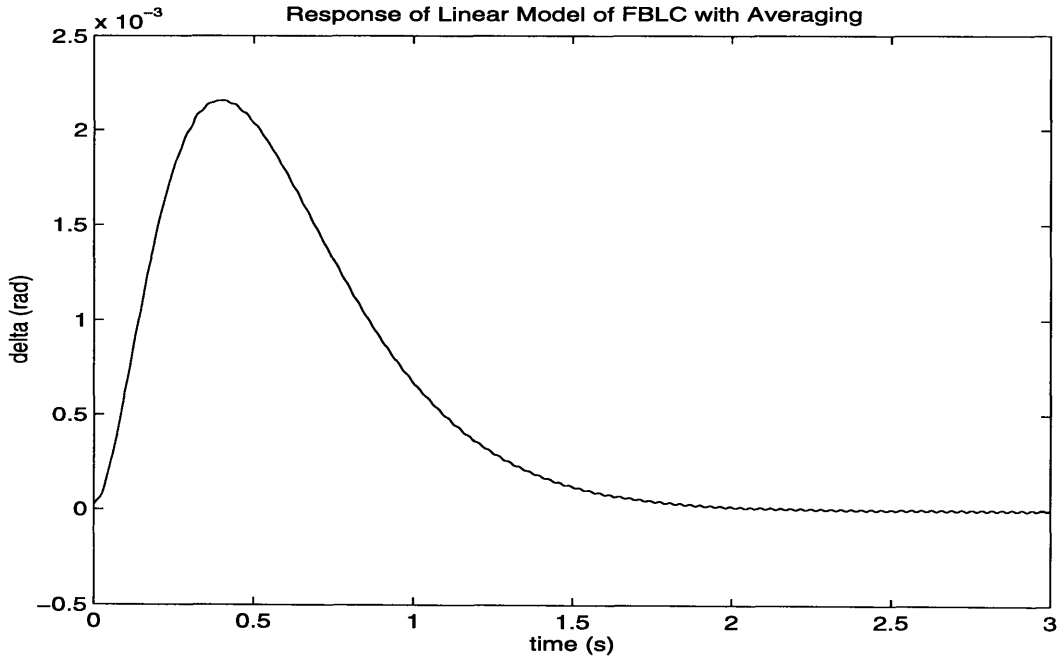

Figure 5-9: Disturbance response of $\delta - \delta_o$ calculated by the linear model.

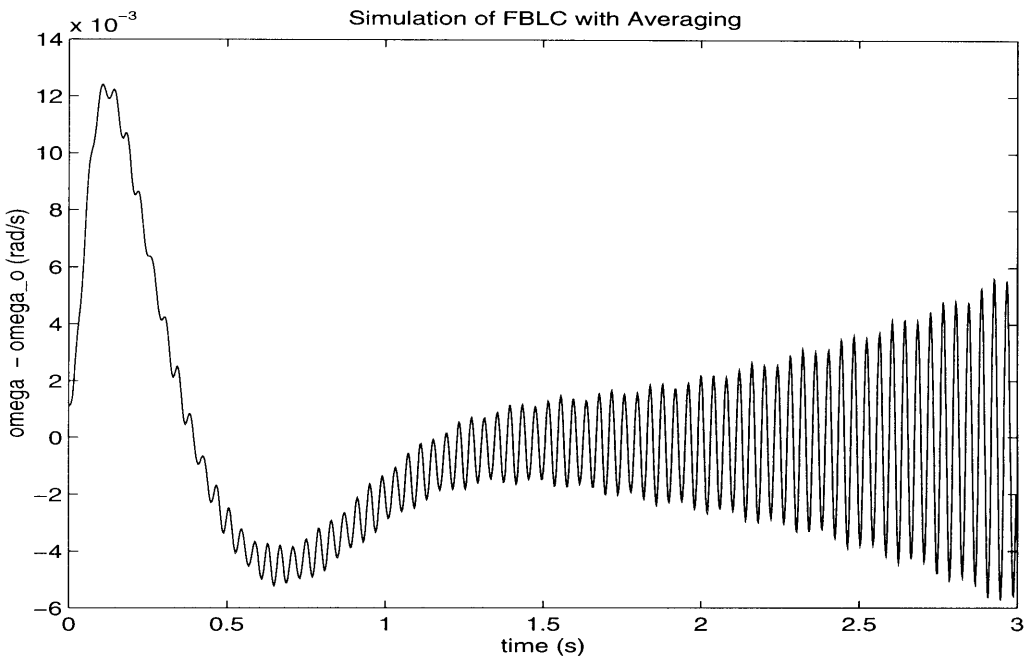

Figure 5-10: Simulated response of $\omega - \omega_o$ to a small disturbance with averaged FBLC.

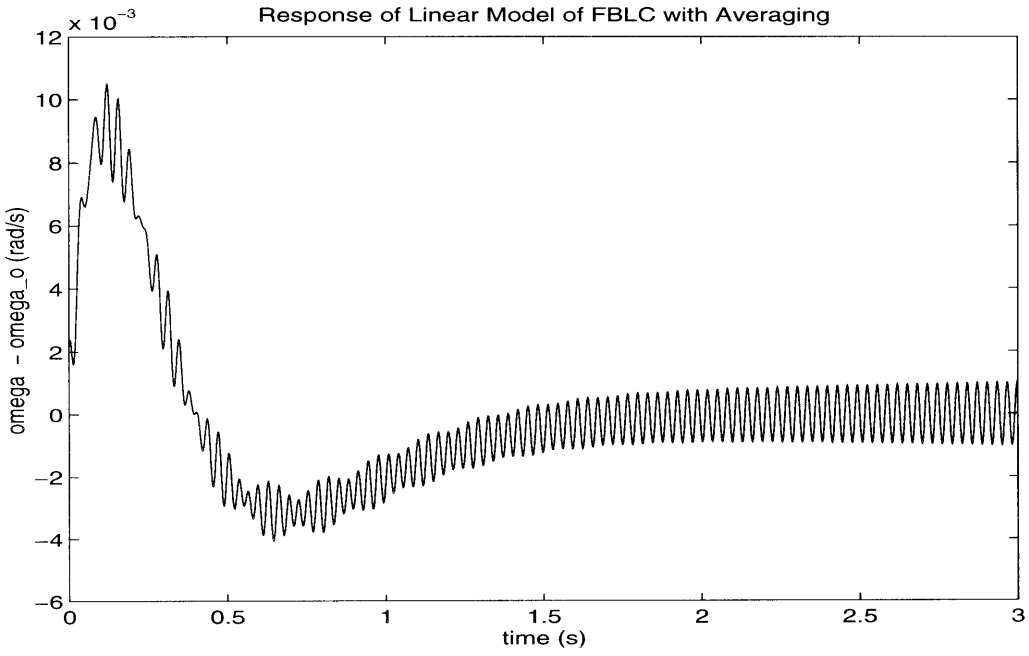

Figure 5-11: Disturbance response of $\omega - \omega_o$ calculated by the linear model.

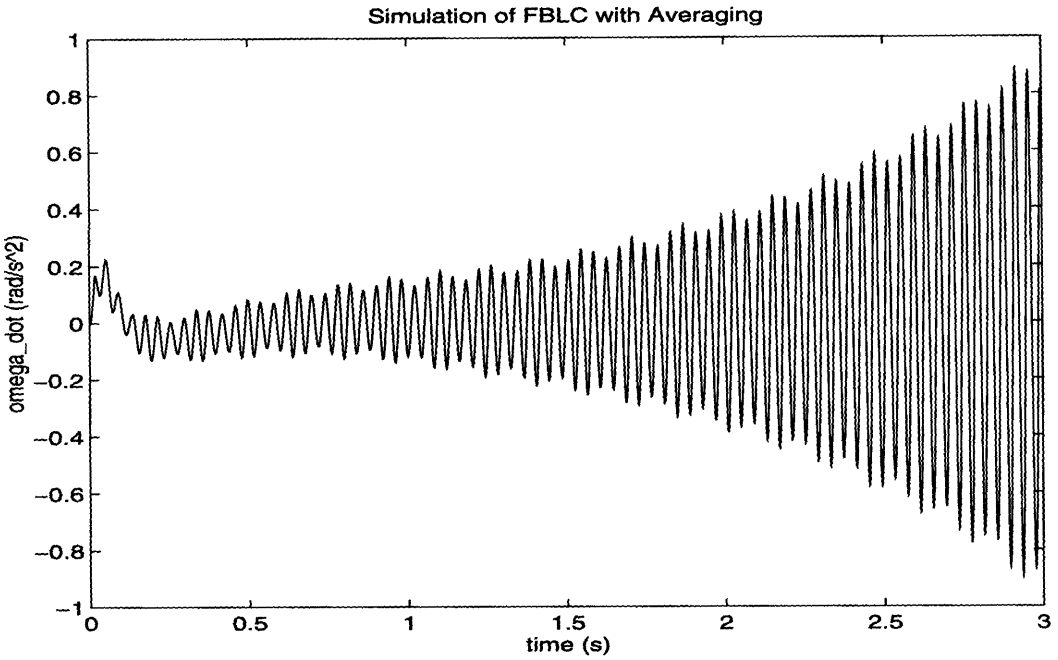

Figure 5-12: Simulated response of $\dot{\omega}$ to a small disturbance with averaged FBLC.

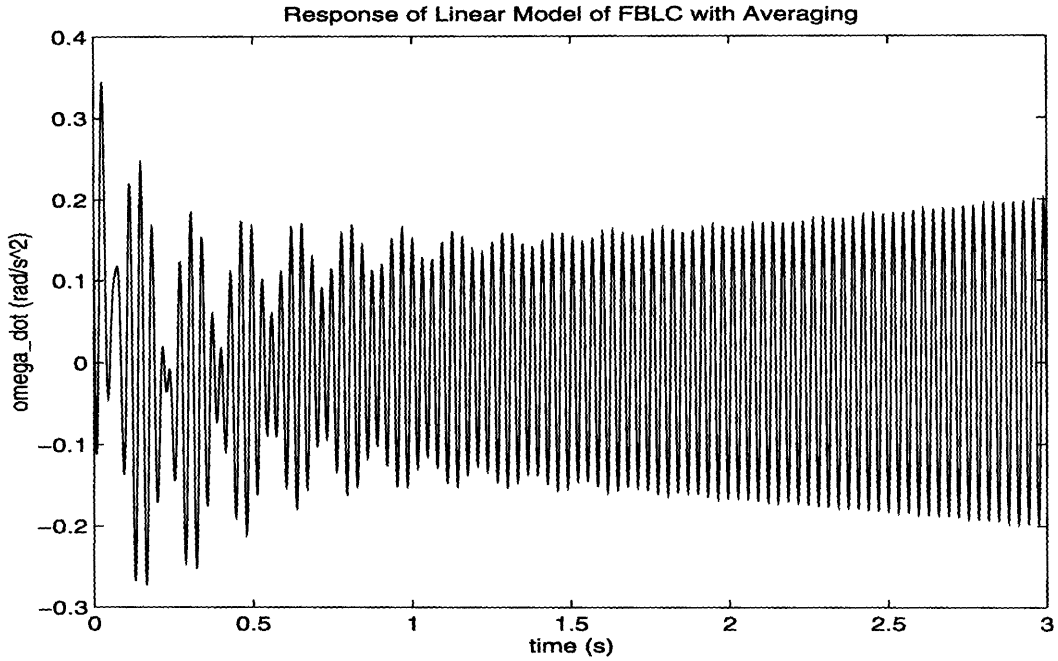

Figure 5-13: Disturbance response of $\dot{\omega}$ calculated by the linear model.

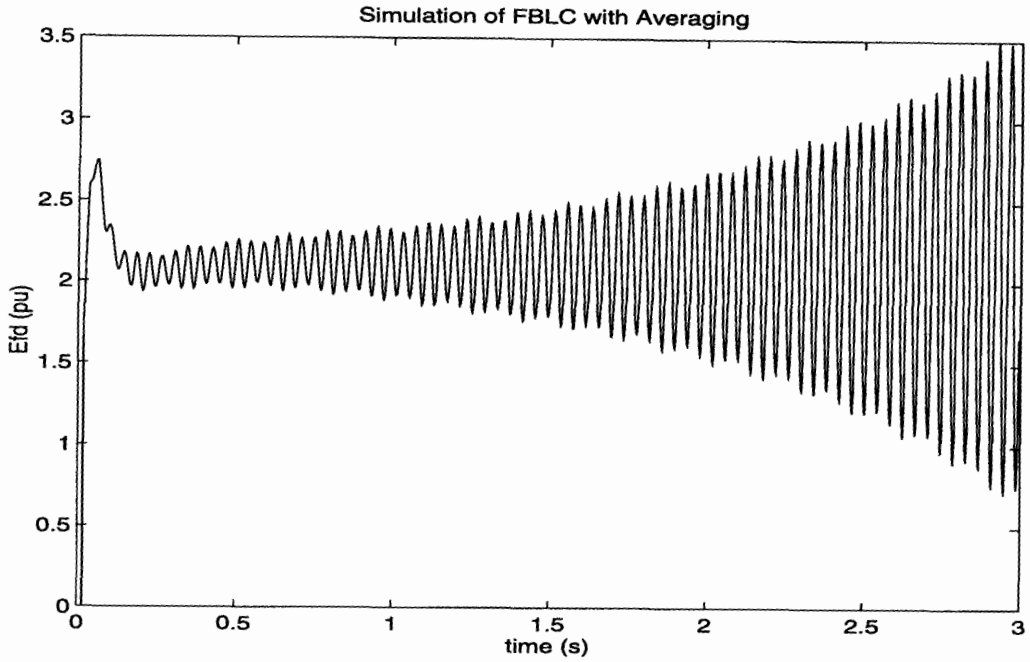

Figure 5-14: Simulated response of E_{fd} to a small disturbance with averaged FBLC.

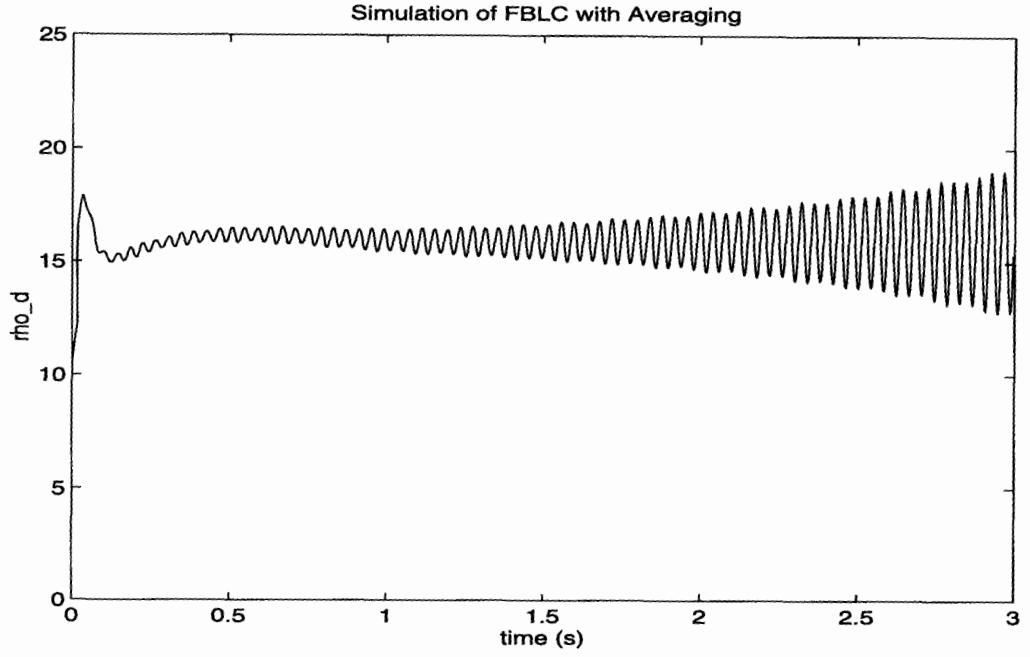

Figure 5-15: Simulated response of $\rho_d(\mathbf{x}_g)$ to a small disturbance with averaged FBLC.

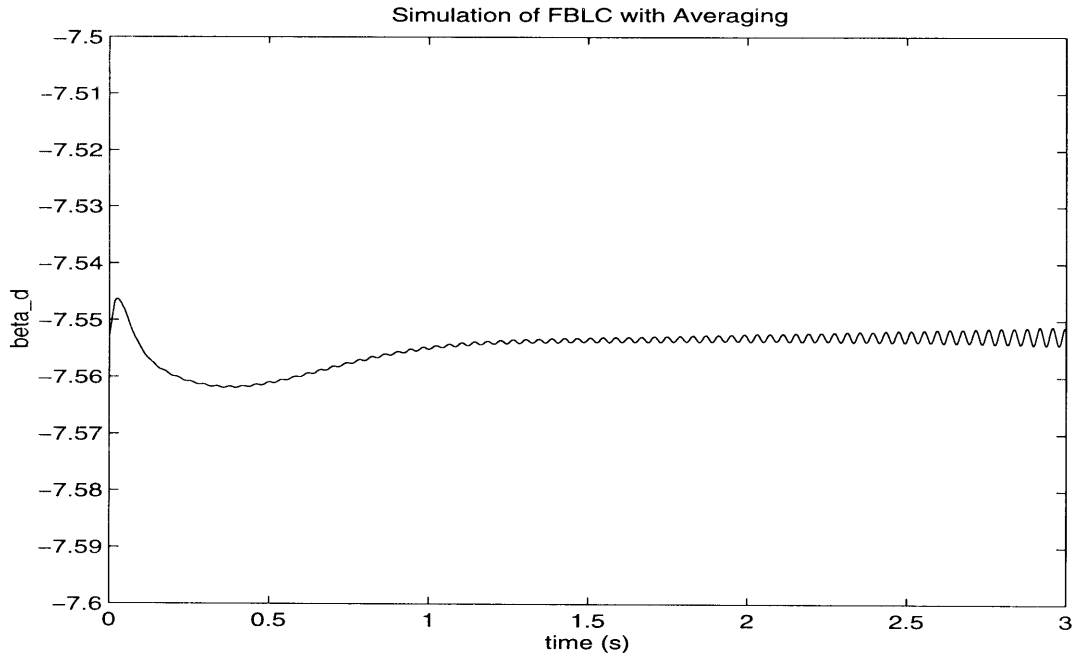

Figure 5-16: Simulated response of $\beta_d(\mathbf{x}_g)$ to a small disturbance with averaged FBLC.

Chapter 6

Butterworth Filtering of the Acceleration Measurement

In the last chapter, we saw that averaging of the field voltage did not succeed in attenuating the torsional oscillations and even led to instability. We will now try to generalize the concept of field voltage averaging by instead adding a low pass Butterworth filter to the acceleration measurement. This approach has the same pitfalls as field voltage averaging, but the filter design can be adjusted to prevent the phase shifts that lead to instability.

6.1 Description of a Butterworth filter

The transfer function of a Butterworth filter of order N will be written as $H_N(s)$ and is defined by [18]:

$$H_N(s)H_N(-s) = \frac{1}{1 + (s/j\omega_c)^{2N}} \tag{6.1}$$

where ω_c is the cutoff frequency in rad/s. By solving the denominator for $s = 0$, it is not hard to see that the poles of $H_N(s)H_N(-s)$ will be located at:

$$s = (-1)^{1/2N}(j\omega_c) \tag{6.2}$$

which are evenly spaced around the origin on a circle of radius ω_c. If s_p is a pole of $H_N(s)$, then $-s_p$ will be a pole of $H_N(-s)$. To create a stable and causal Butterworth filter, we need to choose the poles that are in the left half plane. By definition, a Butterworth filter has no zeros [18]. We will use Butterworth filters of first, second, and fourth order, all with a cutoff frequency of 10 Hz, or $\omega_c = 20\pi$. This cutoff frequency is chosen since it lies below the natural frequency of most shaft dynamics.

As before, we will use a frequency separation argument to obtain a linear model of the system. However, since only the acceleration measurement is being filtered, and the filter is linear, then the entire system with a third order generator model is itself linear! This means that we now have two linear models: a full order model, and a reduced order model of seventh order derived using the same arguments as

in Chapter 5. This gives us an excellent opportunity to test the accuracy of the frequency separation argument used in the last chapter. If the reduced order model is accurate, then clearly the extra modes arising from the filter are decoupled from the rest of the system. We note that if $\dot{\omega}$ is filtered, the attenuation coefficient $C(\omega)$ is equal to the transfer function $H_N(j\omega)$ of the filter.

6.2 First Order Butterworth Filter

We begin with the simplest Butterworth filter. From equation (6.2), the poles of $H_1(s)H_1(-s)$ are at $-\omega_c$ and ω_c. We clearly desire that the pole of $H_1(s)$ be at $-\omega_c$, so the transfer function becomes [18]:

$$H_1(s) = \frac{\omega_c}{s + \omega_c} \tag{6.3}$$

The transfer function is normalized such that $H_1(0) = 1$. This transfer function may also be represented as a first order dynamic system. It can be converted directly to a state-space description in controllability canonical form [5]:

$$\dot{x}_{f1} = -\omega_c x_{f1} + u_f \tag{6.4}$$

$$y_f = \omega_c x_{f1} \tag{6.5}$$

u_f represents the filter input, x_{fi} is filter state i, and y_f is the filter output. We will use the same notation for higher order filters.

6.2.1 Reduced Order Model of FBLC with First Order Butterworth Filter

Using the same arguments as the last chapter, we can derive a seventh-order model of the feedback linearized system with a first order Butterworth filter placed on the acceleration measurement. The first three modes in Table 3.1 are assumed to vary slowly and included directly in the reduced order model. The other modes are calculated with an iterative technique, using $C(\omega) = H_1(j\omega)$. The eigenvalues of this system are shown in Table 6.1. The system is still predicted to be stable, although the torsional modes have less damping than before.

6.2.2 Full Linear Model of FBLC with First Order Butterworth Filter

The full order model of this system is actually quite easy to produce. The filter input u_f is equal to α_e. Note that only E_{fd} depends on the filtered acceleration measurement; consequently, $\rho_d(\mathbf{x}_g)$ depends on y_f, the filtered measurement of α_e, while $\rho(\mathbf{x}_g)$ is a function of the actual quantity α_e. Therefore, the state equation for

Number(s)	Eigenvalue	Frequency (Hz)
1	-6.99	–
2,3	$-4.12 \pm j1.04$	0.1662
4,5	$-0.41 \pm j197.57$	31.44
6,7	$-1.85 \pm j155.96$	24.82

Table 6.1: Eigenvalues and frequencies of the reduced linear model of feedback linearizing control with a first order Butterworth filter of acceleration.

$\dot{\alpha}_e$ is:

$$\begin{aligned}\dot{\alpha}_e &= \frac{H}{H_e}\left(a_0(\delta_e - \delta_o) + a_1(\omega_e - \omega_o) + a_2 y_f\right) \\ &\quad - \frac{\omega_o}{2H_e}\left[-K_{2eu}\frac{\omega_2}{\omega_o} + K_{2eu}\frac{\omega_e}{\omega_o} + D_{eu}\frac{\alpha_e}{\omega_o} - D\frac{y_f}{\omega_o}\right] \end{aligned} \tag{6.6}$$

When this equation and the dynamics of the filter are incorporated into the full state model, the result is:

$$\dot{\mathbf{x}}_{b1} = \mathbf{A}_{b1}\mathbf{x}_{b1} \tag{6.7}$$

$$\mathbf{x}_{b1} = \begin{bmatrix} \delta_e - \delta_o \\ \omega_e - \omega_o \\ \alpha_e \\ \delta_1 - \delta_{10} \\ \omega_1 - \omega_o \\ \delta_2 - \delta_{20} \\ \omega_2 - \omega_o \\ x_{f1} \end{bmatrix} \tag{6.8}$$

Number(s)	Eigenvalue	Frequency (Hz)
1	-17.36	–
2,3	$-3.18 \pm j1.38$	0.2197
4,5	$-0.41 \pm j197.57$	31.44
6,7	$-1.81 \pm j156.00$	24.83
8	-35.08	–

Table 6.2: Eigenvalues and frequencies of the linear model of feedback linearizing control with a first order Butterworth filter of acceleration.

$$\mathbf{A}_{b1} = \begin{bmatrix} 0 & 1 & 0 & 0 & 0 & 0 & 0 & 0 \\ 0 & 0 & 1 & 0 & 0 & 0 & 0 & 0 \\ \frac{a_0 H}{H_e} & \frac{2a_1 H - K_{2eu}}{2H_e} & -\frac{D_{eu}}{2H_e} & 0 & 0 & 0 & \frac{K_{2eu}}{2H_e} & \frac{\omega_c(2a_2 H + D)}{2H_e} \\ 0 & 0 & 0 & 0 & 1 & 0 & 0 & 0 \\ 0 & 0 & 0 & -\frac{K_{12u}}{2H_1} & -\frac{D_{1u}}{2H_1} & \frac{K_{12u}}{2H_1} & 0 & 0 \\ 0 & 0 & 0 & 0 & 0 & 0 & 1 & 0 \\ \frac{K_{2eu}}{2H_2} & 0 & 0 & \frac{K_{12u}}{2H_2} & 0 & -\frac{K_{12u}+K_{2eu}}{2H_2} & -\frac{D_{2u}}{2H_2} & 0 \\ 0 & 0 & 1 & 0 & 0 & 0 & 0 & -\omega_c \end{bmatrix} \tag{6.9}$$

This model was verified by using the same techniques as in Section 3.7. The eigenvalues of this system are shown in Table 6.2. Note that the torsional eigenvalues are nearly identical to those given by the reduced order model, but the low frequency dynamics do not match up so well. It would appear that the errors can be attributed to the approximation that these modes were constant; according to their eigenvalues, they decay fast enough to be affected by the filter.

6.2.3 Response of First Order Filtering to a Small Disturbance

We now have three models to simulate; a full linear description, a reduced order linear model, and a higher order dynamic model which includes subtransient generator

dynamics. All of these models were simulated using an initial condition of:

$$\mathbf{x}_{b1} = \begin{bmatrix} 1.71 \times 10^{-5} \\ 1.24 \times 10^{-2} \\ -3.48 \times 10^{-1} \\ 0 \\ 0 \\ 0 \\ 0 \\ 0 \end{bmatrix} \tag{6.10}$$

The simulation results are shown in Figures 6-1 through 6-12. The simulated response is in good agreement with the response of the full order linear model. The reduced order model exhibits little difference from the other models in the response of $\dot{\omega}$ but a significant difference in the magnitude of the peak in δ. However, all three models agree on the amount of damping present in the shaft modes.

6.3 Second Order Butterworth Filtering

Next, we will look at using a second order filter. The poles of $H_2(s)$ occurs at $\omega_c e^{j(3\pi/4)}$ and $\omega_c e^{-j(3\pi/4)}$, and the transfer function can be written as:

$$H_2(s) = \frac{\omega_c^2}{(s - \omega_c e^{j(3\pi/4)})(s - \omega_c e^{-j(3\pi/4)})} \tag{6.11}$$

The denominator can be multiplied out to produce:

$$H_2(s) = \frac{\omega_c^2}{s^2 - \omega_c(e^{j(3\pi/4)} + e^{-j(3\pi/4)})s + \omega_c^2} \tag{6.12}$$

The sum of the complex exponentials is $-\sqrt{2}$, so the second order Butterworth transfer function is [18]:

$$H_2(s) = \frac{\omega_c^2}{s^2 + \omega_c s\sqrt{2} + \omega_c^2} \tag{6.13}$$

The dynamic model of this filter may be represented as:

$$\begin{bmatrix} \dot{x}_{f1} \\ \dot{x}_{f2} \end{bmatrix} = \begin{bmatrix} 0 & 1 \\ -\omega_c^2 & -\omega_c\sqrt{2} \end{bmatrix} \begin{bmatrix} x_{f1} \\ x_{f2} \end{bmatrix} + \begin{bmatrix} 0 \\ 1 \end{bmatrix} u_f \tag{6.14}$$

$$y_f = \begin{bmatrix} \omega_c^2 & 0 \end{bmatrix} \begin{bmatrix} x_{f1} \\ x_{f2} \end{bmatrix} \tag{6.15}$$

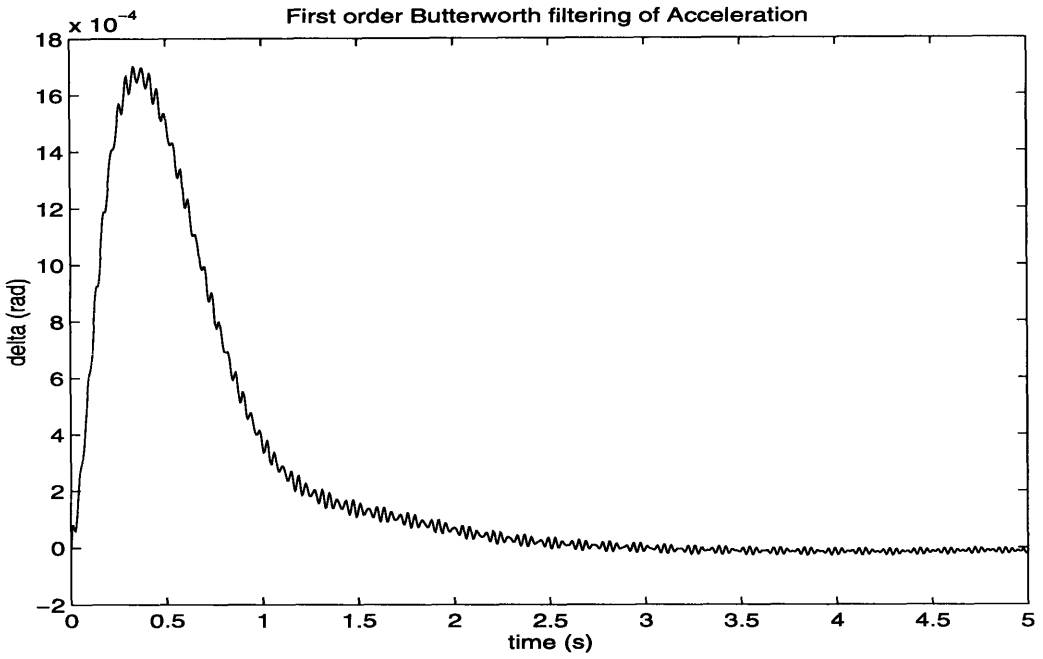

Figure 6-1: Simulated response of $\delta - \delta_o$ to a small disturbance with first order Butterworth filtering of $\dot{\omega}$.

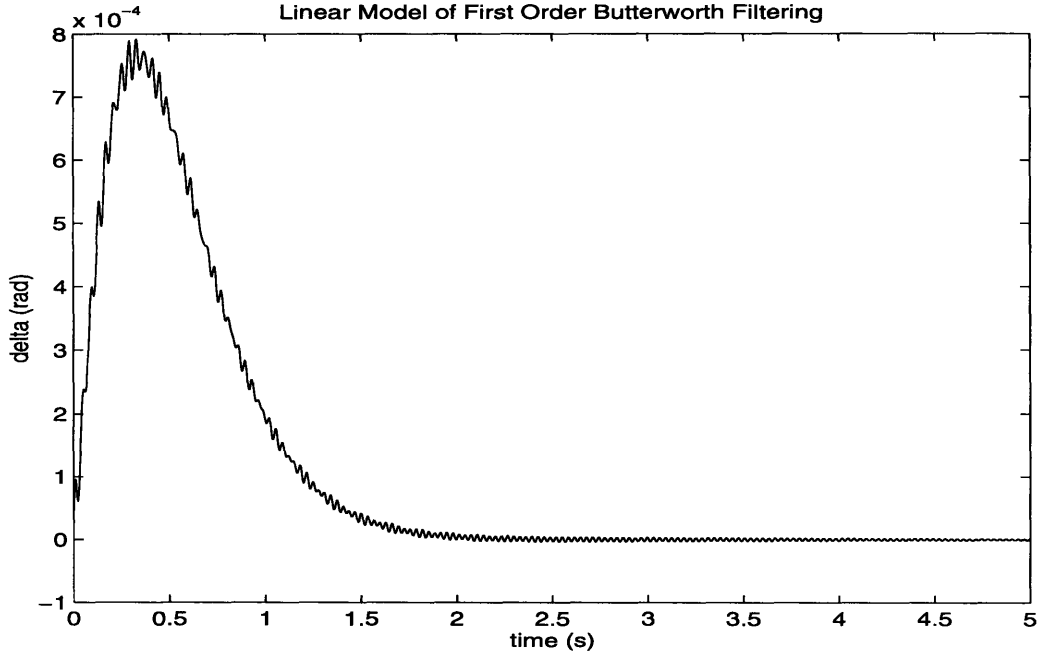

Figure 6-2: Disturbance response of $\delta - \delta_o$ calculated by the reduced linear model.

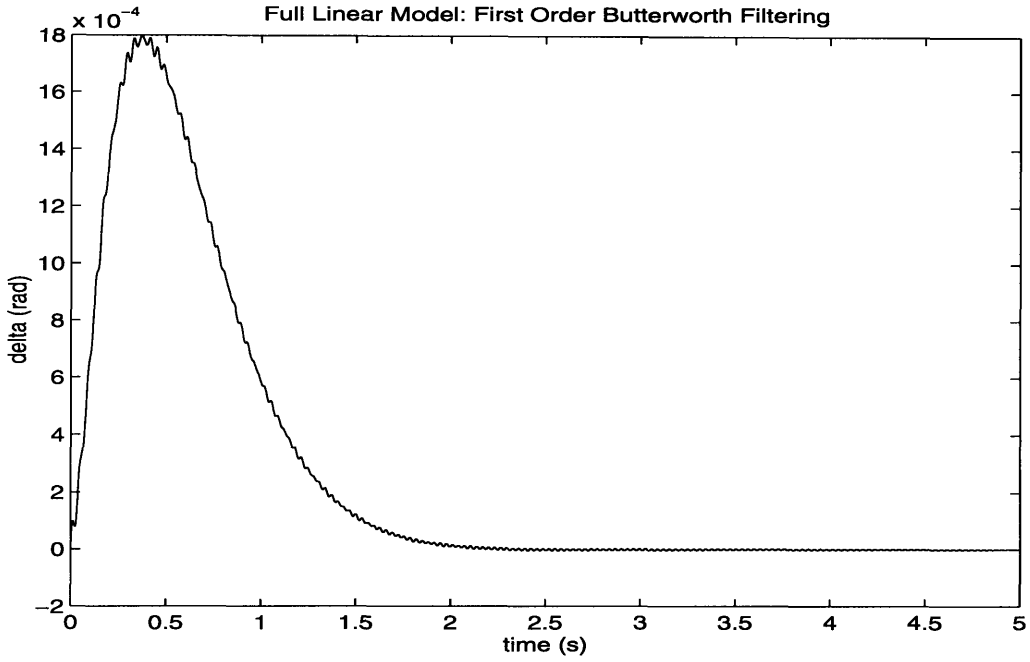

Figure 6-3: Disturbance response of $\delta - \delta_o$ calculated by the linear model.

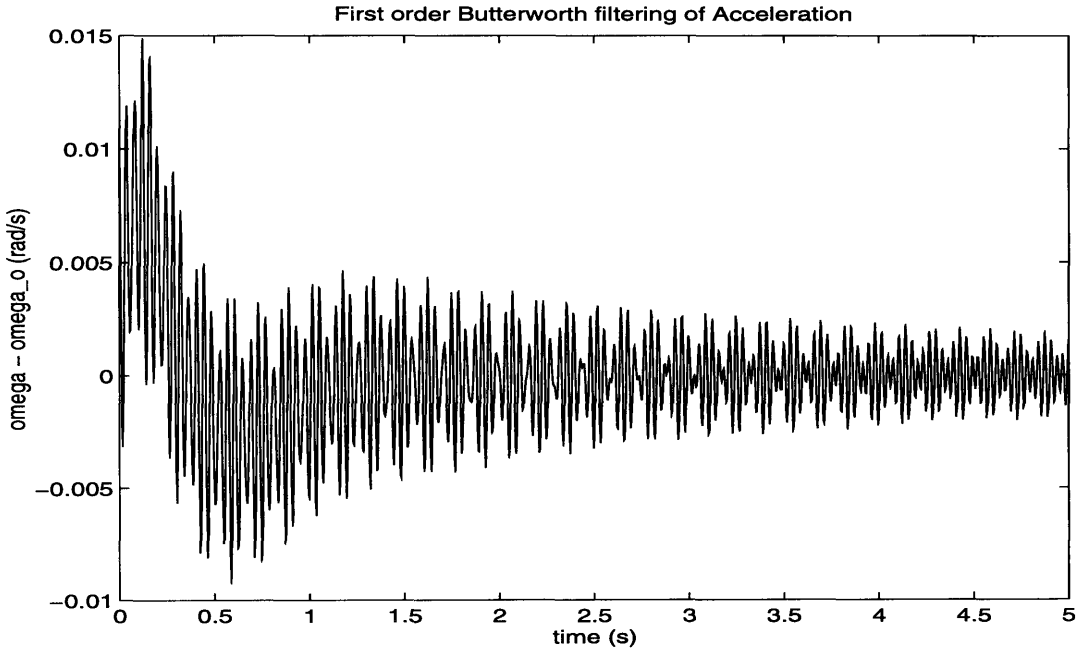

Figure 6-4: Simulated response of $\omega - \omega_o$ to a small disturbance with first order Butterworth filtering of $\dot{\omega}$.

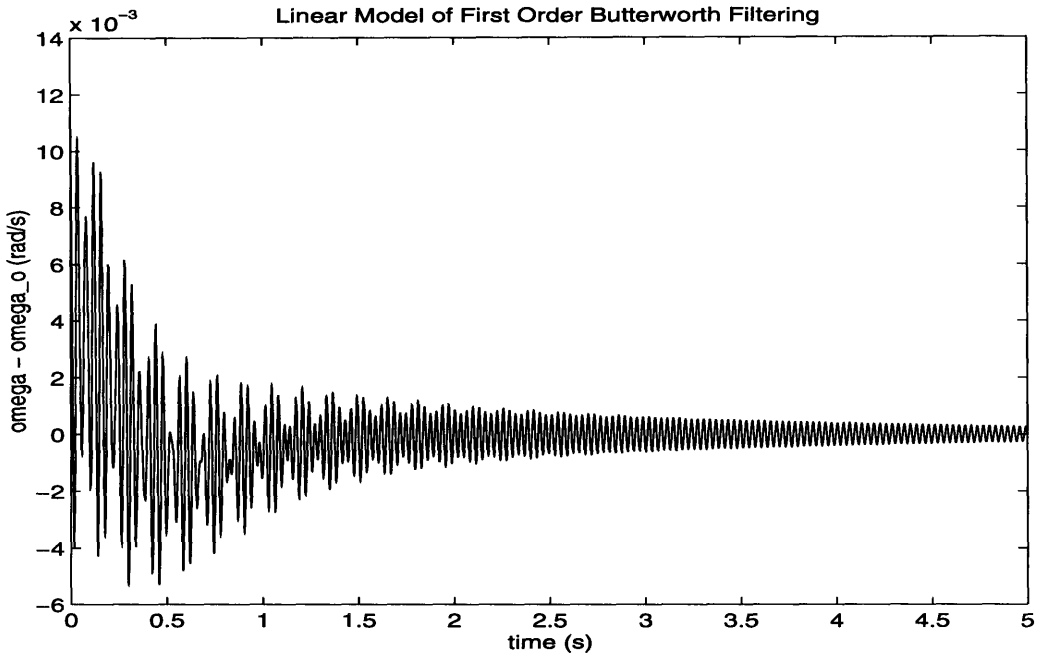

Figure 6-5: Disturbance response of $\omega - \omega_o$ calculated by the reduced linear model.

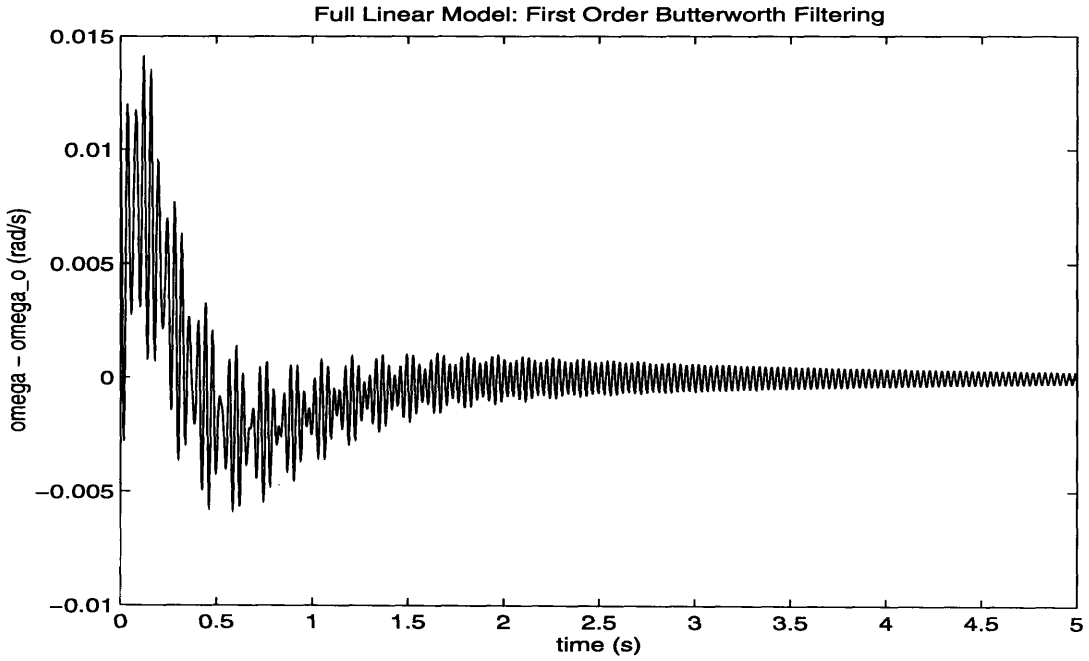

Figure 6-6: Disturbance response of $\omega - \omega_o$ calculated by the linear model.

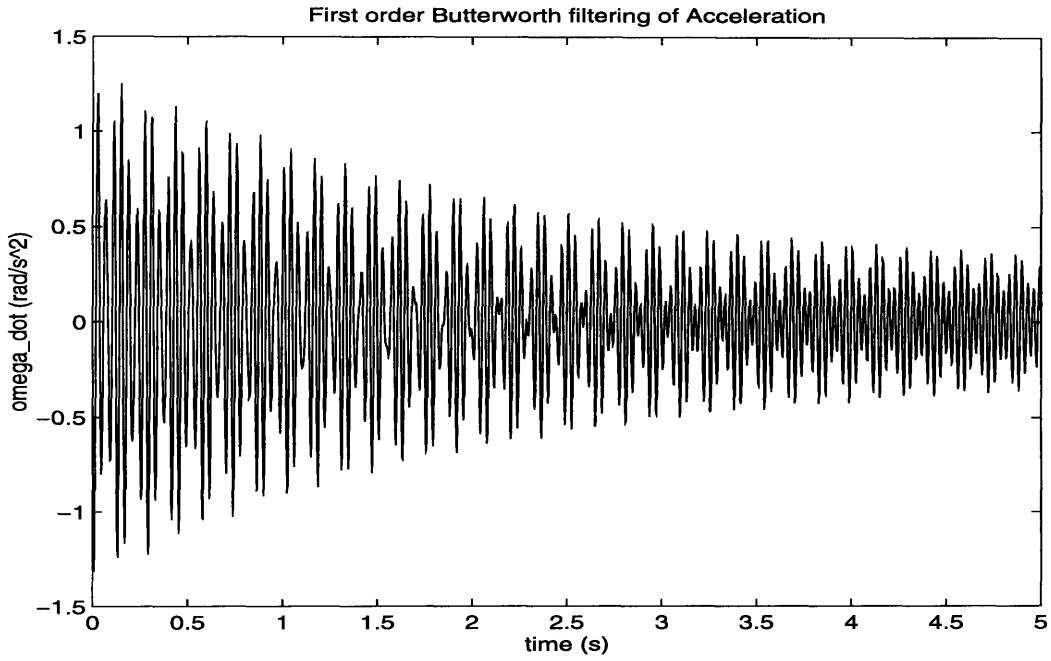

Figure 6-7: Simulated response of $\dot{\omega}$ to a small disturbance with first order Butterworth filtering of $\dot{\omega}$.

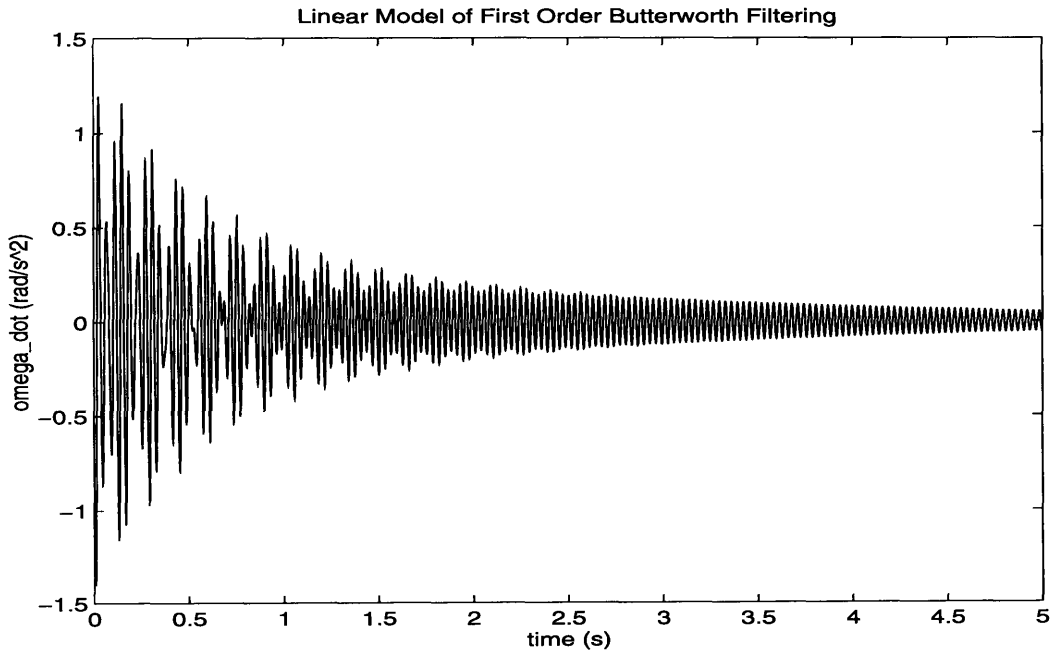

Figure 6-8: Disturbance response of $\dot{\omega}$ calculated by the reduced linear model.

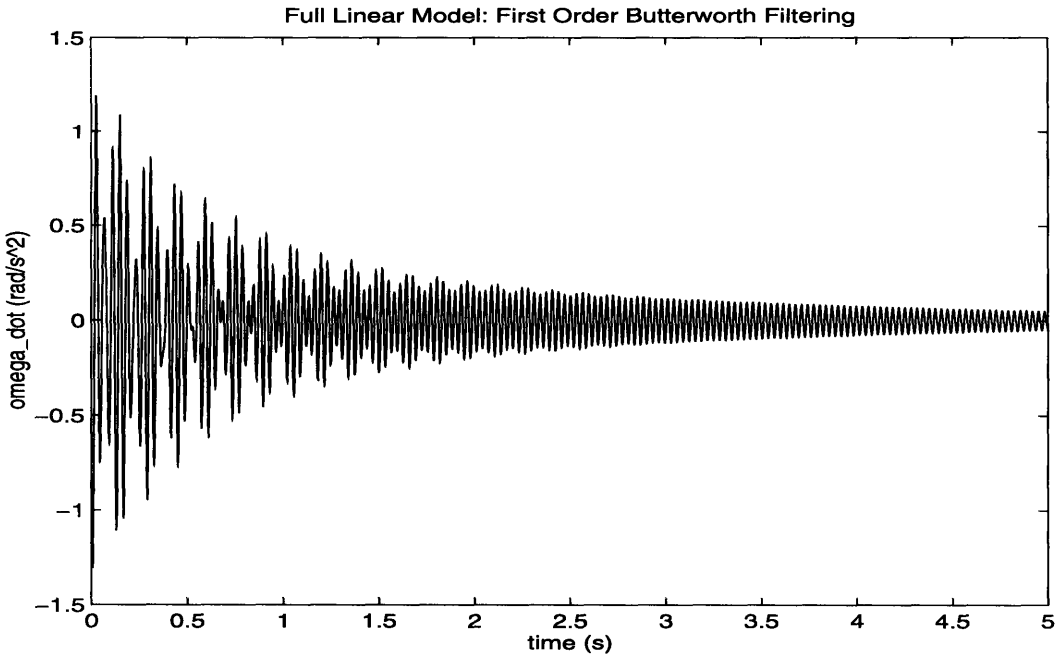

Figure 6-9: Disturbance response of $\dot{\omega}$ calculated by the linear model.

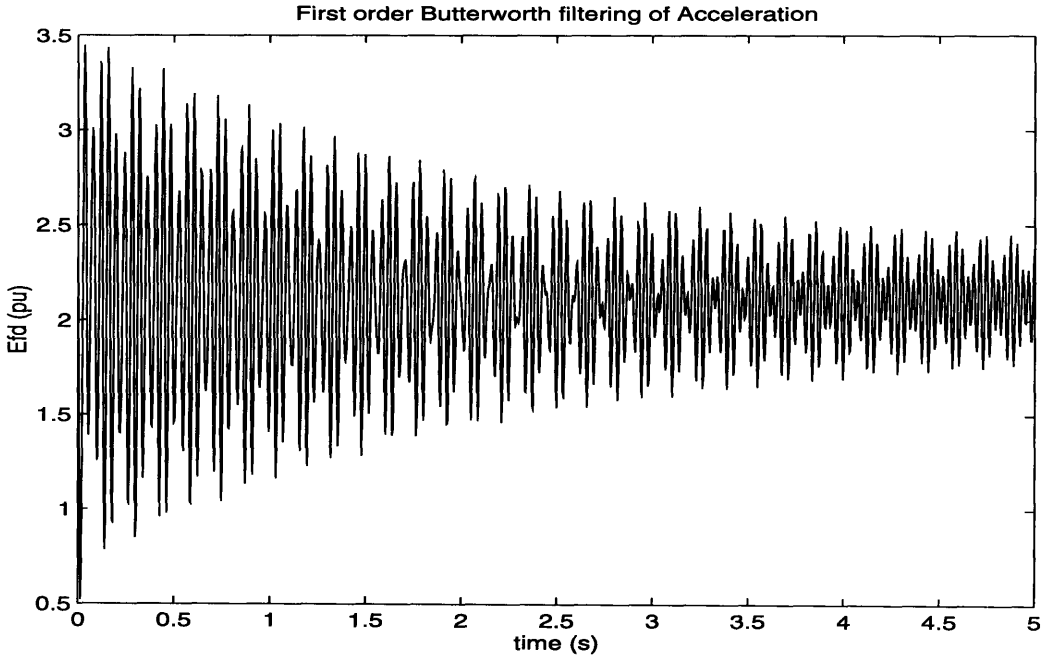

Figure 6-10: Simulated response of E_{fd} to a small disturbance with first order Butterworth filtering of $\dot{\omega}$.

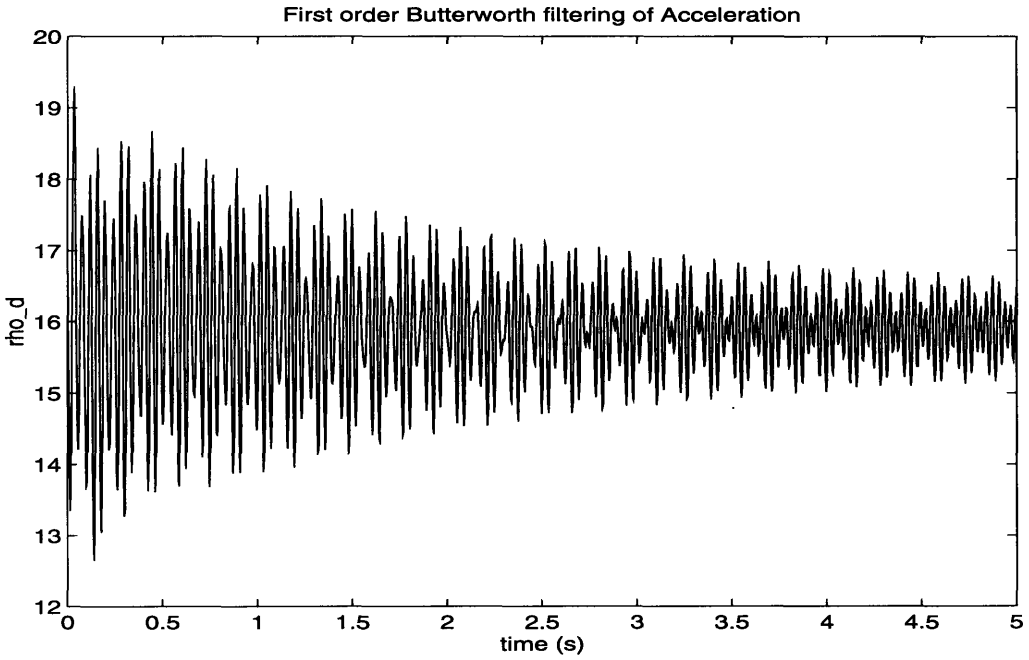

Figure 6-11: Simulated response of $\rho_d(\mathbf{x}_g)$ to a small disturbance with first order Butterworth filtering of $\dot{\omega}$.

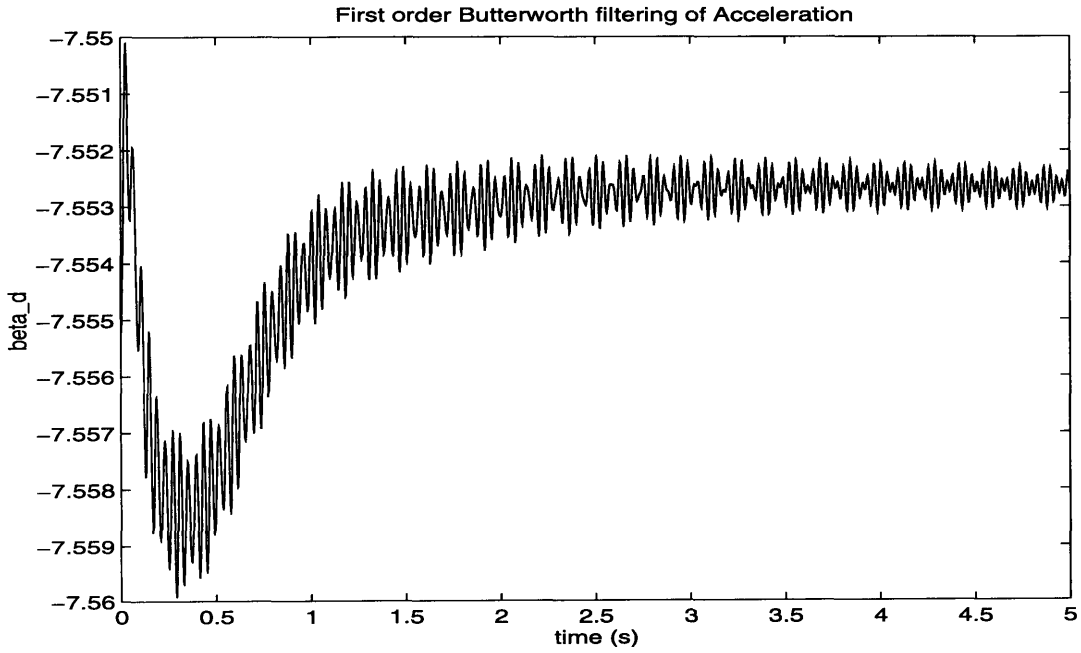

Figure 6-12: Simulated response of $\beta_d(\mathbf{x}_g)$ to a small disturbance with first order Butterworth filtering of $\dot{\omega}$.

Number(s)	Eigenvalue	Frequency (Hz)
1	-6.99	-
2,3	$-4.12 \pm j1.04$	0.1662
4,5	$0.22 \pm j196.74$	31.31
6,7	$1.63 \pm j152.80$	24.32

Table 6.3: Eigenvalues and frequencies of the reduced linear model of feedback linearizing control with a second order Butterworth filter of acceleration.

Number(s)	Eigenvalue	Frequency (Hz)
1	-21.07	-
2,3	$-3.02 \pm j1.41$	0.2247
4,5	$0.22 \pm j196.74$	31.31
6,7	$1.60 \pm j152.82$	24.32
8,9	$-32.88 \pm j31.23$	4.97

Table 6.4: Eigenvalues and frequencies of the linear model of feedback linearizing control with a first order Butterworth filter of acceleration.

6.3.1 Linear Models of FBLC with Second Order Butterworth Filtering

As before, we develop a seventh-order model of the system by calculating a matrix $\mathbf{A}_{C(\omega_i)}$ for each frequency. The eigenvalues of this model are shown in Table 6.3. The model predicts that both torsional modes are unstable. This result is expected since a second order Butterworth filter inverts the signals in the stopband.

The full order linear model is derived by the same procedure as before; setting $u_f = \alpha_e$, and feeding y_f into the equation for E_{fd}. Table 6.4 gives the eigenvalues of this linear model, which has nine states.

6.3.2 Simulations of Second Order Butterworth Filtering

We will now simulate the response of the three models available to describe FBLC with second order Butterworth filtering of the acceleration measurement. The initial

conditions are:

$$\mathbf{x}_{b2} = \begin{bmatrix} 2.77 \times 10^{-7} \\ 1.74 \times 10^{-3} \\ -1.08 \times 10^{-2} \\ 0 \\ 0 \\ 0 \\ 0 \\ 0 \\ 0 \end{bmatrix} \tag{6.16}$$

The responses of the three models are shown in Figures 6-13 to 6-24. All three models give basically the same response, although the oscillations grow a little more rapidly in the reduced linear model than in the other two models. As predicted earlier, the -180^o phase shift in the stopband excites the torsional oscillations.

6.4 Fourth Order Butterworth Filter

Finally, we will look at the fourth order Butterworth filter. The phase shift in the stopband of this filter is a full -360^o, so we expect that the torsional modes will not be excited when the fourth order filter is used. First, we derive the transfer function of the filter. According to equation (6.2), the poles are located at $s = \omega_c e^{j(5\pi/8)}$, $\omega_c e^{j(7\pi/8)}$, $\omega_c e^{-j(5\pi/8)}$, $\omega_c e^{-j(7\pi/8)}$. The transfer function of the filter may therefore be written as:

$$H_4(s) = \frac{\omega_c^4}{(s^2 - \omega_c(e^{j(5\pi/8)} + e^{-j(5\pi/8)})s + \omega_c^2)(s^2 - \omega_c(e^{j(7\pi/8)} + e^{-j(7\pi/8)})s + \omega_c^2)} \tag{6.17}$$

Summing the complex exponentials gives:

$$H_4(s) = \frac{\omega_c^4}{(s^2 + 0.7654\omega_c s + \omega_c^2)(s^2 + 1.8478\omega_c s + \omega_c^2)} \tag{6.18}$$

Finally, multiplying out the denominator, we have:

$$H_4(s) = \frac{\omega_c^4}{s^4 + 2.6131\omega_c s^3 + (2 + \sqrt{2})\omega_c^2 s^2 + 2.6131\omega_c^3 s + \omega_c^4} \tag{6.19}$$

The value 2.6131 is an approximation of $2\cos\pi/8 + 2\cos 3\pi/8$.

The dynamic model of this filter may be derived using the same procedure as

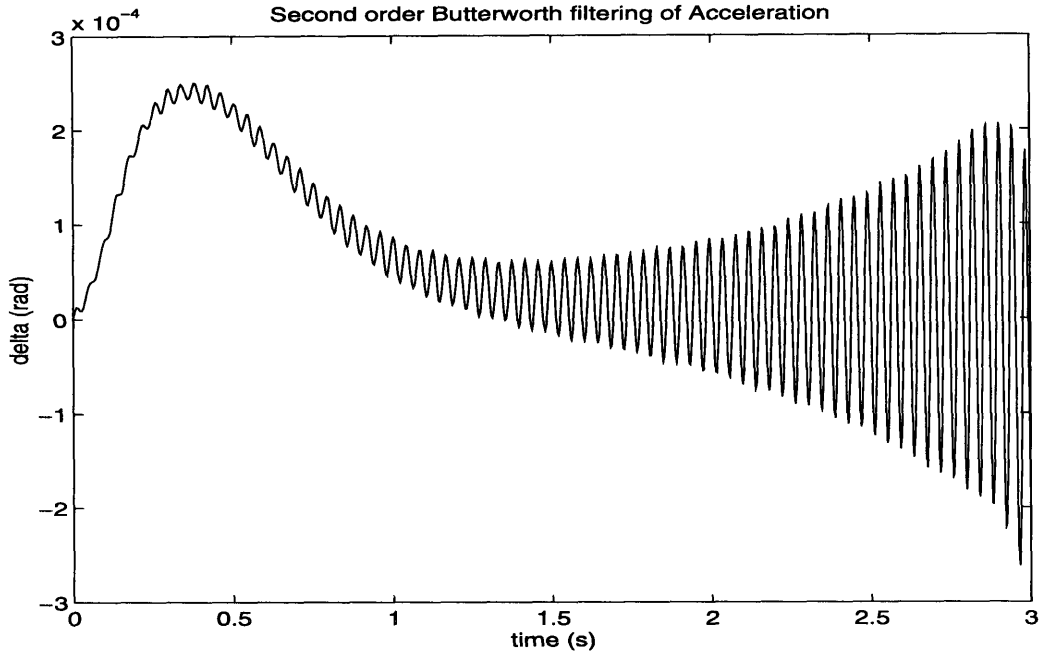

Figure 6-13: Simulated response of $\delta - \delta_o$ to a small disturbance with second order Butterworth filtering of $\dot{\omega}$.

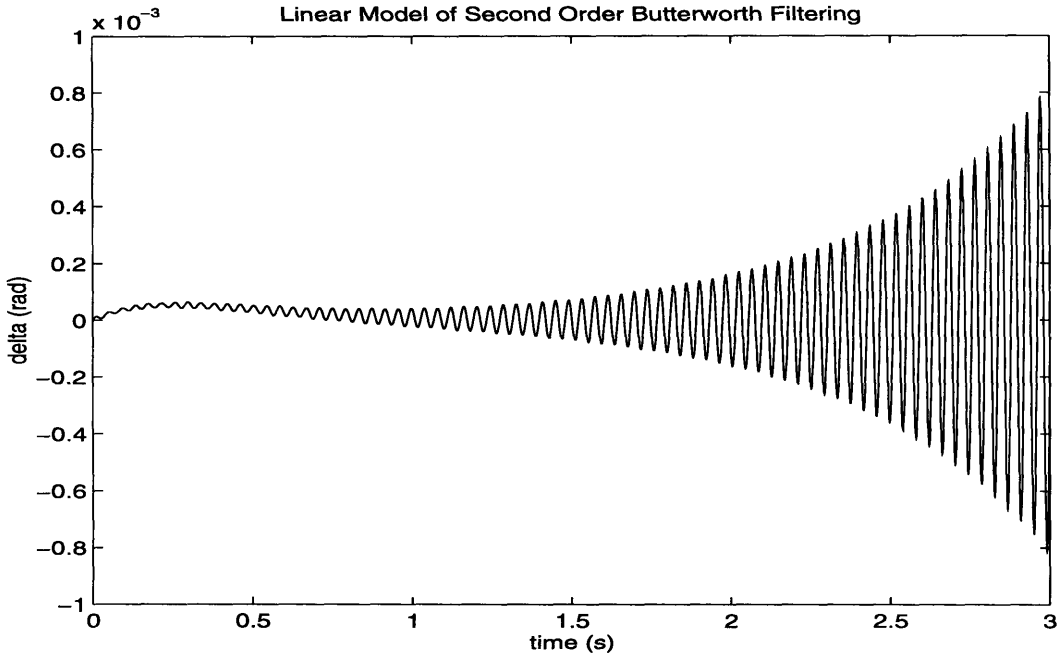

Figure 6-14: Disturbance response of $\delta - \delta_o$ calculated by the reduced linear model.

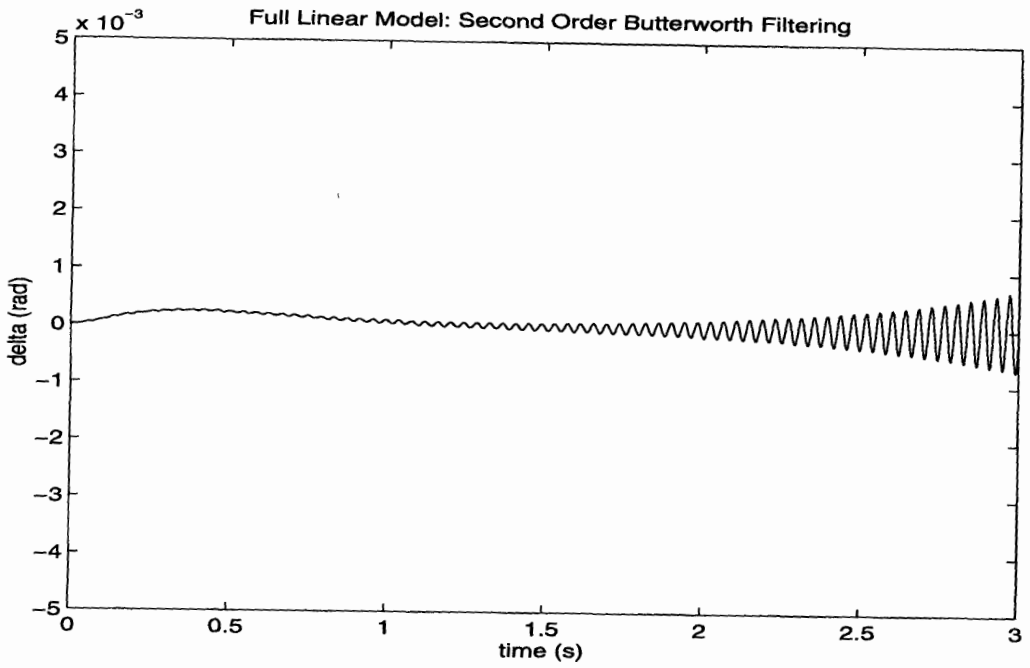

Figure 6-15: Disturbance response of $\delta - \delta_o$ calculated by the linear model.

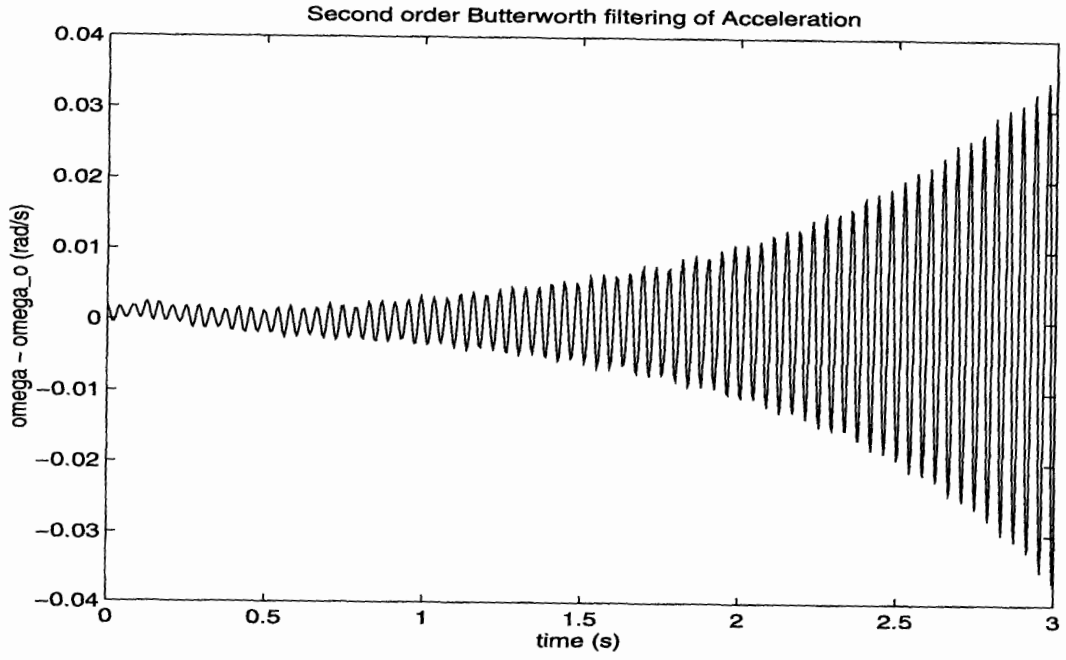

Figure 6-16: Simulated response of $\omega - \omega_o$ to a small disturbance with second order Butterworth filtering of $\dot{\omega}$.

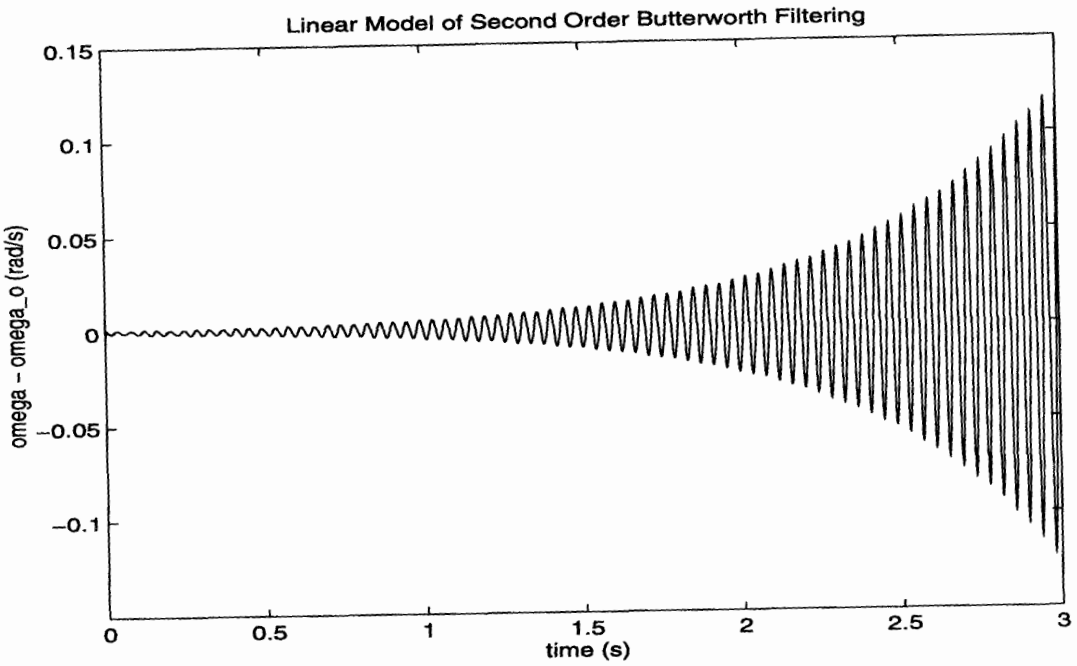

Figure 6-17: Disturbance response of $\omega - \omega_o$ calculated by the reduced linear model.

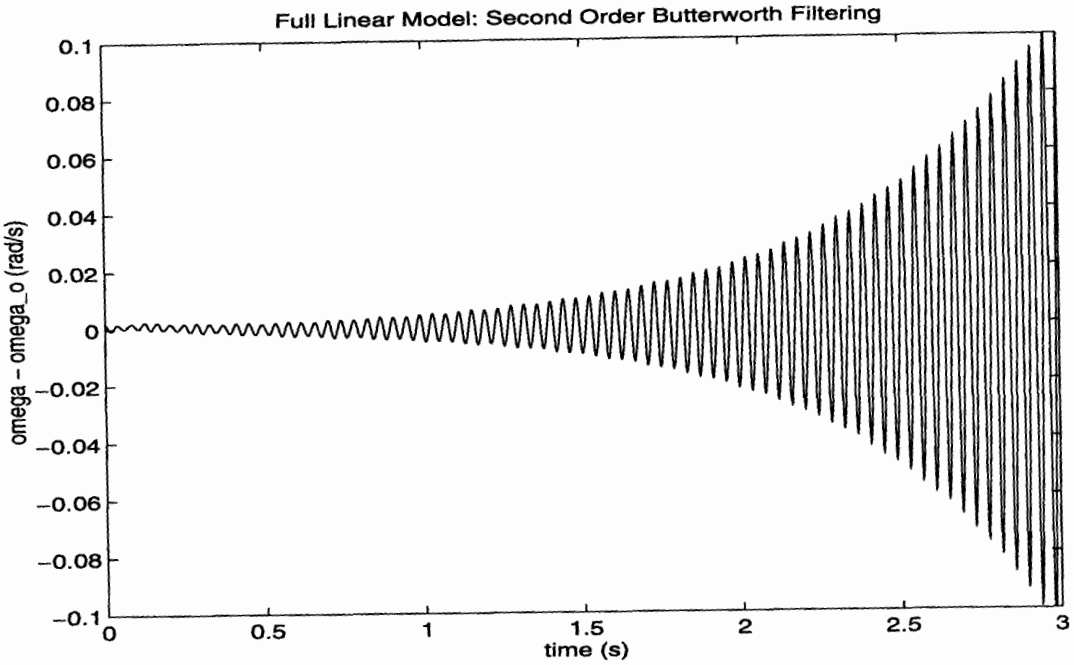

Figure 6-18: Disturbance response of $\omega - \omega_o$ calculated by the linear model.

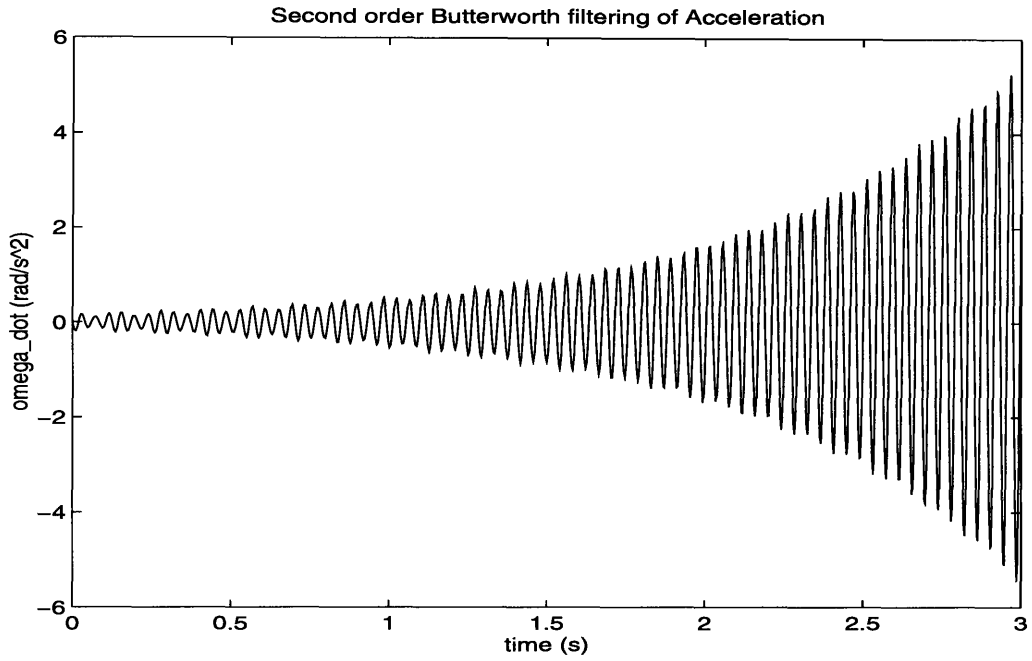

Figure 6-19: Simulated response of $\dot{\omega}$ to a small disturbance with second order Butterworth filtering of $\dot{\omega}$.

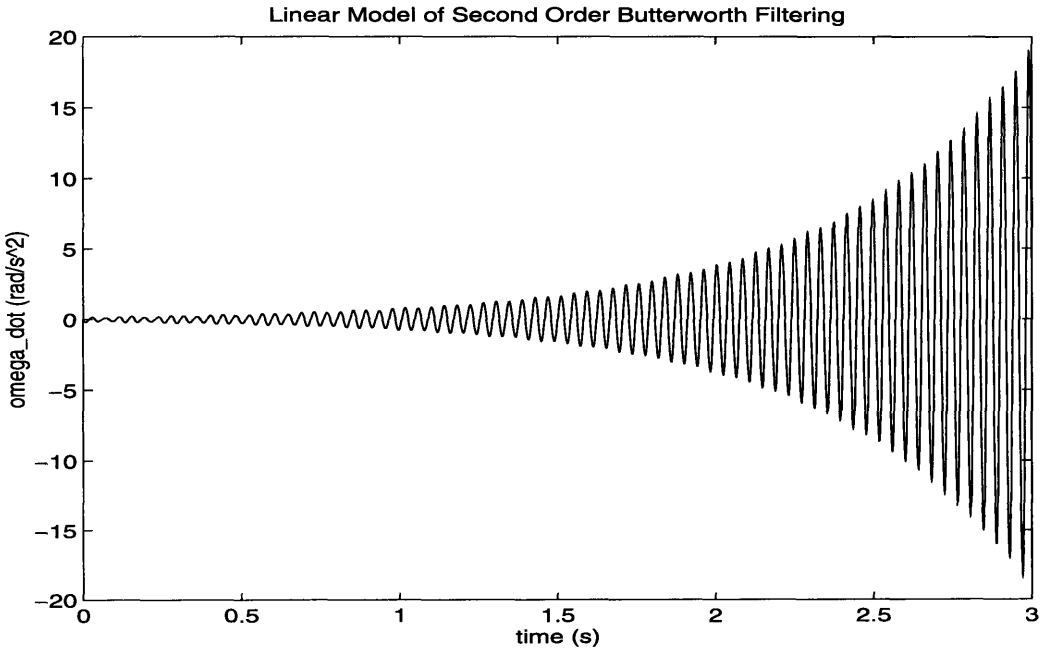

Figure 6-20: Disturbance response of $\dot{\omega}$ calculated by the reduced linear model.

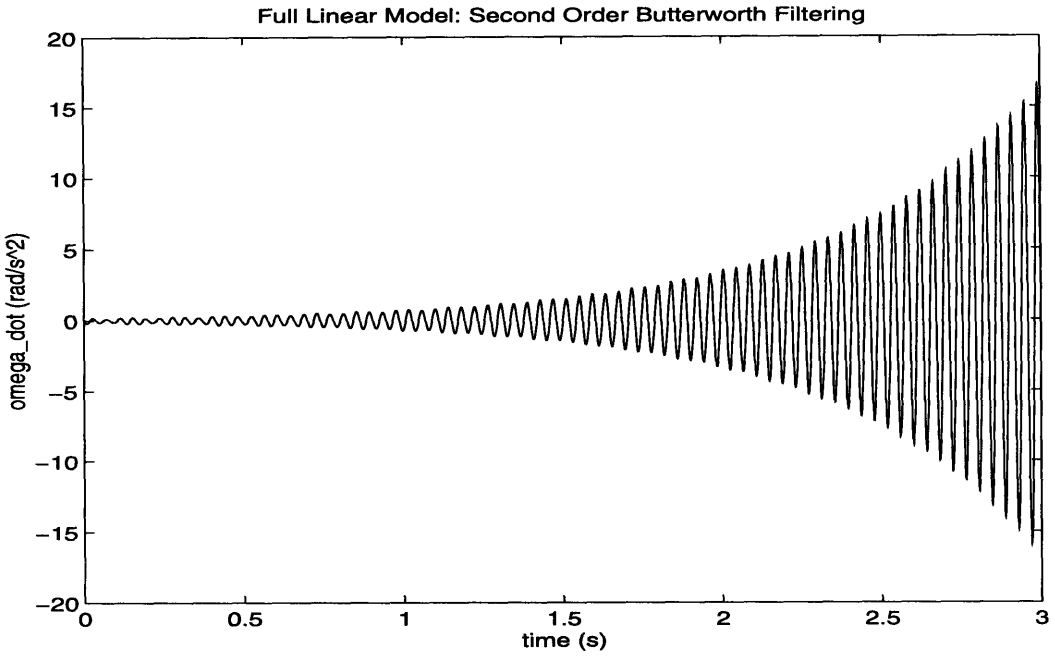

Figure 6-21: Disturbance response of $\dot{\omega}$ calculated by the linear model.

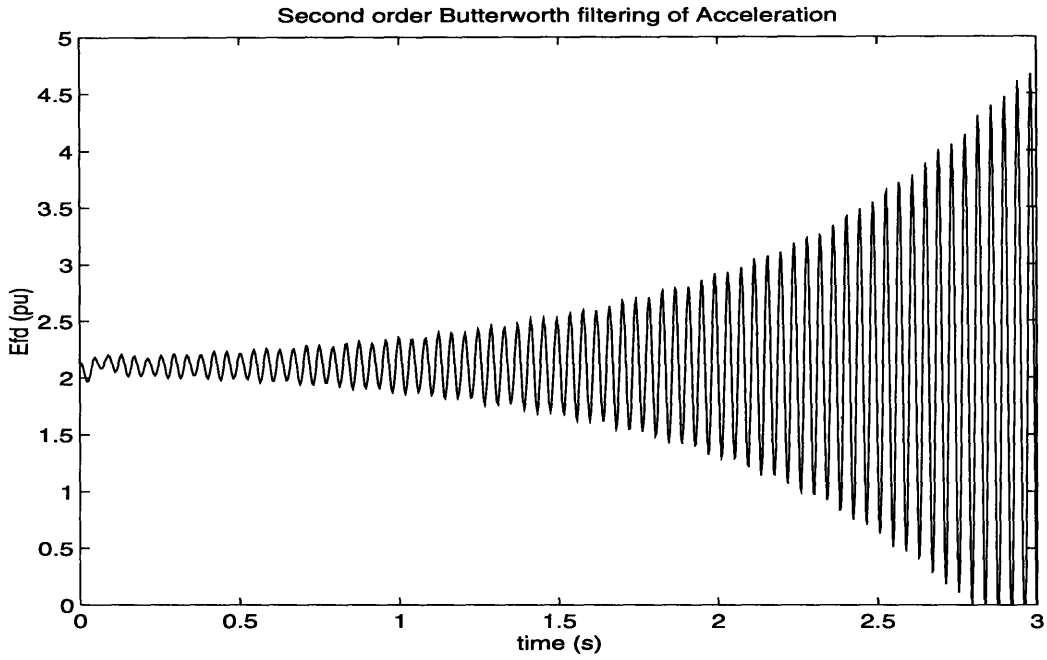

Figure 6-22: Simulated response of E_{fd} to a small disturbance with second order Butterworth filtering of $\dot{\omega}$.

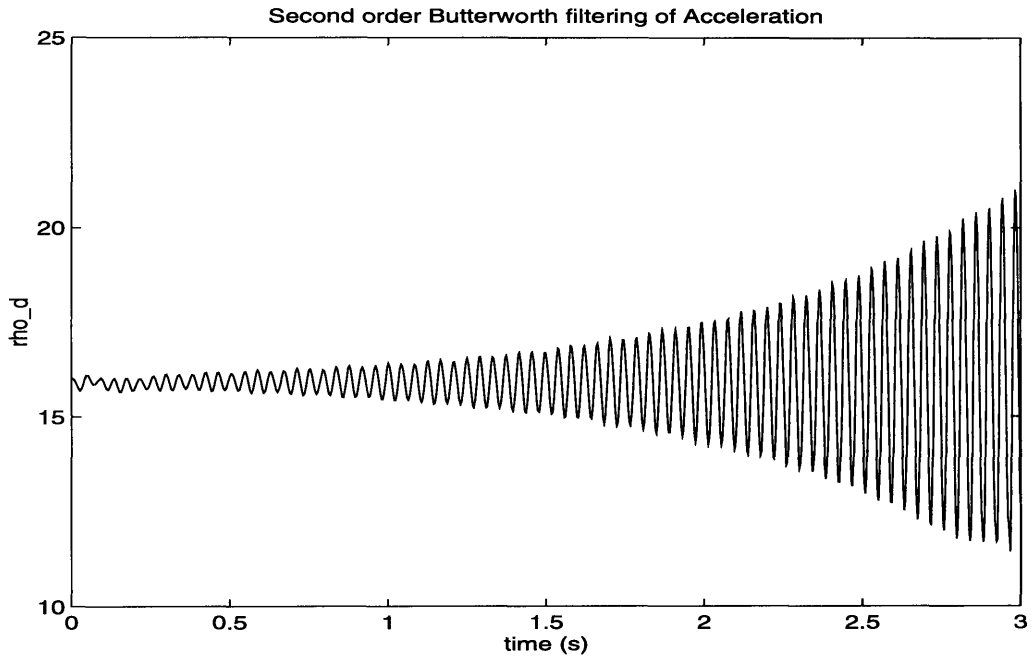

Figure 6-23: Simulated response of $\rho_d(\mathbf{x}_g)$ to a small disturbance with second order Butterworth filtering of $\dot{\omega}$.

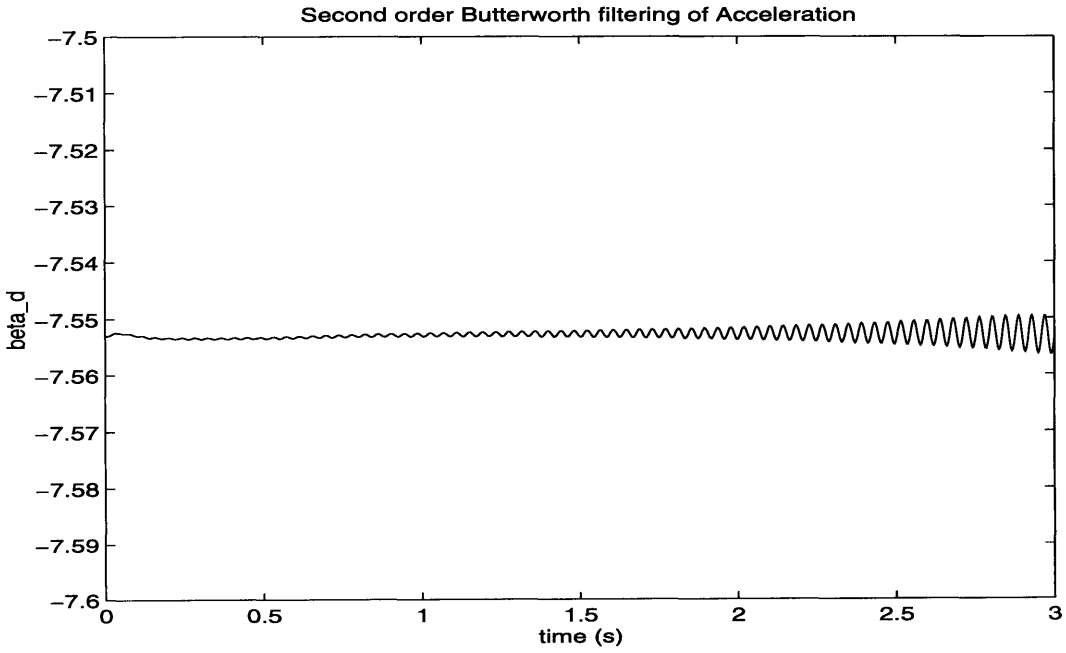

Figure 6-24: Simulated response of $\beta_d(\mathbf{x}_g)$ to a small disturbance with second order Butterworth filtering of $\dot{\omega}$.

Number(s)	Eigenvalue	Frequency (Hz)
1	-6.99	–
2,3	$-4.12 \pm j1.04$	0.1662
4,5	$-0.09 \pm j196.59$	31.29
6,7	$-0.22 \pm j151.31$	24.08

Table 6.5: Eigenvalues and frequencies of the reduced linear model of feedback linearizing control with a fourth order Butterworth filter of acceleration.

Number(s)	Eigenvalue	Frequency (Hz)
1,2	$-0.09 \pm j196.59$	31.29
3,4	$-0.22 \pm j151.31$	24.08
5	-71.68	–
6,7	$-31.57 \pm j58.06$	9.24
8,9	$-2.70 \pm j1.44$	0.2287
10,11	$-11.87 \pm j22.89$	3.64

Table 6.6: Eigenvalues and frequencies of the linear model of feedback linearizing control with a first order Butterworth filter of acceleration.

before:

$$\begin{bmatrix} \dot{x}_{f1} \\ \dot{x}_{f2} \\ \dot{x}_{f3} \\ \dot{x}_{f4} \end{bmatrix} = \begin{bmatrix} 0 & 1 & 0 & 0 \\ 0 & 0 & 1 & 0 \\ 0 & 0 & 0 & 1 \\ -\omega_c^4 & -2.6131\omega_c^3 & -(2+\sqrt{2})\omega_c^2 & -2.6131\omega_c \end{bmatrix} \begin{bmatrix} x_{f1} \\ x_{f2} \\ x_{f3} \\ x_{f4} \end{bmatrix} + \begin{bmatrix} 0 \\ 0 \\ 0 \\ 1 \end{bmatrix} u_f \tag{6.20}$$

$$y_f = \begin{bmatrix} \omega_c^4 & 0 & 0 & 0 \end{bmatrix} \begin{bmatrix} x_{f1} \\ x_{f2} \\ x_{f3} \\ x_{f4} \end{bmatrix} \tag{6.21}$$

6.4.1 Linear Modeling of FBLC with Fourth Order Butterworth Filter

Once again, we create a full linear model and a reduced linear model of the feedback linearized system with fourth order Butterworth filtering of the acceleration measurement. The eigenvalues of the reduced order linear model are in Table 6.5, and Table 6.6 contains eigenvalues of the full linear model.

6.4.2 Simulation of FBLC with Fourth Order Butterworth Filtering

We use the same procedure as before; the two linear models and the nonlinear model are simulated. The initial condition is:

$$\mathbf{x}_{b4} = \begin{bmatrix} 3.55 \times 10^{-7} \\ 1.95 \times 10^{-3} \\ -1.29 \times 10^{-2} \\ 0 \\ 0 \\ 0 \\ 0 \\ 0 \\ 0 \\ 0 \\ 0 \end{bmatrix} \tag{6.22}$$

and the responses, simulated and predicted, are given in Figures 6-25 to 6-36. The stopband phase shift is now one full cycle (-360^o), so the shaft modes are not excited, although they remain lightly damped. The three models show good agreement on the response of the system, particularly for the rotor acceleration. As with the first order filter, the reduced linear model shows a much larger peak in the response of the rotor angle, although the shape of the response is fundamentally the same.

With a fourth order filter, the high frequency attenuation is large enough in the torsional range to reduce the oscillations in E_{fd} to a very small amplitude. It is therefore natural to ask whether this system will perform well if a larger fault is applied. The half second fault that was used earlier was simulated, and the results are shown in Figures 6-37 to 6-42. The resulting performance is the best of any simulation so far with torsional dynamics. The response of δ is close to the response that had been previously obtained without torsional dynamics. The torsional dynamics are noticeable in ω, E_{fd}, and especially $\dot{\omega}$, although they do not appear to affect the response of the rotor angle. However, it must be cautioned that use of this technique involves some risk; any unmodeled dynamics near the cutoff frequency of the filter are very likely to be excited.

6.5 Conclusions

The Butterworth filtering tests reinforce the assertion that the stopband phase shift in the filter of the acceleration measurement causes the dynamics with frequencies in the stopband to become excited. The fourth order Butterworth filter delays signals in its stopband by one full cycle, so that dynamics at these frequencies do not become unstable. The simulations of the fourth order Butterworth filter produced impressive results in the rotor angle response, even though the torsional oscillations continue for a long time following the disturbance in ω and $\dot{\omega}$.

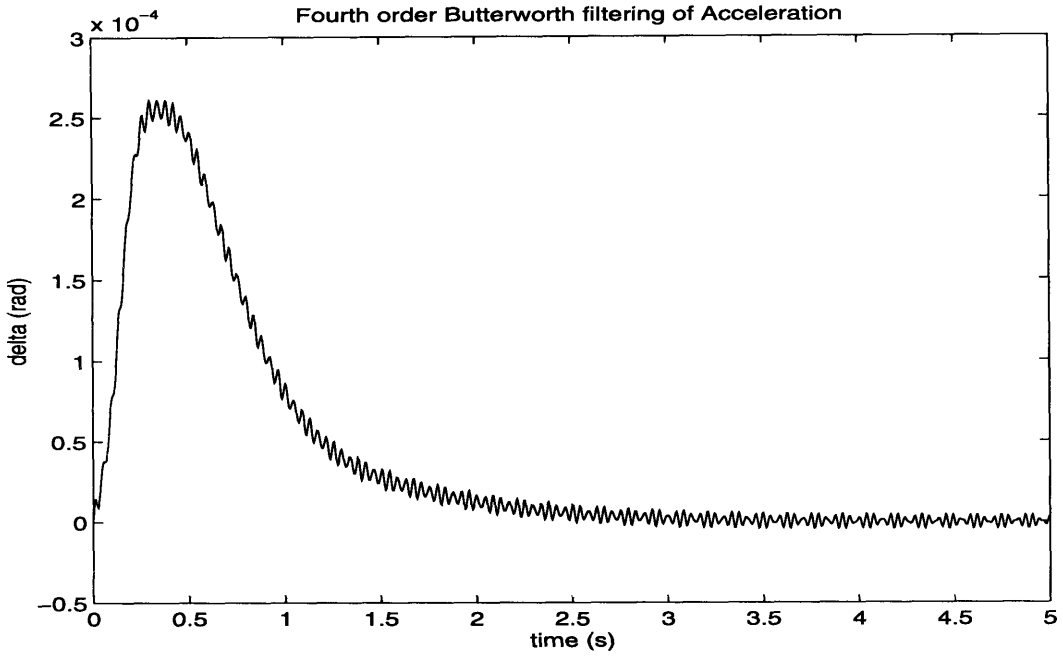

Figure 6-25: Simulated response of $\delta - \delta_o$ to a small disturbance with fourth order Butterworth filtering of $\dot{\omega}$.

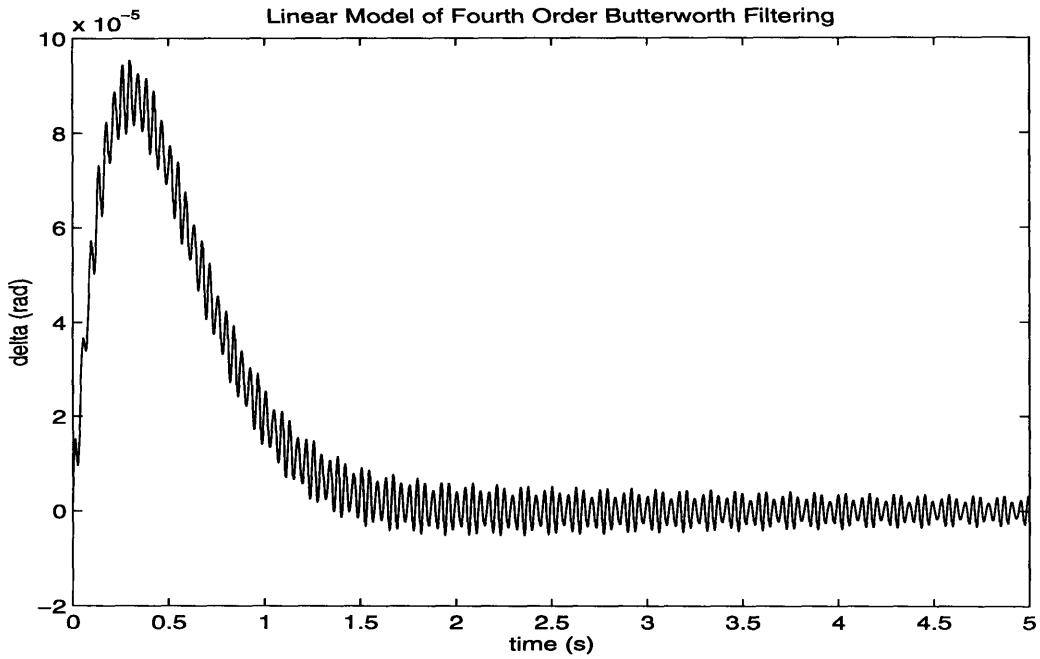

Figure 6-26: Disturbance response of $\delta - \delta_o$ calculated by the reduced linear model.

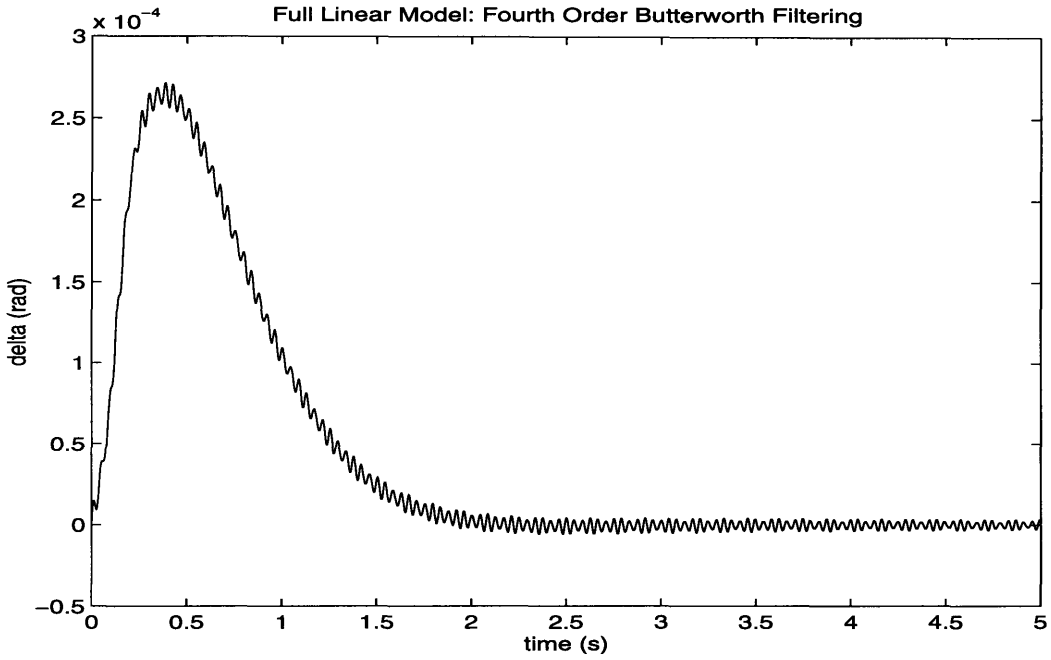

Figure 6-27: Disturbance response of $\delta - \delta_o$ calculated by the linear model.

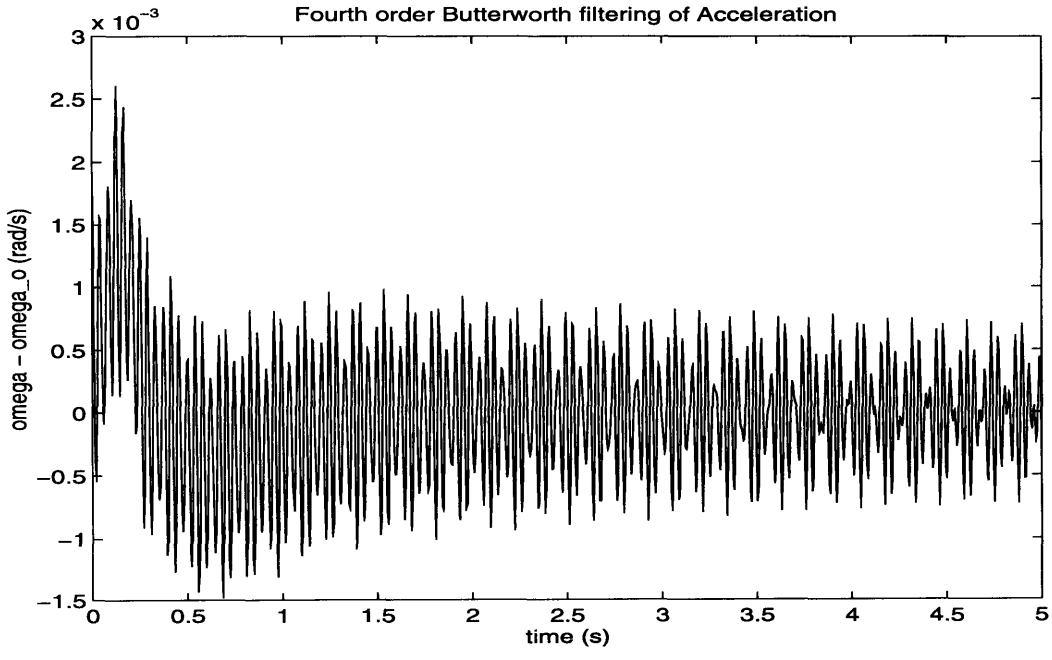

Figure 6-28: Simulated response of $\omega - \omega_o$ to a small disturbance with fourth order Butterworth filtering of $\dot{\omega}$.

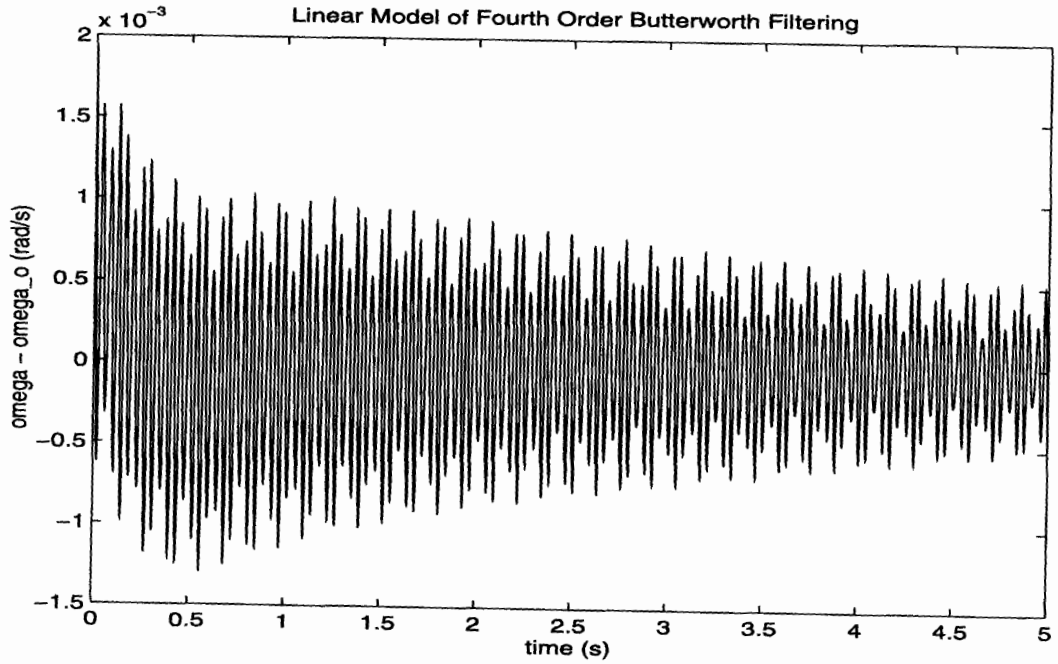

Figure 6-29: Disturbance response of $\omega - \omega_o$ calculated by the reduced linear model.

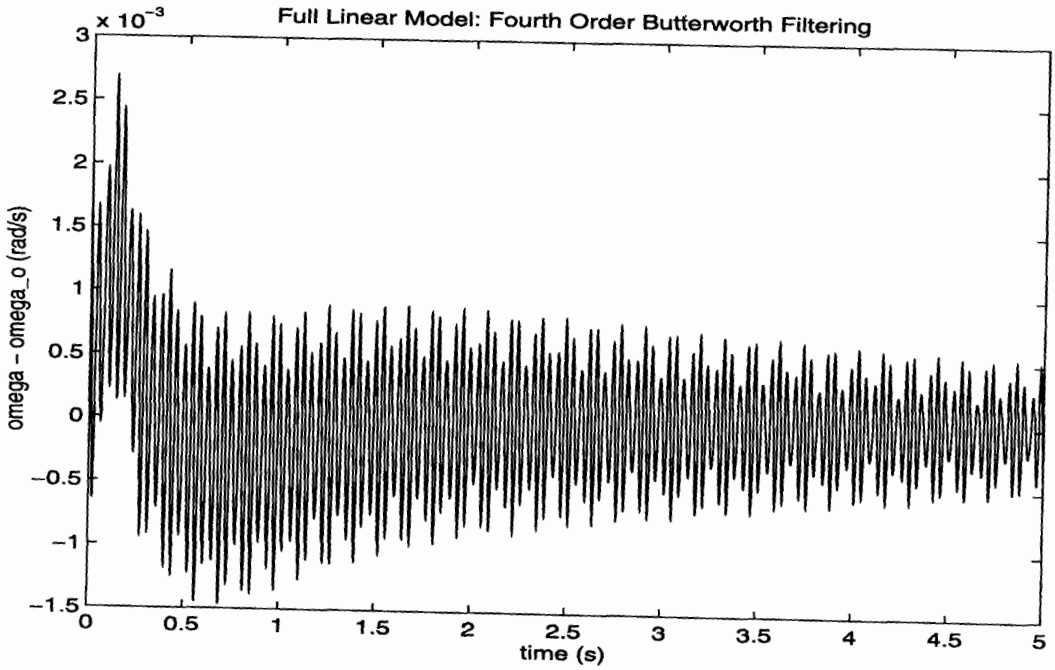

Figure 6-30: Disturbance response of $\omega - \omega_o$ calculated by the linear model.

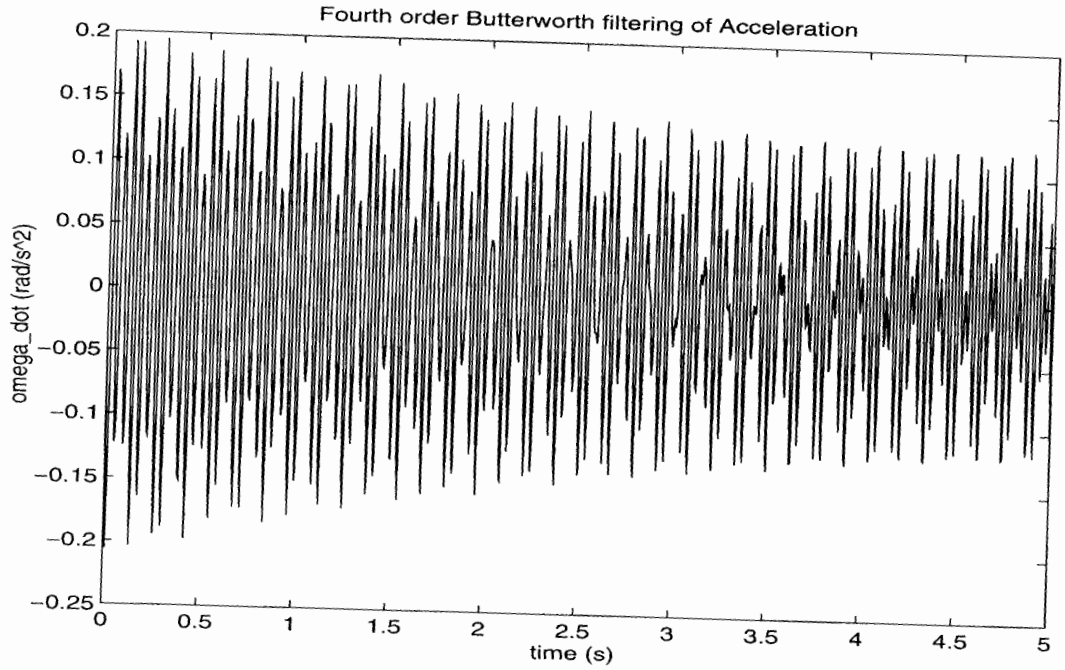

Figure 6-31: Simulated response of $\dot{\omega}$ to a small disturbance with fourth order Butterworth filtering of $\dot{\omega}$.

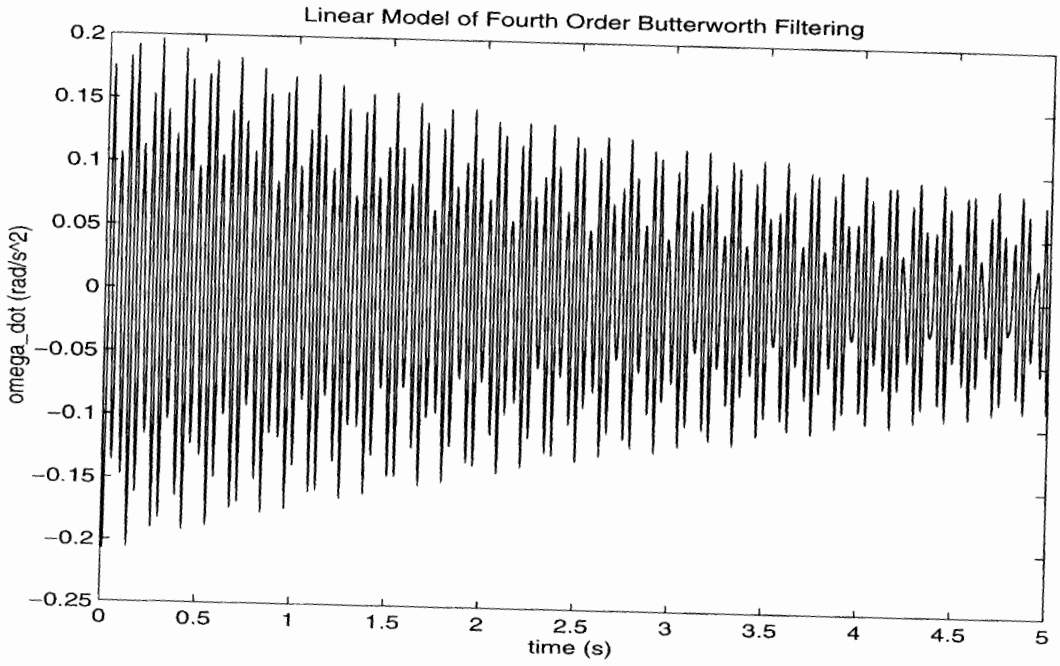

Figure 6-32: Disturbance response of $\dot{\omega}$ calculated by the reduced linear model.

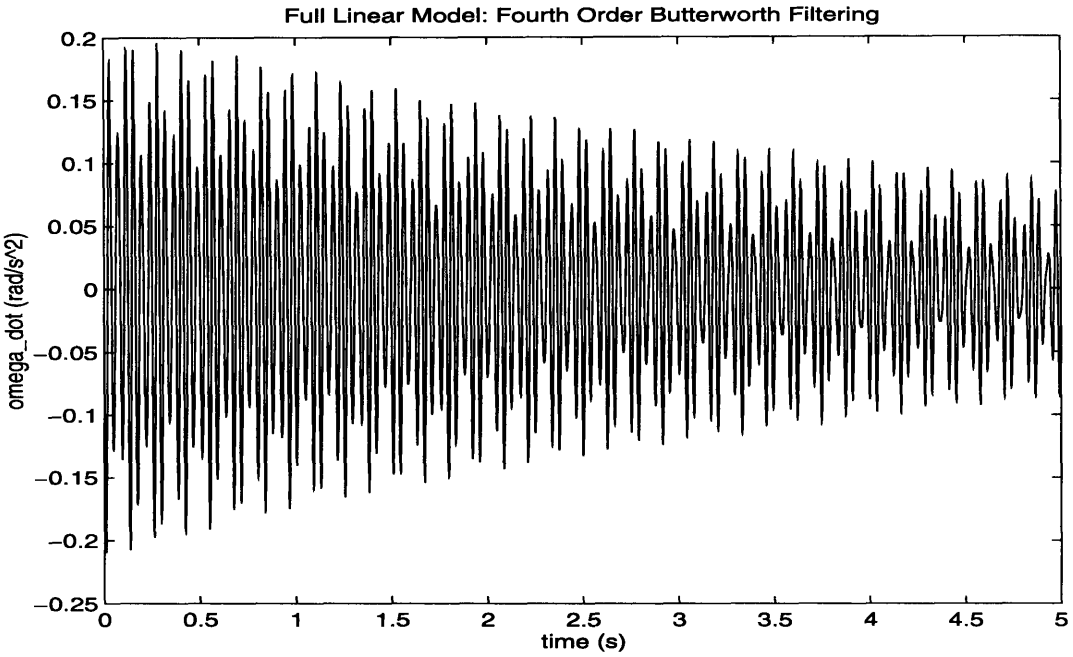

Figure 6-33: Disturbance response of $\dot{\omega}$ calculated by the linear model.

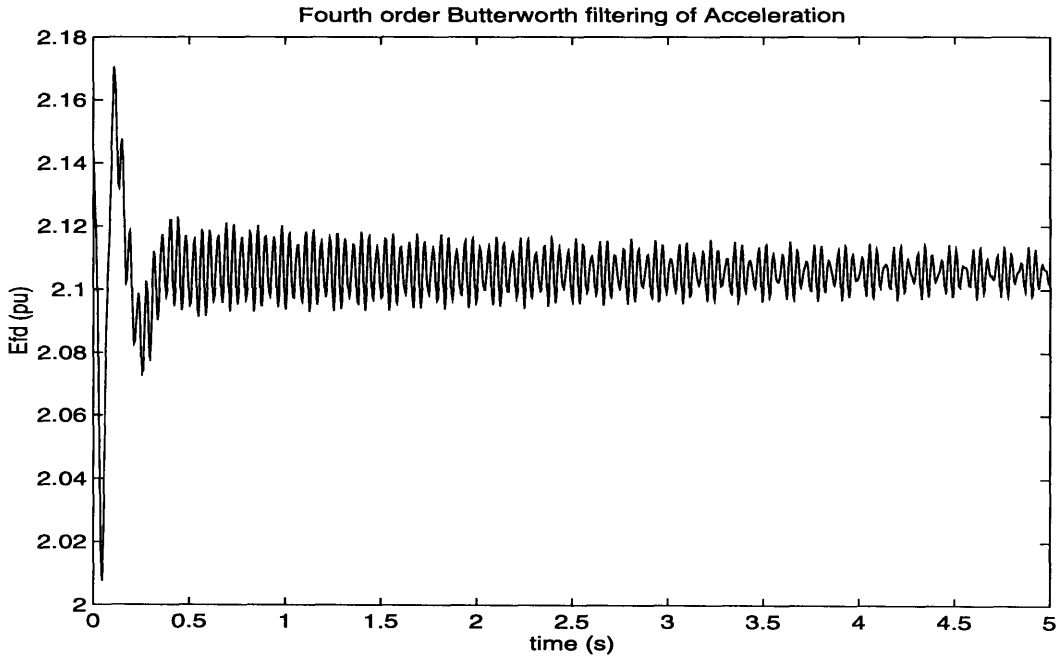

Figure 6-34: Simulated response of E_{fd} to a small disturbance with fourth order Butterworth filtering of $\dot{\omega}$.

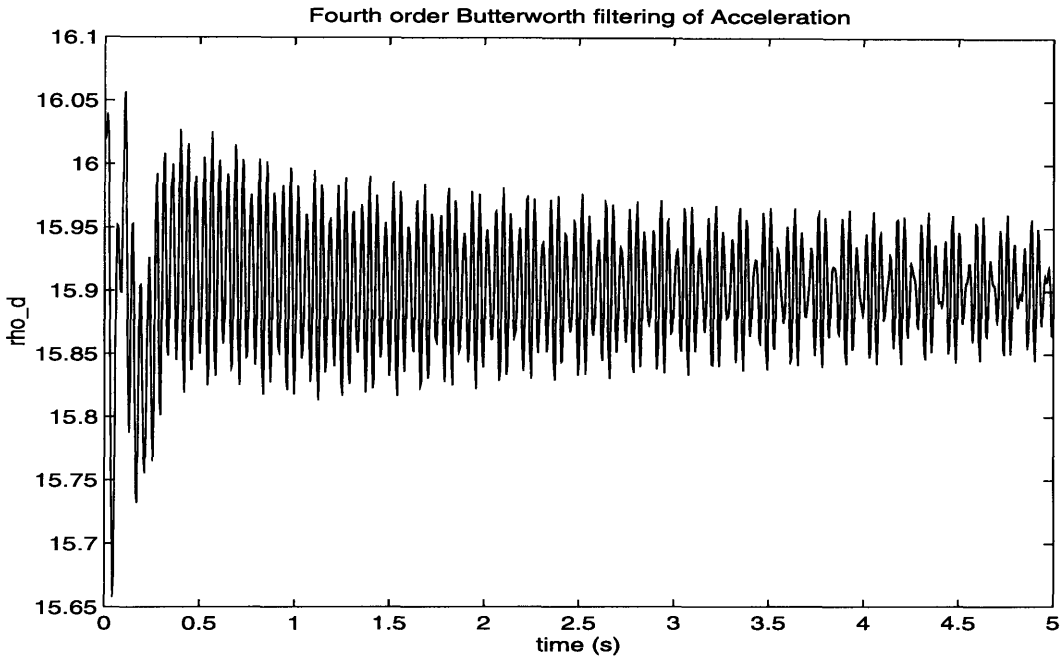

Figure 6-35: Simulated response of $\rho_d(\mathbf{x}_g)$ to a small disturbance with fourth order Butterworth filtering of $\dot{\omega}$.

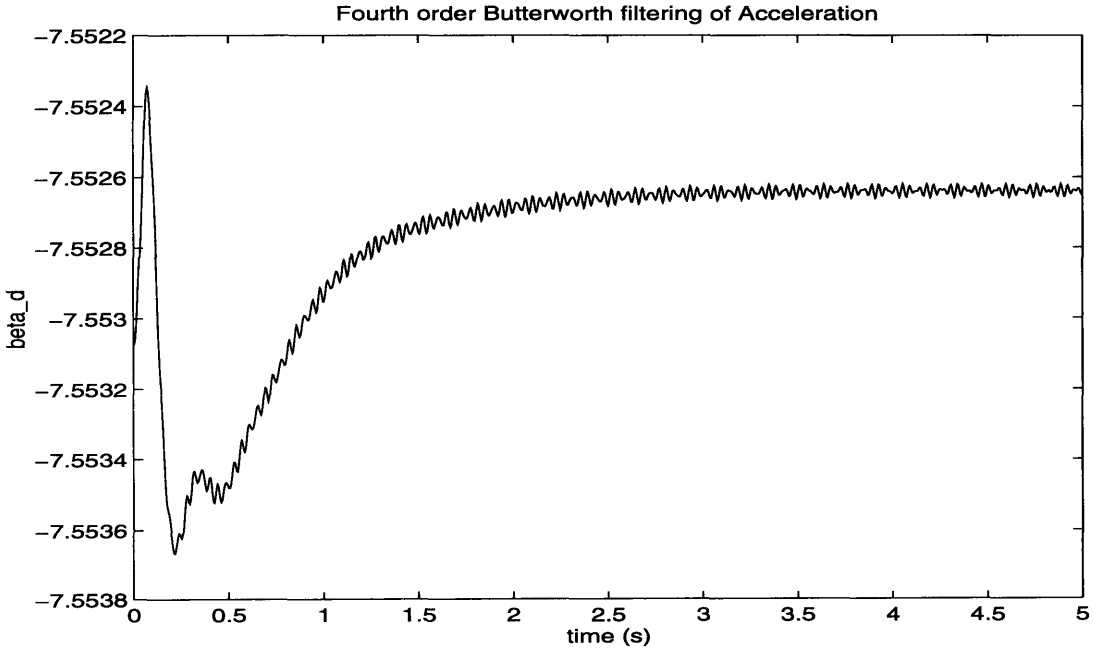

Figure 6-36: Simulated response of $\beta_d(\mathbf{x}_g)$ to a small disturbance with fourth order Butterworth filtering of $\dot{\omega}$.

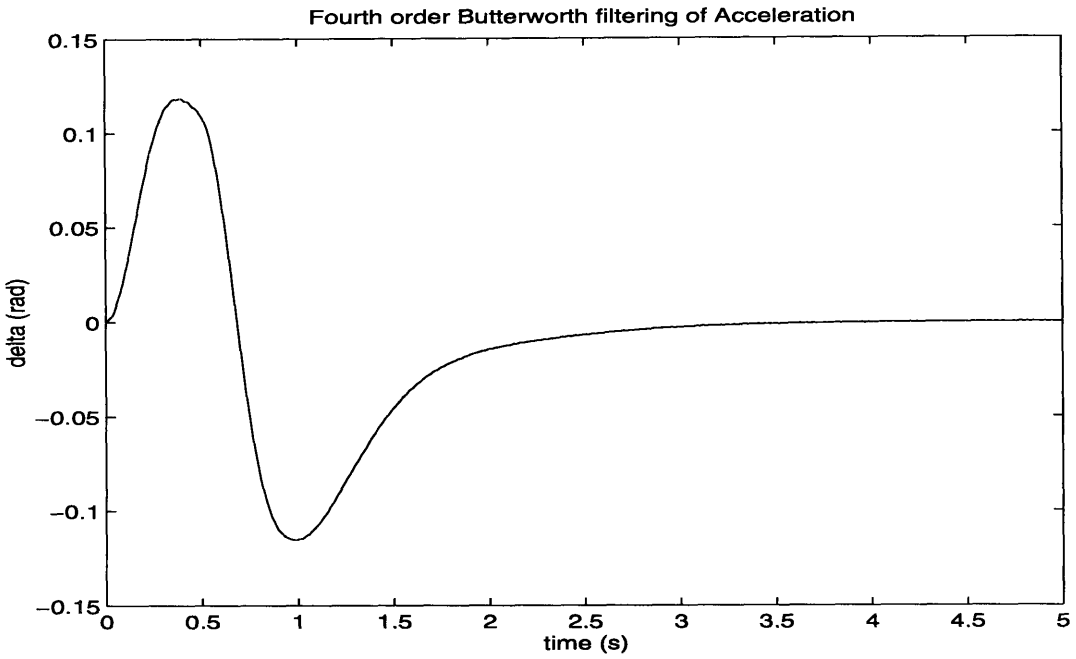

Figure 6-37: Simulated response of $\delta - \delta_o$ to a 0.5 second fault with fourth order Butterworth filtering of $\dot{\omega}$.

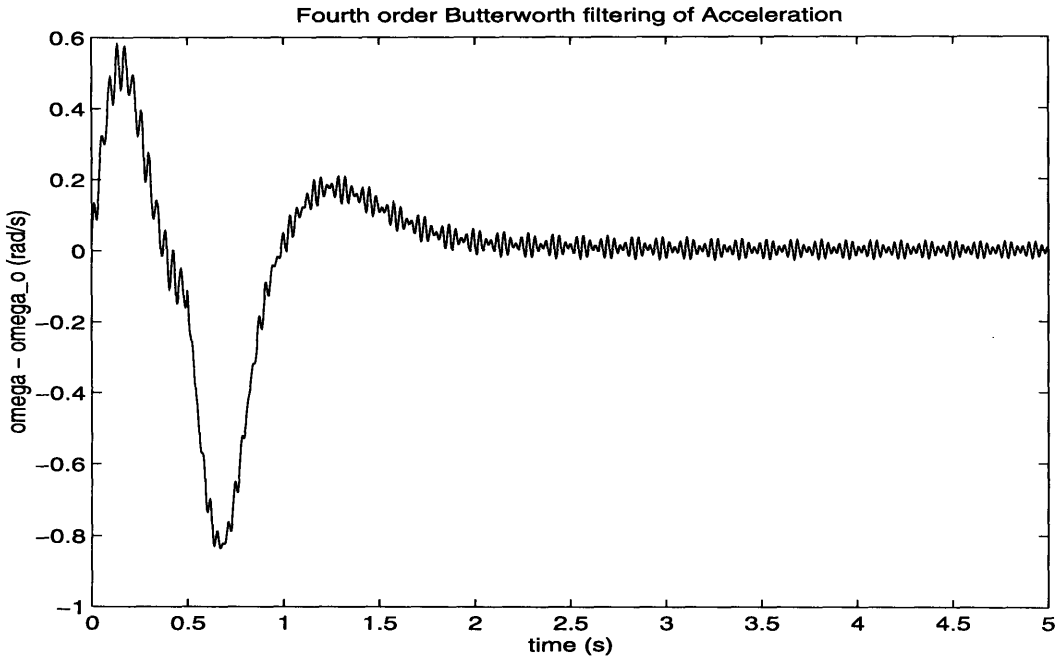

Figure 6-38: Simulated response of $\omega - \omega_o$ to a 0.5 second fault with fourth order Butterworth filtering of $\dot{\omega}$.

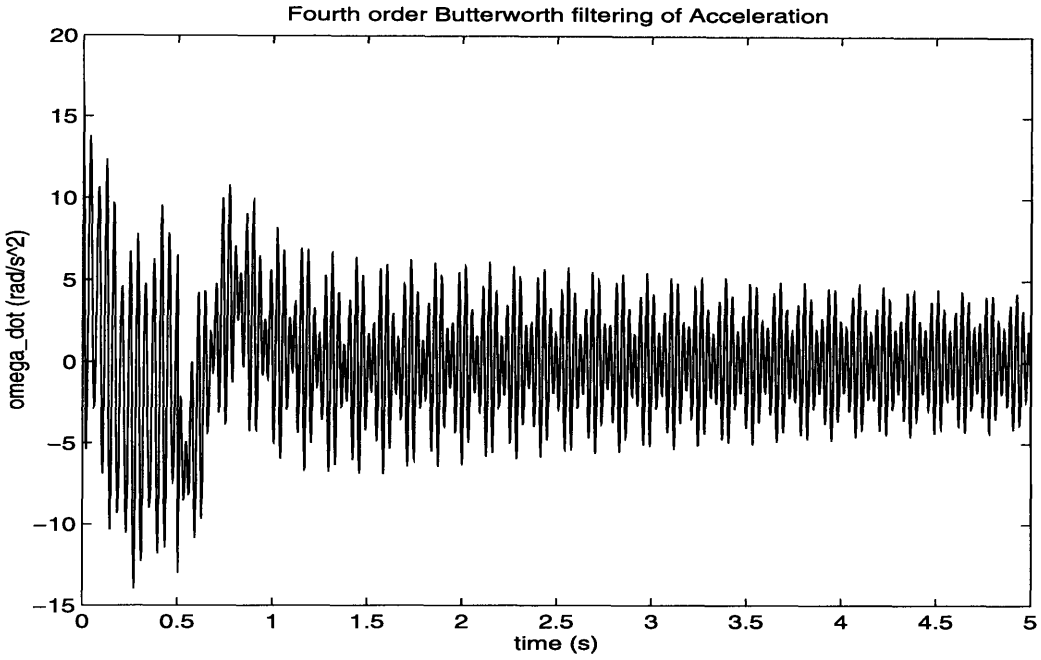

Figure 6-39: Simulated response of $\dot{\omega}$ to a 0.5 second fault with fourth order Butterworth filtering of $\dot{\omega}$.

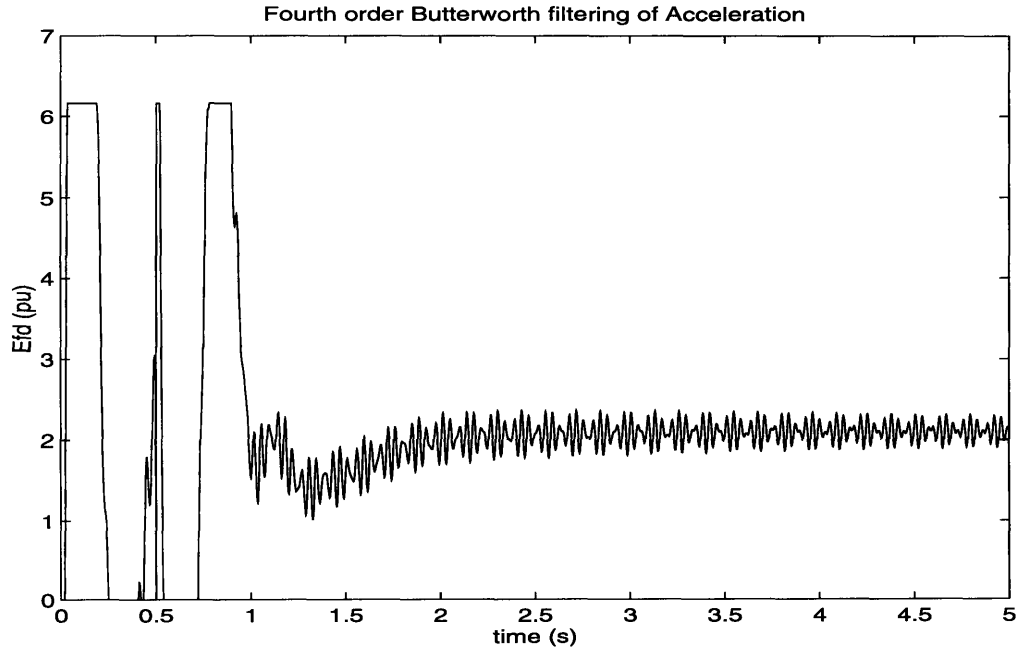

Figure 6-40: Simulated response of E_{fd} to a 0.5 second fault with fourth order Butterworth filtering of $\dot{\omega}$.

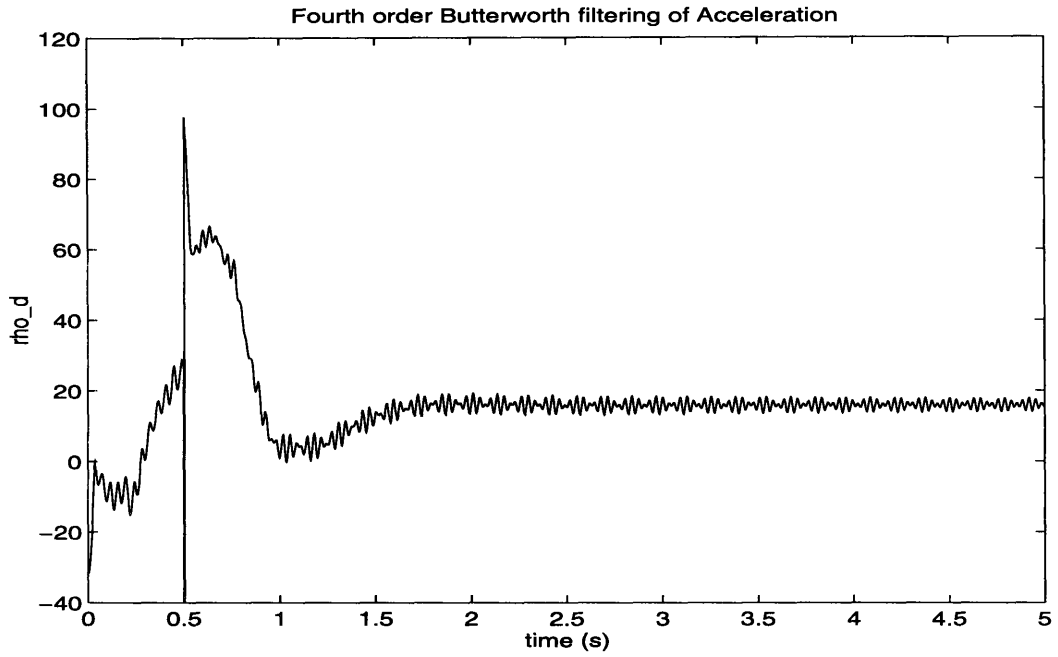

Figure 6-41: Simulated response of $\rho_d(\mathbf{x}_g)$ to a 0.5 second fault with fourth order Butterworth filtering of $\dot{\omega}$.

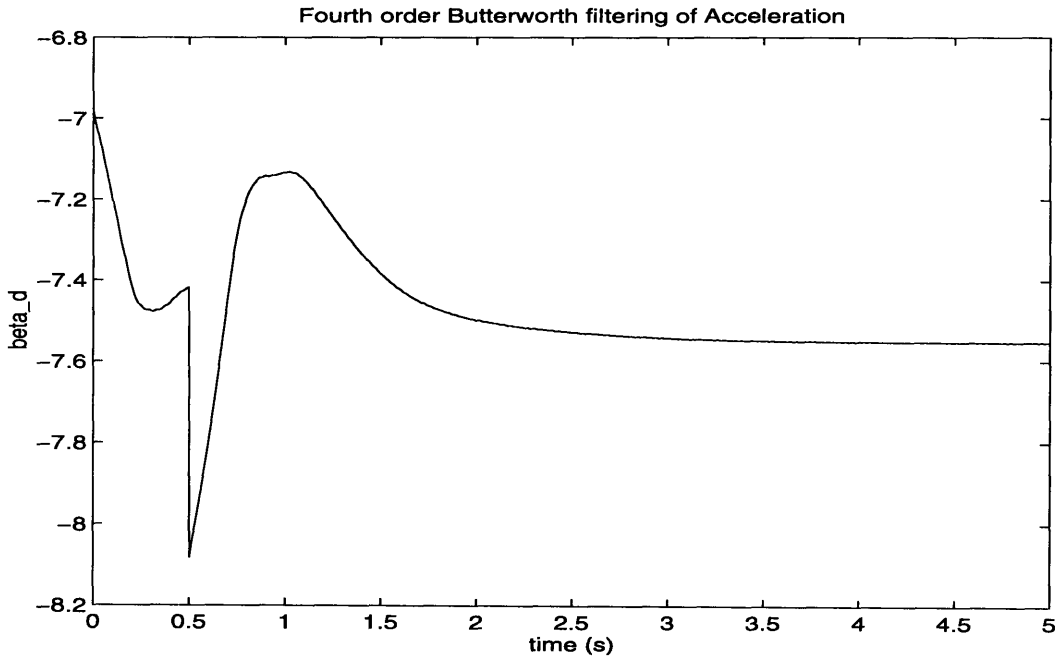

Figure 6-42: Simulated response of $\beta_d(\mathbf{x}_g)$ to a 0.5 second fault with fourth order Butterworth filtering of $\dot{\omega}$.

The examples in this chapter also provide a basis for evaluating the frequency separation argument for developing a linear model of a system with filtered signals. The resulting linear models produced very accurate results for the torsional modes, but the results for the low frequency modes were not nearly as good. This observation can be explained by noticing that the torsional modes have eigenvalues with real parts near zero, so that the amplitude of the modes remains nearly constant with time. Note that the cutoff frequency of the Butterworth filter is much lower (10 Hz) than the base frequency for the averaging technique (60 Hz); therefore, the low frequency modes decay relatively fast and can not assumed to be unaffected by the filter. The expansion of the frequency separation technique to include the effects of growth and decay of the modes, along with connecting these ideas with existing linear systems theory, is a topic for further research.

Chapter 7

Inclusion of Torsional Dynamics in the Controller Design

In previous sections, we used a controller design that did not account for the presence of shaft oscillations. We now wish to modify the control design to account for these previously unmodeled dynamics.

7.1 Measurement of the Shaft State Variables

As illustrated by the singular modal analysis, it will be necessary to include some shaft states in our analysis, particularly δ_2. There are several possible approaches to obtaining values of these states.

7.1.1 Direct Measurement of δ_2

An obvious approach to finding δ_2 is to simply use another shaft encoder to directly measure its value. This method has the advantage of not depending on estimates of shaft and generator parameters. However, a second shaft encoder involves more expense, and physically accessing the shaft to place an encoder at the turbine closest to the generator may be quite difficult.

7.1.2 Direct Calculation of δ_2

Recall from the feedback linearizing controller equations that four states were measured: δ_e, ω_e, $\dot{\omega}_e$, and E'_q. Since the generator was assumed to be a third order model, one of these values was redundant; given any three of these measurements, it is theoretically possible (although computationally difficult) to find the fourth.

However, since we are no longer treating the shaft as rigid, it turns out that the four measurements taken by the controller actually provide information about four

states of the system: δ_e, ω_e, E'_q, and δ_2. Indeed, recall from equation (3.2) that:

$$\dot{\omega}_e = \frac{\omega_o}{2H_e}\left[K_{2eu}\frac{\delta_2}{\omega_o} - K_{2eu}\frac{\delta_e}{\omega_o} - D_{eu}\frac{\omega_e}{\omega_o} - E'_d i_d - E'_q i_q\right] \tag{7.1}$$

Notice that every quantity in this equation, except for δ_2, may be measured. We can therefore use this equation to find δ_2 from the measurements of the other states:

$$\delta_2 = \delta_e + \frac{1}{K_{2eu}}[2H_e\dot{\omega}_e + D_{eu}\omega_e + \omega_o(E'_q i_q + E'_d i_d)] \tag{7.2}$$

This equation may be used to provide torsional state information to the controller so that the controller can compensate for the presence of shaft dynamics. However, before continuing, there are several important points to make. First, we are usually concerned with the shaft angle difference $\delta_2 - \delta_e$ instead of the value of δ_2 with respect to a fixed reference; therefore, we do not normally need to use δ_e in this equation. Second, this estimate of δ_2 depends on good estimates of system parameters, especially the shaft spring constant K_{2eu}. Third, since the form of the controller equation requires $\omega_2 - \omega_e$, equation (7.2) must be differentiated numerically in order to be used by the controller; this process can introduce further errors. Although there are numerous possible sources of error, this technique can nevertheless provide a good measurement of δ_2 without inserting another shaft encoder to measure δ_2 directly; in simulations, the measurement of δ_2 via this method is identical to the value of the actual state variable.

7.1.3 Estimating Shaft States by Using an Observer

It is theoretically possible to design an observer to estimate the shaft states based on estimated values of the system parameters; however, this task is left for future research.

7.2 Design of Feedback Linearizing Control with Torsional States

Now that we have calculated δ_2 (and implicitly ω_2), we may redesign our feedback linearizing controller to take advantage of the new information. The resulting closed-loop system should have poles placed very close to the intended locations. For extremely small perturbations, the system behavior is as expected; in Figure 7-1, the simulation response of δ with the modified controller is seen to agree with the predicted response of a linear system with all closed-loop poles at -5. However, the field voltage saturates very easily, and once this occurs, the system experiences large swings and does not settle for a significant time. Simulations of a larger disturbance are shown in Figures 7-2 through 7-7. When the controller is redesigned to include torsional effects, the oscillations in $\rho(\mathbf{x}_g)$ are enormous. The available range of E_{fd}

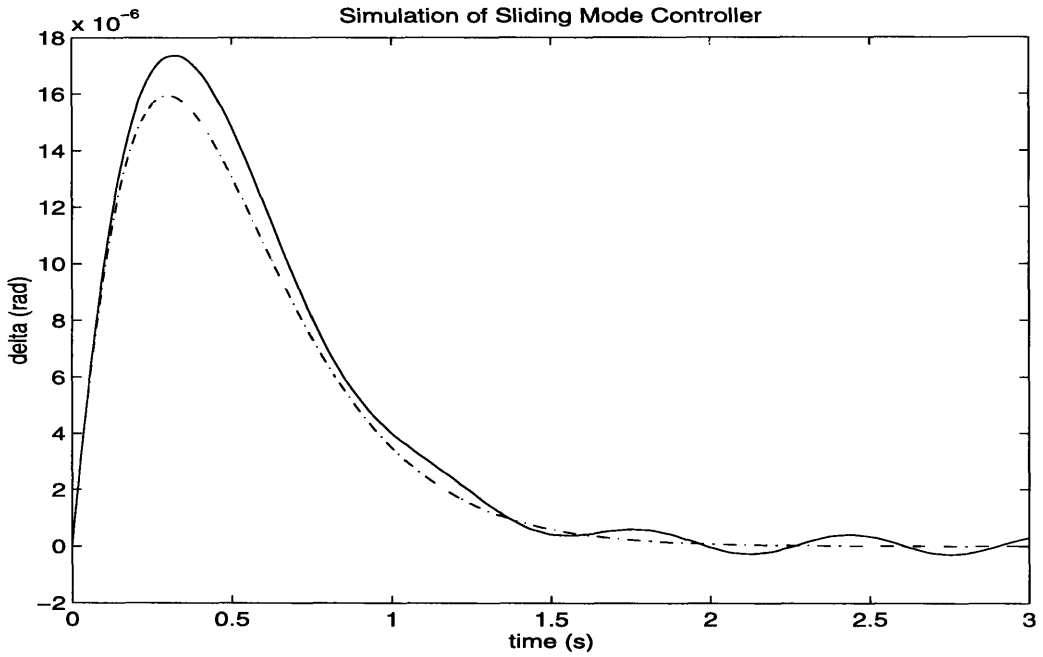

Figure 7-1: Response of $\delta - \delta_o$ (solid line) and expected response (dashed line). The two responses are essentially identical; the differences appear to be caused by simulator error.

is not nearly sufficient to handle torsional vibrations. Note: The simulations in this section used a third order generator model.

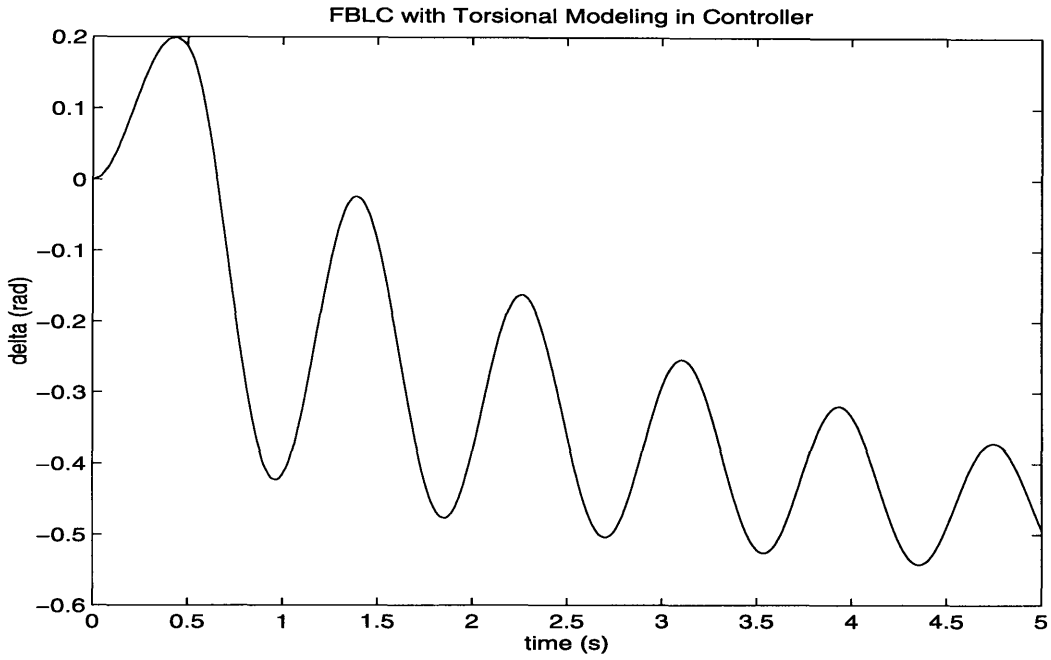

Figure 7-2: Response of $\delta - \delta_o$ to a 0.5 second fault with FBLC that accounts for torsional oscillations.

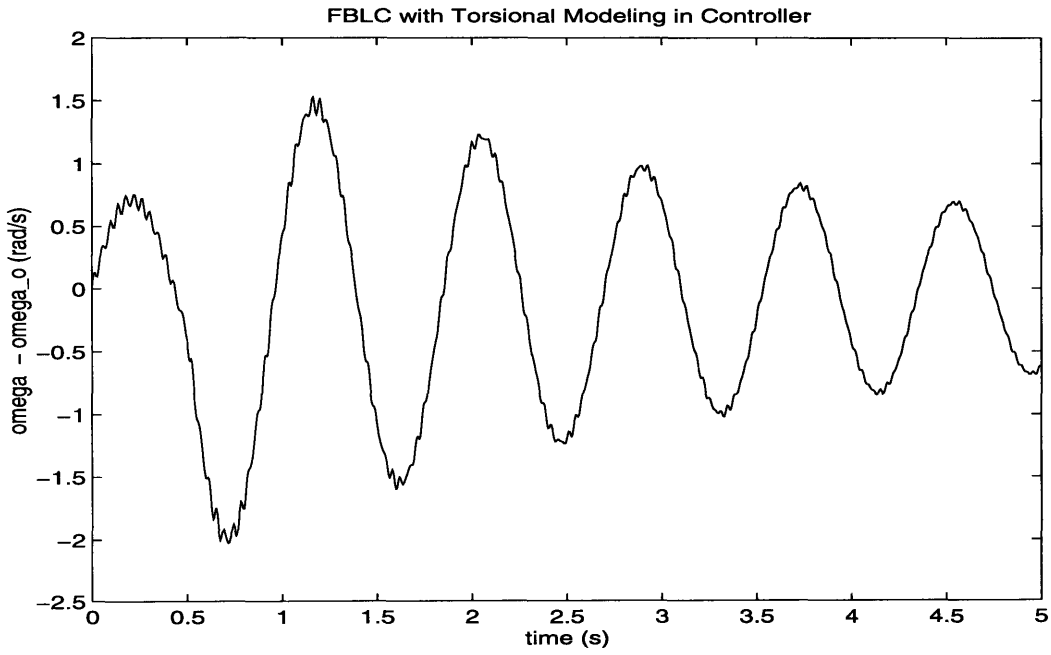

Figure 7-3: Response of $\omega - \omega_o$ to a 0.5 second fault with FBLC that accounts for torsional oscillations.

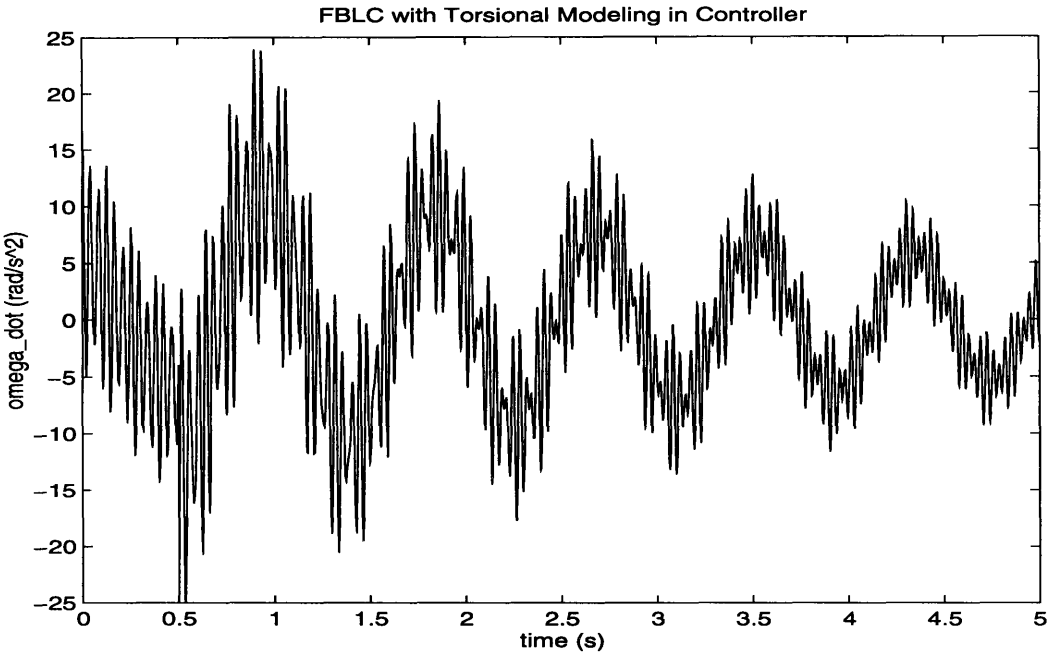

Figure 7-4: Response of $\dot{\omega}$ to a 0.5 second fault with FBLC that accounts for torsional oscillations.

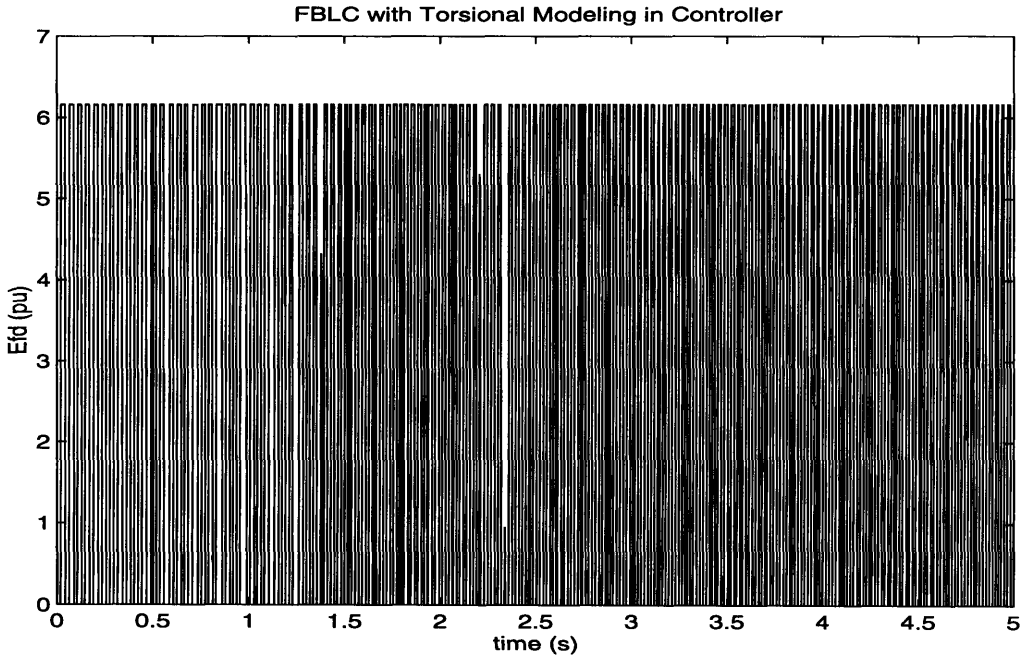

Figure 7-5: Response of E_{fd} to a 0.5 second fault with FBLC that accounts for torsional oscillations.

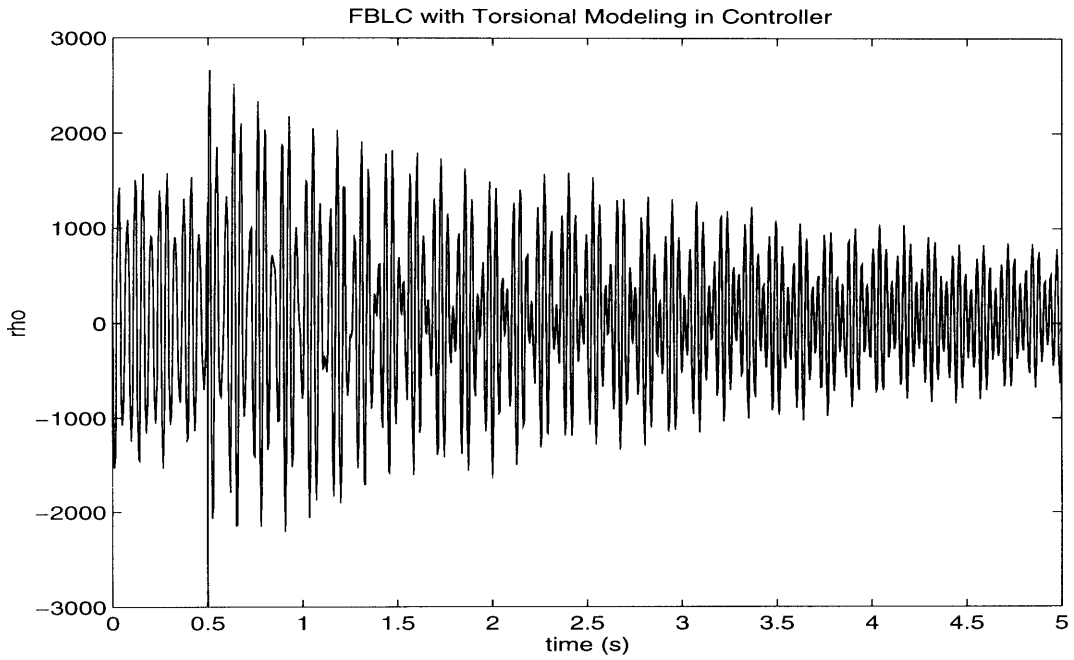

Figure 7-6: Response of $\rho(\mathbf{x}_g)$ to a 0.5 second fault with FBLC that accounts for torsional oscillations.

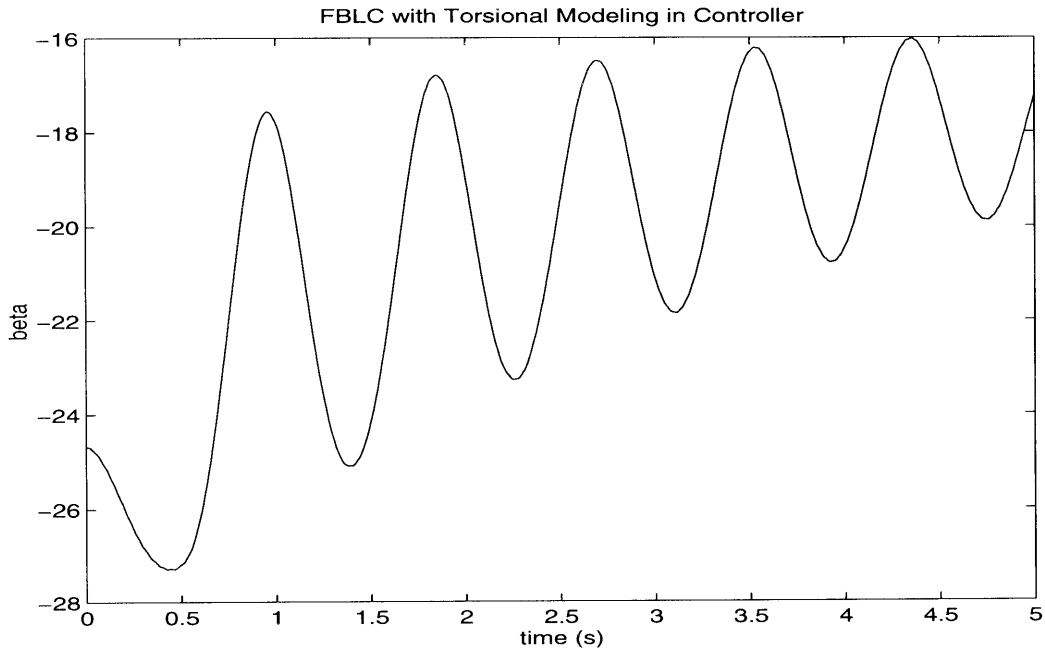

Figure 7-7: Response of $\beta(\mathbf{x}_g)$ to a 0.5 second fault with FBLC that accounts for torsional oscillations.

Chapter 8

Effects of Feedback Linearizing Control on Subsynchronous Resonance

We saw in Chapter 3 that feedback linearizing control greatly increases the damping of the shaft modes in the system. We would now like to see what effect the increased damping has on subsynchronous resonance, since the torsional dynamics play a pivotal role in this phenomenon.

8.1 Introduction

Subsynchronous resonance is normally associated with the use of series capacitor compensation on transmission lines. By placing a capacitor in series with a transmission line, the reactance of the line appears reduced from the generator's perspective, and more power can be transferred on the transmission line. However, there is a price to pay: the capacitor in series with the inductance of the transmission line produces an RLC network which oscillates at its natural frequency. These oscillations produce a subsynchronous current (frequency below 60 Hz) which is negatively damped by the generator. If the positive damping of the subsynchronous current in the system is insufficient, the system will be unstable, and the subsynchronous oscillations will grow with time [8, 9, 19, 20, 21].

The phenomenon of subsynchronous resonance has been discussed in the literature for over fifty years. Originally, only the electrical and magnetic dynamics of the generator were considered when studying subsynchronous resonance. However, in 1970, unstable subsynchronous oscillations resulted in two shaft failures at the Mohave generating station in Nevada; this event illustrated that the torsional dynamics of the generator shaft, which have natural frequencies in the subsynchronous range, play a major role in subsynchronous resonance [10].

8.2 Model of the Network

In order to analyze subsynchronous resonance, it is necessary to develop models for the generator, the generator shaft, and the network. The generator and shaft models have been developed in earlier chapters. However, in order to properly model the effects of capacitively compensated transmission lines, it will be necessary to create a dynamic model for the network.

The electrical network is usually modeled with ideal resistors, inductors, and capacitors that have the following voltage-current relations [22]:

$$\hat{V}_R = \hat{Z}_R \hat{I}_R \tag{8.1}$$

$$\hat{V}_L = L\frac{d\hat{I}_L}{dt} + \hat{Z}_L \hat{I}_L \tag{8.2}$$

$$\hat{I}_C = C\frac{d\hat{V}_C}{dt} + \hat{Y}_C \hat{V}_C \tag{8.3}$$

Normally, the voltage and current phasors are assumed to vary slowly with time, so the time derivatives are ignored. However, subsynchronous currents appear in phasor notation with a time-varying component. For example, a subsynchronous current of 30 Hz:

$$i(t) = 5\cos 60\pi t \tag{8.4}$$

is represented by the phasor:

$$\hat{I} = 5e^{-j60\pi t} \tag{8.5}$$

since $i(t) = \Re(\hat{I}e^{j\omega_o t})$, where $\omega_o = 120\pi$. Therefore, the time derivatives in equations (8.2) and (8.3) can not be neglected. In fact, these derivatives can be used to set up a state-space model for the network.

The network we will consider is shown in Figure 8-1. It consists of a generator, a transmission line, a series capacitor, and an infinite bus. As described earlier, the transmission line resistance and reactance includes generator resistance and transient reactance, so that we can treat the states E'_d and E'_q as the voltage at the generator bus (after an inverse Park transform). The voltage and current at bus 3 (the connection between the transmission line and the series capacitor) will be the state variables for the network. Note that we neglect any shunt capacitance to ground on the transmission line. The current is therefore the same throughout the network.

Since the current through the transmission line inductance is simply $\hat{I}_3$, we may write:

$$\hat{V}_1 - \hat{V}_3 = \frac{X}{\omega_o}\frac{d\hat{I}_3}{dt} + (R + jX)\hat{I}_3 \tag{8.6}$$

The capacitance voltage is equal to $\hat{V}_3 - \hat{V}_2$, where $\hat{V}_2 = W_d + jW_q$ is the infinite bus voltage. This observation leads to the following equation:

$$\hat{I}_3 = C\frac{d\hat{V}_3}{dt} + j\omega_o C(\hat{V}_3 - W_d - jW_q) \tag{8.7}$$

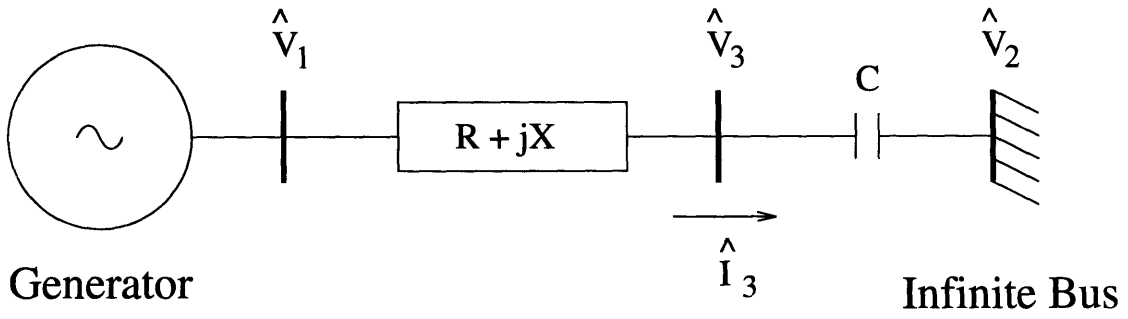

Figure 8-1: Network for subsynchronous resonance simulation.

These equations can be used to define two complex-valued or four real-valued states. Denoting $\hat{I}_3 = I_{d3} + jI_{q3}$ and $\hat{V}_3 = V_{d3} + jV_{q3}$, we have the following state equations for a fourth order network with capacitive compensation:

$$\dot{I}_{d3} = \frac{\omega_o}{X}[V_{d1} - V_{d3} - RI_{d3} + XI_{q3}] \tag{8.8}$$

$$\dot{I}_{q3} = \frac{\omega_o}{X}[V_{q1} - V_{q3} - RI_{q3} - XI_{d3}] \tag{8.9}$$

$$\dot{V}_{d3} = \frac{1}{C}I_{d3} + \omega_o(V_{q3} - w_q) \tag{8.10}$$

$$\dot{V}_{q3} = \frac{1}{C}I_{q3} - \omega_o(V_{d3} - w_d) \tag{8.11}$$

8.2.1 Natural Frequency of the Network

The network resonance frequency is very close to the frequency at which the inductive and capactive reactances are equal. (The resistive damping causes a tiny shift in the resonance frequency.) Since $\hat{Z}_L = j\omega L$ and $\hat{Z}_C = (j\omega C)^{-1}$, we can estimate the natural frequency by finding $\omega = \omega_n$ such that $\hat{Z}_L = -\hat{Z}_C$; this occurs when:

$$\omega = \sqrt{\frac{1}{LC}} \tag{8.12}$$

Because the generator rotates at 60 Hz, currents oscillating at the resonance frequency appear to the generator as supersynchronous currents at $\omega_1 = 120\pi + \omega_n$ and subsynchronous currents at $\omega_2 = 120\pi - \omega_n$. The supersynchronous currents are generally well damped by the system and pose no threat; it is the subsynchronous currents that can cause instability, particularly if they excite one of the shaft modes[8, 9].

8.2.2 Sample Network Parameters

As before, we will now select parameter values from typical examples in order to perform our simulations of the system. For the transmission line, $R = 0.058526$ and $X = 0.89497$; this corresponds to the admittance given in Chapter 1. $\hat{V}_2$, the infinite bus voltage, was chosen so that $\hat{V}_3$ maintained an equilibrium value of $0.9164 + j0.20473$ regardless of the capacitance selected; this was done so that the system would maintain the same equilibrium point while examining different capacitor values. With these network constraints, the generator will have the same equilibrium as in previous simulations. Series capacitance values are normally expressed as a percentage of compensation, which is equal to the ratio $-\hat{Z}_C/\hat{Z}_L$ with both impedances calculated at $\omega_o = 120\pi$. Note that smaller values of C have larger reactances and therefore provide more compensation; however, smaller compensating series capacitors also make the system less stable, as demonstrated by the simulation results.

8.3 Simulation Results

Once the models are determined, it is a fairly straightforward process to simulate them. The simulations were performed by disturbing the line current slightly from its equilibrium value and then observing the system.

8.3.1 Constant Exciter Control

First, a constant exciter control was used to demonstrate the natural dynamics of the system. The simulator includes a routine to numerically derive a linearized state-space representation of a system at any given operating point. The resulting eigenvalues of the linearized model for three selected capacitance values are shown in Figure 8.1. The eigenvalues clearly show the supersynchronous and subsynchronous current modes, the torsional modes, and the generator modes. With a large capacitor in series with the transmission line, the system remains stable. However, at 23.0% compensation, the subsynchronous frequency drops to about 31.3 Hz and interacts with a torsional mode at that frequency, causing instability. Figures 8-2 and 8-3 show the rotor angle and line current for this system, which illustrate the growing subsynchronous oscillations. These types of oscillations caused the shaft failures at Mohave. At 35.9% compensation, the subsynchronous currents interact with the torsional mode at 24 Hz, again leading to instability. It is interesting to note that a model of the system that neglects torsional dynamics suggests that the system is stable for all of these capacitance values, thus illustrating the important role that the torsional dynamics have in subsynchronous resonance.

8.3.2 Power System Stabilizer Control

In order to provide a means of evaluating the performance of FBLC, a standard power system stabilizer (PSS) design was simulated extensively in [1, 2, 12]. This design is also used here in order to determine the effectiveness of a power system stabilizer in

Compensation	Eigenvalue	Frequency (Hz)
2.96%	$-9.90 \pm j441.1$	70.20
	$-8.95 \pm j312.6$	49.75
	$-0.058 \pm j196.6$	31.29
	$-0.051 \pm j151.6$	24.13
	-34.84	–
	-30.90	–
	$-0.459 \pm j6.71$	1.07
	-4.88	–
	-0.328	–
23.0%	$-10.41 \pm j557.4$	88.71
	$-7.95 \pm j196.1$	31.21
	$0.808 \pm j196.5$	31.27
	$0.061 \pm j152.2$	24.22
	-35.87	–
	-32.25	–
	$-0.644 \pm j7.65$	1.22
	-0.356	–
	-5.03	–
35.9%	$-10.55 \pm j602.7$	95.92
	$-0.053 \pm j196.4$	31.26
	$-9.35 \pm j151.7$	24.15
	$3.85 \pm j151.5$	24.11
	-36.79	–
	-33.60	–
	$-0.832 \pm j8.40$	1.34
	-0.378	–
	-5.14	–

Table 8.1: Eigenvalues and frequencies of the linearized system for three example series capacitor values.

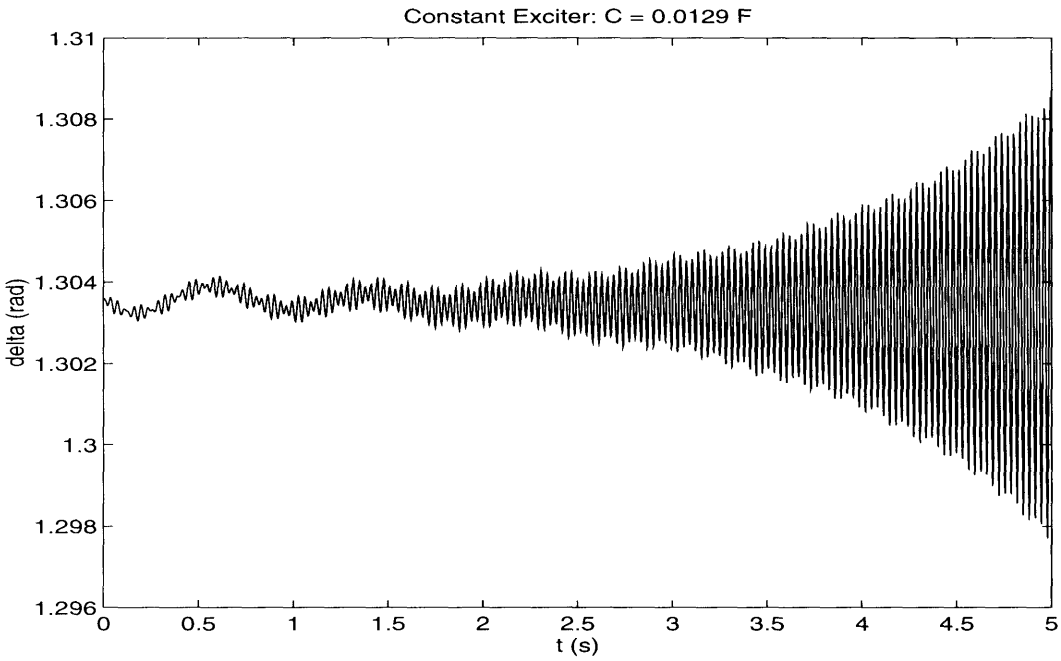

Figure 8-2: Rotor angle (δ) of a system prone to subsynchronous resonance, illustrating the growing subsynchronous oscillations.

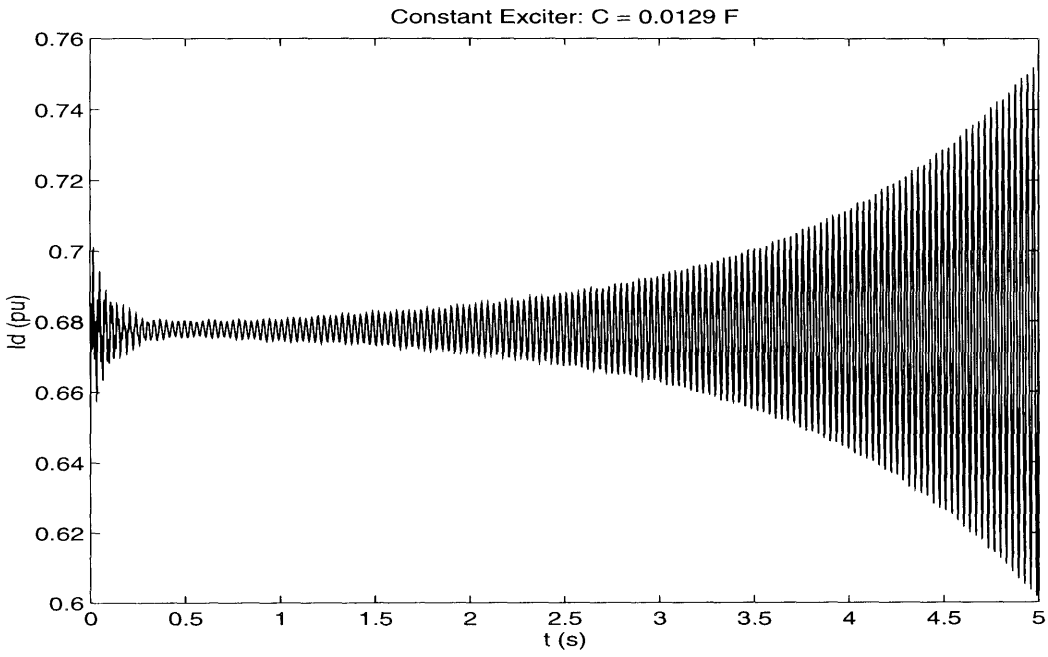

Figure 8-3: Line current (real part) of a system exhibiting subsynchronous resonance.

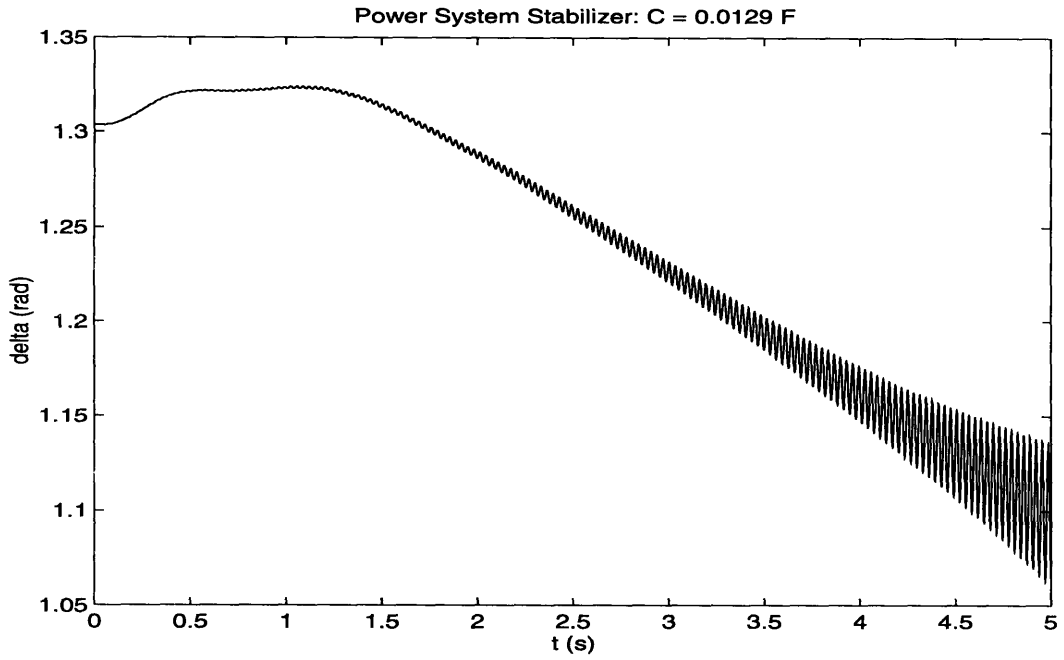

Figure 8-4: Rotor angle (δ) of a series compensated network with a PSS controlled generator. The PSS is not able to prevent the subsynchronous oscillations from growing.

suppressing high frequency oscillations. The simulation results of a generator with a PSS controller and the network shown in Figure 8-1 with 23.0% compensation are presented in Figures 8-4 through 8-6. Clearly, the PSS is not able to damp out the subsynchronous oscillations.

8.3.3 Feedback Linearizing Control

The next step is to examine what effect FBLC has when placed on a system prone to subsynchronous resonance. The results of a test run with FBLC poles at -5 and 23.0% series compensation are shown in Figures 8-7 through 8-12. These simulations show that even though the series capacitance is at a critical value, FBLC is capable of stabilizing the system. Note that the field voltage reacts at a high frequency during the transient. Although these results seem quite surprising, the placement of the poles at -5 causes the generator to act as a low pass filter and damp out high frequency components, such as subsynchronous oscillations. If the poles are moved out to -50, then the subsynchronous oscillations will no longer be damped by the system, and the torsional dynamics are likely to be excited by subsynchronous currents. This is indeed the case, as shown by Figures 8-13 through 8-18.

The large, fast swings in E_{fd} shown in Figure 8-12 are generally undesirable. To reduce these swings, a fourth order Butterworth filter was added to the acceleration

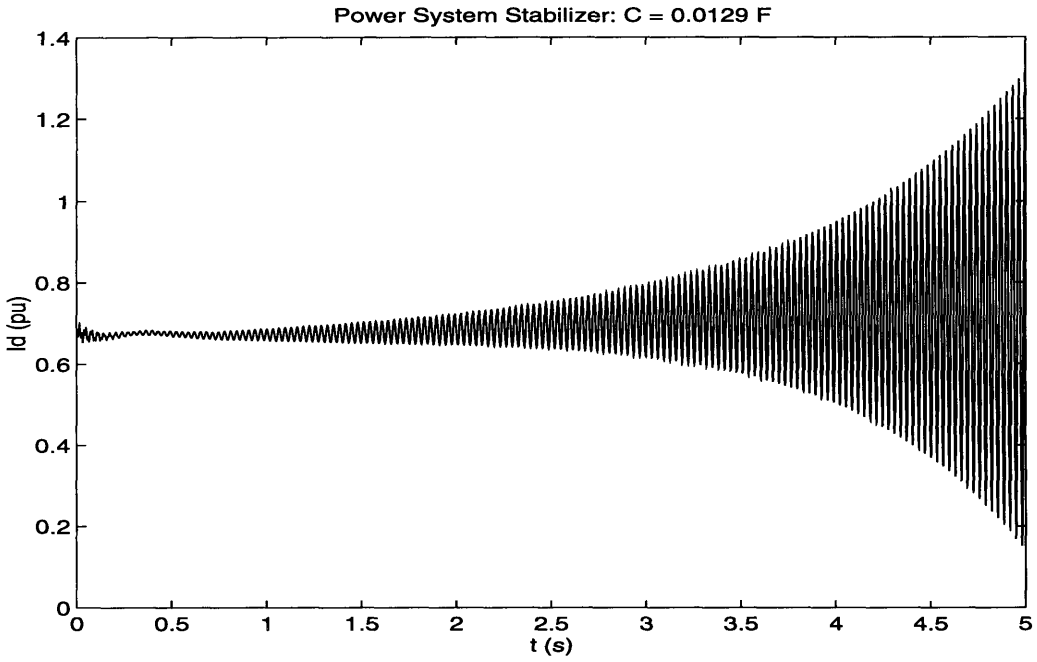

Figure 8-5: Line current (real part) of a series compensated network with a PSS controlled generator.

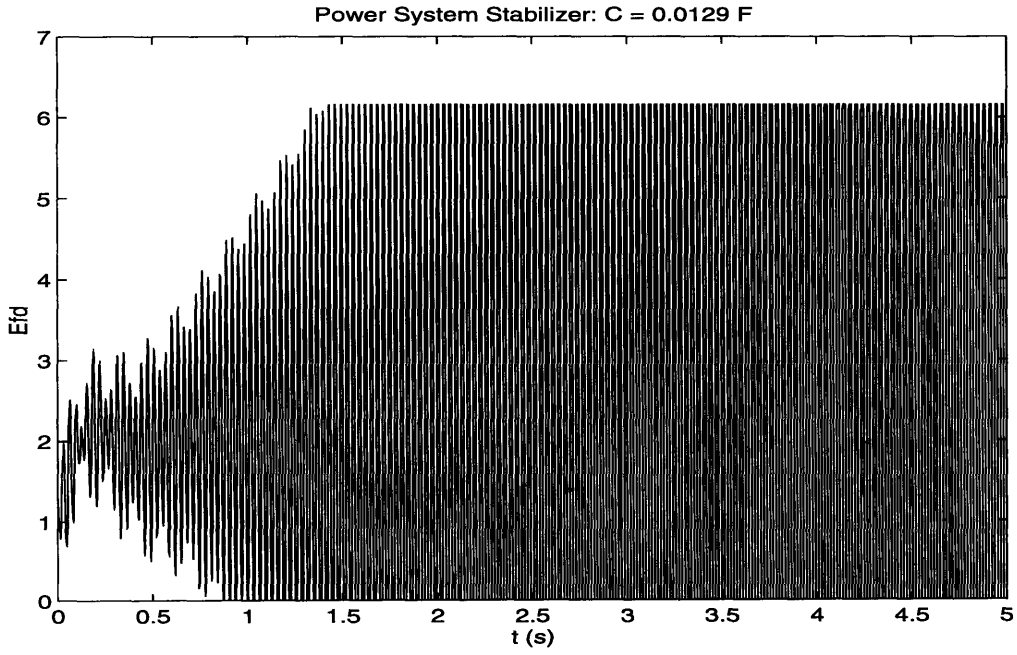

Figure 8-6: Field voltage of a series compensated network with a PSS controlled generator.

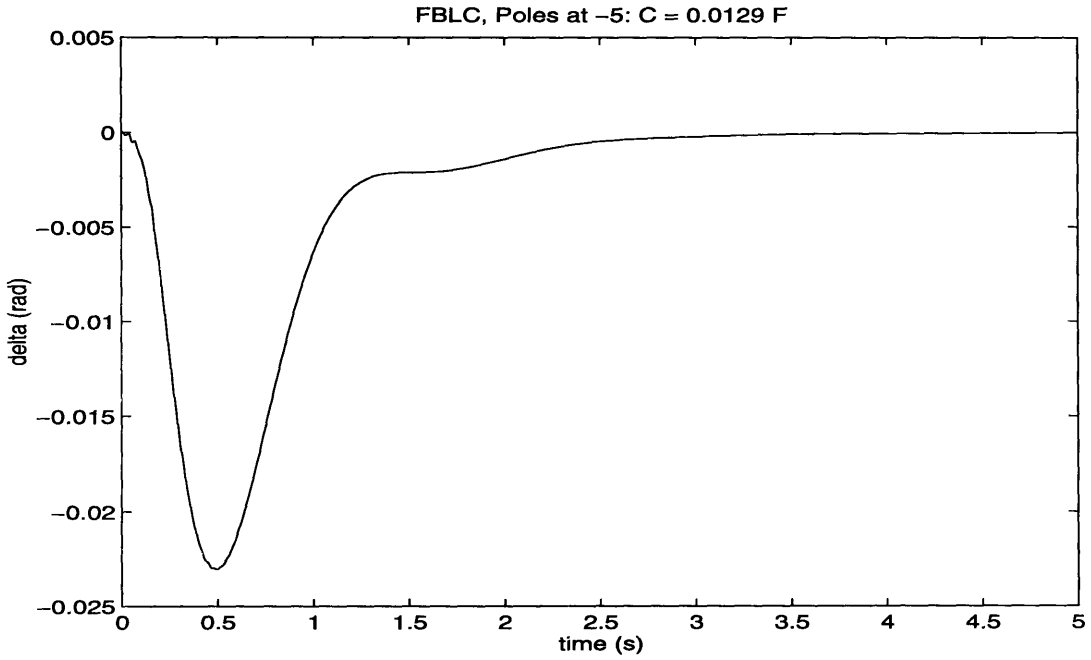

Figure 8-7: Rotor angle $(\delta - \delta_o)$ of a system with FBLC. FBLC has damped out the subsynchronous oscillations.

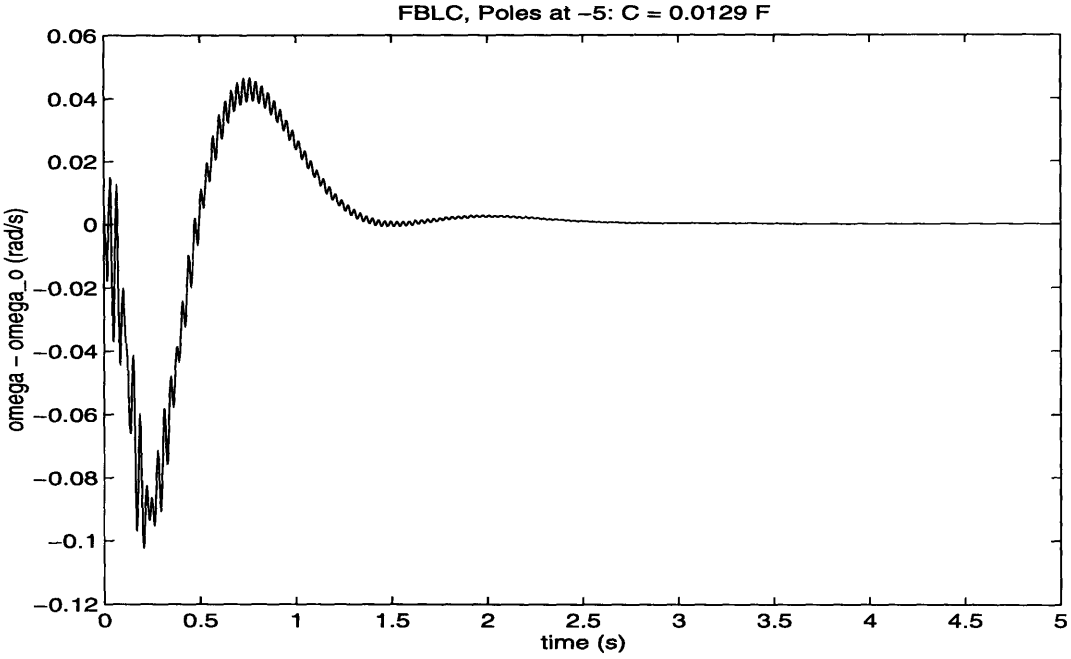

Figure 8-8: Plot of $\omega - \omega_o$ for a system with FBLC.

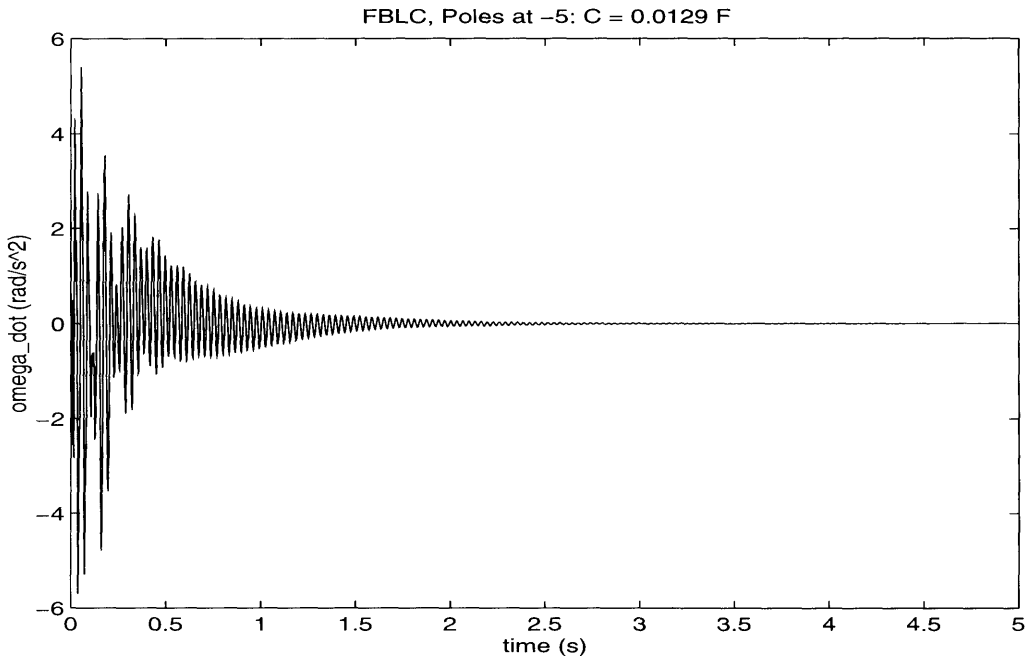

Figure 8-9: Rotor acceleration ($\dot{\omega}$) for a system with FBLC. The subsynchronous oscillations die out rapidly, even though they are excited by the subsynchronous currents in the network.

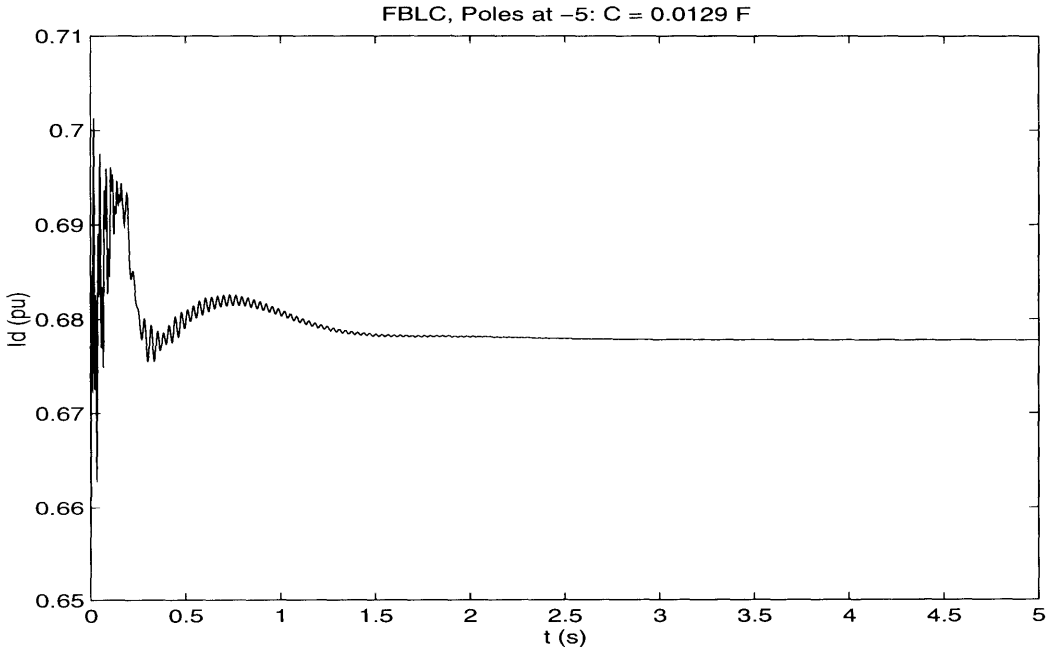

Figure 8-10: Line current (real part) of a system with FBLC.

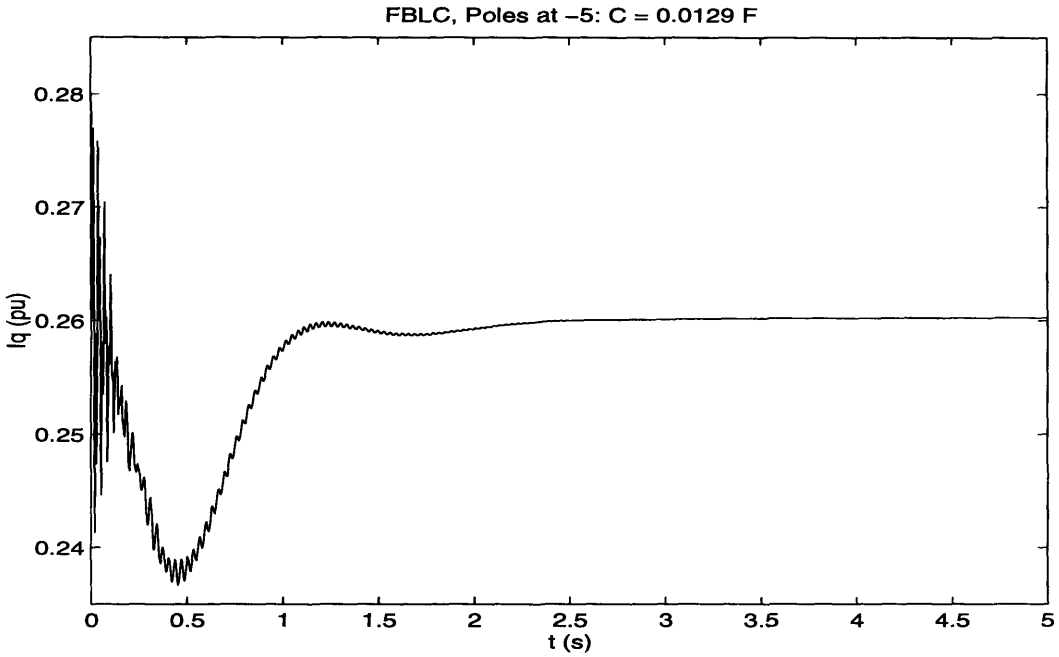

Figure 8-11: Line current (imaginary part) of a system with FBLC.

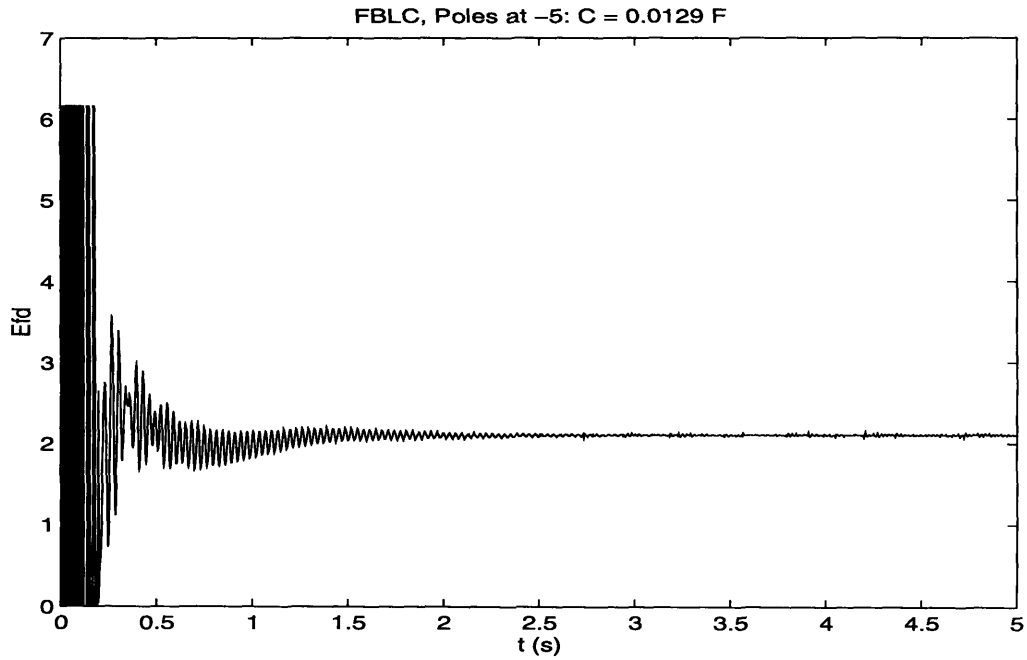

Figure 8-12: Field voltage of a system with FBLC, showing the large, rapid swings to counteract the subsynchronous oscillations.

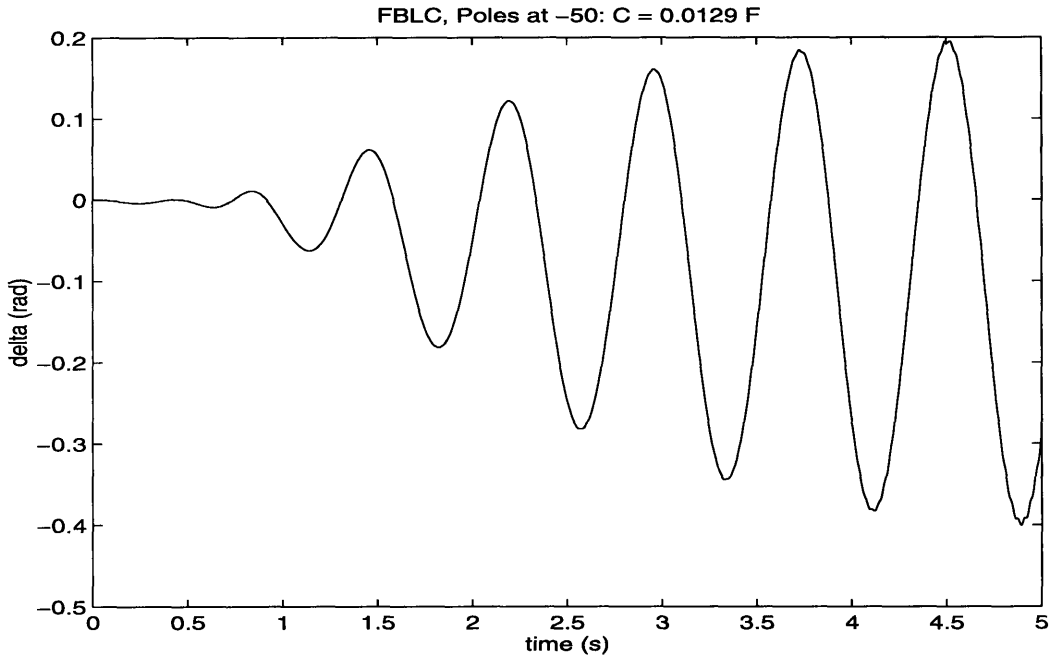

Figure 8-13: Rotor angle $(\delta - \delta_o)$ of a system with FBLC, poles at -50. FBLC does not stabilize the system.

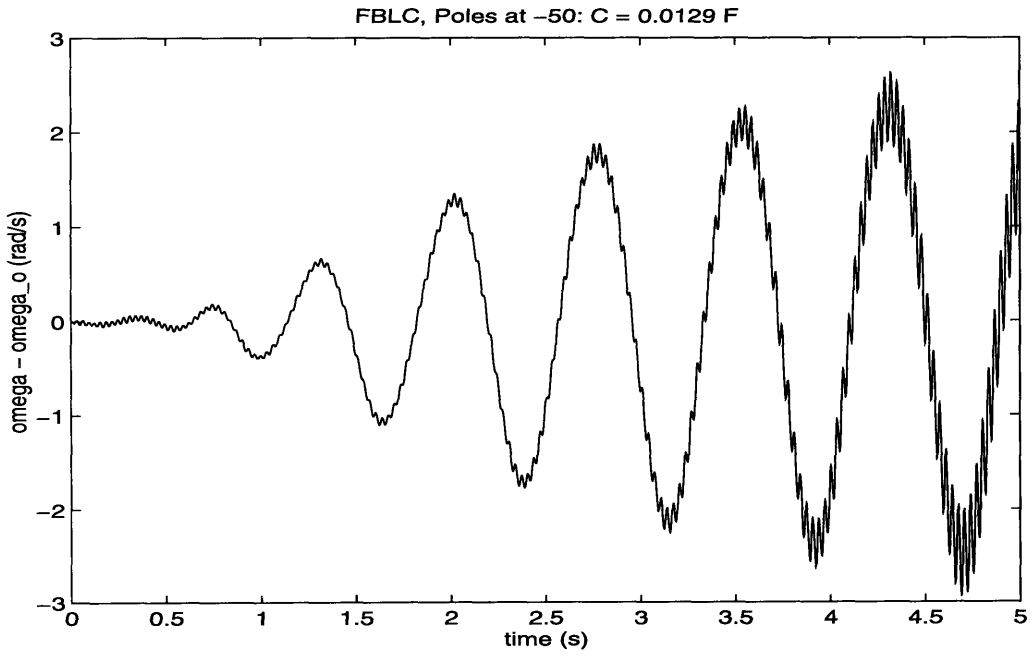

Figure 8-14: Plot of $(\omega - \omega_o)$ of a system with FBLC, poles at -50.

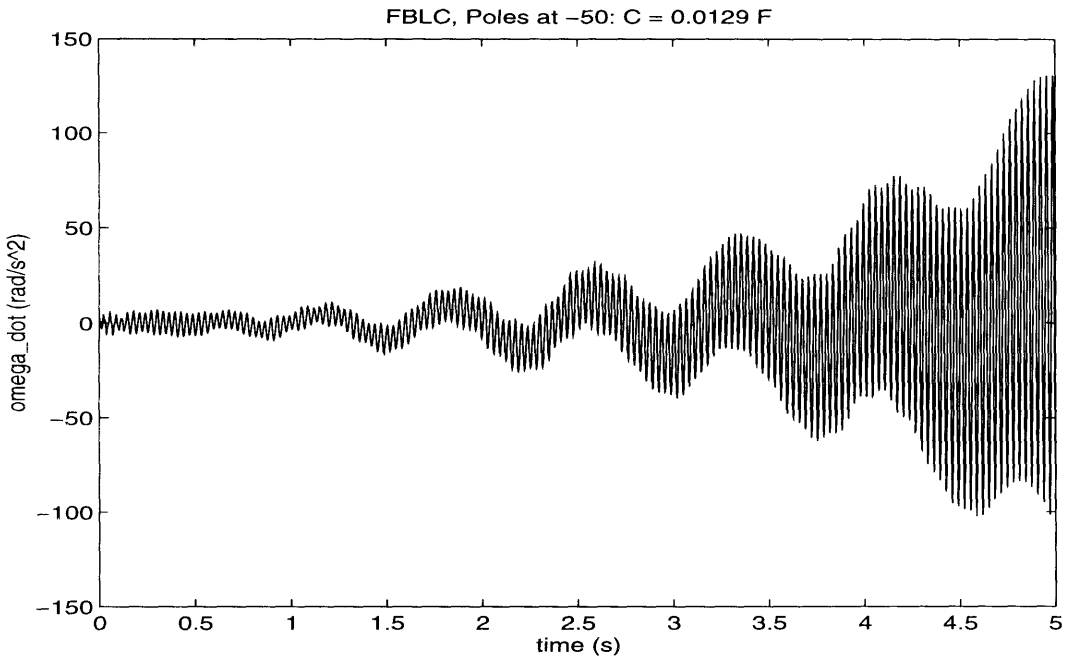

Figure 8-15: Rotor acceleration ($\dot{\omega}$) of a system with FBLC, poles at -50.

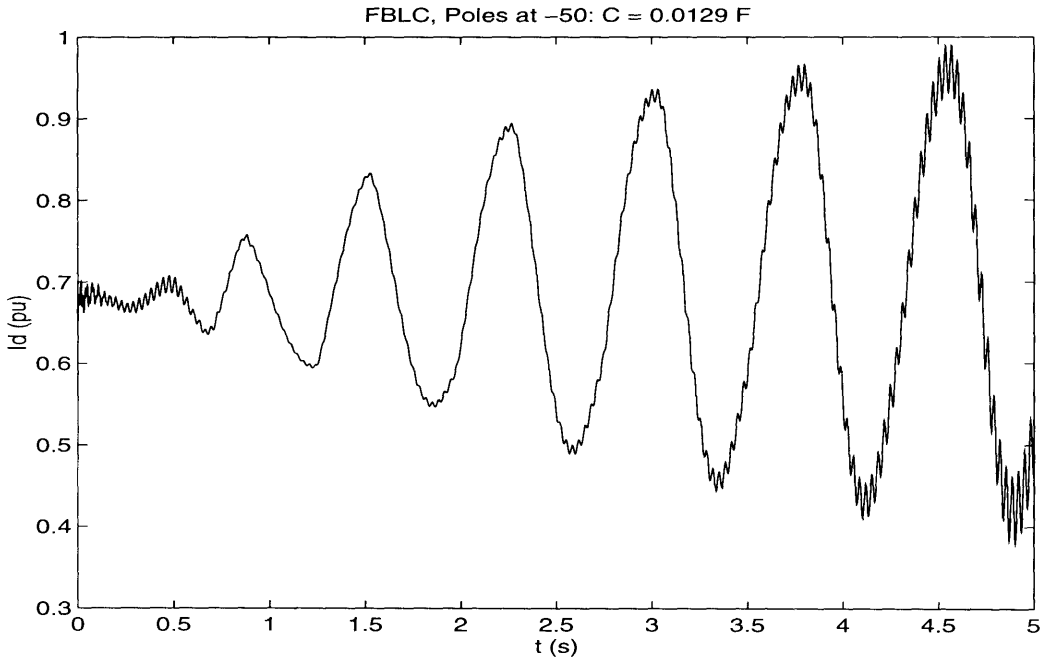

Figure 8-16: Line current (real part) of a system with FBLC, poles at -50.

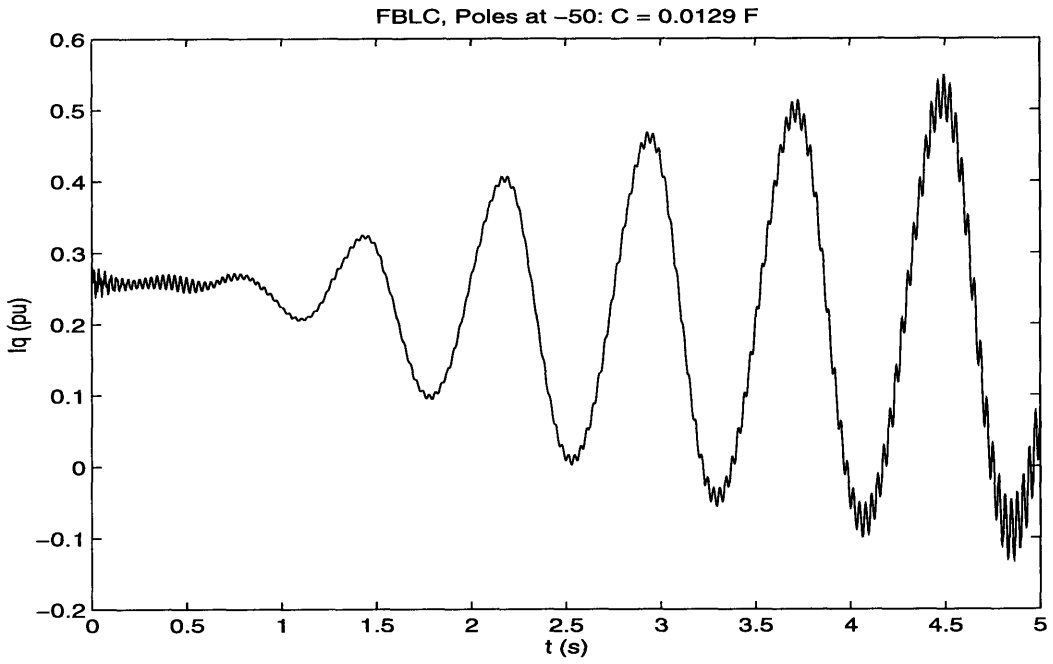

Figure 8-17: Line current (imaginary part) of a system with FBLC, poles at -50.

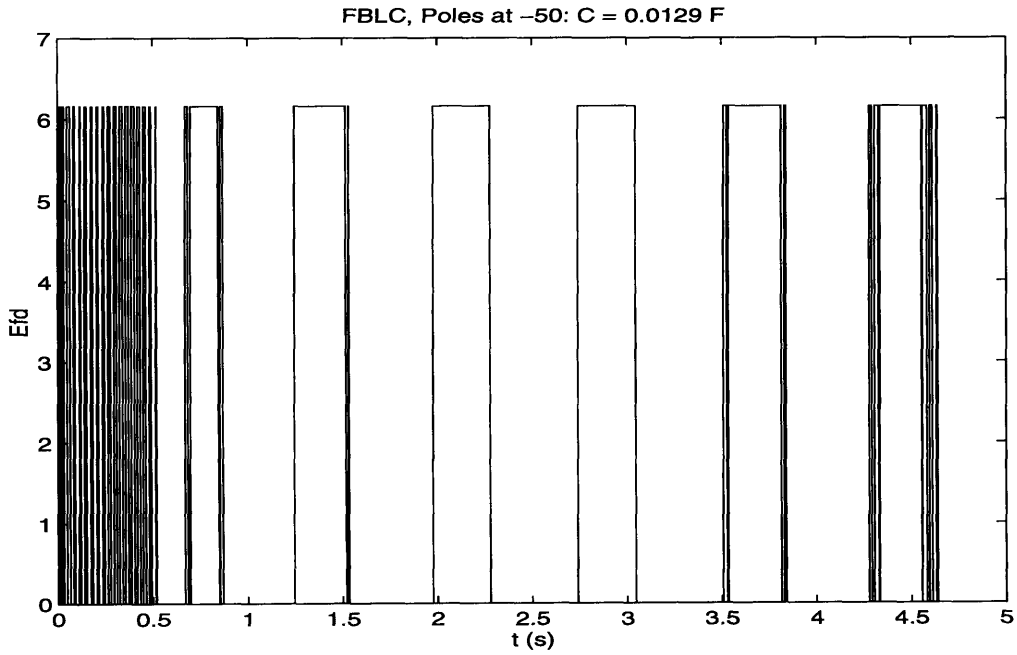

Figure 8-18: Field voltage of a system with FBLC, poles at -50. The voltage actually swings less frequently with the faster poles but it does not effectively counteract the subsynchronous oscillations.

measurement to reduce the swings while still providing the control necessary to stablize the system. The results of the acceleration filtering method with poles placed at -5 is shown in Figures 8-19 through 8-24. These results are very surprising, since we might expect that the high frequency oscillations in the field voltage are too small to stabilize the subsynchronous modes. However, the simulations reveal that the torsional modes do not grow. Since we know that the subsynchronous oscillations do grow if the field voltage is constant, we know that an equilibrium point cannot be reached with a constant E_{fd}. We will try simulating a smaller disturbance to see what happens. The results of a smaller disturbance are shown in Figures 8-25 to 8-30. The system appears to reach a state of dynamic equilibrium where the subsynchronous oscillations maintain a constant amplitude.

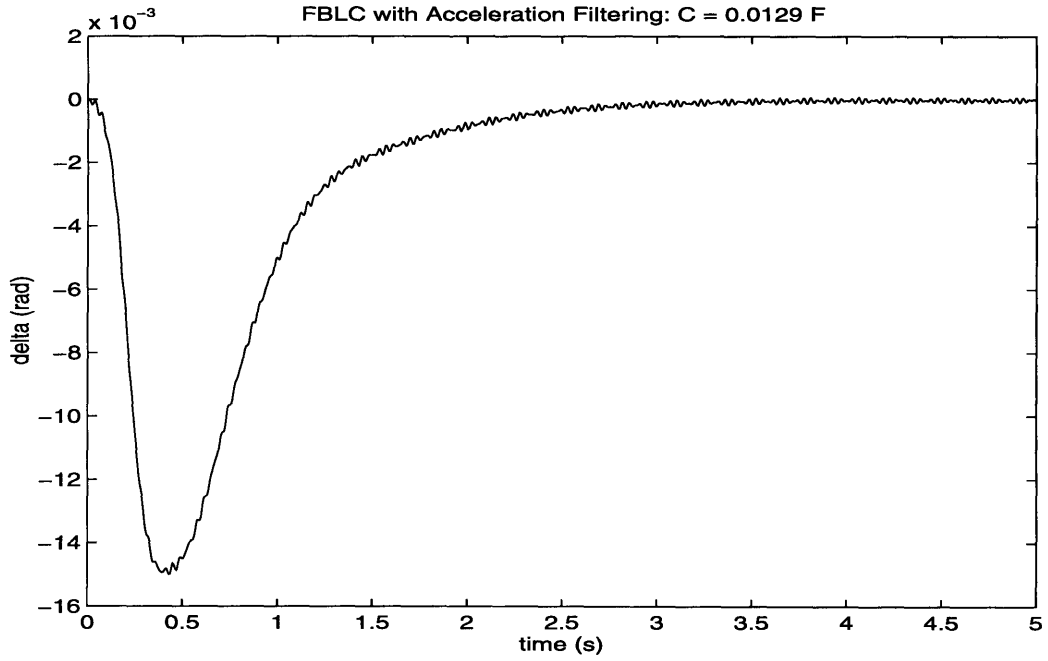

Figure 8-19: Rotor angle $(\delta - \delta_o)$ of a system with FBLC and a filtered acceleration measurement. The control input is able to stabilize the system.

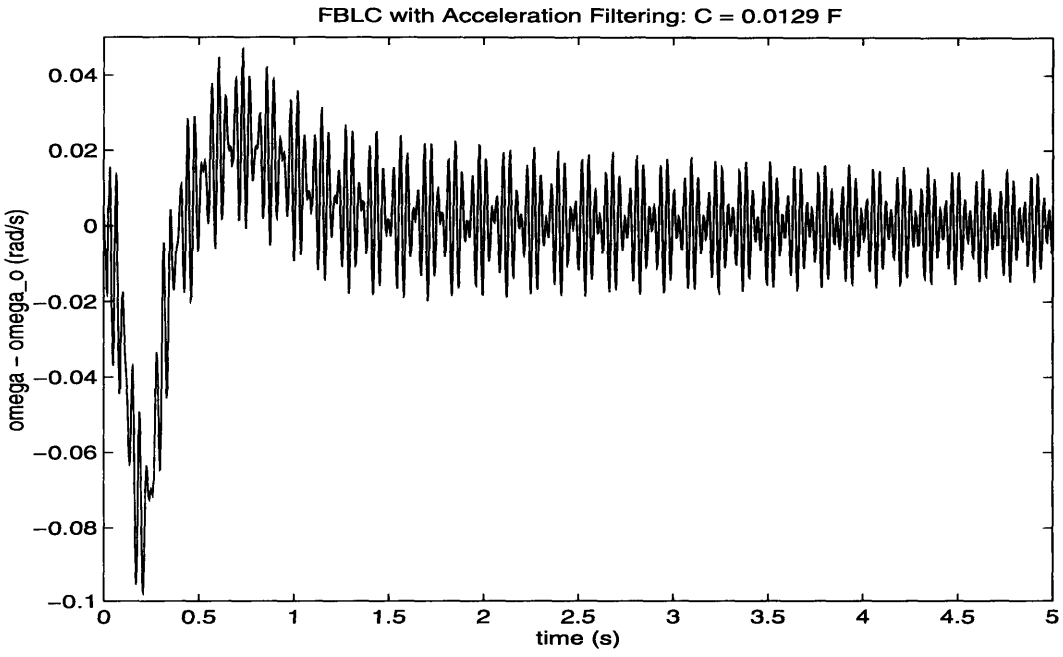

Figure 8-20: Plot of $\omega - \omega_o$ for a system with FBLC and a filtered acceleration measurement.

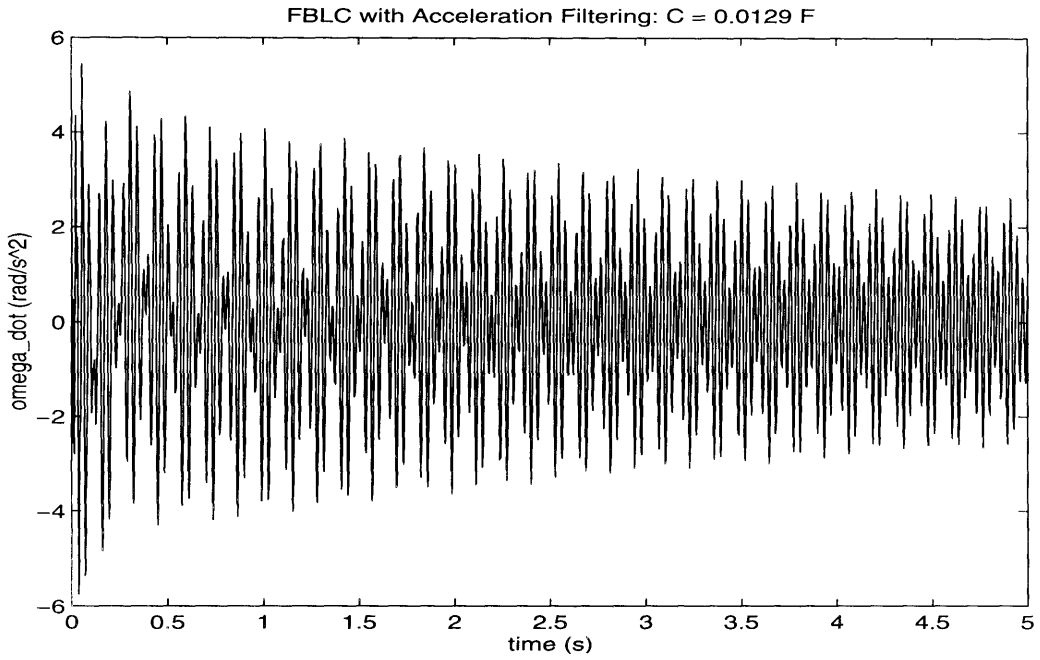

Figure 8-21: Rotor acceleration ($\dot{\omega}$) of a system with FBLC and a filtered acceleration measurement. The torsional oscillations decay very slowly, although they remain stable.

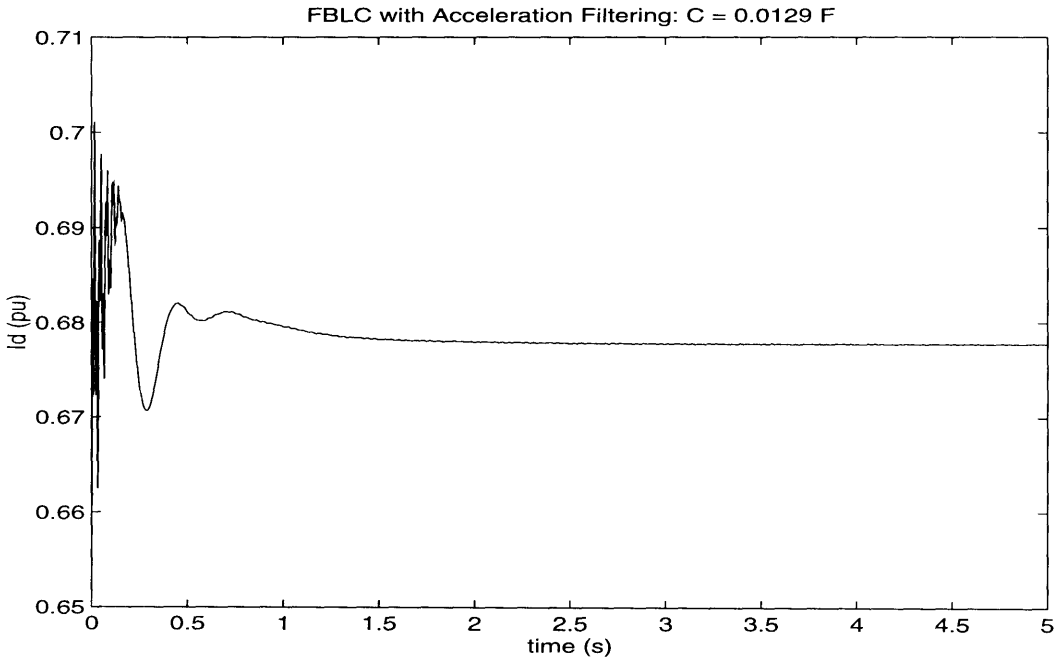

Figure 8-22: Line current (real part) of a system with FBLC and a filtered acceleration measurement.

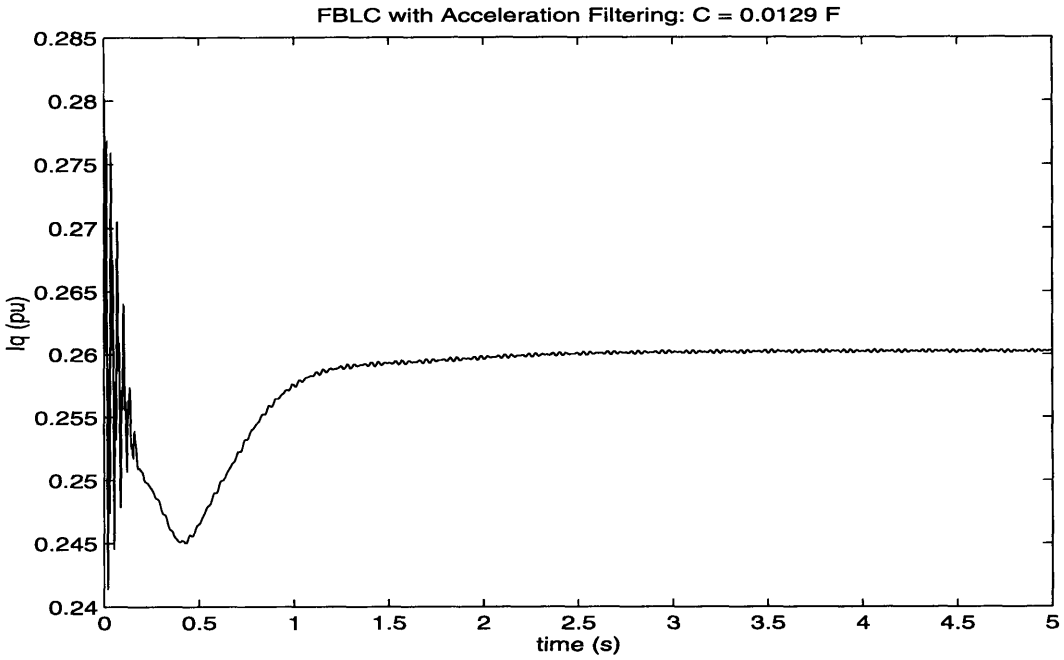

Figure 8-23: Line current (imaginary part) of a system with FBLC and a filtered acceleration measurement.

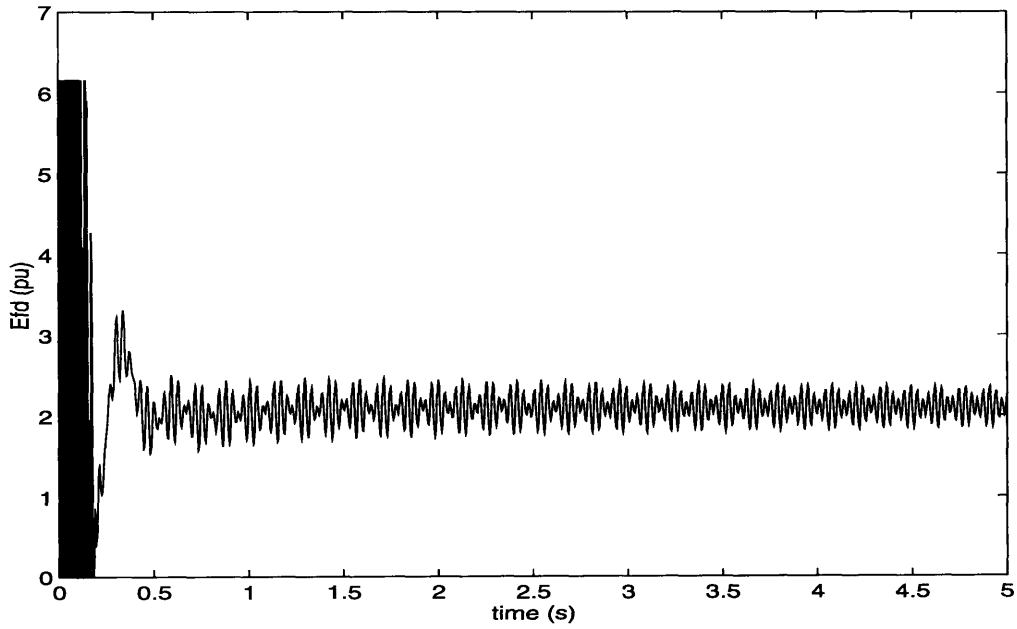

Figure 8-24: Field voltage of a system with FBLC averaging and a filtered acceleration measurement.

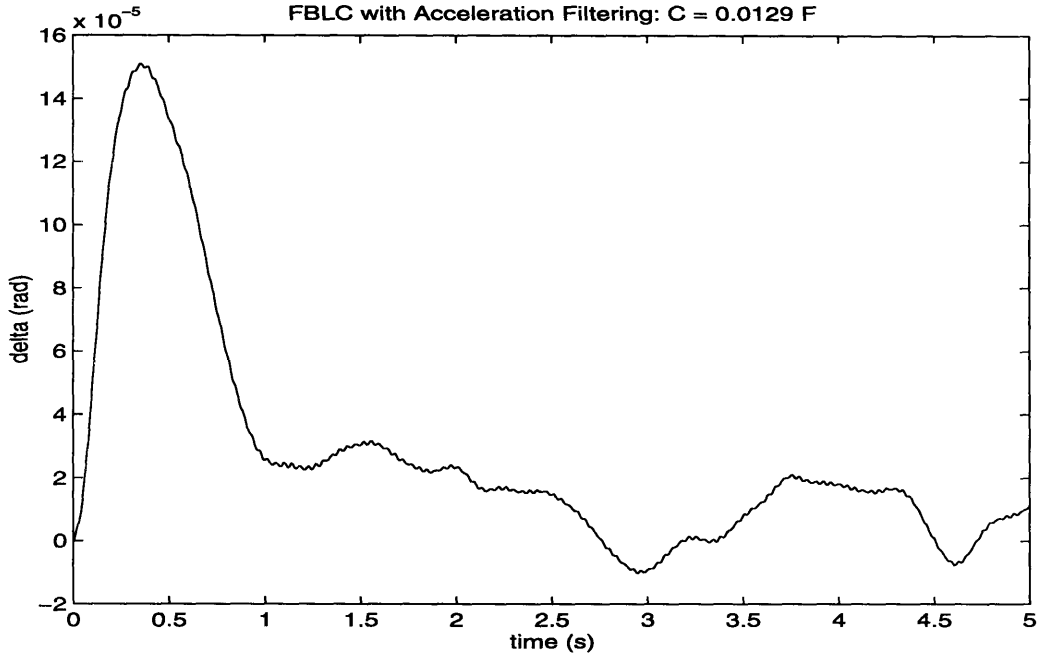

Figure 8-25: Rotor angle ($\delta - \delta_o$) of a system with FBLC and a filtered acceleration measurement.

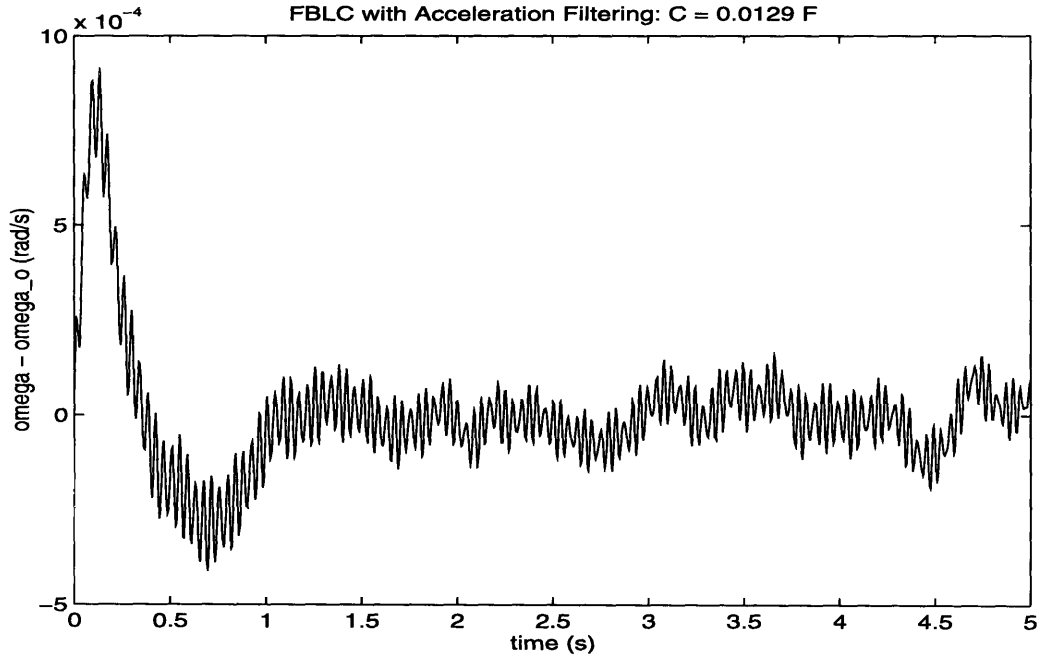

Figure 8-26: Plot of $\omega - \omega_o$ for a system with FBLC and a filtered acceleration measurement.

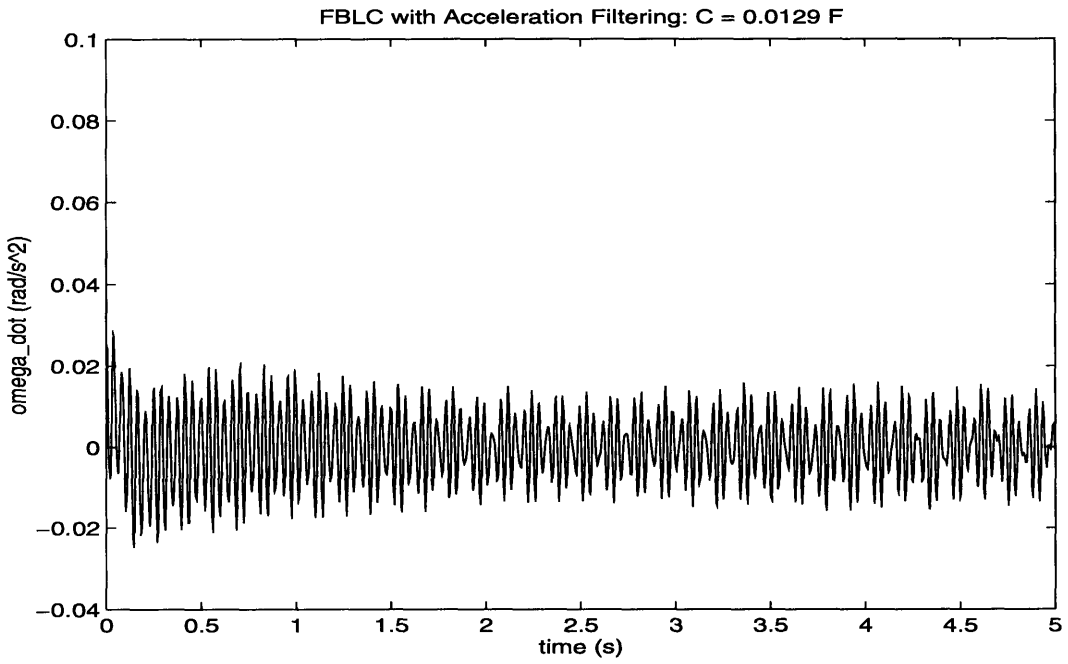

Figure 8-27: Rotor acceleration ($\dot{\omega}$) of a system with FBLC and a filtered acceleration measurement. The torsional oscillations maintain a constant amplitude over time.

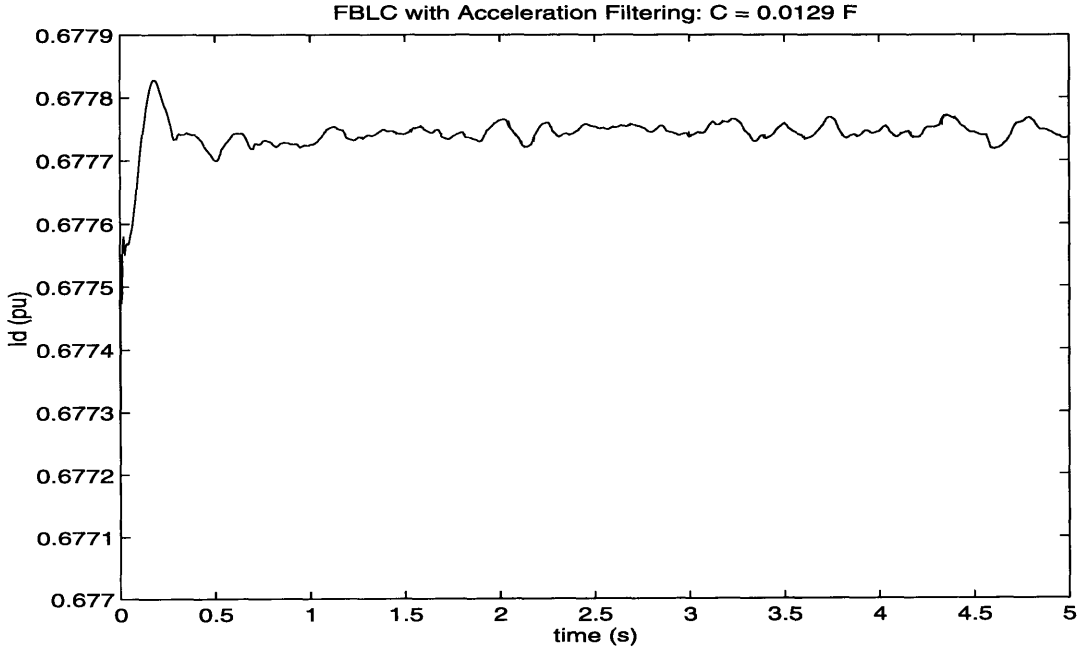

Figure 8-28: Line current (real part) of a system with FBLC and a filtered acceleration measurement.

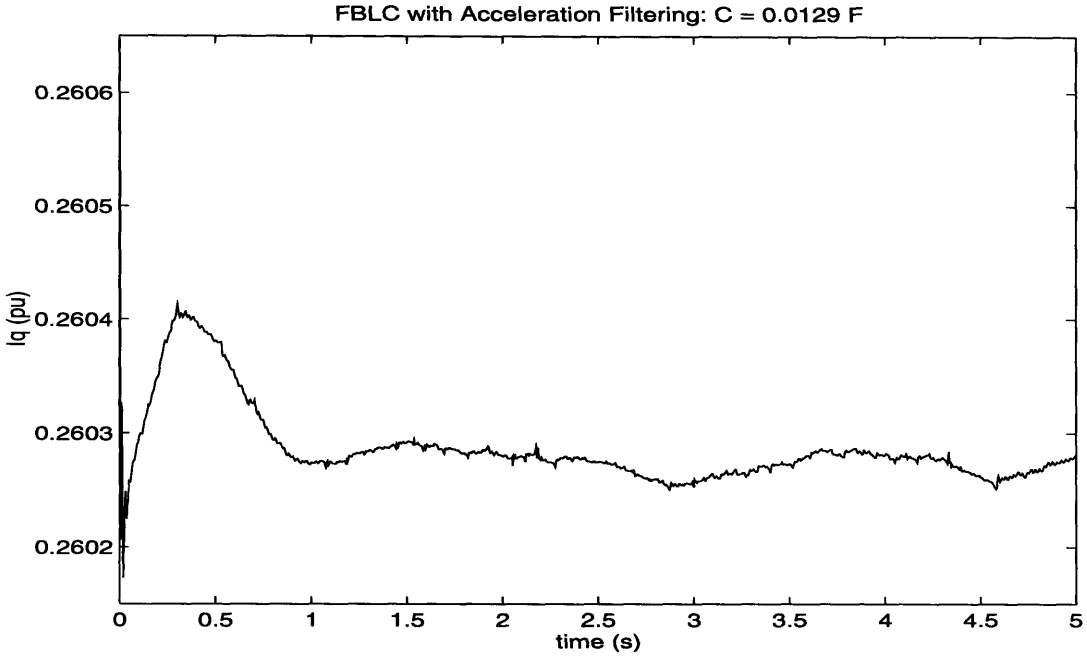

Figure 8-29: Line current (imaginary part) of a system with FBLC and a filtered acceleration measurement.

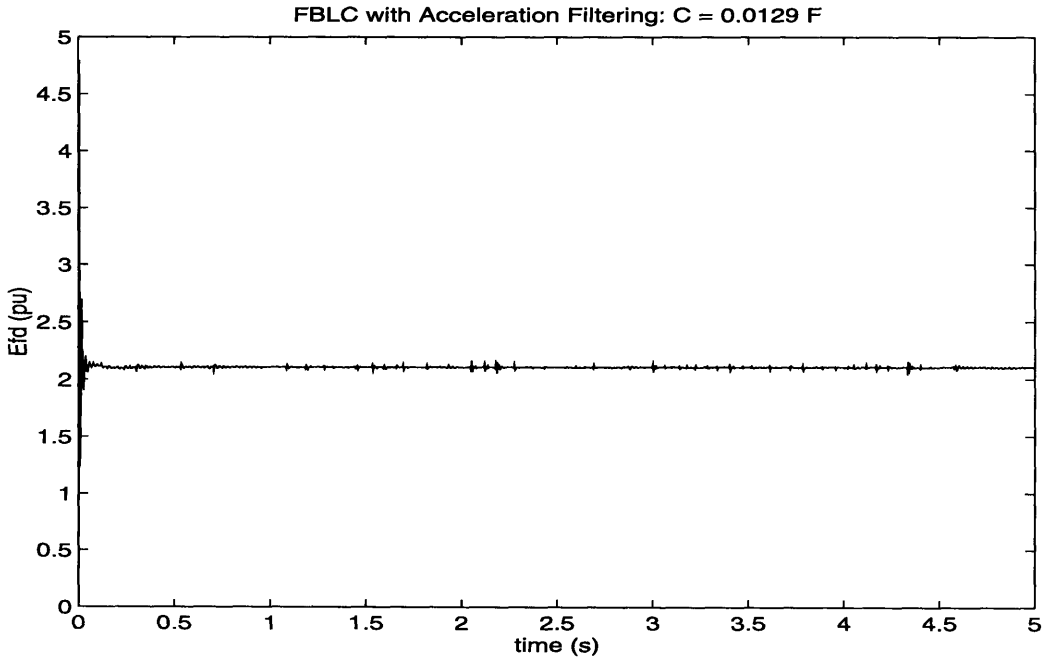

Figure 8-30: Field voltage of a system with FBLC averaging and a filtered acceleration measurement.

Chapter 9

Robust Stability of Feedback Linearizing Control to Torsional Dynamics

As shown earlier, when the shaft dynamics are added to the feedback linearizing control model, the composite model is still linear. Furthermore, the model was stable for the typical parameter values that were chosen and is even capable of damping out torsional oscillations that would otherwise be unstable. We will now examine whether feedback linearizing control remains stable for a wide range of shaft parameters. To perform this task, we will use known techniques for stability robustness analysis of linear systems [23]. Fortunately, since the shaft dynamics preserve the linearity of the closed-loop system, these techniques are applicable, whereas in most cases, unmodeled dynamics result in a nonlinear system, which is much more difficult to analyze.

9.1 Characteristic Polynomial of the System

Most robust stability literature is concerned with the stability of the roots of a polynomial whose coefficients are unknown, but within a certain known range. In our case, we wish to determine whether the roots of:

$$\chi(s) = |s\mathbf{I} - \mathbf{A}| = 0 \tag{9.1}$$

all lie in the left half plane (i.e. have negative real parts). The matrix $\mathbf{A}$ is defined in equation (3.40). Since the matrix is rather sparse, the characteristic polynomial of $\mathbf{A}$ may be calculated by using cofactor expansion. The resulting polynomial is:

$$\chi(s) = s^7 + c_6 s^6 + c_5 s^5 + c_4 s^4 + c_3 s^3 + c_2 s^2 + c_1 s + c_0 \tag{9.2}$$

$$c_6 = \frac{D_{1u}}{2H_1} + \frac{D_{2u}}{2H_2} + \frac{D_{eu} - D - 2a_2 H}{2H_e}$$

$$
\begin{aligned}
c_5 &= \frac{K_{12u}}{2H_1} + \frac{K_{12u}+K_{2eu}}{2H_2} + \frac{D_{1u}D_{2u}}{4H_1H_2} + \frac{K_{2eu}-2a_1H}{2H_e} \\
&\quad + \frac{D_{1u}(D_{eu}-D-2a_2H)}{4H_1H_e} + \frac{D_{2u}(D_{eu}-D-2a_2H)}{4H_2H_e} \\
c_4 &= \frac{(K_{12u}+K_{2eu})D_{1u}+K_{12u}D_{2u}}{4H_1H_2} + \frac{D_{1u}(K_{2eu}-2a_1H)+K_{12u}(D_{eu}-D-2a_2H)}{4H_1H_e} \\
&\quad + \frac{D_{2u}(K_{2eu}-2a_1H)+(K_{12u}+K_{2eu})(D_{eu}-D-2a_2H)}{4H_2H_e} \\
&\quad + \frac{D_{1u}D_{2u}(D_{eu}-D-2a_2H)}{8H_1H_2H_e} - a_0\frac{H}{H_e} \\
c_3 &= \frac{K_{12u}K_{2eu}}{4H_1H_2} + \frac{K_{12u}(K_{2eu}-2a_1H)-2D_{1u}a_0H}{4H_1H_e} \\
&\quad + \frac{K_{12u}(K_{2eu}-2a_1H)-2D_{2u}a_0H-2K_{2eu}a_1H}{4H_2H_e} \\
&\quad + \frac{([K_{12u}+K_{2eu}]D_{1u}+K_{12u}D_{2u})(D_{eu}-D-2a_2H)+D_{1u}D_{2u}(K_{2eu}-2a_1H)}{8H_1H_2H_e} \\
c_2 &= -\frac{K_{12u}a_0H}{2H_1H_e} - \frac{(K_{12u}+K_{2eu})a_0H}{2H_2H_e} + \frac{K_{12u}K_{2eu}(D_{eu}-D-2a_2H)}{8H_1H_2H_e} \\
&\quad + \frac{K_{12u}(D_{1u}+D_{2u})(K_{2eu}-2a_1H)-2D_{1u}K_{2eu}a_1H-2D_{1u}D_{2u}a_0H}{8H_1H_2H_e} \\
c_1 &= \frac{-([K_{12u}+K_{2eu}]D_{1u}+K_{12u}D_{2u})a_0H-K_{12u}K_{2eu}a_1H}{4H_1H_2H_e} \\
c_0 &= \frac{-K_{12u}K_{2eu}a_0H}{4H_1H_2H_e}
\end{aligned}
$$

In these equations, H_1, H_2, H_e, K_{12u}, K_{2eu}, D_{1u}, D_{2u}, and D_{eu} are all shaft parameters which are not known precisely and may vary significantly for a given system. H and D are controller constants and are fixed, known values. These quantities are used to estimate the total rotational inertia and damping of the shaft. For the sample parameter values from Section 2.4, the characteristic polynomial is:

$$
\begin{aligned}
\chi(s) &= s^7 + 45.66s^6 + (6.17\times10^4)s^5 + (2.02\times10^6)s^4 + (8.94\times10^8)s^3 \\
&\quad + (1.34\times10^{10})s^2 + (6.63\times10^{10})s + 1.10\times10^{11}
\end{aligned} \tag{9.3}
$$

9.2 Definition of Robust Stability

It is now time to define precisely what is meant by robust stability. The terms introduced here are developed in [23].

Given a polynomial:

$$
p(s,\mathbf{q}) = a_n(\mathbf{q})s^n + a_{n-1}(\mathbf{q})s^{n-1} + \cdots + a_1(\mathbf{q})s + a_0(\mathbf{q}) \tag{9.4}
$$

where the coefficients $a_i(\mathbf{q})$ are real functions of uncertain quantities $\mathbf{q} = [q_1\ q_2\ \ldots\ q_m]^T$

and $q_i^- \leq q_i \leq q_i^+$, the polynomial $p(s, \mathbf{q})$ is robustly stable if and only if all roots of $p(s, \mathbf{q}) = 0$ are in the left half plane for all $\mathbf{q} \in Q$, where Q denotes the set of all possible uncertainty vectors $\mathbf{q}$. Furthermore, it is assumed that $a_n(\mathbf{q}) \neq 0$ for all $\mathbf{q} \in Q$. This condition is equivalent to stating that $p(s, \mathbf{q})$ has invariant degree, meaning that the number of roots is the same for all $\mathbf{q}$. Clearly, equation (9.2) has invariant degree.

The manner in which the uncertain quantities q_i appear in the polynomial coefficients is known as the uncertainty structure. If each q_i appears in only one coefficient, the polynomial has an independent uncertainty structure. If at least one q_i appears in more than one coefficient, but every term of every coefficient has at most one uncertain quantity, the uncertainty structure is affine linear. If there are terms which contain products of different q_i, but there are no powers of any q_i greater than one, the structure is multilinear. An uncertainty structure with higher powers of at least one q_i is polynomic. The uncertainty structure for the torsional shaft/generator system with FBLC is a multilinear structure.

9.3 Kharitonov's Theorem

Perhaps the most well-known and simplest tool for robust stability analysis is Kharitonov's Theorem. Kharitonov's Theorem is a conclusive test for the stability of an independent uncertainty structure. Such a polynomial may be written as:

$$p(s, \mathbf{q}) = q_n s^n + q_{n-1} s^{n-1} + \cdots + q_1 s + q_0 \tag{9.5}$$

where, as before, $q_i^- \leq q_i \leq q_i^+$. Kharitonov's Theorem asserts that p(s, $\mathbf{q}$) = 0 is robustly stable if and only if the following four Kharitonov polynomials are stable [23]:

$$K_1(s) = q_0^- + q_1^- s + q_2^+ s^2 + q_3^+ s^3 + q_4^- s^4 + q_5^- s^5 + q_6^+ s^6 + q_7^+ s^7 + \cdots \tag{9.6}$$

$$K_2(s) = q_0^+ + q_1^+ s + q_2^- s^2 + q_3^- s^3 + q_4^+ s^4 + q_5^+ s^5 + q_6^- s^6 + q_7^- s^7 + \cdots \tag{9.7}$$

$$K_3(s) = q_0^+ + q_1^- s + q_2^- s^2 + q_3^+ s^3 + q_4^+ s^4 + q_5^- s^5 + q_6^- s^6 + q_7^+ s^7 + \cdots \tag{9.8}$$

$$K_4(s) = q_0^- + q_1^+ s + q_2^+ s^2 + q_3^- s^3 + q_4^- s^4 + q_5^+ s^5 + q_6^+ s^6 + q_7^- s^7 + \cdots \tag{9.9}$$

The proof of Kharitonov's Theorem is outlined in the next section.

The good news about this theorem is that it provides a simple, conclusive test for robust stability. By calculating the roots of four polynomials, we will have information about an entire set of an infinite number of polynomials. The bad news is that the required uncertainty structure rarely occurs in practice. It is possible to apply Kharitonov's Theorem to any uncertainty structure by finding the minimum and maximum values of each coefficient; this technique is called overbounding [23]. However, the results of overbounding are conservative; if Kharitonov's Theorem concludes stability for the overbounded structure, then the original structure is robustly stable; however, the converse is not true. If Kharitonov's Theorem determines that the

overbounded structure is not robustly stable, we need other techniques to determine whether the original system is robustly stable.

9.4 Value Set and the Zero Exclusion Condition

For any generalized uncertainty structure, robust stability may be determined by means of the value set. The value set at a given frequency ω_o is defined as the region covered by $p(j\omega_o, \mathbf{q})$ for all $\mathbf{q} \in Q$. For specialized uncertainty structures, the value set has a distinct shape, which will be discussed later [23].

The value set is used to conclusively determine robust stability of $p(s, \mathbf{q})$ through the Zero Exclusion Condition. This condition states that $p(s, \mathbf{q})$ is robustly stable if and only if at least one member of $p(s, \mathbf{q})$ is stable, and the value set $p(j\omega, \mathbf{q})$ does not include the point zero at any frequency ω, where $0 \leq \omega \leq \infty$. The proof of the Zero Exclusion Condition is based on the following argument: Clearly, if $p(s, \mathbf{q})$ is robustly stable, then the roots of $p(s, \mathbf{q}) = 0$ must always be in the left half plane, and $p(j\omega, \mathbf{q})$ can never be zero, since $j\omega$ is on the imaginary axis. Furthermore, if $p(s, \mathbf{q})$ is not robustly stable, then for some $\mathbf{q}_s \in Q$ and $\mathbf{q}_u \in Q$, $p(s, \mathbf{q}_s)$ is stable while $p(s, \mathbf{q}_u)$ is not. As $\mathbf{q}$ travels on a path from $\mathbf{q}_s$ to $\mathbf{q}_u$, at least one root of $p(s, \mathbf{q})$ travels from the left half plane to the right half plane; for some $\mathbf{q}^*$ on the path, that root crosses the imaginary axis at $j\omega^*$, and therefore $p(j\omega^*, \mathbf{q}^*) = 0$. Note that because the coefficients of $p(s, \mathbf{q})$ are assumed to be real, it is sufficient to check the positive imaginary axis, since imaginary roots occur in conjugate pairs. A formal proof may be found in [23].

9.4.1 The Kharitonov Rectangle

The Zero Exclusion Condition is the basis for the proof of Kharitonov's theorem. It turns out that the value set for an independent uncertainty structure is a rectangle. To see this, note from equation (9.5):

$$p(j\omega_o, \mathbf{q}) = (q_0 - q_2\omega_o^2 + q_4\omega_o^4 - \cdots) + j(q_1\omega_o - q_3\omega_o^3 + \cdots) \tag{9.10}$$

Assuming that $\omega_o \geq 0$, the real part of $p(j\omega_o, \mathbf{q})$ is maximized when $q_0 = q_0^+, q_2 = q_2^-, q_4 = q_4^+, \cdots$ and is minimized when $q_0 = q_0^-, q_2 = q_2^+, q_4 = q_4^-, \cdots$. Similarly, the imaginary part reaches a maximum at $q_1 = q_1^+, q_3 = q_3^-, q_5 = q_5^+, \cdots$ and a minimum at $q_1 = q_1^-, q_3 = q_3^+, q_5 = q_5^-, \cdots$. Since the real and imaginary parts are maximized or minimized independently, the value set will have the shape of a rectangle, as shown in Figure 9-1. Notice that the Kharitonov polynomials mark the vertices of the rectangle [23]. It is possible to show [23] that the Zero Exclusion Condition for the Kharitonov rectangle is satisfied if and only if the four Kharitonov polynomials are stable.

9.4.2 Affine Linear and Multilinear Uncertainty Structures

If the uncertainty structure is affine linear, it can be shown that the value set will be a convex polygon [23]. For multilinear uncertainty structures, the value set no longer

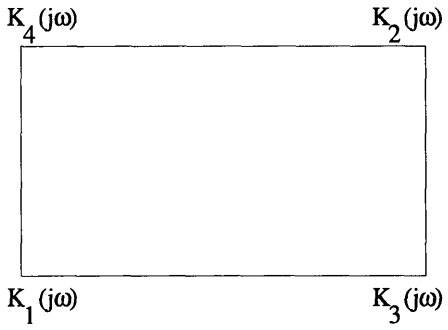

Figure 9-1: The Kharitonov rectangle, showing the Kharitonov polynomials as the vertices.

has a well defined shape. However, an upper bound for the value set of a multilinear structure may be determined using the Mapping Theorem [23]. First, it is necessary to calculate $p(j\omega, \mathbf{q})$ for all of the extreme points of $\mathbf{q}$. The extreme points are the points where each q_i is at either its minimum or maximum value. Notice that Q has the shape of a box; the extreme points correspond to the corners of the box. Furthermore, the number of extreme points is equal to 2^m, where m is the number of uncertainties.

Next, the value set $p(j\omega, \mathbf{q})$ is included within the convex hull of the extreme points. The convex hull of a set of points is the polygon which has a subset of the points as vertices and leaves none of the points outside of the polygon. (See [23] for a formal definition of convex hull.) If the uncertainity structure is affine linear, then the convex hull of the extreme points is the value set.

9.5 Analyzing the Torsional Shaft/Generator System

We now have the required tools to analyze the robust stability of the shaft/generator system. Notice that since the coefficients a_i are always negative (it is clearly undesirable to place the FBLC closed-loop poles in the right half plane), all of the terms in each coefficient of the characteristic polynomial are positive. This feature makes it easy to find the minimum and maximum values of these coefficients. However, this is the only "nice" feature of the characteristic polynomial; it has a multilinear uncertainty structure, and as we shall see, it is not possible, without an exorbitant amount of computation, to conclusively establish robust stability over a wide variation of many system parameters.

Coefficient	$K_1(s)$	$K_2(s)$	$K_3(s)$	$K_4(s)$
c_6	46.74	45.26	45.26	46.74
c_5	6.17×10^4	6.18×10^4	6.17×10^4	6.18×10^4
c_4	2.00×10^6	2.06×10^6	2.06×10^6	2.00×10^6
c_3	8.94×10^8	8.93×10^8	8.94×10^8	8.93×10^8
c_2	1.37×10^{10}	1.32×10^{10}	1.32×10^{10}	1.37×10^{10}
c_1	6.63×10^{10}	6.63×10^{10}	6.63×10^{10}	6.63×10^{10}
c_0	1.10×10^{11}	1.10×10^{11}	1.10×10^{11}	1.10×10^{11}

Table 9.1: The coefficients of the four Kharitonov polynomials used to examine robust stability for variations in the damping constants.

9.5.1 Damping Parameters

We will first examine whether the system remains stable when the damping coefficients vary over a wide range. Assume that the per unit damping terms lie within the following ranges:

$$0 \leq D_{1u} \leq 0.32$$
$$0 \leq D_{2u} \leq 2$$
$$0 \leq D_{eu} \leq 1.2$$

while the other parameters are fixed. Overbounding with Kharitonov's theorem is sufficient to establish that the system is robustly stable to these parameter variations. The coefficients of the four Kharitonov polynomials are shown in Table 9.1. It is easy to show that the roots of these polynomials are all in the left half plane.

9.5.2 Spring Constant Parameters

Next, we would like to know whether the system is robustly stable to a large variation in the spring constants K_{12u} and K_{2eu}, while the other parameters remain constant. We will set the ranges of the spring constants as:

$$10000 \leq K_{12u} \leq 40000$$
$$20000 \leq K_{2eu} \leq 80000$$

Unfortunately, Kharitonov's theorem with overbounding does not provide a conclusion of robust stability. It is necessary to resort to calculation of the value set for $0 \leq \omega \leq 1000$. Note that at $\omega_c = 1000$:

$$\omega_c^7 > \sum_{i=0}^{6} c_i \omega_c^i \tag{9.11}$$

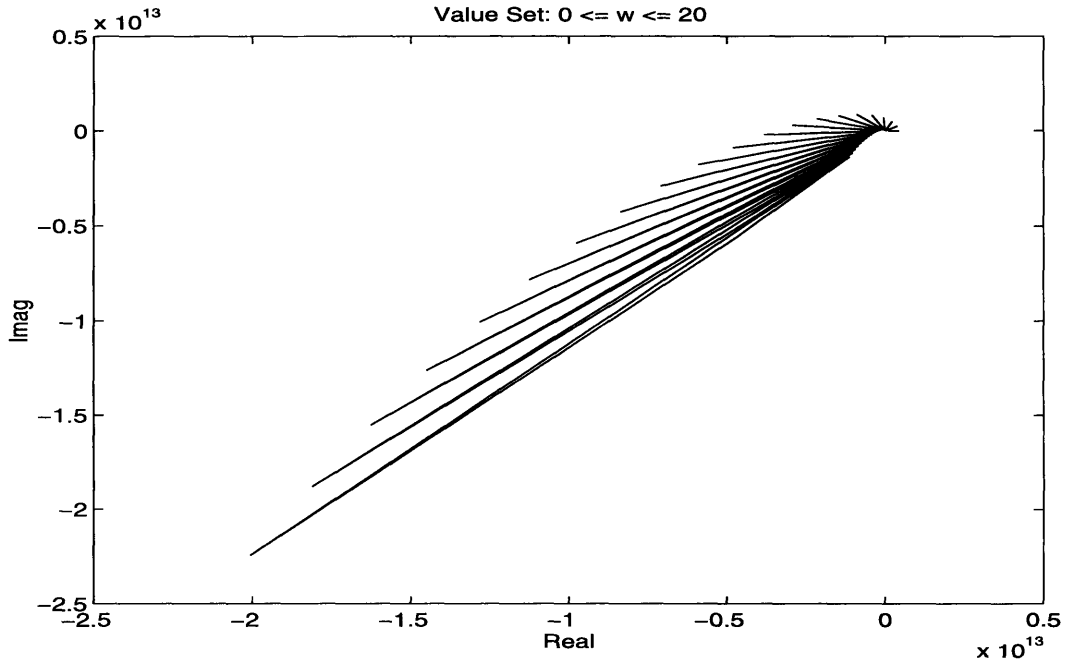

Figure 9-2: Value set for $0 \leq \omega \leq 20$.

and therefore $p(j\omega, \mathbf{q})$ can not be zero for $\omega > \omega_c$. ω_c is known as the cutoff frequency. A cutoff frequency exists for every $p(j\omega, \mathbf{q})$ [23], so that it is not necessary to generate an infinite number of value sets in order to verify the Zero Exclusion Condition.

The value sets for $0 \leq \omega \leq 1000$ are shown in Figures 9-2 through 9-8. For $135 \leq \omega \leq 265$, the convex hull of the extreme points does include the zero point. To show that the value set at these frequencies does not include zero, two convex hulls are generated: one for $10000 \leq K_{12u} \leq 10000 * (\omega/131)^2$, and another for $10000 * (\omega/131)^2 \leq K_{12u} \leq 40000$. The value set $p(j\omega, \mathbf{q})$ is contained in the union of the two smaller convex hulls. Since the value set does not include zero at any frequency, we conclude that the system is robustly stable to the specified parameter variations in the spring constants.

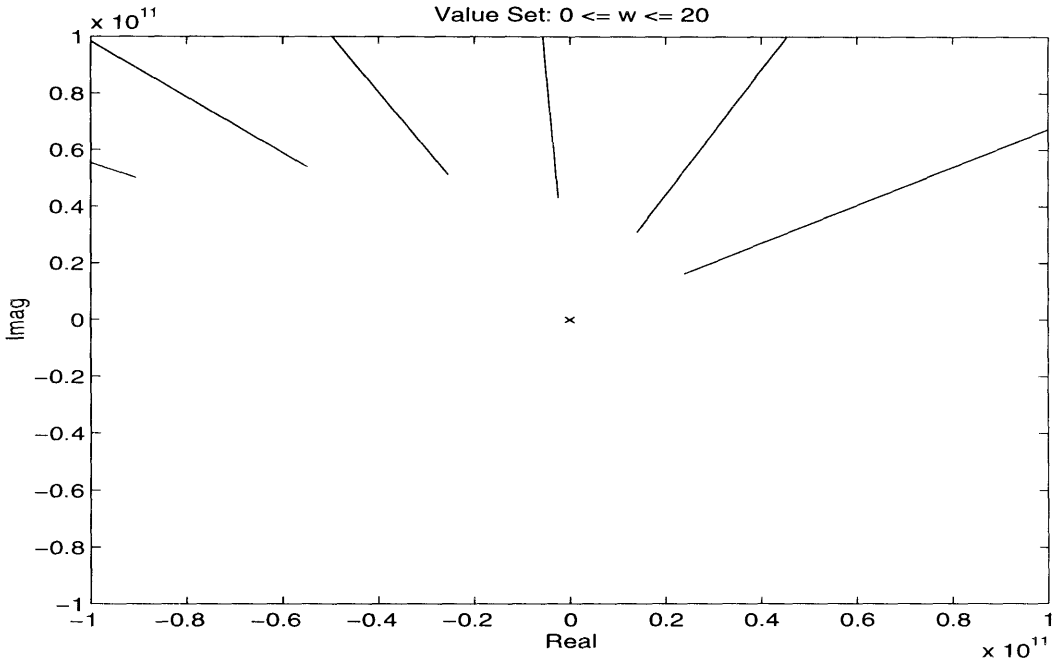

Figure 9-3: Value set for $0 \leq \omega \leq 20$.

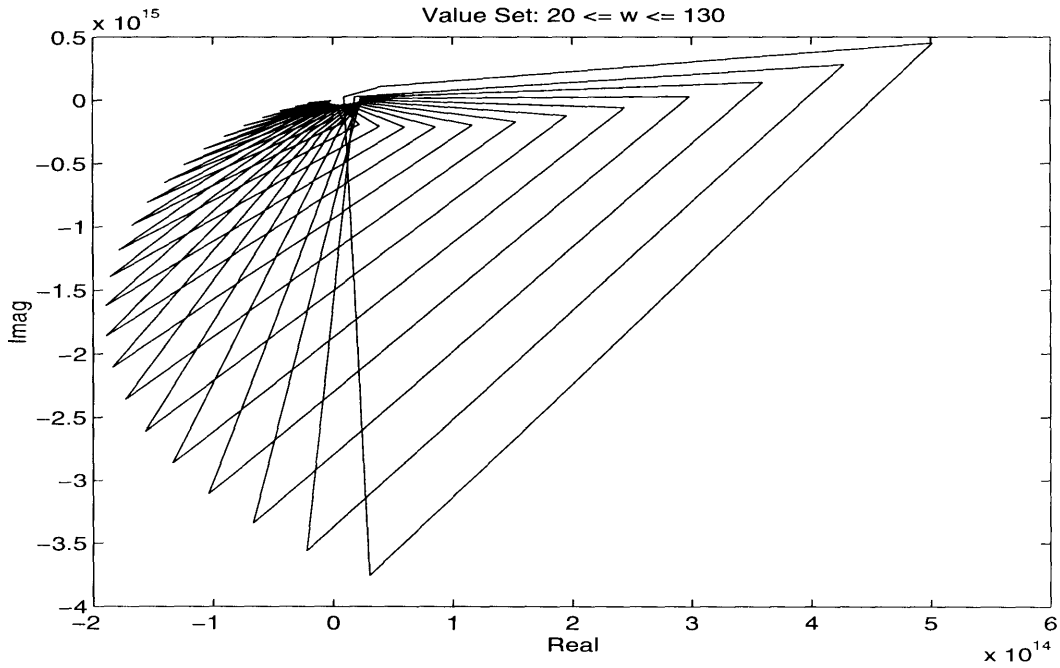

Figure 9-4: Value set for $20 \leq \omega \leq 130$.

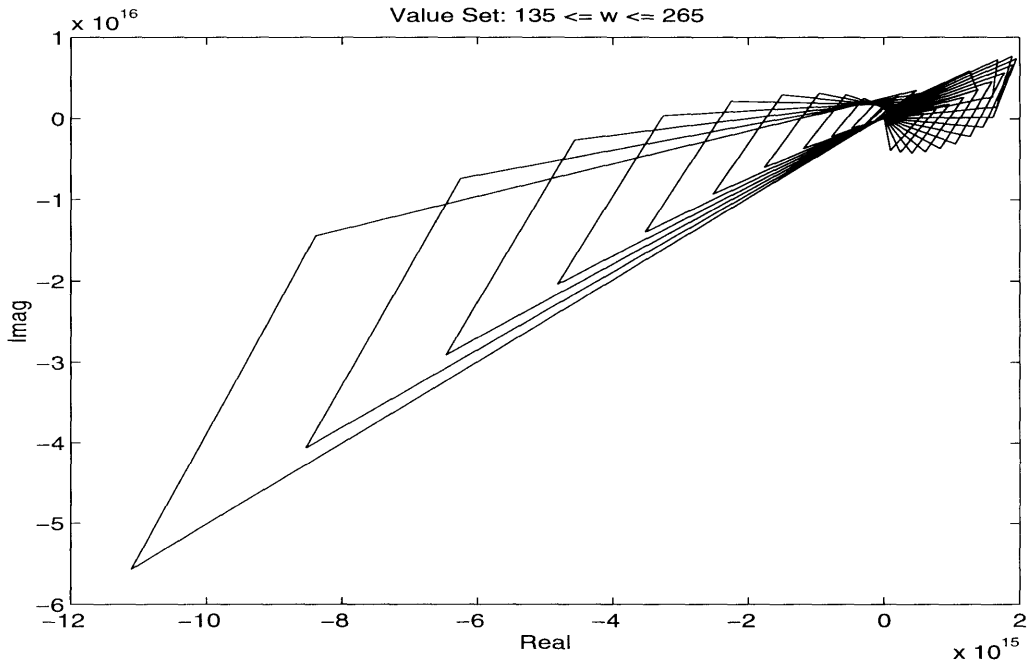

Figure 9-5: Value set for $135 \leq \omega \leq 265$.

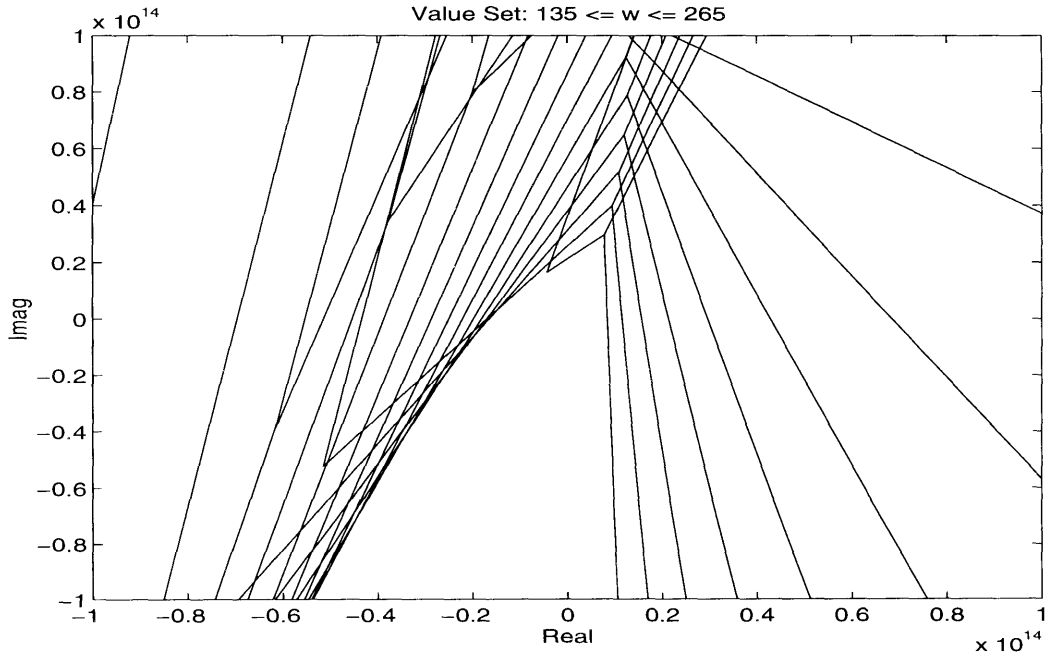

Figure 9-6: Value set for $135 \leq \omega \leq 265$.

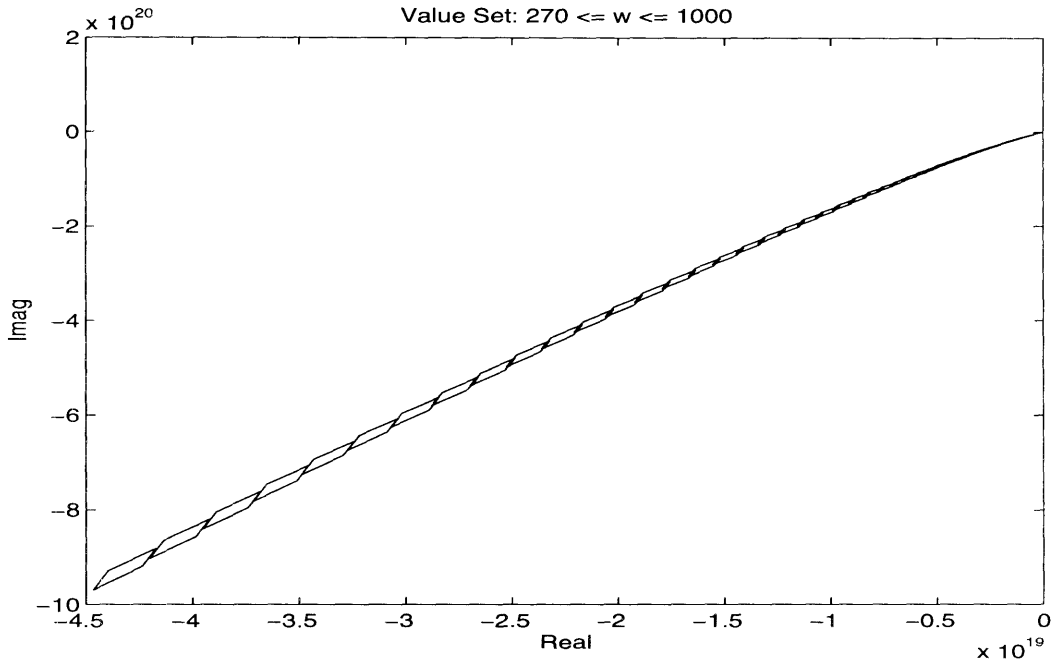

Figure 9-7: Value set for $270 \leq \omega \leq 1000$.

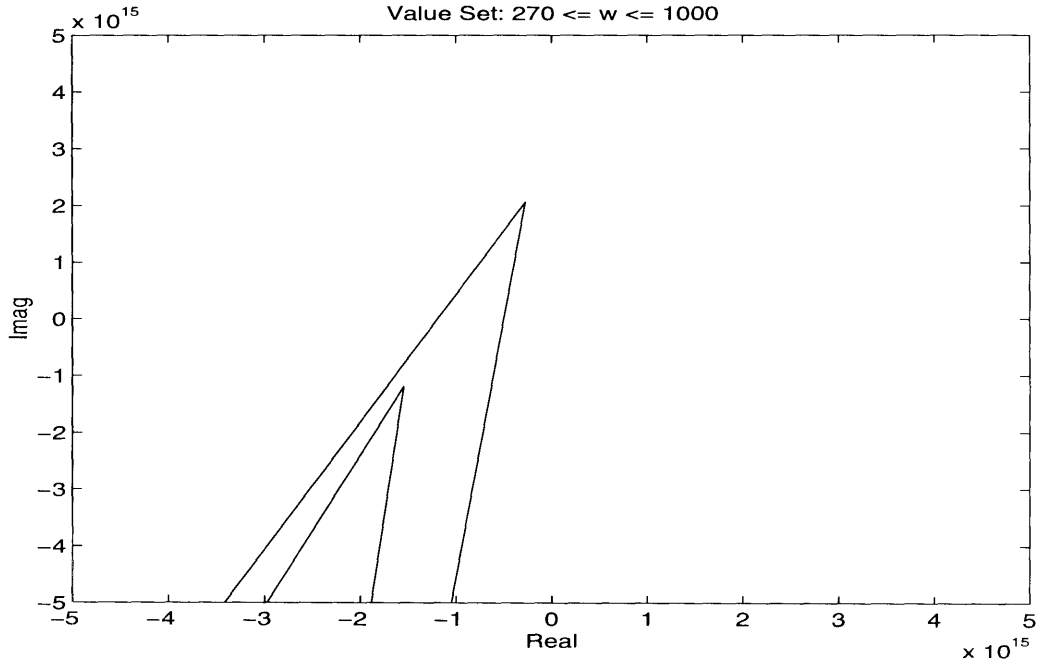

Figure 9-8: Value set for $270 \leq \omega \leq 1000$.

Chapter 10

Sliding Control

Since the torsional vibrations in the shaft produce uncertainties in $\rho(\mathbf{x}_g)$ and $\beta(\mathbf{x}_g)$, we would like to try using a control methodology that is designed to account for these uncertainties. One such method is known as sliding control [24]. In a sliding control design, the system states are designed to follow a desired trajectory despite inaccuracies in the model. We will choose the desired trajectory to reflect the response of a linear system. The sliding control equations are designed for a system in Brunovsky form. Recall that the third order generator can be placed in Brunovsky form:

$$\dot{z}_1 = z_2 \tag{10.1}$$

$$\dot{z}_2 = z_3 \tag{10.2}$$

$$\dot{z}_3 = \rho(\mathbf{z}) + \beta(\mathbf{z})u \tag{10.3}$$

with $\mathbf{z} = [(\delta - \delta_o)\,(\omega - \omega_o)\,\alpha]^T$ and $u = E_{fd}$. The control is designed so that $\mathbf{z}(t)$ will follow a specified trajectory, which we will denote as $\mathbf{z}^*(t)$. The tracking error will be written as:

$$\tilde{\mathbf{z}} = \mathbf{z} - \mathbf{z}^* \tag{10.4}$$

10.1 The Sliding Surface

Sliding control gets its name because the system states move along a time-varying surface. The surface is a function of both time and the state vector $\mathbf{z}(t)$ and is defined as $s(\mathbf{z}, t) = 0$, where [24]:

$$s(\mathbf{z}, t) = \left(\frac{d}{dt} + \lambda\right)^{n-1} \tilde{z}_1 \tag{10.5}$$

where λ is a positive constant and n is the order of the system. In our case, we know that $n = 3$, and therefore:

$$s(\mathbf{z}, t) = \ddot{\tilde{z}}_1 + 2\lambda\dot{\tilde{z}}_1 + \lambda^2\tilde{z}_1 \tag{10.6}$$

which may be written as:

$$s(\mathbf{z},t) = \tilde{z}_3 + 2\lambda\tilde{z}_2 + \lambda^2\tilde{z}_1 \tag{10.7}$$

If the initial state is such that:

$$\mathbf{z}(0) = \mathbf{z}^*(0) \tag{10.8}$$

then the tracking problem $\mathbf{z}(t) = \mathbf{z}^*(t)$ or $\tilde{\mathbf{z}} = \mathbf{0}$ is equivalent to $s(\mathbf{z},t) = 0$. This means that perfect tracking is achieved if equation (10.8) is satisfied and $\mathbf{z}(t)$ remains exactly on the surface for all time. If $\mathbf{z}(0) \neq \mathbf{z}^*(0)$, but $s(\mathbf{z},t) = 0$, then s forms a differential equation in $\tilde{z}_1$ whose solution consists of decaying exponentials. This means that if $\mathbf{z}(t)$ is on the surface for all time, $\mathbf{z}(t)$ approaches $\mathbf{z}^*(t)$ exponentially with a time constant of $(n-1)/\lambda$. When z is on the surface, the system is said to be in sliding mode. The key of sliding control is that a first order problem in s replaces an n-th order vector problem [24].

We therefore desire that $s = 0$ for all time. This constraint will be achieved if the control input u is selected so that, for $s \neq 0$ and a positive constant η:

$$\frac{1}{2}\frac{d}{dt}s^2 \leq -\eta|s| \tag{10.9}$$

This condition means that all system trajectories that are off of the surface must travel toward the surface. The time to reach the surface will be less than $s(t=0)/\eta$ [24]. Furthermore, equation (10.9) guarantees that $\mathbf{z}(t)$ will reach the surface in a finite time, if $\mathbf{z}(0)$ is not on the surface.

10.2 Choosing a Control Input

We can formulate a control law for the sliding controller by differentiating s with respect to time:

$$\dot{s} = \dot{\tilde{z}}_3 + 2\lambda\dot{\tilde{z}}_2 + \lambda^2\dot{\tilde{z}}_1 \tag{10.10}$$

Substituting for the derivatives and setting $\dot{s} = 0$:

$$\rho_d(\mathbf{z}) + \beta_d(\mathbf{z})u - \dot{z}_3^* + 2\lambda\tilde{z}_3 + \lambda^2\tilde{z}_2 = 0 \tag{10.11}$$

where $\rho_d(\mathbf{z})$ and $\beta_d(\mathbf{z})$ represent the estimated values of these quantities that are used by the controller. Solving for $u = u_e$ gives the nominal control input:

$$u_e = \frac{-\rho_d(\mathbf{z}) + \dot{z}_3^* - 2\lambda\tilde{z}_3 - \lambda^2\tilde{z}_2}{\beta_d(\mathbf{z})} \tag{10.12}$$

In order to ensure that u satisfies equation (10.9) despite the presence of uncertainties in $\rho(\mathbf{z})$ and $\beta(\mathbf{z})$, an extra term is added to the control input:

$$u = \frac{-\rho_d(\mathbf{z}) + \dot{z}_3^* - 2\lambda\tilde{z}_3 - \lambda^2\tilde{z}_2 - k\,\mathrm{sgn}(s)}{\beta_d(\mathbf{z})} \tag{10.13}$$

$\text{sgn}(s)$ is the sign function, defined as:

$$\text{sgn}(s) = \begin{array}{ll} 1 & s > 0 \\ -1 & s < 0 \end{array} \tag{10.14}$$

If the error $|\rho(\mathbf{z}) - \rho_d(\mathbf{z})| \leq F$ and $B^{-1} \leq \beta(\mathbf{z})/\beta_d(\mathbf{z}) \leq B$, then the control input will satisfy equation (10.9) if:

$$k \geq B(F + \eta) + (B - 1)|u_e| \tag{10.15}$$

The implementation of equation (10.13) as a control law results in a system that tracks the desired trajectory very closely. However, note that the control input in equation (10.13) is discontinuous across the surface. Consequently, because switching does not occur at an infinite speed, the control will chatter as s rapidly oscillates around zero [24]. In the next section, we will see how to prevent chattering while still maintaining good performance.

10.3 The Boundary Layer

In order to prevent chattering, it is necessary to remove the constraint that s be perfectly zero; instead we will constrain $|s| \leq \Phi$. Conceptually, this means that instead of trying to remain exactly on the surface, we will remain near the surface within a boundary layer of thickness Φ. It can be shown that if $\mathbf{z}(0) = \mathbf{z}^*(0)$ and $|s| \leq \Phi$ for all time, then the tracking error will be limited such that [24]:

$$|\tilde{z}_i(t)| \leq (2\lambda)^i \frac{\Phi}{\lambda^{n-1}} \tag{10.16}$$

If $\mathbf{z}(0) \neq \mathbf{z}^*(0)$, then this bound is approached exponentially with a time constant of $(n-1)/\lambda$ if $|s| \leq \Phi$ for all time.

Outside of the boundary layer, the control law for u is the same as before. To achieve a boundary layer, we simply change the control law to:

$$u = \frac{-\rho_d(\mathbf{z}) + \dot{z}_3^* - 2\lambda\dot{\tilde{z}}_2 - \lambda^2\dot{\tilde{z}}_1 - k\,\text{sat}(s/\Phi)}{\beta_d(\mathbf{z})} \tag{10.17}$$

$\text{sat}(s)$ is the saturation function, defined as:

$$\text{sat}(s) = \begin{array}{ll} 1 & s > 1 \\ -1 & s < -1 \\ s & -1 \leq s \leq 1 \end{array} \tag{10.18}$$

Since equation (10.9) is still satisfied for all points outside the boundary layer, all trajectories must point towards the layer. We will treat the boundary layer thickness Φ as constant, although it can be allowed to vary with time [24].

10.4 Selection of Controller Parameters

The sliding mode controller design includes several parameters. The parameter λ is referred to as the control bandwidth. As shown by equation (10.16), a larger λ results in less tracking error, even if large modeling errors are present. However, the maximum allowable λ is limited by the presence of high frequency unmodeled dynamics and time delays.

The parameter η represents the time required for the states to reach the surface. Note from equation (10.15) that increasing k results in an increase in η, reducing the reaching time. However, a larger k increases the tendency and magnitude of control chattering, which means that a larger Φ will be needed; consequently, the tracking error on the surface will be larger. The boundary layer thickness Φ is generally chosen to be as small as possible while still preventing control chattering [24].

10.5 Sliding Mode Controller Design for a Generator

We are now ready to design a sliding control design for the third order generator model. Because the field voltage can not vary infinitely, the following design is actually a hybrid FBLC/sliding control scheme. First, we choose the desired trajectory to be the response of the following linear system:

$$\dot{\mathbf{z}}^* = \mathbf{A}\mathbf{z}^* \tag{10.19}$$

$$\mathbf{A} = \begin{bmatrix} 0 & 1 & 0 \\ 0 & 0 & 1 \\ a_0 & a_1 & a_2 \end{bmatrix}$$

This is the same system that we were trying to create using FBLC. The trajectory may therefore be written as the following time function:

$$\mathbf{z}^*(t) = e^{\mathbf{A}t}\mathbf{z}(0) \tag{10.20}$$

where we have chosen $\mathbf{z}^*(0) = \mathbf{z}(0)$ so that the control always operates on the surface. Although the calculation of the trajectory seems to be a formidable task, the appropriate time functions are the solutions of the differential equation:

$$z_1^{*(3)} - a_2\ddot{z}_1^* - a_1\dot{z}_1^* - a_0 z_1^* = 0 \tag{10.21}$$

If $a_2 = -15$, $a_1 = -75$, and $a_0 = -125$ (eigenvalues at -5, just as we did with FBLC), the desired trajectory is:

$$z_1^*(t) = A_1 e^{-5t} + A_2 t e^{-5t} + A_3 t^2 e^{-5t} \tag{10.22}$$

$$z_2^*(t) = (-5A_1 + A_2)e^{-5t} + (-5A_2 + 2A_3)te^{-5t} - 5A_3 t^2 e^{-5t} \tag{10.23}$$

$$z_3^*(t) = (25A_1 - 10A_2 + 2A_3)e^{-5t} + (25A_2 - 20A_3)te^{-5t} + 25A_3t^2e^{-5t} \tag{10.24}$$

$$A_1 = z_1(0)$$

$$A_2 = 5z_1(0) + z_2(0)$$

$$A_3 = 12.5z_1(0) + 5z_2(0) + 0.5z_3(0)$$

The controller parameters were selected as $\lambda = 5$, $k = 1$, and $\Phi = 0.25$.

To handle field voltage saturation, the following algorithm was used. Initially, $\mathbf{z}^* = \mathbf{0}$ so that the desired trajectory is at equilibrium and constant for all time. The controller is implemented as a discrete time system with sampling frequency of 100 Hz. At each time step, the controller calculates a new value of E_{fd} using the sliding control laws. If E_{fd} saturates at either limit, then at the next time step, the value of E_{fd} is calculated by the FBLC control law, i.e.:

$$E_{fd} = \frac{\mathbf{a}^T\mathbf{z} - \rho_d(\mathbf{z})}{\beta_d(\mathbf{z})} \tag{10.25}$$

As long as the value of E_{fd} remains saturated, the FBLC control law is applied. When E_{fd} comes out of saturation, the state vector $\mathbf{z}$ at that time step becomes the initial state of the desired trajectory, and sliding control is again applied to the system. Sliding control is maintained as long as E_{fd} does not saturate. In this algorithm, FBLC is used to monitor the field voltage and determine when to restart sliding mode control.

10.6 Simulations of a Sliding Mode Control

In order to examine the effects of torsional dynamics on a sliding mode controller, numerical simulations are performed. The controller is tested by simulating the same 0.5 s fault that was used in earlier simulations. Plots of the simulation results are shown in Figures 10-1 to 10-8. According to the simulations, the response of sliding mode control to torsional oscillations is virtually the same as that of FBLC. The uncertainty in $\rho(\mathbf{x}_g)$ because of torsional oscillations is clearly very large, although because the oscillations are at a high frequency, it appears that they are averaged out by the controller and the resulting performance is no different from FBLC. A plot of $\omega_e - \omega_2$ is given in Figure 10-9; since $\rho(\mathbf{x}_g)$ includes the quantity $K_{2eu}(\omega_e - \omega_2)$, where K_{2eu} is on the order of 10^4, the spring constant terms dominate the quantity $\rho(\mathbf{x}_g)$. Since the uncertainties in $\rho(\mathbf{x}_g)$ are so large, even large changes in the parameters λ, k and Φ of the controller did not affect the simulation results.

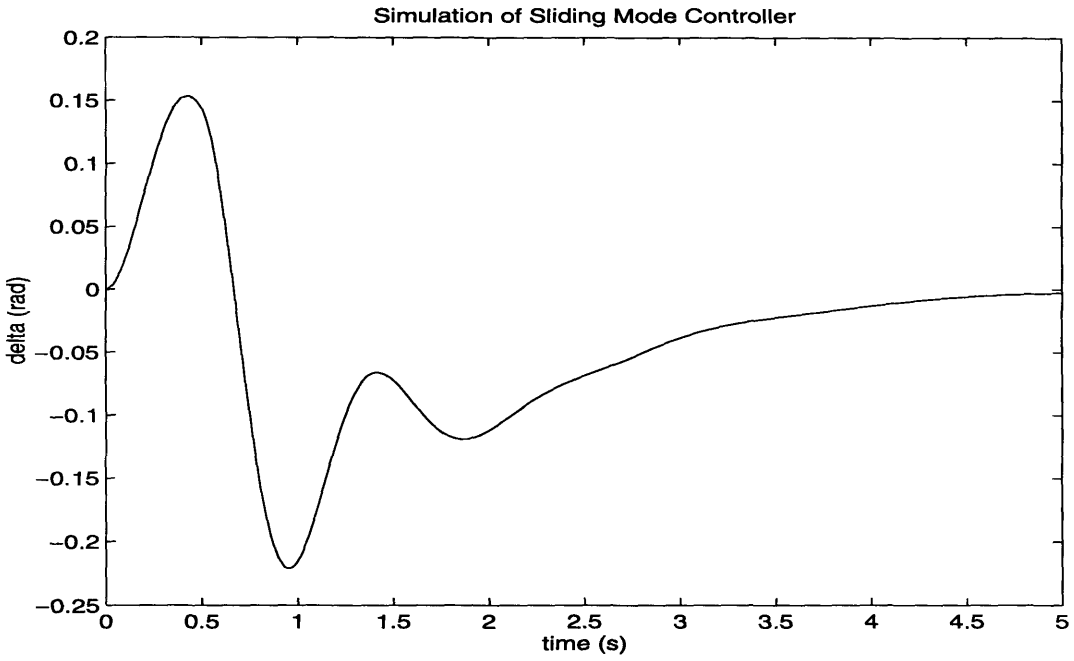

Figure 10-1: Response of $\delta - \delta_o$ to a 0.5 second fault with sliding control.

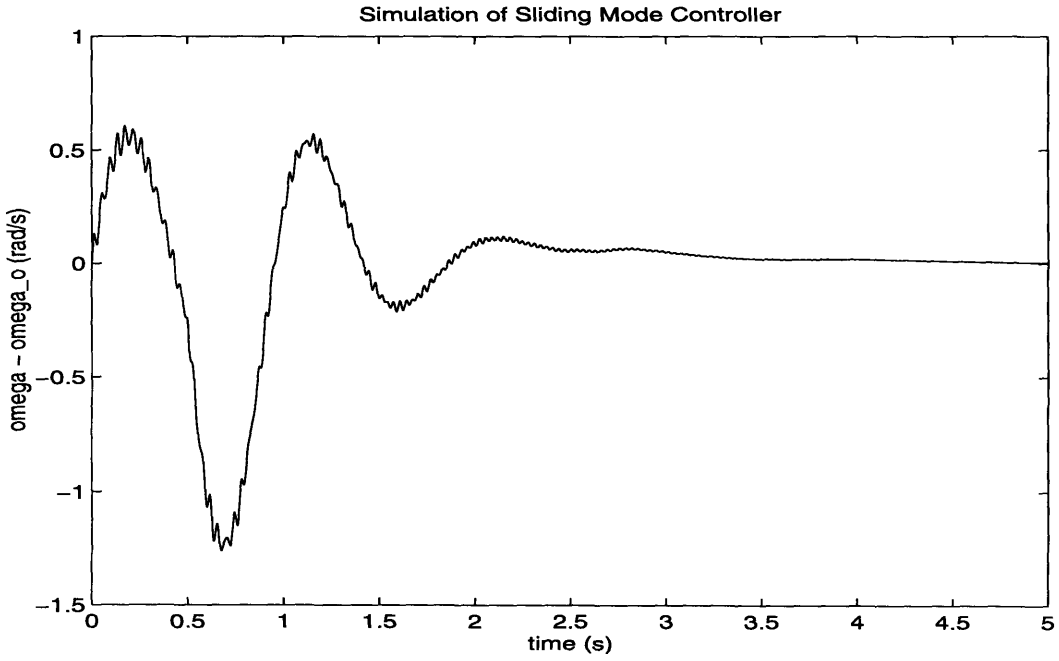

Figure 10-2: Response of $\omega - \omega_o$ to a 0.5 second fault with sliding control.

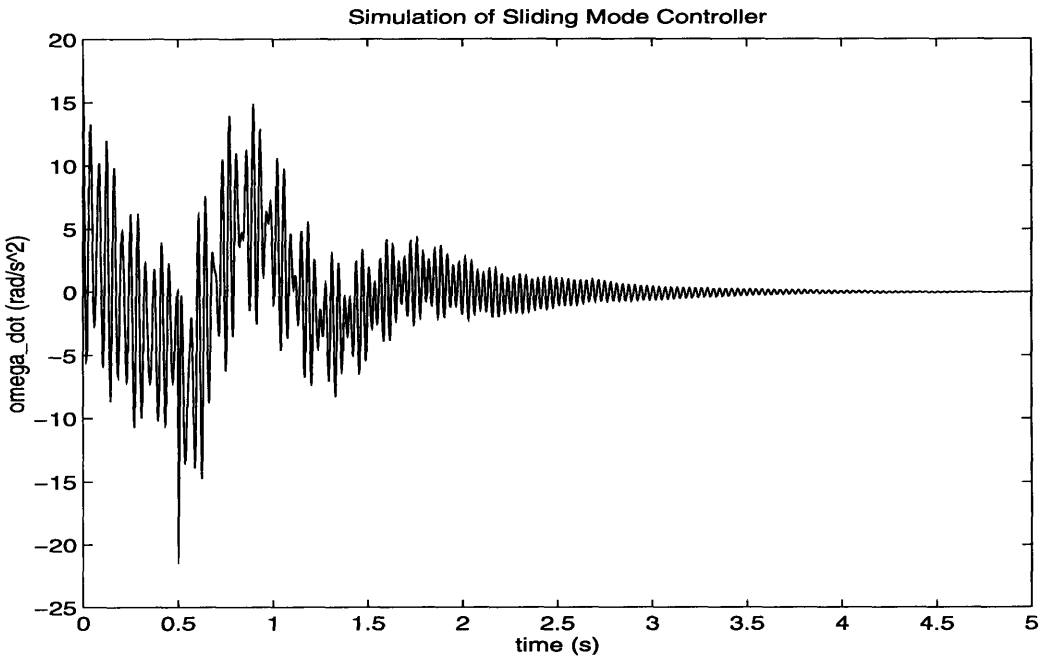

Figure 10-3: Response of $\dot{\omega}$ to a 0.5 second fault with sliding control.

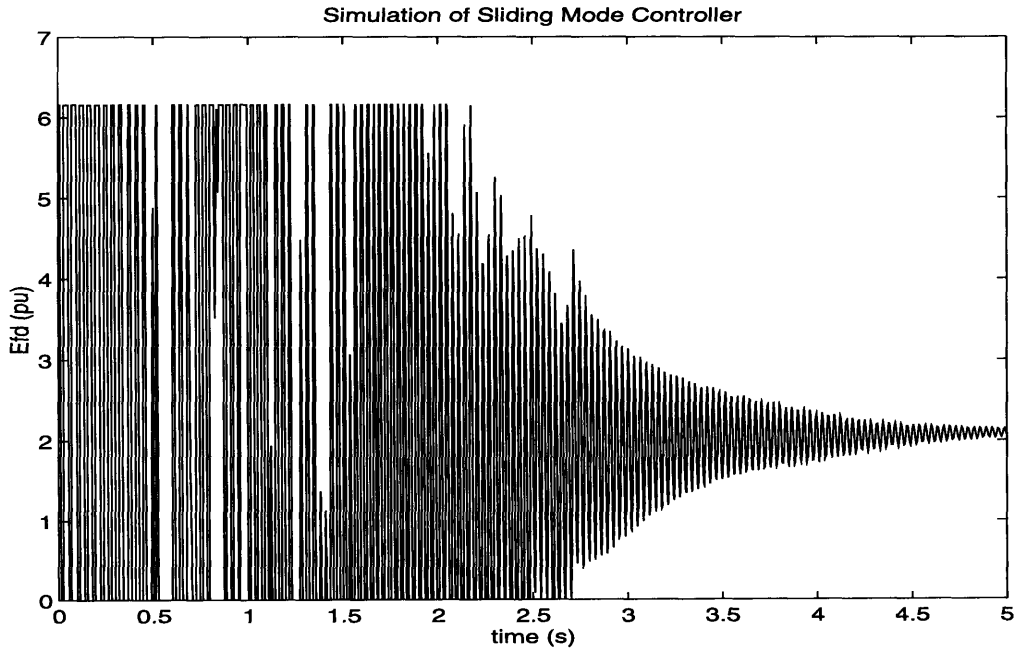

Figure 10-4: Response of E_{fd} to a 0.5 second fault with sliding control.

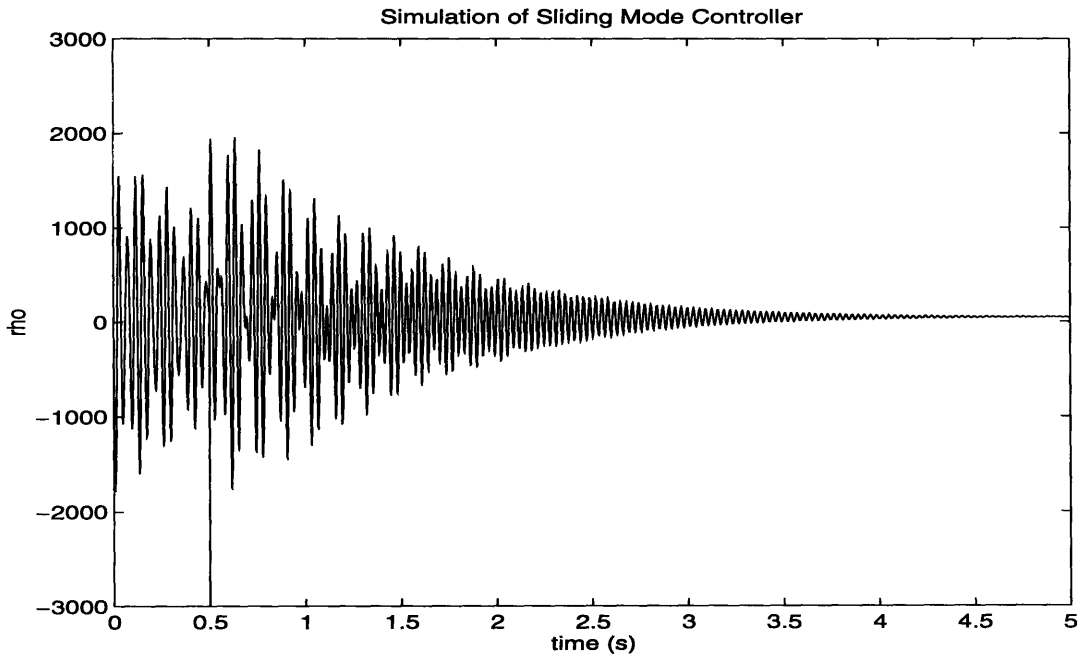

Figure 10-5: Response of $\rho(\mathbf{x}_g)$ to a 0.5 second fault with sliding control.

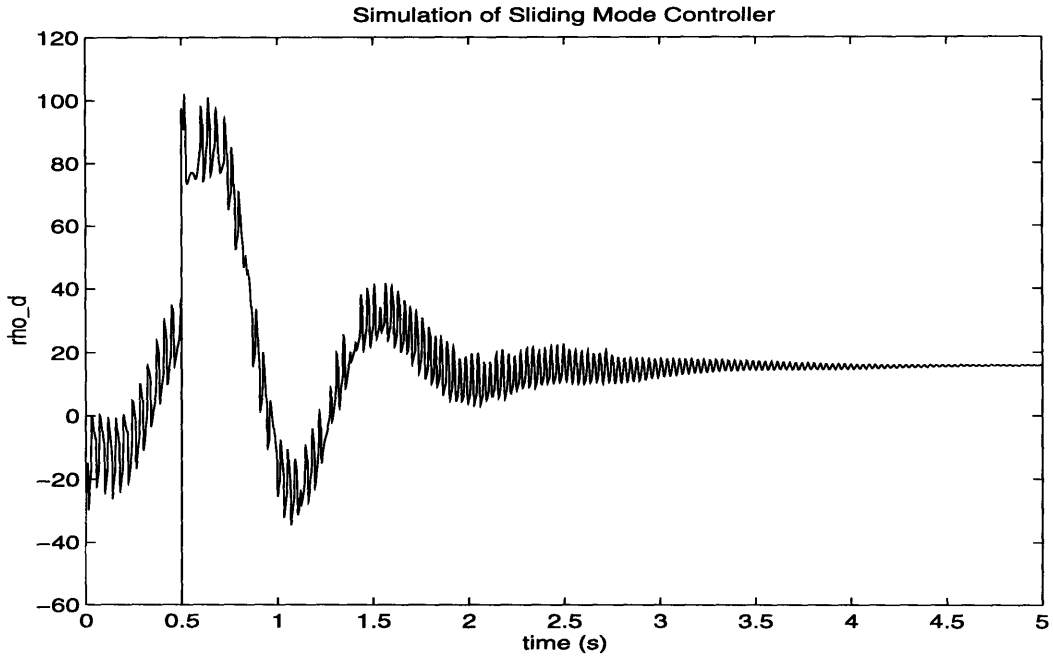

Figure 10-6: Response of $\rho_d(\mathbf{x}_g)$ to a 0.5 second fault with sliding control.

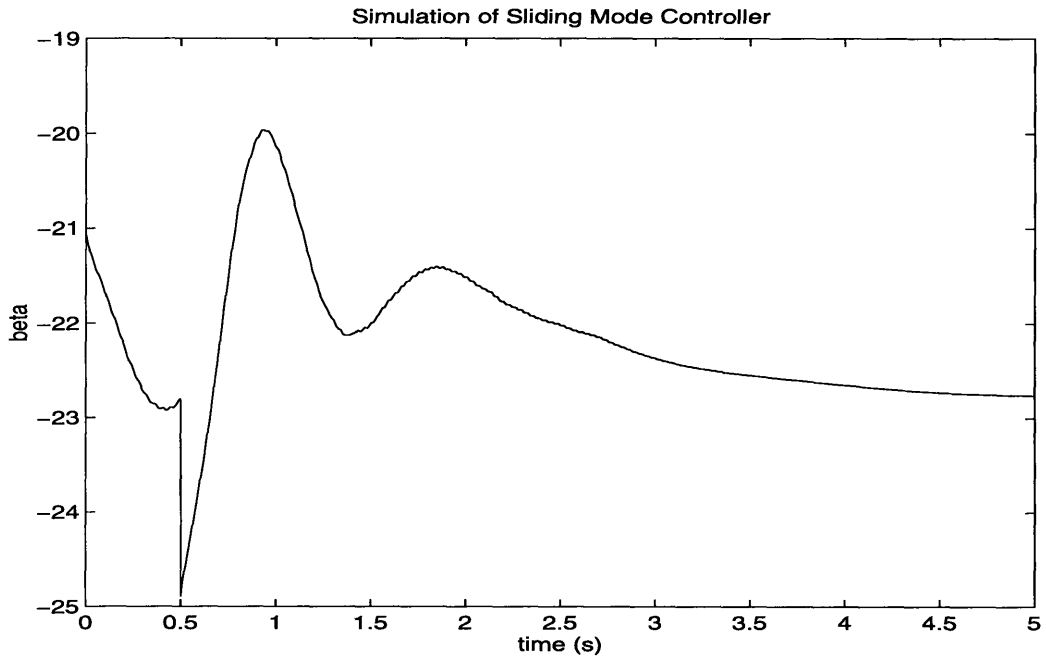

Figure 10-7: Response of $\beta(\mathbf{x}_g)$ to a 0.5 second fault with sliding control.

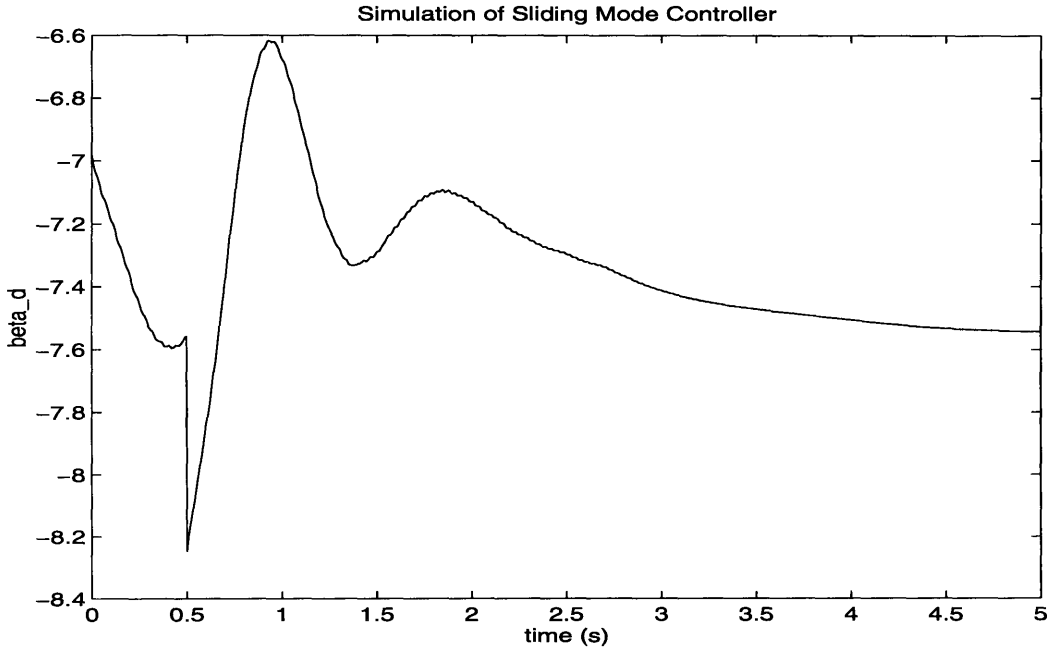

Figure 10-8: Response of $\beta_d(\mathbf{x}_g)$ to a 0.5 second fault with sliding control.

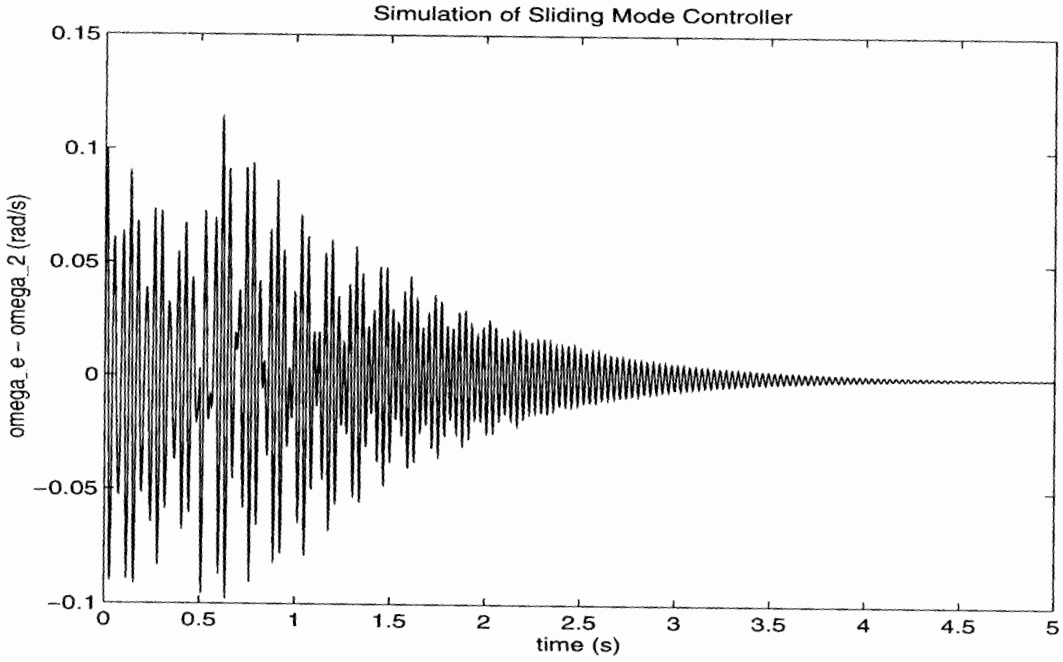

Figure 10-9: Plot of $\omega_e - \omega_2$ for a 0.5 second fault. The speed difference multiplied by K_{2eu} dominates the quantity $\rho(\mathbf{x}_g)$.

Chapter 11

Conclusions

The purpose of this thesis is to determine the effects that torsional shaft oscillations have on nonlinear generator control methods; specifically, feedback linearizing control and sliding mode control. The torsional oscillations are of interest because they greatly influence the acceleration of the generator rotor, and this acceleration measurement is an integral part of nonlinear control methods.

The model that was used to represent the torsional dynamics, which is typical of most models used, has oscillatory modes that are lightly damped. It is both interesting and important that the torsional model couples with the model of an FBLC-controlled generator in such a way that the composite model remains linear. This result is helpful since linear systems are much more easily analyzed and understood than nonlinear systems. The addition of FBLC greatly improves the damping of the shaft modes, a result that is in retrospect not surprising since the placement of the FBLC closed-loop eigenvalues was intended to filter out high frequency disturbances, including frequencies in the torsional range.

Although the theoretical model of feedback linearizing control with torsional dynamics is well behaved, the torsional oscillations create large amplitude oscillations in the field voltage that cause the field voltage to swing rapidly between its upper and lower bounds. Even with the field voltage saturation, the low frequency components of E_{fd} are generally still sufficient to provide a good response to simulated faults, although the time required to return to equilibrium is lengthened with the additional dynamics present.

Since the rail-to-rail swings in E_{fd} are undesirable, an attempt was made to remove these swings by averaging the field voltage over 1/60 of a second. However, the results of this technique were not impressive; in a simulated fault, the rotor angle did not return to equilibrium, and the torsional modes were found to be unstable around equilibrium. In fact, the lack of damping on the torsional modes caused E_{fd} to swing from limit to limit for an even longer time than without the field voltage averaging.

A theoretical, though imperfect, linear model was developed for studying the effects of averaging and explaining the results. The model showed that:

1. The amplitude reduction of the high frequency components of the acceleration eliminates any damping of the torsional modes created by the controller; the only remaining damping is the natural damping in the shaft system itself.

2. The phase shift of the high frequency components resulting from the filtering of the acceleration measurement is capable of exciting the shaft modes and causing instability.

These hypotheses from eigenvalue analysis of the model were confirmed by the simulated results of placing a Butterworth filter on the acceleration measurement. The torsional modes were lightly damped with the presence of any filter on $\dot{\omega}$. The second order Butterworth filter, with a phase shift of -180^o in the stopband excited the torsional modes, while a fourth order Butterworth filter did not excite the modes, since it has a stopband phase shift of -360^o. Therefore, it is clear from the simulations and modeling that lowpass filtering of the field voltage or acceleration measurement is capable of producing an unstable system, although the fourth order Butterworth filter did result in improved performance of FBLC in the simulations.

Another method of compensating for torsional dynamics is to change $\rho(\mathbf{x}_g)$ and $\beta(\mathbf{x}_g)$ in the controller to include torsional state information. For miniscule signals, this method indeed produces the desired results; the response of the generator states is isolated from the torsional states, and the eigenvalues of the linear system are placed at the intended locations. However, the torsional dynamics introduce very large oscillations in $\rho(\mathbf{x}_g)$ and $\beta(\mathbf{x}_g)$; for even a small disturbance, the range of E_{fd} is much too small to provide adequate control, and the generator states are observed to take a long time to return to equilibrium.

FBLC is observed to greatly improve the damping of the shaft dynamics. In fact, this additional damping is strong enough to stabilize a system that would otherwise be unstable due to subsynchronous resonance. If filtering is applied to the acceleration measurement to reduce the field voltage swings, the controller is much less effective at damping torsional modes in this situation, although the controller is able in simulations to limit the amplitude of the shaft oscillations and prevent them from growing indefinitely.

Since it may not be desirable to modify FBLC in order to improve its performance in the presence of shaft dynamics, it is natural to ask whether the torsional dynamics can interact in such a way as to cause FBLC to become unstable. The stability robustness tests strongly suggest that the answer is no, although the proof of this assertion for all possible combinations of shaft parameters has not been shown.

Finally, the sliding mode control is observed to provide no improvement in performance over FBLC. The uncertainties in the model are of large amplitude and high frequency, and the sliding mode controller is unable to compensate for them. Consequently, like FBLC, the low frequency component of the field voltage is able to provide a reasonable response, although the performance is not able to match the results obtained when torsional dynamics are not modeled in the simulations.

Appendix A

Linear Matrix Models of FBLC with Torsional Dynamics

This appendix contains the state matrix of the linear model of feedback linearizing control with torsional dynamics. Also included are the reduced linear models used to examine Butterworth filtering of the acceleration measurement along with the linear model of FBLC with field voltage averaging over 60 Hz. In all cases, the state vector is given by equation (3.39).

Linear model of FBLC with torsional dynamics:

$$\mathbf{A} = \begin{bmatrix} 0 & 1 & 0 & 0 & 0 & 0 & 0 \\ 0 & 0 & 1 & 0 & 0 & 0 & 0 \\ -377.2 & -17564 & -45.39 & 0 & 0 & 0 & 17338 \\ 0 & 0 & 0 & 0 & 1 & 0 & 0 \\ 0 & 0 & 0 & -29009 & -0.13 & 29009 & 0 \\ 0 & 0 & 0 & 0 & 0 & 0 & 1 \\ 10092 & 0 & 0 & 5058 & 0 & -15150 & -0.14 \end{bmatrix} \tag{A.1}$$

Linear model of FBLC with field voltage averaging:

$$\mathbf{A}_{avg} = \begin{bmatrix} 0 & 1 & 0 & 0 & 0 & 0 & 0 \\ 0 & 0 & 1 & 0 & 0 & 0 & 0 \\ -310370 & -21353 & -19.08 & -67123 & 578.1 & 377050 & 20515 \\ 0 & 0 & 0 & 0 & 1 & 0 & 0 \\ 0 & 0 & 0 & -29009 & -0.13 & 29009 & 0 \\ 0 & 0 & 0 & 0 & 0 & 0 & 1 \\ 10092 & 0 & 0 & 5058 & 0 & -15150 & -0.14 \end{bmatrix} \tag{A.2}$$

Reduced linear model of FBLC with first order Butterworth filtering of the accel-

eration measurement:

$$\mathbf{A}_{br1} = \begin{bmatrix} 0 & 1 & 0 & 0 & 0 & 0 & 0 \\ 0 & 0 & 1 & 0 & 0 & 0 & 0 \\ -258500 & -19346 & -19.50 & -11591 & 247.1 & 269680 & 18857 \\ 0 & 0 & 0 & 0 & 1 & 0 & 0 \\ 0 & 0 & 0 & -29009 & -0.13 & 29009 & 0 \\ 0 & 0 & 0 & 0 & 0 & 0 & 1 \\ 10092 & 0 & 0 & 5058 & 0 & -15150 & -0.14 \end{bmatrix} \quad \text{(A.3)}$$

Reduced linear model of FBLC with second order Butterworth filtering of the acceleration measurement:

$$\mathbf{A}_{br2} = \begin{bmatrix} 0 & 1 & 0 & 0 & 0 & 0 & 0 \\ 0 & 0 & 1 & 0 & 0 & 0 & 0 \\ -300450 & -17915 & -11.28 & 14551 & 86.59 & 285500 & 17599 \\ 0 & 0 & 0 & 0 & 1 & 0 & 0 \\ 0 & 0 & 0 & -29009 & -0.13 & 29009 & 0 \\ 0 & 0 & 0 & 0 & 0 & 0 & 1 \\ 10092 & 0 & 0 & 5058 & 0 & -15150 & -0.14 \end{bmatrix} \quad \text{(A.4)}$$

Reduced linear model of FBLC with fourth order Butterworth filtering of the acceleration measurement:

$$\mathbf{A}_{br4} = \begin{bmatrix} 0 & 1 & 0 & 0 & 0 & 0 & 0 \\ 0 & 0 & 1 & 0 & 0 & 0 & 0 \\ -260140 & -17463 & -15.59 & -1731.8 & -32.76 & 261490 & 17271 \\ 0 & 0 & 0 & 0 & 1 & 0 & 0 \\ 0 & 0 & 0 & -29009 & -0.13 & 29009 & 0 \\ 0 & 0 & 0 & 0 & 0 & 0 & 1 \\ 10092 & 0 & 0 & 5058 & 0 & -15150 & -0.14 \end{bmatrix} \quad \text{(A.5)}$$

Bibliography

[1] J. W. Chapman et al, "Stabilizing a Multimachine Power System via Decentralized Feedback Linearizing Control," *IEEE Transactions on Power Systems*, Vol. 8, No. 3, pp. 830-839, August, 1993.

[2] J. Chapman, "Feedback Linearizing Generator Excitation Control for Enhanced Power System Stability," Master's thesis, Electrical Engineering, Massachusetts Institute of Technology, 1992.

[3] F. K. Mak, "Analysis and Control of Voltage Dynamics in Electric Power Systems," Ph.D. thesis, University of Illinois at Urbana-Champaign, 1990.

[4] D. G. Luenberger. *Introduction to Dynamic Systems, Theory, Models, and Applications.* N.Y.: John Wiley and Sons, 1979.

[5] M. Dahleh, 6.241 Class Notes, Massachusetts Institute of Technology, Fall Semester 1994.

[6] The MathWorks, Inc., *SIMULAB User's Guide,* 1990.

[7] P. Anderson, B. Agrawal, and J. Van Ness. *Subsynchronous Resonance in Power Systems.* N.Y.: IEEE Press, 1990.

[8] C. Bowler, D. Ewart, and C. Concordia, "Self Excited Torsional Frequency Oscillations with Series Capacitors," *IEEE Transactions on Power Apparatus and Systems,* Vol. PAS-92, No. 5, pp. 1688-1695, 1973.

[9] J. Ballance and S. Goldberg, "Subsynchronous Resonance in Series Compensated Transmission Lines," *IEEE Transactions on Power Apparatus and Systems,* Vol. PAS-92, No. 5, pp. 1649-1658, 1973.

[10] D. Walker, C. Bowler, and R. Jackson, "Results of Subsynchronous Resonance Test at Mohave," *IEEE Transactions on Power Apparatus and Systems,* Vol. PAS-94, No. 5, pp. 1878-1886, 1975.

[11] M. Jackson, "Effects of System Disturbances and Breaker Operations on Turbogenerator Shaft Systems," Electrical Engineer's thesis, Electrical Engineering, Massachusetts Institute of Technology, 1978.

[12] J. W. Chapman and M. Ilić, "Large-Signal Generator Control and its Impact on Improved Power Transfer Flexibility," Final report, ESEERCO Project EP90-45, Laboratory for Electromagnetic and Electronic Systems, Massachusetts Institute of Technology, September 1993.

[13] Power Technologies, Inc., "PTI Power System Simulator, PSS/E, GENROU (Round Rotor Generator Model)," data sheet.

[14] P. Kokotović, H. K. Khalil, and J. O'Reilly, *Singular Perturbation Methods in Control: Analysis and Design,* Academic Press, Orlando, FL, 1986.

[15] H. Anton and C. Rorres. *Elementary Linear Algebra, Applications Version, Sixth Edition.* N.Y.: John Wiley and Sons, 1991.

[16] I. J. Pérez-Arriaga, G. C. Verghese, and F. C. Schweppe, "Selective Modal Analysis with Applications to Electric Power Systems, Part I: Heuristic Introduction," *IEEE Transactions on Power Apparatus and Systems,* Vol. PAS-101, No. 9, pp. 3117-3134, 1982.

[17] R. S. Burington. *Handbook of Mathematical Tables and Formulas, Third Edition.* Sandusky, OH: Handbook Publishers, 1948.

[18] A. V. Oppenheim and A. S. Willsky with I. T. Young. *Signals and Systems.* Englewood Cliffs, NJ: Prentice-Hall, 1983.

[19] R. Bodine, C. Concordia, and G. Kron, "Self-Excited Oscillations of Capacitor-Compensated Long-Distance Transmission Systems," *AIEE Transactions,* Vol. 62, pp. 41-44, 1943.

[20] H. Rustebakke and C. Concordia, "Self-Excited Oscillations in a Transmission System Using Series Capacitors," *IEEE Transactions on Power Apparatus and Systems,* Vol. PAS-89, No. 7, pp. 1504-1512, 1970.

[21] L. Kilgore, L. Elliott, and E. Taylor, "The Prediction and Control of Self-Excited Oscillations Due to Series Capacitors in Power Systems," *IEEE Transactions on Power Apparatus and Systems,* Vol. PAS-90, No. 3, pp. 1305-1311, 1971.

[22] M. Ilic and J. Zaborsky, "Dynamics and Control of the Large Electric Power Systems," 6.686 class notes, Massachusetts Institute of Technology, Fall Semester 1994.

[23] B. R. Barmish. *New Tools for Robustness of Linear Systems.* N.Y.: Macmillan Publishing Company, 1994.

[24] J. J. E. Slotine and W. Li. *Applied Nonlinear Control.* Englewood Cliffs, NJ: Prentice-Hall, 1991.